Vegetal Route for the Synthesis of Iron Oxide and its Composite Nanostructures for Cr(VI) Decontamination

A

Thesis Submitted

In Fulfilment of the Requirements

for the degree of

DOCTOR OF PHILOSOPHY

by

Aquib Jawed

(Roll no. 176152009)

Under the supervision of

Prof. Lalit Mohan Pandey & Prof. Animes Kumar Golder

June - 2024

Centre for the Environment

Indian Institute of Technology Guwahati

Guwahati-781039, Assam, India

Dedicated

To

My Parents

INDIAN INSTITUTE OF TECHNOLOGY GUWAHATI

भारतीय प्रौद्योगिकी संस्थान गुवाहाटी

Center for the environment, Guwahati 781039, Assam, India

पर्यावरण केंद्र, गुवाहाटी 781039, असम, भारत

DECLARATION

It is to declare that the content embodied in this thesis entitled **"Vegetal Route for the Synthesis of Iron Oxide and its Composite Nanostructures for Cr(VI) Decontamination"** is the result of investigations carried out by me at the **Centre for the Environment, Indian Institute of Technology, Guwahati, Assam, India** under the supervision of **Prof. Lalit Mohan Pandey** & **Prof. Animes Kumar Golder** for the award of the **Doctor of Philosophy**. The work has not been submitted elsewhere for any degree or diploma of any institute or university. I wish to state that to the best of my knowledge and undertaking nothing in this report amounts to plagiarism.

In keeping with the general practice of reporting scientific observations, due acknowledgements have been made wherever the work described is based on the findings of other investigators.

Date: 21st June 2024

Aquib Jawed

Centre for the Environment

Indian Institute of Technology, Guwahati

Guwahati – 781039, Assam, India

INDIAN INSTITUTE OF TECHNOLOGY GUWAHATI

भारतीय प्रौद्योगिकी संस्थान गुवाहाटी

Center for the environment, Guwahati 781039, Assam, India

पर्यावरण केंद्र, गुवाहाटी 781039, असम, भारत

CERTIFICATE

This is to certify that the thesis entitled **"Vegetal Route for the Synthesis of Iron Oxide and its Composite Nanostructures for Cr(VI) Decontamination"** submitted by **Mr. Aquib Jawed (Roll No.: 176152009)** for the award of the **degree of Doctor of Philosophy,** is an authentic record of results obtained from the research work carried out under the supervision and guidance at the **Centre for the Environment, Indian Institute of Technology Guwahati, Assam, India.** The thesis has fulfilled all requirements as per the regulations of the Institute and has reached the standard required for submission. The work documented in this thesis has not been submitted to any other University or Institute for the award of any degree.

Prof. Lalit Mohan Pandey
(Thesis Supervisor)
Professor
Department of Bioscience and Bioengineering
IIT Guwahati
Guwahati – 781039
Assam, India

Prof. Animes Kumar Golder
(Thesis Supervisor)
Professor
Department of Chemical Engineering
IIT Guwahati
Guwahati – 781039
Assam, India

ACKNOWLEDGEMENT

First and foremost, I am the most profound gratitude to my Ph.D. supervisors, **Prof. Lalit Mohan Pandey** and **Prof. Animes Kumar Golder** for believing in me and providing me the opportunity to work on such an excellent topic. I am very much inspired by their rich experience and knowledge and approach to problems, immense patience, and extreme care. They have taught me, both consciously and unconsciously, the importance of hard work and patience. I am highly obligated to them for their persistent devotion and willingness. I could not have imagined having a better advisor and mentor than them. I enjoyed every moment of working under their supervision and learned many things from them. It is truly a dream come true for me to have them as supervisors.

I would like to thank my Doctoral Committee members, **Prof. Debasish Das (committee chairman)** from the Department of Biosciences and Bioengineering, **Prof. Pankaj Tiwari** from the Department of Chemical Engineering and **Prof. Soumen Kumar Maiti** from the Department of Biosciences and Bioengineering for their research-oriented teaching, which helped me during my Ph.D. I take this opportunity to thank all the faculty members for their valuable suggestions and cooperation during my course work.

I would like to thank former Directors **Prof. T. G. Sitharam**, **Prof. Rajeev Ahuja** and current Director **Prof. Devendra Jalihal,** IITG, for providing the necessary facilities and a conducive academic environment.

I am highly obliged to the **Centre for The Environment**, Indian Institute of Technology Guwahati, for giving me this opportunity to be a part of this prestigious Institution. I am extremely grateful to the former Heads of the Centre for the Environment **Prof. Vikas Kumar Dubey**, **Prof. Mihir Kumar Purkait, Prof. Utpal Bora** and current Head **Prof. Animes Kumar Golder**, all faculty members, scientific officer **Dr. Deepmoni Deka**, technical staffs **Dr. Partha Protim Bakal**, **Mr. Supriyo Kumar Das**, **Mr. Kaustubh Rakshit** and **Mr. Mridul Das** for their kind co-operation during the entire course of my research period. My acknowledgment also goes to the **Ministry of Human Resource Development (MHRD)**, India for financial support throughout my research tenure.

I am very thankful to the **Central Instrument Facility** of the Indian Institute of Technology Guwahati for allowing me to conduct my analyses using various sophisticated instruments such as FESEM, FETEM, BET, DSC/TGA, XRD, XPS, and FESEM-EDS which has been very important in this research work. In this regard, I would like to acknowledge all the members of CIF for their assistance.

I would also thank **Commonwealth Commission, UK**, for providing me with the Commonwealth Split-site Fellowship-2019. My great appreciation goes to **Dr. K. H. Aaron Lau** for accepting the proposal for hosting me as a Commonwealth Scholar in his lab. I thank all the lab members of the K. H. Aaron Lau research group at the University of Strathclyde for making my stay at Glasgow pleasant. A special mention goes to Dr. Abshar Hasan, Dr. Varun Saxena, Dr. Smruti Ranjan Dash and Mr. Mano Balaji Gandhi to be my constant mental support and made the stay in Glasgow stress free and enjoyable.

I also extend my special thanks to my seniors **Dr. Abshar Hasan**, **Dr. Poulami Datta**, **Dr. Varun Saxena, Dr. Rahul Verma and Dr. Swati Sharma** for their guidance in the initial days of my research. They helped me by providing the proforma of annual progress reports, synopsis reports and various presentations. I appreciate the efforts of my lab-mates **Dr. Pagidi Madhukar, Mrs. Gayatri**, **Mr. Aman**, **Mr. Rushikesh**, **Mr. Vivek**, **Mr. Anurag, Ms. Mehak, Mr. Chinmaya, Ms. Shalini, Ms. Smrity, Ms. Debsmita**, **Mr. Akshay**, **Mr. Gyan**, **Mr. Ravi** and **Mr. Mohit** from the **Biointerface and Environmental Engineering (BIEEL) laboratory**.

Finally, I would like to express my sincere gratitude to my family, father **Sri Mohd Nazim**, mother **Smt. Naeema Begum** and brother **Rameez Raja** whose blessings and never-ending support are the real stimulus that constantly inspires me to do my best.

I would like to thank all the people who contributed in some way to the work described in this thesis and supported me in completing my Ph.D. Working on this Ph.D. has been an unforgettable experience for me and it would not be possible without these people.

Above all, I would like to thank the "**Almighty GOD**" for blessing me and providing me the unseen moral support that directed me through my good as well as hard times.

Aquib Jawed

Abstract

Access to clean water is vital for all living organisms, including humans. Nevertheless, due to industrial and human activity, many harmful contaminants are being discharged into water sources in enormous quantities. Hexavalent chromium is a prime example of this type of pollutants. Many diseases, including cancer, have been linked to exposure to hexavalent chromium. The World Health Organization and the Indian Standard (IS:10500) have established a permissible limit for hexavalent chromium in drinking water at 0.05 mg/L.

Removal of Cr(VI) through its adsorption, specifically using nanoparticles synthesized from green sources (plant part extract), is an environmentally benign technology that does not require harmful chemicals. This doctoral study utilizes phytochemicals from matured Tea (*Camellia sinensis var. Assamica*) leaves extract and polyphenols (tannic acid) to synthesize engineered Iron oxide nanoparticles (IONPs) for the adsorption of hexavalent chromium from aqueous solution. Chapter 1 and Chapter 2 demonstrate the introduction and literature review on various Cr(VI) removal methods, along with a brief overview of green synthesized IONPs, specifically for chromium removal.

Chapter 3 focuses on producing and investigating IONPs from tea leaves extract of *Camellia sinensis var. assamica* for Cr(VI) removal from aqueous solution. The conditions for IONPs synthesis (time, temperature, and iron precursors/leaves extract ratio (v/v)) were optimized using the RSM-CCD to achieve IONPs of the desired quality. The various removal conditions (pH, temperature, contact time, doses, and initial Cr(VI) concentration) of Cr(VI) through synthesized IONPs were also optimized. The kinetics, thermodynamics, and isotherm analysis were performed based on experimental outcomes. The adsorption process followed a pseudo-second-order kinetic and Langmuir adsorption isotherm, with a remarkably higher maximum adsorption capacity of 1272 mg g^{-1} of IONPs.

In Chapter 4, reusable and bi-functional composite chitosan (CS) beads (CS/IONPs) were developed by infusing IONPs in the CS matrix and applied for Cr(VI) adsorption and detoxification from synthetic wastewater. The adsorption parameters such as pH, temperature, contact time, doses, and initial Cr(VI) concentration were optimized. At the optimized conditions (pH 3, 25°C, 480 min, 2.5 g/L of CS/IONPs beads, and 150 mg/L of Cr(VI)), 98.71% removal of Cr(VI) was observed. The synthesized adsorbent (CS/IONPs) was tested for reusability, and a gradual decay was perceived in Cr(VI) removal within 5^{th} cycles of adsorption.

In Chapter 5, the investigation focuses on synthesizing multifunctional beads utilizing sodium alginate (Alg) and tannic acid (TA). These formed Alg-TA beads possess distinctive properties, including metal(s) ion adsorption, antimicrobial effects, and metal particle generation. In addition, the ability of the Alg-TA beads to convert Fe(III) into Fe complexes or IONPs contained within them was demonstrated for enhanced Cr(VI) removal and antibacterial performance from aqueous solution. Thus, formed Alg-TA75-Fe beads facilitates the removal of 95% Cr(VI) from 20 mg/L aqueous solution at pH-4 and a dosage of 2 g/L, respectively. Also, Alg-TA75-Fe beads improved antibacterial performance by 3.89 and 1.37 times for *E.coli* and *E.hirea*, respectively, compared to Alg-TA75 beads.

Chapter 6 investigates on CS/IONPs and Alg-TA55-Fe adsorbent beads for Cr(VI) removal in a fixed-bed column from an aqueous solution. The study focuses on the effect of different column parameters, specifically bed heights and flow rates. The duration of the breakthrough time (t_b) was increased from 5 to 22 h and 0.75 to 4.5 h with an increase in bed height from 5 to 15 cm at a flow rate of 1 mL/min for CS/IONPs and Alg-TA55-Fe beads, respectively. On the other hand, when the flow rate increased from 1 to 3 mL/min, the t_b values for CS/IONPs and Alg-TA55-Fe beads dropped from 5 to 1.5 h and 0.75 to 0.37 h, respectively. A maximum bed capacity of 391.9 and 60 mg g^{-1} was achieved with a 5 cm bed height and 1 mL/min flow rate at a fixed 20 mg/L Cr(VI) influent concentration for CS/IONPs and Alg-TA55-Fe beads, respectively. The adsorption data was well-fitted to various known fixed-bed adsorption models, including the Yoon-Nelson, Thomas, Adams-Bohart, Clark, and Bed Depth Service Time models. The adsorbents (CS/IONPs and Alg-TA55-Fe) were regenerated in the same column for two cycles of Cr(VI) re-adsorption performance. The reusability studies revealed that CS/IONPs beads outperformed Alg-TA55-Fe beads due to its high Cr(VI) adsorption performance in batch mode, exhibiting a longer breakthrough time and high adsorption capacity.

Keywords: Nature-inspired process; Plant-based polyphenols; Iron oxide nanoparticles; Central composite design; Green synthesis process; Cr(VI) adsorption; Bi-functional composite adsorbent; Cr(III) co-precipitation; Hydrogel beads; Antibacterial functionality; Fixed-bed column; Breakthrough curve; Adsorbent regeneration and reuse

Table of Contents

List of Tables

List of Figures

Abbreviations

AAE	Ascorbic Acid Equivalent
Alg	Alginate
BDST	Bed Depth Service Time
BET	Brunauer–Emmett–Teller
CCD	Central Composite Design
CPCB	Central Pollution Control Board
CS	Chitosan
Cr	Chromium
D-R	Dubinin- Radushkevich
ECGC	Epigallocatechin Gallate
EDS	Energy dispersive X-ray Spectroscopy
Eq	Equation
FESEM	Field Emission Scanning Electron Microscope
FETEM	Field-Emission Transmission Electron Microscope
FRP	Ferric Reducing Power
FTIR	Fourier Transform Infrared Spectroscopy
g	grams
GAE	Gallic Acid Equivalent
Cr(VI)	Hexavalent Chromium
IONPs	Iron Oxide Nanoparticles
IPD	Intra-Particle Diffusion
PFO	Pseudo-First-Order
PSO	Pseudo-Second-Order
QE	Quercetin Equivalent
RMSE	Root Mean Square Error
R-P	Redlich-Peterson
SFR	Scavenge Free Radicals
SRSC	Superoxide Radical Scavenging Capacity
TA	Tannic acid

TFC	Total Flavonoid Content
TPC	Total Polyphenolic Content
UV-Vis	Ultraviolet–Visible Spectroscopy
BDST	Bed Depth Service Time
BIS	Bureau of Indian Standard
h	Hour
HPLC	High Performance Liquid Chromatography
min	Minutes
MW	Molecular Weight
NPs	Nanoparticles
nZVI	Nano zero valent iron NPs
OD	Optical Density
ppm	Parts Per Million
rpm	Revolutions Per Minute
RSM	Response Surface Methodology
t	Time
Temp	Temperature
TGA	Thermal Gravimetric Analysis
USEPA	U.S. Environmental Protection Agency
WHO	World Health Organization
XRD	X-ray Powder Diffraction

Symbols

q_e	Adsorption Capacity at Equilibrium Time (mg g^{-1})
q_t	Adsorption Capacity at Time t (mg g^{-1})
n	Adsorption Intensity (L g^{-1})1/n
K_B	Bed Depth Service Time Rate Constant (L min^{-1} g)
D	Diameter of Adsorption Column (cm)
H	Height of Adsorption Column (cm)
h	Bed Height (cm)
K_{BA}	Bohart-Adams Rate Constant (L mg^{-1} h^{-1})
ΔH	Change in Enthalpy (J mol^{-1})
ΔS	Change in Entropy (J mol^{-1} K^{-1})
ΔG	Change in Gibbs free energy (J mol^{-1})
r	Clark model constant (min^{-1})
t_b	Column Breakthrough Time (h)
t_e	Column Exhaustion Time (h)
t_s	Column Saturation Time (h)
R^2	Correlation Coefficient
°C	Degree Celsius
W_d	Dry weight (g)
β	Dubinin-Radushkevich Constant (mol^2 J^{-2})
V_{eff}	Effluent Volume Leaving the Column (L)
β	Elovich Model Desorption Constant (g mig^{-1})
α	Elovich Model Initial Adsorption Rate (mg g min^{-1})
EBCT	Empty Bed Contact Time (min)
EBV	Empty Bed Volume
C_e	Equilibrium Concentration of Adsorbate (mg/L)
q_{eq}	Equilibrium Metal Adsorption Capacity of the column (mg g^{-1})
Q	Flow Rate (mL/min)
K_F	Freundlich Constant (mg g^{-1})
>	Greater than

C_0	Initial concentration of Adsorbate (mg/L)
K_L	Langmuir Isotherm Constant (L mg^{-1})
Q_m	Maximum Adsorption Capacity (mg g^{-1})
E	Mean Adsorption Energy (KJ mol^{-1})
%	Percentage
ε	Polanyi Potential (J mol^{-1})
k_1	Pseudo-First-Order Rate Constant (min^{-1})
k_2	Pseudo-Second-Order Rate Constant (g mg^{-1} min^{-1})
$q_{ads,t}$	Quantity of Adsorbate Adsorbed onto the Column (mg)
$q_{in,t}$	Quantity of Adsorbate in the Column (mg)
$q_{out,t}$	Quantity of Unadsorbed Adsorbate in the Column (mg)
K_{RP}	Redlich-Peterson adsorption capacity constant (L g^{-1})
α_{RP}	Redlich-Peterson Isotherm Constant (L mg^{-1})g
K_S	Sips Isotherm Constant (L mg^{-1})
<	Smaller than
b_T	Temkin Constant Related to the Heat of Sorption (J mol^{-1})
A_T	Temkin Isotherm Constant (L g^{-1})
T	Temperature (K)
K_{TH}	Thomas Rate Constant (L mg^{-1} h)
R	Universal Gas Constant (8.314 J mol^{-1} K^{-1})
V	Volume of Solution (L)
W	Weight of the Adsorbent (g)
W_T	Wet weight (g)
K_{YN}	Yoon-Nelson Rate Constant (min)

Chapter 1

Background of the Work

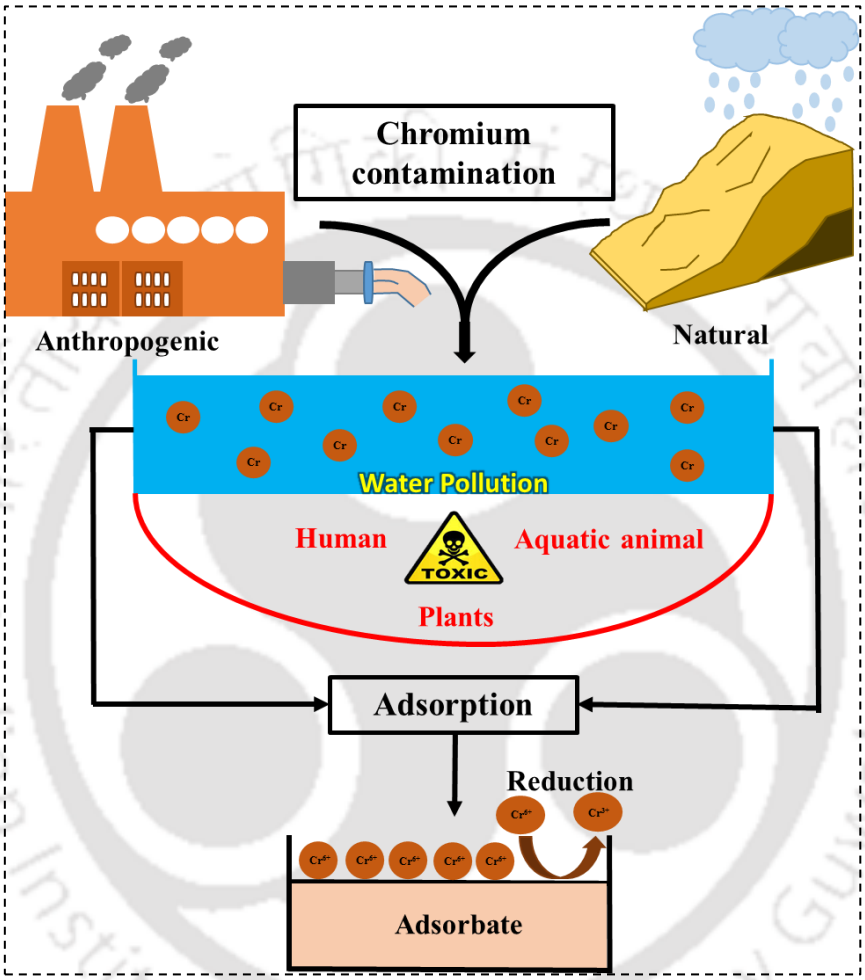

This chapter provides a background on the current work as well as an outline of an understanding of chromium contamination and its remedial methods.

1.1. Background

Potable water is an essential requirement for all living species, including humans. In addition to consumption, water is required for various other functions such as household, industrial, and agricultural needs. Since the dawn of civilization, humans have embarked on a quest to uncover the valuable resources concealed within the depths of the earth, such as natural

gas, petroleum, and mineral ores. Consequently, the industrial revolution occurred in various fields, resulting in the rise of mining activities and the further generation of different toxic chemicals. The issue of effectively addressing these produced harmful chemicals and their byproducts remained unresolved. As a result, significant quantities of hazardous chemicals, metals, dyes, and similar substances were discharged directly into aquatic streams like rivers. Humans have been compelled to create pollution due to a lack of alternatives. Pollution refers to the release of unwanted hazardous compounds into the environment, including heavy metals, pigmenting agents, chemicals, etc.

Heavy metals are naturally occurring elements with a high atomic weight and at least five times the density of water [1]. Based on this definition, the list of heavy metals includes Lead, Chromium, Zinc, Copper, Iron, Platinum, and many others. Chromium (Cr) has garnered significant attention due to its widespread use, impact on the environment, and considerable health risks, including cancer. Cr is a noxious heavy metal which typically exists in an aqueous system in two stable oxidation states: Cr (III) and Cr(VI). Cr(VI) has been categorized as one of the 20 most dangerous chemicals that pose a significant risk to the general public well-being [2]. Cr(VI) is a known carcinogen that emanates from a variety of industrial effluents such as electroplating [3], manufacturing of chromate [4], leather processing [5], alloy manufacturing [6], and textile [7] with concentration varying between a wide range (0.5 - 270,000 mg/L) [8]. Additionally, Cr enters surface waters via various natural means like the erosion of rocks and volcanic eruptions [9]. Cr pollution has become a significant concern in India and globally [10]. Highly soluble Cr(VI) oxyanions, namely, CrO_4^{2-} and $Cr_2O_7^{2-}$, are the most common forms of Cr(VI) and cause extremely carcinogenic (Group 1 as per World Health Organization) and mutagenic health effects [11]. Cr(III) can cause membrane disturbances in erythrocytes and skin irritation. However, it is vital for regulating the metabolism of proteins, lipids, and carbohydrates. On the other hand, Cr(VI) is 500 times more hazardous than Cr(III) [12]. Also,

the higher mobility of Cr(VI) allows it to penetrate through skin cells, where it could generate reactive oxygen species leading to the damage of DNA [13]. The existence of Cr(VI) in soil and waterbodies causes its ubiquitous exposure to the ecosystem and seriously affects the likelihood of humans.

Various strategies have been employed to remove Cr(VI) from polluted water, including membrane filtration, photocatalysis, chemical precipitation, ion exchange, electrocoagulation, and adsorption [14-16]. Nevertheless, it is noteworthy that many of these technologies come with inherent challenges, such as high operational and maintenance costs, limited effectiveness in metal removal, substantial energy demands, and the generation of hazardous residual metal sludge, which presents a significant challenge in terms of proper disposal [17]. Given the current situation, adsorption is the most straightforward and economically efficient approach for wastewater containing Cr(VI) [18]. However, a substantial cost associated with commercially available adsorbents is one of the main challenges of the adsorption process. Consequently, developing affordable nanoadsorbents through environmentally friendly synthesis methods has become a prominent goal for many researchers and scientists [19].

The present thesis explores the utilization of green synthesized Iron oxide and its composite nanostructures for the removal of Cr(VI) from synthetic wastewater through adsorption. Firstly, tea leaves extract-mediated synthesis of Iron oxide nanoparticles (IONPs) were synthesized and applied to remove Cr(VI) from the aqueous solution. In addition, the IONPs were ex-situ infused in the chitosan (CS) matrix to form reusable CS/IONPs beads for the removal of Cr(VI). Also, tannic acid (TA) mediated IONPs were formed over sodium alginate (Alg) beads to enhance their Cr(VI) removal capability and antibacterial functionality. Moreover, the synthesized CS/IONPs and Alg-TA-Fe beads were subsequently employed as the adsorbent material in a fixed-bed adsorption column for the removal of Cr(VI).

1.2. Objectives

In order to address the knowledge lacuna identified in Chapter 2, this thesis has the following objectives:

i. To develop a vegetal route for the synthesis of iron oxide nanoparticles (IONPs) by using *Camellia sinensis var. assamica* leaf extract for Cr(VI) adsorption

ii. To infuse IONPs into chitosan (CS) matrix for the formulation of reusable CS/IONPs composite adsorbents for Cr(VI) removal

iii. To develop tannic acid (TA) assisted IONPs/sodium alginate (Alg) composite adsorbent (Alg-TA-Fe) for simultaneous Cr(VI) uptake and antibacterial functionality

iv. To investigate CS/IONPs and Alg-TA-Fe beads in a continuous adsorption process for the decontamination of Cr(VI)

1.3. Thesis Outline

The thesis has been organized into seven chapters in accordance with the four objectives listed above. A chapter-wise thesis outline is presented as follows.

Chapter 2

This chapter provides an overview of water contamination, treatment through nanoadsorbents, and different synthesis methods of nanoparticles. A brief review on green synthesis of IONPs and using them to remove hexavalent chromium from contaminated water is presented in this chapter.

Chapter 3

Chapter 3 focused on producing and investigating IONPs from tea leaves extract of *Camellia sinensis var. assamica* for Cr(VI) removal from aqueous solution. The conditions for IONPs synthesis (time, temperature, and iron precursors/leaves extract ratio (v/v)) were

optimized using the Response Surface Methodology-Central Composite Design (RSM-CCD) to achieve IONPs of desired quality.

Chapter 4

In Chapter 4, reusable and bi-functional composite CS beads (CS/IONPs) were developed by infusing IONPs in the CS matrix and applied for Cr(VI) adsorption and detoxification from synthetic wastewater. The reusability of synthesized CS/IONPs beads was evaluated in terms of the number of adsorption cycles.

Chapter 5

In Chapter 5, the investigation focused on synthesizing multifunctional beads utilizing Alg and TA. These formed Alg-TA beads possess distinctive properties, including metal(s) adsorption, antimicrobial effects, and metal particle generation. In addition, we demonstrate the ability of the Alg-TA beads to convert iron (Fe) salts into IONPs contained within them (Alg-TA-Fe) for enhanced Cr(VI) removal and antibacterial performance from aqueous solutions.

Chapter 6

Chapter 6 employed CS/IONPs and Alg-TA-Fe adsorbent beads for Cr(VI) removal in a fixed-bed column from an aqueous solution. The study investigated the impact of different column parameters, specifically bed heights and flow rates.

Chapter 7

The salient findings of the present investigation are summarized in this Chapter. The recommendations for future work directions are appended at the end of this chapter.

Chapter 2

Review of Literature and Objectives

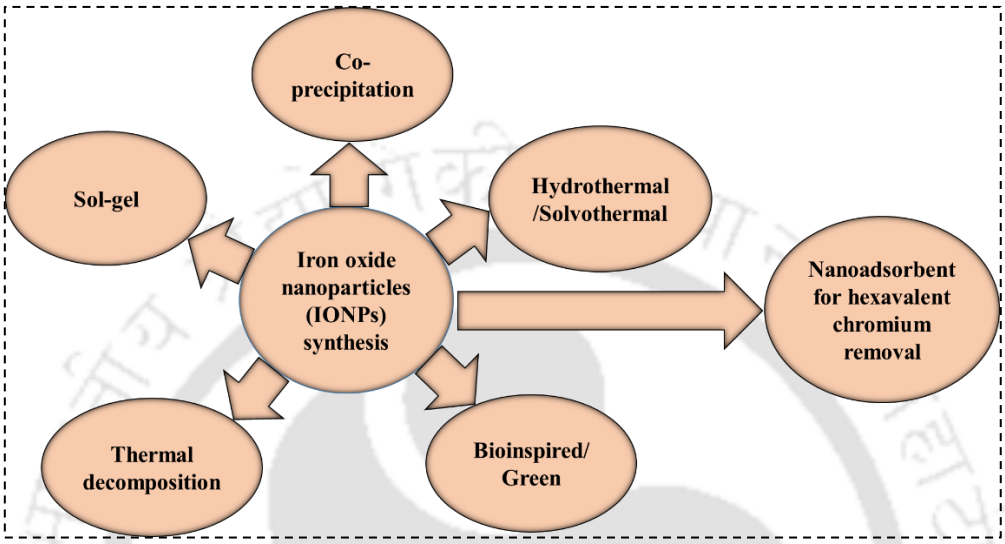

*(Plant-polyphenol-mediated synthesis of iron oxide nanomaterials for heavy metal removal: A review. **Aquib Jawed**, Swati Sharma, Animes K. Golder, and Lalit M. Pandey, Elsevier, p. 115-129)*

This chapter provides a background on water contamination and chromium: sources, effects, and removal techniques. Also, a brief literature review on green synthesized IONPs applied for Cr(VI) removal, along with an overview of the different synthesis methods of IONPs, is provided in this chapter.

2.1. Sources of water and need for freshwater

Water is nature's most precious gift to humanity and all living creatures. Water is vital in various aspects of human life, encompassing agriculture, hydration, industrial processes, and other uses. Water exists in the biosphere as thin shells surrounding the globe. In addition, it is abundantly present in oceans and below the surface of the Earth as aquifers. Specifically, in the atmosphere and surface of Earth, it exists in the form of vapor, droplets, tiny particles of

ice, and largely, in the liquid phase. For the successful continuation of various biosphere processes, water acts as a passage for supplying nutrients and chemicals into the system. In addition, it also serves as a commodity in our day-to-day events and plays an essential role in developing socio-economic processes [20]. The Earth's surface is predominantly covered by water, accounting for approximately 71% of its total area. This vast water coverage is essential for supporting various forms of life. Oceans contain 96.5% of the Earth's water, while glaciers and the ice masses of Antarctica and Greenland hold 1.7% and 0.001% in the air as clouds, vapour, and precipitation, respectively. Merely 2.5% of the total water on Earth is classified as freshwater, with a significant portion of 98.8% found in ice and groundwater. Less than 0.3% of freshwater is in rivers, lakes, and the atmosphere; a minimal amount (0.003%) also exists in living organisms and manufactured things [21]. Understanding the source of freshwater and significance of protecting a pristine water supply is crucial for assuring the continuous accessibility of this vital resource for present and future generations. Freshwater sources play a crucial role in ensuring the long-term viability of life on the Earth. Clean and potable water comes from a variety of natural reservoirs and spots. The main sources include surface water features such as lakes, rivers, and reservoirs, which offer easily accessible water for various needs like industrial, drinking, and agriculture. Groundwater, located below the Earth's surface in aquifers, functions as a concealed yet plentiful reservoir of potable water, frequently accessed through wells. Rainwater, collected via watershed networks and stored in tanks, provides an environmentally beneficial option to achieve freshwater. In areas with limited access to freshwater sources, desalination technologies are crucial for converting seawater into potable water. Water on Earth undergoes a continuous movement known as the hydrological cycle. This cycle involves evaporation, transpiration (evapotranspiration), runoff, condensation, and precipitation. Ultimately, the water typically ends up in the sea. The

processes of evaporation and transpiration have a significant role in the generation of precipitation across terrestrial regions.

Freshwater is an essential resource that is vital for sustaining life on Earth. Primarily, it plays a crucial role in protecting human survival, acting as the foundation for cooking, drinking, and hygiene, the lack of which would significantly endanger our health and general welfare. In addition, agriculture, a crucial component of the global food supply, heavily depends on freshwater for activities such as irrigation and livestock care. Freshwater also plays a vital role in industrial operations, serving as a medium for calming and cleansing, and is essential in processes ranging from production to energy generation. Also, freshwater supports many ecosystems, such as rivers, lakes, and wetlands. These ecosystems provide habitats for numerous species and play a crucial role in maintaining environmental stability through biodiversity and complex food chains. The global decline of this valuable natural resource can be attributed to the rapid processes of urbanization, industrialization, and climate change [22]. Water scarcity is an eminent and formidable obstacle that confronts our contemporary society in the current era [23]. Freshwater scarcity can harm various aspects of a community, including the economy, environment, and impoverished individuals. The meteoric rise of the global population is also accelerating the depletion of the finite reserves of freshwater, propelling humanity towards an impending water crisis [24]. This instance arises due to the perception of water as an inexhaustible and costless resource. Even in areas with adequate or abundant supplies, there is a growing risk to water resources due to pollution and increasing demand. The water demand will continue to rise by 2050 due to the projected global population growth, which is estimated to reach between 9.4 and 10.2 billion [25]. The water strain will be exacerbated by disparities in population growth across various regions, which are not influenced by local resources. Ensuring the protection and long-term stewardship of this valuable resource is crucial for the well-being and overall health of our planet.

2.1.1 Water contamination

The issue of freshwater contamination is increasing globally, presenting a substantial risk to both human well-being and the natural surroundings. This problem stems from multiple sources, such as agricultural runoff, incorrect disposal of household chemicals, effluent from various industries, and insufficient wastewater treatment [26]. Substances such as pesticides, heavy metals, pathogens, and pharmaceuticals can infiltrate freshwater reservoirs, rendering them unfit for human consumption and detrimental to the health of aquatic ecosystems [27]. The consequences of potable water contamination are widespread. Water contamination is among the leading causes of human health issues. Every year, 4 billion incidences of water-related diseases cause 3.4 million deaths worldwide, primarily in children under 5 years old [28]. An estimated 37.7 million Indians are annually afflicted with waterborne diseases; alone, diarrhoea is responsible for the deaths of 1.5 million children [29]. In addition, contaminated water can adversely impact agriculture and food safety. This is due to the fact that when polluted water is utilized for irrigation, it can contaminate crops. Further, the presence of harmful compounds in aquatic environments has a detrimental impact on the watery living organisms. This disruption of food chains and habitats reduces biodiversity and causes long-lasting ecological harm [30]. Hence, preserving water quality, encompassing intricate and delicate interconnections among physical, hydrological, chemical, and biological attributes, is of the utmost importance. From the user's perspective, water quality refers to the physical, chemical, and biological characteristics of water that individuals use to consider for their suitability. Water contamination is a significant global issue that has garnered considerable attention from researchers worldwide. The urgent need for a sustainable solution to decontaminate polluted water and produce potable water has become a focal point in this current era.

2.1.2 Sources of contaminated water

The sources of contaminated water are diverse and widespread, presenting a significant challenge for both human health and the environment. Contaminated water sources can introduce pollutants and pathogens, leading to waterborne diseases and other health risks. The primary sources of contaminated water are well described below [31]:

- Point sources - It comprises easily identifiable origins or outlets via which pollutants or impurities are purposefully or unintentionally transported directly into aquatic ecosystems, including bodies of water such as lakes, rivers, or seas. These sources typically have a clear and specific pollution point and are often connected to accidental spills, residential wastewater systems, storm overflow, and industrial wastes.
- Industrial effluent - Industries frequently discharge contaminants into natural streams. These discharges are comprised of toxic dyes, heavy metals, and other harmful substances.
- Mining activities - The various mining practices release significant amounts of heavy metals and hazardous compounds into water bodies located in their proximity. Persistent in nature, these pollutants can cause detrimental long-term consequences for aquatic organisms and human well-being.
- Non-point sources - It is a pervasive form of pollution that originates from multiple sources, making it difficult to manage. This category encompasses pollution from various sources, such as lawns, road runoff, and farming practices.
- Agricultural runoff - The use of fertilizers in farming leads to contaminate rivers, streams, and groundwater. This contamination poses significant threats to aquatic ecosystems and the safety of drinking water supplies.
- Solid waste - Toxic chemicals and harmful substances can seep into the groundwater from landfills. Over time, these leached pollutants move towards adjacent surface water sources, impacting the quality of potable water and causing harm to ecosystems.

- Erosion - Erosion of soil, which occurs due to construction activities, deforestation, and agricultural practices, can result in the deposition of sediment in bodies of water.
- Wastewater - Untreated wastewater from domestic and industrial sources is a major contributor to water pollution. This raw wastewater threatens human health and aquatic life due to the presence of pathogens, as well as medications and chemicals.
- Natural contaminants - Geological formations can give birth to natural pollutants. Specific geographical areas display natural accumulations of inorganic substances such as fluoride, arsenic, or radon. As a result, when groundwater passes through these layers of rock and soil, it can absorb harmful compounds, which noticeably affect the quality of drinking water [32].

2.1.3 Water contaminants

The presence of contaminants in water is a multifaceted and pervasive problem, impeding the environment and public health in substantial ways. Contaminated water, naturally or polluted by human activity, can introduce several toxic compounds and pathogens into aquatic environments, resulting in significant consequences. Concerning water pollution, there are three main types of contaminants.

- Organic contaminants
- Inorganic contaminants
- Biological contaminants

Organic contaminants - Freshwater often contains organic contaminants that have been detected on a large scale, and a significant number of these compounds are classified as human carcinogens. Over 200 organic pollutants have been identified in groundwater, and this figure continues to rise [33]. Some organic pollutants degrade naturally, whereas others endure. Most biodegradable organic pollutants come from human waste and industrial effluent. Some are naturally derived from lipids, proteins, oils, and carbohydrates. Microorganisms have the

ability to convert these substances into stable inorganic compounds. Although they do not immediately harm living organisms, they can potentially lower dissolved oxygen levels in groundwater. Typical organic pollutants include pesticides, plasticizers, personal care items, dyes, pharmaceutical compounds, hydrocarbons, volatile organic chemicals, and halogenated compounds [34, 35]. Exposure to organic compounds can lead to severe health issues such as hormone imbalances, neurological disorders, and cancer [36]. Household garbage, pesticides, and industrial contaminants are the primary sources of organic pollution of freshwater caused by human activity [37]. Due to the slow degradation or lack thereof, these compounds pose a long-term risk to groundwater quality, potentially impacting its suitability for drinking purposes.

Inorganic contaminants – These include chemical substances or elemental components found in natural, unmodified water ecosystems such as lakes, rivers, and underground aquifers. Inorganic hazardous substances like cadmium (Cd), lead (Pb), chromium (Cr), copper (Cu), cyanide, arsenic (As), and mercury (Hg) threaten the well-being of human populations and the natural environment. These contaminants can infiltrate drinking water through natural sources, industrial operations, and plumbing systems [34].

Cd, with an acceptable limit (AL) of 0.003 mg/L in drinking water [38], is primarily released into the aquatic environment through natural sources such as rocks and volcanoes in the earth's crust. Anthropogenic activities like household usage, industrial development, waste management, plantation, and animal husbandry are the primary causes of Cd pollution in the environment, accounting for approximately 80% - 90% of the total contribution. The toxic effects of Cd primarily occur through the generation of free radicals, specifically reactive oxygen species. The build-up of these unpaired electrons ultimately leads to oxidative stress, causing oxidation, which harms vital biological macromolecules such as lipids, DNA, and proteins. Furthermore, the interaction of Cd can disrupt the regular operations of the -SH, which

possesses biological structures [39]. *Pb* (AL 0.01 mg/L) [38] contamination is becoming a growing concern in urban areas with aging water infrastructure. Water gradually erodes the lead present in urban water networks. This can result in a diverse array of developmental challenges for youngsters and hypertension and renal disorders in older individuals [40]. *Cr*, with an AL of 0.05 mg/L [38], is a naturally occurring element in the ground. It is commonly utilized in the electroplating and leather industries. Typically, it enters aquatic bodies through the runoff from previous mining activities and these enterprises' inappropriate trash disposal. Excessive chromium exposure results in kidney and liver damage and respiratory issues [41]. *Cu* (AL 0.05 mg/L) [38] can infiltrate water sources through natural occurrences in rock and soil or, more commonly, due to the corrosion of domestic plumbing systems. Temporary exposure to copper causes minor gastrointestinal discomfort, whereas prolonged exposure can result in kidney impairment or irreversible liver [42]. *Cyanide* (AL 0.05 mg/L) [38] typically contaminates water due to inadequate waste disposal practices. Exposure to cyanide has been demonstrated to cause deadly damage to the brain, liver, and spleen in people [43]. *As* (AL 0.01 mg/L) [38] contamination is a significant issue, particularly in India and Bangladesh. Arsenicosis is a disease that occurs as a result of drinking water contaminated with arsenic. The toxicity and elimination of arsenic substances and their metabolites are heavily influenced by their oxidation states, specifically Arsenite (As(III)) and Arsenate (As(V)) and methylation level of arsenicals. It has been observed that As(III) is 10 times more toxic than As(V) [44]. *Hg* (AL 0.001 mg/L) [38] enters potable water through agricultural drainage, seepage from waste dumps, and certain industrial operations. Hg in water leads to cognitive dysfunction, neurological diseases, stunted growth in children, miscarriages, and alteration of the hormonal system [34]. Furthermore, a sub-class of inorganic pollutants i.e. radiological pollutants result from the presence of radioactive materials. The potential sources of radioactive substances include soils or rocks that the water permeates or certain industrial waste. The radiation (α, β,

and γ) emitted by soil and rock is influenced by their mineralogical composition. Minerals having higher concentrations of thorium, uranium, and potassium demonstrate significant levels of natural radioactivity. Typically, the source rock's radioelements (thorium, potassium, and uranium) concentration is reflected in soils. Radioelements are typically less of an issue in surface water than in groundwater. As per the USEPA National Interim Primary Drinking Water Regulations, radium-226 holds significant importance among the naturally occurring radionuclides that could be found in public drinking water supplies [45]. The maximum concentration level of radium-226 and α particles, as per the US Environmental Protection Agency (US-EPA), was set at 5 pCi/L and 15 pCi/L, respectively, in drinking water systems [46]. Radiation contamination of any kind raises the risk of cancer [34].

Biological contaminants - Waterborne biological contamination results from living organisms, including algae, bacteria, viruses, phytoplankton, or protozoa. Each one of these can contribute to their specific water quality issues. Algae consist of diverse species, ranging from tiny, single-celled organisms to enormous, eukaryotic seaweeds. These are pretty widespread and rely on water nutrients, namely phosphorus. Most often, the nutrients come from industrial pollutants or residential runoff. The proliferation of algae causes taste and odor issues in water. In addition to this, it also obstructs water filters and leads to undesirable slime deposits around the carriers [34]. Bacteria are single-celled microorganisms that play diverse roles in natural and human-created environments. There are several harmful microorganisms (pathogens) like *Escherichia coli*, *Pseudomonas aeruginosa*, *Campylobacter jejuni*, etc. in water that have the potential to cause waterborne diseases such as gastroenteritis, dysentery, and cholera [47]. Certain nonpathogenic bacteria, such as *crenothrix* iron, can lead to taste and odor issues in water, although not hazardous [34]. Similarly, Protozoans include a variety of unicellular, tiny eukaryotic microbes that are classified under the domain Eukarya. Protozoans such as *Giardia* and *Cryptosporidium* are frequently present in bodies of water, such as rivers

and lakes, that have been polluted with animal waste or wastewater discharge sites of sewage treatment facilities [48]. These microbes can cause abdominal pain, nausea, diarrhea, headaches, exhaustion, and dehydration [34]. Viruses are the tiniest living entities that have the ability to cause infections and induce diseases. Hepatitis, Noroviruses, Sapoviruses, and Enteroviruses are frequently detected in freshwater that has been contaminated [47].

2.2 Heavy metals contaminations

Freshwater that is contaminated contains both inorganic and organic pollutants, including chemical pesticides, laundry detergents, medicinal products and heavy metals. The heavy metals found in the crust of earth are resistant to deterioration or destruction. Looking at the periodic table of elements, heavy metals comprise a block of all the metals in Groups 3 to 16 that are in periods 4 and above, encompassing the transition metals, post-transition metals, and lanthanides [49]. Heavy metals specific gravity and density are higher than 5.0 and 5.0 g/cm^3, respectively. These are called "toxic metals" due to their intoxicating properties, even at minute concentrations. Some heavy metals are micronutrients like iron (Fe), zinc (Zn), Cu, cobalt (Co), and nickel (Ni) but are toxic in excess concentrations. Heavy metals like Cd, As, Cr, Cu, Hg, Ni, Pb, etc., have contaminated surface and groundwater sources [50]. Heavy metals are often released into the environment through several human-caused (Industries: electroplating, mining, leather tanning, etc.) and natural routes (erosion, mineral deposits, weathering of rocks, and volcanic eruptions), each of which has important implications for both ecosystems and human health. Heavy metals exhibited detrimental effects on all living organisms. They attach to and disrupt the operation of crucial cellular processes. The accumulation of non-biodegradable heavy metals like Hg, Cd, Se, Pb, Fe, Cr, and As in their various oxidation states by humans and plants causes severe issues with health and the environment [51]. The toxicity of these hazardous heavy metals depends on the duration and dosage of exposure to live

organisms. Extended exposure to heavy metals through skin contact, inhalation, and contaminated food consumption can lead to the emergence of various illnesses in both individuals and additional creatures [52]. Cr has garnered significant attention among these heavy metals due to its extensive usage, discharged into the environment, and considerable health risks, including the development of cancer [53].

2.2.1 Chromium

In 1797, the remarkable discovery of chromium was made by French chemist Louis Vauquelin. This groundbreaking finding involved the identification of chromium in the intriguing Siberian red lead ore, also known as Crocoite. The name "chromium" is inspired by the Greek word "Chroma," which means colour. This stimulation is due to the wide range of naturally occurring colorful compounds of chromium.

Chromium (Cr; MW = 51.99 g/mol) is the 7th most abundant element in the earth's crust [54] and has been categorized as one of the topmost pollutants and listed among 13 other major hazardous heavy metals. India is 4th in the world in terms of yearly chromite production. In 2022, India's chromite production reached 4.2 million metric tons, accounting for almost 10.24 % of the global chromite mining output of 41 million metric tons [55]. Various natural sources of Cr are plants, animals, volcanic dust, rocks, and gases [56]. In nature, a significant proportion of Cr exists in the form of insoluble chromites, which get converted to soluble form through weathering, oxidation, sorption, desorption, dissolution, reduction, and precipitation, adding a little to the deposits of Cr in water and soil [57]. However, the concentration of Cr is increasing tremendously in soil and water due to various anthropogenic activities resulting in the contamination of the environment. The Cr(VI) and Cr(III) are the most stable oxidation states of Cr, whereas the others (-2 to +5) are short-lived and degenerate soon [57]. The toxicity of these two stable oxidation forms of Cr contradicts each other. The trace component Cr(III) is

essential for plants and humans [58] and is a growth promoter (not essential) for plants at low concentrations [59]. It has low mobility and is almost insoluble in water, which renders it less toxic [60, 61]. However, Cr(VI) is considered a potential carcinogen [62, 63] because of its excellent solubility in water, high mobility across biological membranes, and strong oxidizing potential. Moreover, free radicals were produced during the reduction of Cr(VI) to Cr(III) inside the plant system [64, 65]. The two ionic species of Cr occur in diverse forms in the environment. Cr(VI) is found as chromate oxyanions ($Cr_2O_4^{2-}$ and $Cr_2O_7^{2-}$), whereas Cr(III) forms complexes of oxides, hydroxides, and sulfates [66-68].

2.2.2 Permissible limits for chromium

Several regulatory agencies have established the maximum allowable chromium concentrations in potable water and industrial effluent. The World Health Organization and the Bureau of Indian Standards have specified an acceptable limit for Cr(VI) in drinking water as 0.05 mg/L [38, 69]. The US-EPA recognizes Cr(VI) as hazardous. The US-EPA includes total chromium in the drinking water standard, with a permissible limit of 0.1 mg/L [46]. The European Union has set the maximum allowable level of total chromium in drinking water at 0.05 mg/L [70]. The permissible limits of Cr(VI) and total chromium in wastewater generated from various industries, as set by the Central Pollution Control Board (CPCB, Schedule VI), are 0.1 mg/L and 2 mg/L, respectively, for discharging effluent in inland surface water [71].

2.2.2 Various sources of chromium

Soil, water, and air are the three main components of the environment. In this way, there are two categories of environmental pollutants: natural and anthropogenic. Any source of pollution that is connected to human activity is considered anthropogenic. Chromium often infiltrates surface and groundwater systems through both natural and anthropogenic sources.

2.2.2.1 Natural sources

- Chromium is found in nature mainly in two forms: chromite ($FeCr_2O_4$) and crocoite ($PbCrO_4$). Chromite ore often possesses a high level of hardness (5.5 hardness on Mohs hardness index), exhibits a lustrous appearance, and displays a colour resembling steel grey. The composition of chromite ore can vary, with Cr content ranging from 40 to 68%. Crocoite is a mineral that displays a vibrant, orange-red colour and has a relatively low Mohs hardness index of 2.5-3. The chromium element was initially derived from the crocoite [72]
- Chromium possesses distinct geochemical behaviour in natural water systems. Chromium is found in natural waters in minute amounts as Cr(III), the predominant form of chromium in the environment, exhibiting extremely low mobility. Under conditions of intense oxidation, chromium can exist as Cr(VI) and persist in polyatomic anionic form as CrO_4^{2-} [72].
- Chromium is present in the atmosphere due to mainly two phenomena: windblown sand and volcanic activity. The global deposition of chromium to soil was estimated to be around 4.6×10^4 metric tons per year, indicating its long-lasting presence in the atmosphere [72].

2.2.2.2 Anthropogenic sources

The sources of chromium caused by human activity include polluted soils, airborne emissions from industrial activities, and contaminated groundwater. Chromium pollution is commonly associated with wastewater and sludge generated by various industrial activities, including metal finishing, chromate manufacturing, electroplating, wood preservation and pulp production facilities, and textile dyeing and processing industries [16]. These industries are major sources of harmful chromium residues in freshwater streams, resulting in significant detrimental effects on animal well-being and indirectly harming aquatic ecosystems. A

significant portion of the anthropogenic chromium pollution comes from the leather tanning industrial effluent. In tanning, chromium salts play a significant role in producing high-quality leather resistant to deterioration [73]. Various physicochemical characteristics of leather tannery in Dindigul town (Tamil Nadu), electroplating in Panchkula (Haryana), and textile in Erode (Tamil Nadu) effluents are listed in Table 2.1, and it was found that the value of Cr(tot) (total chromium) was well above the permissible limit. The efficiency of chromium metal consumption in the tanning process of leather is only around 60-80%. As a result, the effluent generated in the tanning industry contains a significant quantity of chromium [74]. The chromium species in tanning wastes initially exists in less toxic Cr(III). However, these species undergo oxidation with time and transform into Cr(VI), which is significantly more toxic [75].

Table 2.1: Physio-chemical characteristics of various industrial effluents [76-78].

S. No.	Parameters	Tannery effluent	Electroplating effluent	Textile effluent	Permissible limit as per CPCB for inland surface water
1.	Temperature (°C)	27 ± 0.8	25	-	Shall not exceed 5ºC above the receiving water temperature
2.	pH	6.7 ± 0.48	3.2	8.75	5.5 to 9.0
3.	Turbidity (NTU)	434 ± 30	-	89.6	-
4.	TDS (mg/L)	19713 ±	452	6040	-
5.	Alkalinity total as $CaCO_3$ (mg/L)	1330 ± 858	-	-	-
6.	Calcium (mg/L)	561 ± 52	-	134	-
7.	Magnesium (mg/L)	294 ± 78	-	19	-
8.	Sodium (mg/L)	4388 ± 2071	-	2125	-
9.	Potassium (mg/L)	901 ± 628	-	95	-
10.	Sulphate (mg/L)	966 ± 386	337	190	-
11.	Iron metal (mg/L)	3.41 ± 0.33	-	-	3
12.	Cr(tot) (mg/L)	194 ± 35	47	15.52	2
13.	Biochemical oxygen demand (mg/L)	2152 ± 1064	93	450	30
14.	Chemical oxygen demand (mg/L)	5083 ± 917	561	859	250
15.	Total suspended solids (mg/L)	2244 ± 137	1107	-	100

2.2.2 Adverse effects of chromium

Humans need Cr(III) for the normal breakdown of carbohydrates, fats, and proteins. Both low and high levels of Cr(III) in the body are destructive. In contrast, Cr(VI) is 500 times more hazardous than Cr(III) [79]. Cr(VI) toxicity is influenced by the route of exposure and the composition and amount of Cr(VI) compounds. Cr(VI) exerts its toxic effects due to negatively charged Cr species complexes that can easily pass through cell membranes via the channel of ionic sulphate. Subsequently, the Cr(VI) undergoes fast reduction to the non-toxic Cr(III) via biological reducers, including ascorbate and glutathione, leading to the formation of several harmful reactive intermediates [2]. The detrimental impact of Cr(VI) can result in various health issues, including respiratory disorders, lung cancer, allergic reactions, and damage to the digestive organs, liver, and kidneys. Exposure to materials containing Cr(VI) through inhalation can lead to respiratory illnesses, including asthma, bronchitis, and bronchogenic cancer [41]. The human carcinogenicity from Cr(VI) inhaling was widely recognized [64]. Cr(VI) is classified as a Group A carcinogen and is known to cause cancer through inhalation, according to the US-EPA [80]. In addition to this, Cr(VI) is one of 127 substances that the International Agency for Research on Cancer has enlisted in Group 1 (probably carcinogenic to humans) as having the highest potential risk to human health when present in urban environments [81]. A study found that people living in small villages with drinking water contaminated by Cr(VI) levels above 0.5 mg/L had a higher mortality rate from stomach cancer [82]. A mortality study focused on ecology found that water contamination with Cr(VI) at levels ranging from 41 to 156 μg/L resulted in a notable rise in liver cancer mortality. The study also revealed elevated rates of lung cancer and malignancies affecting the kidney and other genitourinary organs in women [83]. A separate study was conducted to evaluate the negative health impacts on a population that was exposed to elevated levels of Cr(VI) (~20 mg/L). The findings of this study indicated a small rise in the occurrence of

dermatological and gastrointestinal issues in an area where the groundwater was contaminated with Cr(VI) [84].

2.3. Methods of chromium removal

Water pollution from human activities can pose substantial environmental and individual health hazards. Therefore, this polluted water must be treated before being released into the aquatic streams and land surfaces. Various conventional methods for removing chromium from contaminated water are adopted in this direction, like Adsorption, Electrodialysis, Coagulation, Photocatalysis, Chemical Precipitation, Membrane Filtration, and Ion exchange, as shown in Figure 2.1.

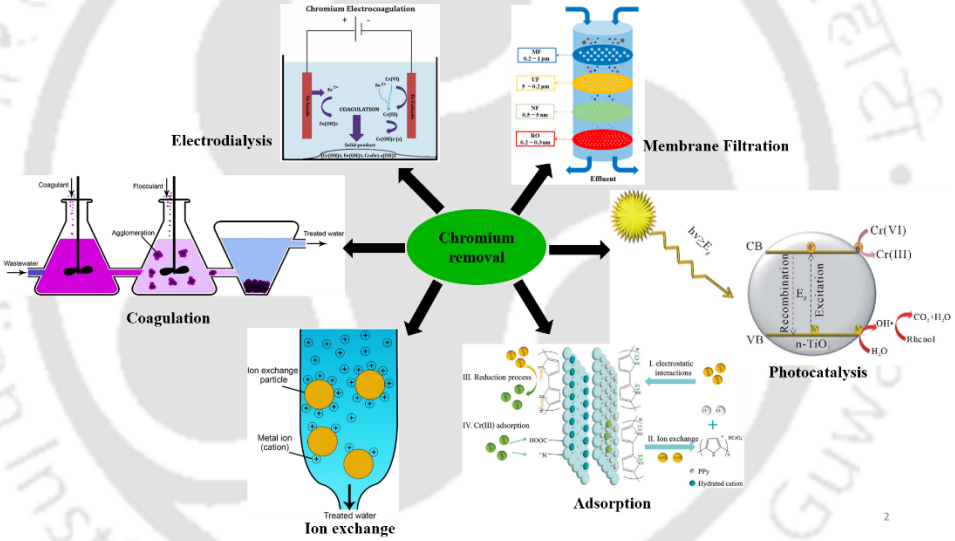

Figure 2.1: Various removal methods of chromium from contaminated water. Adapted and reprinted from Ref. [85-89].

2.3.1 Electrodialysis

In this technique, ions are transported between solutions using a semipermeable membrane in the presence of an electric field. Two electrodes are present that are selective in transporting positive or negative ions. For example, Sadyrbeva achieved a 90 % stripping degree of Cr(VI) in 4 h from 2.95 mg/L of Cr(VI) solution when it passed through a liquid

membrane in an electric field [90]. This method achieved a significant reduction in Cr(VI) levels, although it does come with substantial capital and operating expenses. One additional limitation of Electrodialysis is the frequent fouling of membranes.

2.3.2 Photocatalysis

Photocatalysis is initiated by the semiconductor's electron/hole pair, which gives rise to energy and is simultaneously absorbed by the photon. The hole facilitates the oxidation of water, resulting in the generation of hydroxyl ($OH^{\cdot}$) radicals. These $OH^{\cdot}$ Radicals attack the pollutants present in the water [91, 92]. A photoreduction of 94 % Cr(VI) was reported from a 176.5 mg/L aqueous solution using TiO2 photocatalysts at pH 3 and a dosage of 2 g/L within 60 min. This method suffers several drawbacks, including limited visible light usage, inadequate movement of electrons and holes in semiconductor bands, and fast charge recombination [93].

2.3.3 Ion exchange

Anion exchange-based resin has proven to be highly effective in the removal of Cr(VI). In the process, OH^{-} ions undergo substitution for Cr ions over the resin bed. The bed was revived after depletion through a potent base such as NaOH [94]. Gode *et al.* [95] studied the removal of Cr(VI) using a tertiary amine group-containing ion exchanger, i.e., Lewatit MP 62 and Lewatit M 610. The Cr(VI) removal % was found to be 95 for both Lewatit MP 62 and M 610, respectively, at a pH of 5.0 and dosage of 1 g within 60 min from 100 mg/L aqueous solution. A common issue with this technique is the need for frequent regeneration of the ion exchange bed [96].

2.3.4 Membrane filtration

This treatment technique is based on filtration through various membranes classified by their pore size, with names: microfiltration (MF), ultrafiltration (UF), nanofiltration (NF), and reverse osmosis (RO). MF membranes possess the largest pore sizes (0.1-5 μm). UF pore sizes (0.1-0.001 μm) lie between MF and NF (0.001 – 0.01 μm) membranes. RO has the most diminutive pore sizes (0.0001 to 0.001 μm) among all the membranes. These membranes can capture and retain tiny particles, pathogens, and soluble macromolecules like proteins. Polyamide membranes are commonly employed in the purification of effluents containing chromium. Recently, Wei *et al.* [97] synthesized NF by immobilizing 2, 5-diaminobenzenesulfonic acid into a polyamide layer for Cr(VI) removal. The prepared NF had 10 % and 30 % Cr(VI) rejection performance at pH 4 and 5 from 10 mg/L of aqueous solution. The major limitations of this technique are the deposition of solute on the membrane surface in a large-scale operation and the maintenance/replacement of the membrane filters frequently to enhance the process efficiency. In addition to this, RO-based filtration is not an economical approach for large-scale water treatment due to its fouling problem.

2.3.5 Chemical precipitation

The process of chemical precipitation entails the separation of a substance from a solution through the addition of appropriate chemicals and allowing the resulting precipitate to settle [98]. The reduction of Cr(VI) to Cr(III) through chemical precipitants like ferrous sulphate and lime are widely used for Cr(VI) removal. During the process, Fe^{2+} oxidizes to Fe^{3+}, and Cr(VI) reduced to Cr(III). Afterward, lime precipitates the hydroxide of Cr(III) [99]. In a study by Ramakrishnaiah *et al.* [100] sodium metabisulphite and ferric chloride were used as a reducing agent to achieve 100 % removal efficiency of Cr(VI) from 1000 mg/L of aqueous solution. For this, a pH of 2 and dosages of 80 and 100 mg/L were optimized for Cr(VI)

reduction within 5 min for sodium metabisulphite and ferric chloride, respectively. The method has several disadvantages: high quantity of sludge production and metal removal efficiency depend upon pH of the solution. Additionally, this approach is not recommended for metal ion concentrations that are too low.

2.3.6 Coagulation and Flocculation

Coagulation is the process of adding a coagulant to an aqueous solution in order to disrupt the stability of colloidal suspension. In Flocculation, polymers are added to assist the destabilized particles to clump together and make their settlement easy. This can also be accomplished through gentle stirring, causing the particles to form aggregates termed flocs that further settle through sedimentation. In a study by Haydar *et al.* [101] tannery wastewater was treated with the coagulation-flocculation-sedimentation process by using coagulant alum with both anionic and cationic polymer as a coagulant aid. The results of the study revealed that C-492 resulted in the removal of 97%, 93.5%, 36.2%, and 98.4% of turbidity, total suspended solids (TSS), total chemical oxygen demand (TCOD), and Cr by using the alum combined with a cationic polymer. Further, removed 99.7%, 96.3%, 48.3%, and 99.7% of turbidity, TSS, TCOD, and Cr removal by using the anionic polymer and coagulant combination. The optimum dose of alum and C-492 were reported as 100 and 5 mg/L, respectively. In this technique, significant limitations are the requirement of several chemicals and a high quantity of sludge production.

2.3.7 Adsorption

Adsorption involves the removal of pollutants from contaminated water onto a suitable material through various physical (electrostatic) and chemical (bonds) interactions at the interface. The process of adsorption can be categorized into two types: physical and chemical.

This labelling is based on the nature of the forces responsible for the adsorption, whether Van der Waals or chemical forces, as shown in Figure 2.2. The adsorbent refers to the substance on which the targeted pollutant is adhered, while the pollutants are known as adsorbate. The selection of different adsorbents relies on the specific contaminants that need to be eliminated from the polluted water. Choosing the right adsorbent is essential for enhancing adsorption efficiency. The adsorption process is a cheap and effective technique for removing contaminants in low concentrations. Adsorption also offers benefits such as accessibility, effectiveness, ease of operation, and profitability [102]. The process of adsorption can also be reversed. By utilizing appropriate alkalis, adsorbate can be desorbed from the adsorbent and subsequently reused for further adsorption of adsorbate. For higher efficiency of the adsorption, it can also be carried out in continuous mode (column study). Adsorption is frequently employed in water treatment operations because of its operational convenience, simplicity, and lower initial capital requirements. It is also advantageous as it results in minimal or no creation of hazardous compounds and marginal sludge production. Nowadays, nanoadsorbent (adsorbent particle size < 100 nm) are extensively utilized for the remediation of water and wastewater [103].

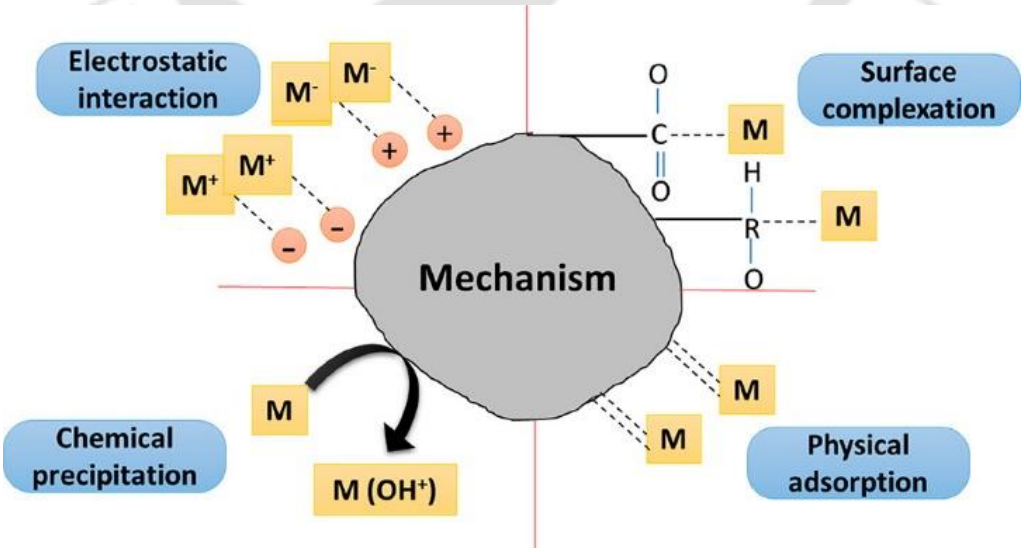

Figure 2.2: Adsorption mechanisms for pollutant removal from water/wastewater. Adapted and reprinted from Ref. [104].

2.3.8 Removal of chromium through various techniques from industrial effluents

The removal of electrolytes from salted or pickled hides was first accomplished in the leather industry by Mellon and associates in 1970 using electrodialysis [105]. Rao *et al.* [106] employed electrodialysis to enhance the uptake of Cr from tannery effluent. The findings demonstrated a notable enhancement in the uptake of Cr following the implementation of electrodialysis. In addition to Cr, they also eliminated the remaining tanning bath salts. The hybrid electrocoagulation-electrodialysis technique is capable of completely removing Cr from tannery wastewater. Electrocoagulation is a pre-treatment technique that prevents the membrane from clogging during electrodialysis [107].

Cavaco *et al.* [3] employed chelating exchange resin and weak cationic resin to extract Cr(III) from the electroplating industry. According to the experiment results, Cr(III) was effectively removed by both resins. In a separate study by Rengaraj *et al*. [108], an aqueous solution containing Cr was treated with a cation exchange resin, resulting in a Cr removal efficiency of more than 95%.

Uddin *et al.* [109] utilized $NaHCO_3$, $CaCO_3$ and MgO as precipitating agents to eliminate and recover Cr from chrome tannery wastewater. The maximum removal efficiency of Cr(III) was found to be 99.97% for $NaHCO_3$ and 99.95% for $CaCO_3$, at pH levels of 8.31 and 8.9, respectively. On the other hand, MgO exhibited the highest removal efficiency of 99.98% at pH 8.91. In a separate study by Kostrzewa *et al.* [110], precipitation of Cr(III) was performed using solutions containing either 3% or 30% NaOH, 10% CaO, 10% $NaHCO_3$ and 10% Na_2CO_3. This solution was used to treat leached out sulfate ions generated from a steel plant. The analysis showed that a significant portion of Cr(III) was successfully precipitated and separated as a solid. At pH 5, the precipitation yields for NaOH, Cao, and $NaHCO_3$ were more than 99%, respectively.

In a study by Amuda *et al.* [111], $FeCl_3$ and organic polymer were utilized as coagulants to remove Cr from beverage industrial wastewater. The $FeCl_3$ dosages spanned from 0 to 500 mg/L, whereas the polymer dosages ranged from 0 to 100 mg/L. The optimal dosages of total Cr removal from the wastewater were found to be 300 mg/L for ferric chloride and 65 mg/L for polymer. The utilization of varying ratios of $FeCl_3$ and polymer resulted in improved removal efficiency, specifically achieving a range of 84-97% for total Cr. Another study by Song *et al.* [112], utilized $FeCl_3$ and $Al_2(SO_4)_3$ as coagulants to reduce the concentration of total Cr in tannery wastewater. The total Cr removal efficiency ranged from 74% to 99% when the initial concentration was 12 mg/L. This efficiency was optimized at 800 mg/L dose of $FeCl_3$ and $Al_2(SO_4)_3$) at pH 7.5.

A study conducted by Mohammad *et al.* [113], examined the recovery of Cr from tannery effluent using RO technology equipped with a UF unit and was found to have a positive impact on Cr recovery. Tripathi *et al.* [114] recovered Cr from tannery effluent using RO. The Cr recovery achieved through RO treatment was 98.66%. This high recovery rate was completed within a pH range of 5.6 to 7, at around 25 °C, and under a pressure of 150 psi.

2.3.7.1 Nanoadsorbent

Various researchers have reported the usefulness of nanomaterials as adsorbents in water treatment due to their larger surface area, reactivity, tiny sizes, and surface-free energy [115-118]. An enormously high ratio of surface area to volume enhanced the adsorption efficacy of the nanoadsorbent [119]. A number of studies have been carried out to eliminate Cr(VI) from water/wastewater by employing nanomaterials as adsorbents [53, 120]; a few of them are also enlisted in Table 2.2.

Carbon has the ability to form carbon-to-carbon long chains due to its binding capability in both straight and complex branching, which enables the double or triple-bond formation and

collection of atoms in different geometrical arrangements [121]. Carbon nanomaterials have been widely used for the removal of heavy metals due to their high sorption capacities and non-toxicity [122]. The synthesized carbon nanotubes (CNTs) by an expensive and advanced two-stage chemical vapor deposition technique having a diameter ranging from 30-33 nm removed 83% of Cr(VI) from 1 mg/L of metallic solution within 120 min at pH 9 and a 9 mg/mL dosage. The Q_m value of CNTs for Cr(VI) removal as per Langmuir isotherm was 2.49 mg g^{-1} [123]. Also, Polyethyleneimine-multiwalled carbon nanotube (MWCNTs) polymeric nanocomposite (PEI-MWCNTs) having an average diameter of 25 nm, pore volume of 2×10^{-3} cm^3/g and surface area of 1.70 m^2/g removed 99% of Cr(VI) from 10 mg/L metallic solution at a dosage of 2 mg/mL within 60 min and pH < 4. The Q_m value of PEI-MWCNTs for Cr(VI) removal was found to be 40 mg g^{-1}. This prepared nano-composite was reused 5 times by losing only 20 % of its adsorption efficiency [124].

Graphene has a honeycomb network structure and was extracted from graphite, and it also possesses good mechanical properties, electrical properties, and thermal conductivity [125]. It was available in many forms, such as graphene oxide (GO) and reduced graphene oxide (r-GO), and also used for the removal of heavy metals from water/wastewater. GO is the oxidative product of graphene (prepared by modified Hummer's method (MHM)), which contains a variety of oxygen functional groups, i.e., carbonyl and epoxy groups [126]. While r-GO is the reduction product of GO, having more structural defects than graphene, it can be easily modified by functional groups such as -OH, $-NH_2$, and -COOH. GOs were combined with Magnetite (Fe_3O_4) nanoparticles (NPs) and functionalized with the different amounts (1.0, 2.0, and 5.0 g) of polydimethyldiallyl (PMDAAC) (denoted as PMDAAC 1.0, PMDAAC 2.0, and PMDAAC 5.0) to enhance the adsorption process by its long chain of carbon atoms. GO functionalized with PMDAAC 2.0 (PMGO-2) removed 99 % of Cr (VI) from 70 mg/L metallic solution at a pH of 4.5 and a dosage of 2 g/L. The Q_m value of PMGO-2 was 95.2 mg g^{-1} [127].

Another group [128] synthesized GO-based inverse spinel nickel ferrite (GONF) nanocomposite by the chemical co-precipitation method. The GONF, having dark and shiny morphology, triangular shape with a surface area of 136 m^2/g and average particle size of 37.25 nm, removed 99.6% of Cr (III) from 10 ppm of metallic solutions at a dosage of 0.75 g/L within 120 min at pH of 6. The chemisorption of metal ions on surfaces of GONF exhibited different surface morphologies compared to bare ones. The Q_m values of the nanocomposite were reported to be 64.10 mg g^{-1} Cr (III) as per Langmuir isotherm, and the nanocomposite was reused up to 3 cycles by losing only 5% of its efficiency.

IONPs have a large prospective for the environmental remediation of a wide range of contaminants due to their low cost, ease of manufacture, and modification. IONPs have a high surface area to volume ratio, superparamagnetism, low toxicity, chemical inertness, and biocompatibility [129] and can easily immobilize other adsorbents over their surface for enhanced activities. Fe-based nanomaterials have been explored in many morphologies, such as NPs, nano-ovals, nanobelts, and nanorings [130-133]. Heavy metal removal through adsorption on IONPs in aqueous solution leads to the aggregation of NPs and competitive adsorption from other adsorbates. These large aggregates, thus formed in the aqueous solution, alter their magnetic properties as well as remove different inorganic and organic pollutants from water/wastewater. This non-dispersion ability of IONPs in aqueous solution can be reduced by synthesis optimization, reducing surface energy, and surface modification methods [134]. Fe_3O_4 NPs is easily separated from water due to their magnetic properties. The most common method of synthesis of Fe_3O_4 NPs in the laboratory is sol-gel method [135]. Fe_3O_4 NPs can be synthesized using ferric chloride tetrahydrate and ferric chloride hexahydrate as the starting raw materials. [136]. Yuan *et al.* [137] used diatomite-supported and unsupported Fe_3O_4 NPs to remove Cr(VI) from synthetic wastewater. The Fe_3O_4 NPs were synthesized using ferric chloride tetrahydrate and ferric chloride hexahydrate as precursors. The kinetic

model was fitted to pseudo-second-order kinetics. Langmuir equation was best fitted to the equilibrium data in the above work. In another study, Fe_3O_4 NPs synthesized with tetramethylammonium hydroxide having spherical particles of 15-30 nm with a surface area of 12.7 m^2/g removed 58.4% of Cr(VI) at pH of 2 from 20 mg/L of chromium solution, respectively at a dosage of 1.0 g/L. The Q_m for Cr(VI) removal was found to be 34.9 mg g^{-1}, and the synthesized Fe_3O_4 NPs were reused two times [138]. Also, silane coupling agents were used to increase IONPs stability and zeta potential. It was reported that Fe_3O_4 NPs fabricated on halloysite nanotubes surfaces and modified by 3-piperazinepropylmethyldi-methoxysilane (KH-108) and anilino-methyl- triethoxysilane (KH-42) removed 81.35% Cr(VI) at pH of 3 and 100% Cr(VI) at pH of 2 from 20 mg/L binary metallic solutions. The zeta potential of both KH-108 and KH-42 modified NPs varies from 10 to -38 mV in the pH range of 2-10. The Q_m values of KH-108 modified NPs for Cr(VI) removal as per Langmuir isotherm were reported to be 59.90 mg g^{-1} at 308K [139].

Surface modifications by attaching different organic molecules/inorganic shells for preventing IONPs oxidation have been explored [140-143]. Functional groups like –COOH and $–NH_2$ groups are found to increase their stability, adsorption efficiency, and surface area for chelating metal ions from water/wastewater [144]. Recently, $–NH_2$ functionalized (Fe_3O_4-NH_2) NPs were formed with enhanced surface area due to the grafting of amino groups over its surface. These prepared Fe_3O_4-NH_2 NPs removed 97.94% Cr (VI) from 1 ppm metallic tap water at pH 6.6. The Q_m values for the Cr (VI) removal as per Langmuir isotherm were reported to be 222.12 mg g^{-1} [145]. A distinct study concluded that $–NH_2$ functionalized Fe_3O_4@SiO_2-NH_2 showed good solvent dispersion ability and magnetic property. In addition [146], Fe_3O_4-NH_2 NPs exhibited excellent rapid chelating properties for metal anions and optimally removed Cr (IV) from 600 ppm metallic solution at pH 6. The Q_m values for Cu (II) an Cr (IV) removal as per Langmuir isotherm were reported to be 11.24 mg g^{-1}. In another study, aminated Fe_3O_4

NPs having an average size of 50 nm were filled into chitosan/polyvinyl alcohol nanofibers to form a nonporous membrane over polyethersulfone. The synthesized membrane of 60 ± 5 µm thickness was found to have optimal removal of Cr(VI) at pH of 2 from 20 mg/L individual metallic solutions with an adsorbent dosage of 0.5 mg/L, respectively. At lower pH values, electrostatic interaction occurred between the amine and hydroxyl groups on the nanofibrous membrane and chromium anions, i.e., $Cr_2O_7^{2-}$ and $HCrO^{4-}$. The Q_m values for Cr(VI) removal were found to be 525.8 mg g^{-1} [147]. A cationic surfactant cetyltrimethylammonium bromide (CTAB) was also used to cap Fe_3O_4 NPs through the electrostatic interaction ($OH^-\cdots NH_4^+$) between surface hydroxyl groups of Fe_3O_4 and the ammonium groups in CTAB (Figure 2.3). These modified NPs showed enhanced removal (95.77%) of Cr(VI) at pH 4 and dosage of 12 mg/mL from 100 mg/L metallic solution as compared to uncapped NPs (74.49%). Cr(VI) adhered to the ammonium functional groups present on the surface and was reduced to insoluble Cr(III) hydroxide [148]. The $–NH_2$ functionalization, as scrutinized in the above examples, elucidates that $–NH_2$ functionalization incorporates high surface area and alters the surface charge over the Fe-based NPs to enhance their adsorption capacity.

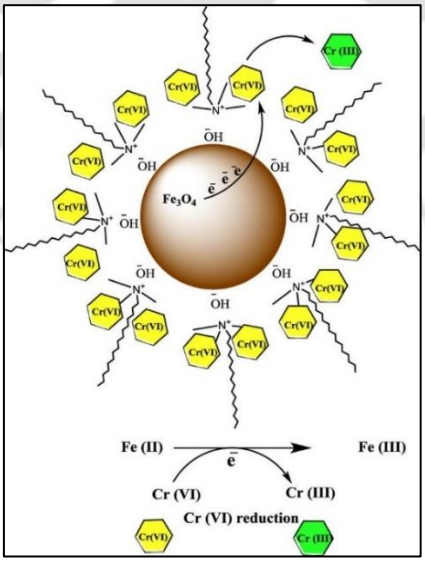

Figure 2.3: Adsorption of Cr(VI) on the surface of CTAB coated Fe_3O_4 NPs. Adapted and reprinted from Ref. [148].

In another study [138], Fe_3O_4 NPs synthesized with tetramethylammonium hydroxide having spherical particles of 15-30 nm with a surface area of 12.7 m^2/g removed 58.4% of Cr (VI) and at pH of 2 in 10 ppm of chromium solution, at a dosage of 1.0 g/L. The Q_m values for Cr (VI) removal were found to be 34.9 mg g^{-1}, and the adsorbent was effectively reused twice. Hematite (α-Fe_2O_3) NPs, as a photocatalysts, also have very good efficiency for metal removal in water. Recently, Wang *et al.* [149] revealed that -OH α-Fe_2O_3 NPs synthesized by the solvothermal method with an average particle size in the range of 11-27 nm were found to remove Cr (VI) in 20 ppm metallic solution at a dosage of 0.5 mg/mL under photocatalytic activity and enhance removal efficiency from 24.8% to 70.2% due to synergetic effect. IONPs appear to follow the right path, making them suitable/potential candidates for Cr(VI) removal.

Table 2.2: Various Nanoadsorbent utilized for Cr(VI) removal.

S. No.	Adsorbent	Synthesis method		Q_m (mg g^{-1})	Optimized conditions	Isotherm fitted	Ref.
		NPs	Composites				
1.	Magnetic iron–nickel oxide	Co-precipitation	-	30	pH-5, Dosage-3-6 mg/mL, reusable upto 4 cycles	Langmuir	[150]
2.	δ-FeOOH-coated γ-Fe_2O_3 magnetic NPs	Sol-gel	-	25.8	pH-2.5, Temperature-25 °C, Dosage-5 mg/mL	Langmuir	[151]
3.	Amino-modified Fe_3O_4 magnetic NPs	Co-precipitation	Diethylenetriamine	11.24	pH-2, Dosage-2.6 mg/mL, Contact time-60 min	Langmuir	[146]
4.	Magnetic Fe_3O_4@SiO_2-chitosan	Solvothermal	Crosslinking	336.7	pH-2, Dosage-0.5 mg/mL, Contact time-1440 min	Langmuir	[152]
5.	Polypyrrole/Fe_3O_4 magnetic nanocomposite	Polymerization	Insitu-polymerization	243.9	pH-2, Initial metal cone 200 mg/L	Langmuir	[153]
6.	Magnetic graphene oxide foam/Fe_3O_4 nanocomposite	Co-precipitation	Microwave-plasma chemical vapor deposition	258.6	pH 2, Contact time-20 min	Langmuir	[154]
7.	Core-shell magnetic Fe_3O_4 @poly(m-Phenylenediamine)	Solvothermal		246.09	pH-2, Dosage-0.1 mg/mL, reused up to 6 times	Langmuir	[155]
8.	Magnetic chitosan beads	Co-precipitation	Cross-linking	69.4	pH-4, reusable up to 10 cycles	Langmuir	[156]
9.	Fe_3O_4@C@MgAl-layered double-hydroxide	Hydrothermal	Modified by AlOOH through sol-gel method	152	pH-6, Dosage-1 mg/mL, Contact time- 60 min, reusable up to 6 cycles	Langmuir	[157]
10.	Humic acid coated Fe_3O_4 NPs	Co-precipitation	Humic acid	3.37	pH-4, Dosage-10 mg/mL	Langmuir	[158]

11.	Mesoporous polydopamine/titanium dioxide composite nanospheres	Hydrothermal	Organic-inorganic self-assembly method	244.5	pH-2, Dosage-0.5 mg/mL, Contact time-35 min	Langmuir	[159]
12.	Titanium oxide-Ag composite	Hydrothermal	Facile solution route	25.70	pH-2, Contact time-35 min, reusable up to 4 cycles	Langmuir	[160]
13.	Magnetic titanium nanotubes coated phosphorene	Hydrothermal	Phosphorene	35	pH-9, Dosage-0.8 mg/mL, reusable up to 5 cycles	-	[161]
14.	RGO/Nickel oxide nanocomposites	Modified hummers method	Dissolve in hydrazine hydrate solution	198	pH-4, Dosage-0.33 mg/mL, Temperature-25°C	Langmuir	[162]
15.	Gallium-doped zinc oxides NPs	Co-precipitation	-	66.36	pH-3.0, Contact time-760 min	Langmuir	[163]
16.	Titanium dioxide NPs	Co-precipitation	-	21.92	pH-4, Dosage-0.1 mg/mL	Langmuir	[164]

2.4. Approaches of IONPs Synthesis

In the last decades, the development of IONPs was done by numerous researchers for Cr(VI) removal [165, 166], and many reports have found various ways to produce control shape, high solvent dispersion, bioactive and stable IONPs [167, 168]. Numerous methods for synthesizing IONPs are available, like Co-precipitation, sol-gel, hydrothermal, thermal, sonochemical, etc.

2.4.1 Co-precipitation method

The co-precipitation method is the simplest method to obtain magnetic particles. The NPs were synthesized by oxidizing the formed ferrous hydroxide suspensions [141] and aging Fe^{2+} and Fe^{3+} hydroxides to form homogeneous spherical Fe_3O_4 NPs [169]. The Fe precursor used of different salts, the Fe^{2+} and Fe^{3+} ions ratio, pH, temperature, and ionic strength decide their physical features [170]. IONPs (Fe_3O_4 or γ-Fe_2O_3) are usually prepared using precursors with both Fe^{2+} and Fe^{3+} ions, as shown in (1). The preparation of Fe_3O_4 NPs follows the below chemical reaction:

$$Fe^{2+} + 2Fe^{3+} + 8OH^- \rightarrow Fe_3O_4 + H_2O \quad (2.1)$$

The formation of Fe_3O_4 should be expected under alkaline conditions with pH ranges between 8 and 14. Also, the reaction should occur in a non-oxidizing environment with a stoichiometric ratio of 2:1 between Fe^{2+} and Fe^{3+}. Nevertheless, the prepared NPs were oxidized to form Maghemite (γ Fe_2O_3), as shown in (2).

$$Fe_3O_4 + 2H^+ \rightarrow \gamma Fe_2O_3 + Fe^{2+} + H_2O \quad (2.2)$$

The method produces particle sizes of various distribution ranges. Kang *et al.* [171] synthesized monodisperse, Fe_3O_4 NPs of spherical shape with a diameter of 8.5 ± 1.3 nm, 0.5 ratios of Fe^{2+}/Fe^{3+} precursor in stoichiometric ratio, and a pH of 11-12. The dispersion of the Fe_3O_4 NPs can be enhanced by aeration of γ-Fe_2O_3 suspension in solutions [170]. Iida *et al.*

[172] also prepared Fe_3O_4 NPs by varying ferrous and ferric salts at various ratios and with base 1,6-hexane diamine. The study revealed that variation in the ratio of Fe^{2+}/Fe^{3+} enhanced the Fe_3O_4 NPs particle size from 9 to 37 nm due to the formation of large-sized hydroxides. Small-sized NPs were formed by increasing the medium pH value and ionic strength [173]. The above parameters affect surface complexity and the zeta potential value of the particles [174]. In the preparation of Fe_3O_4 NPs, temperature also plays a crucial role, below 60°C reaction temperature, Fe_2O_3 was formed, while above 80°C favors the formation of Fe_3O_4 from iron oxide precursors [175, 176]. Oxidation during the synthesis was prevented through nitrogen gas bubbling. Furthermore, N_2 purging formed smaller particles compared to another method without oxygen removal [175, 177].

The main advantages of this process are:

- At a time, the quantity of synthesizing NPs is substantial
- The reaction temperature is on lower side due to the homogeneous mixing of the formed precipitates
- Low-sintering reactive powders of fine metal oxide synthesis are done in a simple way

The main disadvantages of this process are:

- High purity, accurate stoichiometric phase of the synthesized particles is not achieved through the process
- Different solubility and precipitation rates of the reactants affect the particle formation
- Not having a common condition for the synthesis of particles
- The synthesized particles tend to agglomerate due to their small size, which causes high surface energy

2.4.2 Sol-gel method

The process involves gel formation through the wet-chemical technique that utilizes either a chemical solution or colloidal particles. The hydrolysis of the precursor in solution formed a nanoscale "sol." Additionally, condensation and polymerization lead to a metal oxide network denominated as "wet gel." The reactions are carried out at room temperature. Therefore, calcination is done to achieve the ultimate crystalline state [178, 179]. From past studies [180], it was well established that gel properties solely depend upon the 'sol' formed during the process. The process kinetics depend upon the growth of reactions, condensation, and hydrolysis. However, the assembly of the synthesized particles depends upon the solvent used, reaction temperature, concentration of metal precursors engaged, agitation, and pH [181]. For example, Takai *et al.* [182] synthesized Fe_3O_4 NPs by combining sol-gel with vacuum annealing at 200-400ºC. Results showed that various sizes of Fe_3O_4 NPs could be obtained by simply varying the calcination temperature. Also, the material's magnetic property is enhanced with an increase in the particle size in terms of saturated magnetization value (Ms). Lemine *et al.* [135] also synthesized Fe_3O_4 NPs using a modified sol-gel route method. The method included ethanol as a solvent for iron precursor, which was placed in an autoclave after 15 min of stirring and dried under supercritical conditions of ethanol. XRD results also revealed that prepared Fe_3O_4 NPs of pure and single phase without impurities and also peaks are very broad which indicates the formation of very fine particles in the nanoscale range TEM result explored the formation of 8 nm size of Fe_3O_4 NPs. Recently, Gao *et al.* [183] synthesized sol-gel process-based amphiphilic magnetic nanocomposites. In the process, hydrophilic, hydrophobic N-octyltrimethoxysilane and 3-aminopropyltriethoxylsilane were used to modify Fe_3O_4 NPs through one-step sol-gel method and make them both hydrophobic as well as hydrophilic in nature. This hydrophilic nature of Fe_3O_4 NPs makes them quickly disperse in the aqueous solution. The prepared NPs were also used to remove Phthalate esters (PAE) from a different

aqueous solution of various concentrations of PAEs. The PAE was adsorbed through hydrophobic interaction on octyl chains on the prepared NPs.

The main advantages of this process are:

- The prepared NPs are of better homogeneity and purity
- The gel state of the process enhances the geometric complexity of the materials
- Thin bond coating of the metallic substrate with different materials can be accomplished through this route

The main disadvantages of this process are:

- The produce NPs have high permeability, weak bonding, hard porosity control, and low wear-resistance
- The extra time required for sintering of the materials to achieve their crystallinity

2.4.3 Hydrothermal/Solvothermal method

The synthesis refers to the production of IONPs through various chemical reactions occurring in a sealed autoclave at pressure and temperature higher than normal. When a solvent other than water is used to conduct the synthesis, the term "Solvothermal method" is used instead of "Hydrothermal method." The pressure and temperature values can be as high as 2000 psi and above 200ºC [170]. Oxidation and Hydrolysis of metal oxide mixtures took place in this process. The control of particle size is through grain growth and nucleation rating. For example, Zhang *et al.* [184] synthesized the necklace-shaped superstructures self-assembled by Fe_3O_4 NPs coated with poly (vinyl pyrrolidone) (PVP) through the hydrothermal method. The prepared nanostructure consists of an 80 nm size of Fe_3O_4 NPs. The sample exhibited a ferromagnetic behaviour with Ms value of 51.0 emu g^{-1}. In another study by Shibing *et al.* [185] well-dispersed Fe_3O_4 NPs of size 160 nm were produced without sodium sulphate. The electrochemical properties of the synthesized Fe_3O_4 NPs as cathode electrodes of lithium-ion

battery was studied through charge/discharge tests and showed a discharge capacity of 1267 mA h g^{-1} at a current density of 0.1 mA cm^{-2}. Wang *et al.* [186] prepared water-soluble Fe_3O_4 NPs by conventional one-pot hydrothermal method. A 40 mL mixture was formed in the process, which contains 0.2 mmol of $FeCl_3.6H_2O$ and 4 mmol sodium citrate. Further, 0.3 g of polyacrylamide (PAM) and 0.5 mL of ammonia (13.2 mol L^{-1}) were added to the above mixture under continuous stirring at 25ºC. The prepared mixture was placed in a Teflon-lined autoclave for 12 h at 200ºC. The synthesized NPs were found to remove Cr(VI) from the aqueous solution. The NPs were found to have 28 mg/L of water solubility at 18ºC for at least 1 month.

The main advantages of this process are:

- Solubility of the material can be achieved through accurate solvent by heating and pressurizing the system closed to its critical point
- Easy production of various states of the products, i.e., metastable state, intermediate state, and specific phase
- Easy control of the synthesized product's shape distribution, size, and crystallinity through altering reaction factors like precursor type, type of solvent, reaction temperature, etc.

The main disadvantages of this process are:

- Required an autoclave separately for the synthesis
- The reaction takes place at high temperatures and pressure. Therefore, safety is an issue

2.4.4 Thermal decomposition method

The iron precursors were decomposed in hot organic surfactants, and samples of effective size, fine-size dispersal, crystallinity, and water-soluble IONPs were obtained [169]. IONPs with good dispersion ability and fine size can be attained by decomposition of precursors at a higher temperature, such as $[Y^{a+}\ (at)_a\ ]$, (Y= Co, Ni, Fe; a = 2 or 3, at =

acetylacetonate), M^n $(C)_n$ (C as N-nitrosophenyl hydroxylamine and using organic solvents like fatty acids [175]. Alivisatos and co-workers [187] reported that at 250ºC-300ºC, inoculating solutions of $FeCl_3$ in octylamine formed long-chain amines, which resulted in the synthesis of γ-Fe_2O_3 NPs. The synthesized NPs were found to have good dispersion ability, high crystallinity, and a size of 4 to 10 nm. [188]. Monodisperse Fe_3O_4 NPs were prepared at high temperature (265ºC), with sizes ranged from 3 to 20 nm. The size of NPs was control by thermal decomposition and using huge quantities of surfactant and organic solvents. Thermal decomposition of metal organic precursors leads to the formation of metal NPs, but oxidation in this process can develop monodisperse oxides of metal.

The main advantages of this process are:

- Enables simple adjustment of the shape, size, and composition of the synthesized NPs
- Creation of almost uniformly sized NPs

The main disadvantages of this process are:

- Required high temperature for synthesis
- Involvement of organic solvents in synthesis makes it less suitable for biological applications

2.4.5 Sonochemical method

This method has been used as a competitive method for the abovementioned [175]. The effects of ultrasound arise from acoustic cavitation, causing the breakdown of bubbles in the liquid. The temperature and pressure for the bubble to collapse are generally designed at 5000 K and 1000 bar, respectively. Typically, the volatile liquid of low vapour pressure generates this liquid bubble. Titanium horn is irradiated with an ultrasound probe that operates at 20 kHz [181]. Researchers applied this synthesis method for the preparation of IONPs and several nanocomposites [189]. Vijayakumar *et al.* [190] reported a particle size of 10 nm of Fe_3O_4

powder through a sonochemical method. The NPs obtained are superparamagnetic and have a < 1.25 emu g^{-1} magnetization. The prepared NPs were agglomerated, amorphous, and porous. For example, iron carbonyl was sonicated in decalin to form an amorphous iron powder [152, 153] and found to have a 120 $m^2 g^{-1}$ surface area. The powder was annealed at 350ºC, and 50 nm particle size was obtained [181]. Kim *et al.* [191] synthesized Fe_3O_4 NPs using co-precipitation and sonochemical methods. The results revealed that particle synthesizing with the sonochemical method results in higher crystallinity and Ms values.

The main advantages of this process are:

- Enhances the rate of reaction
- The process involves high energies and pressures within a short time frame
- No additives are required

The main disadvantages of this process are:

- Low production of the synthesized NPs
- Inefficient energy

This study primarily examines the implications of bioinspired IONPs in eliminating Cr(VI) from aqueous solution. The following sections comprehensively review the most significant research on the bioinspired synthesis of IONPs.

2.5. Bioinspired/Green Synthesis of IONPs

The chemical synthesis of IONPs is done in the presence of different reactive and toxic chemicals, such as borohydrates and hydroxides, which cause innumerable impacts on the surrounding environment animal and plant life [192, 193]. Hence, there is a vital requirement for environment-friendly methods for the synthesis of IONPs. A few of the main advantages of green synthesis over the conventional chemical synthesis methods include (a) environmental benign analytes, (b) less energy-intensive, and (c) use of renewable resources [194].

In green synthesis, a large variety of biological sources like bacteria, fungi, and plant part extracts are utilized for the synthesis of NPs [195]. Microorganism-based protocols of NPs synthesis have been used by various researchers, while plant-based synthesis is in trend over the past few years [196]. The duration of metal salts reduction into nano-scale is more rapid in plant extracts-based synthesis protocols than in microbes-based methods [197]. Polyphenolic (PPs) constituent of plant extracts has been the area of prime interest due to their congenital chemical characteristics. PPs constitute a broad range of biomolecules, from alkyl aldehydes to alcohols [198].

2.5.1 IONPs using plant extract

Plants have emerged as the most promising creatures for the efficient production of IONPs in recent years, owing to their ease of availability, low cost, and benign nature. The phytochemicals present in plants contribute to a decrease in the size and stabilization of the formed IONPs. Phytochemicals, including polyphenols, flavonoids, amino acids, alkaloids, terpenoids, and tannins, are found in varying concentrations throughout different parts of a plant [199]. During the IONPs synthesis procedure, the formation of NPs is initially indicated by a colour change resulting from the reduction of Fe metal salt precursor by phytochemicals present in the prepared plant extract. This bioinspired reduction also serves as a stabilizing agent for the synthesized IONPs. The key active agent in the synthesis of metal NPs are PPs, which are readily present in various parts of plants (e.g., tea, red grape) like leaf, seed, stem, and root [200, 201]. Routinely, PPs are used by plants for their defense against ultraviolet radiation and pathogens in the surrounding atmosphere. PPs extract from green tea comprises mainly four catechins: epigallocatechin gallate (EGCG), epigallocatechin, epicatechin gallate, and epicatechin. EGCG constitutes almost 50-80 % of the catechins [202].

Wang *et al.* [203] synthesized nano zero valent iron NPs (nZVI) by using extracts of green tea (GT) and eucalyptus leaves (EL). The synthesized GT-Fe and EL-Fe NPs were quasi-spherical in shape with a diameter ranging from 20 to 80 nm. These synthesized NPs were found to be less aggregated as compared to chemically prepared NPs as observed using scanning electron microscopic (SEM). Condés *et al.* [204] also synthesized IONPs by using the extract of GT leaves. The prepared NPs were found to be quasi-spherical in shape with a size of less than 80 nm. Carvalho *et al.* [205] developed a green catalyst of IONPs by using extracts of *Camellia sinensi*. Both black tea (BT) and white tea (WT) were used for the synthesis of BT-Fe and WT-Fe catalysts. The prepared catalysts were irregular, with a dense agglomeration of Fe/PPs. Further, both the prepared NPs were supported over SiO_2, Al_2O_3, CeO_2, and ZrO_2 surfaces to reduce the aggregation of the particles.

Similarly, Chrysochoou *et al.* [206] used GT, BT, and Oolong tea (OT) extracts for the synthesis of IONPs. The NPs prepared from all three GT, BT, and OT extracts were spherical with a diameter ranging from 40-50 nm. The IONPs synthesized from GT extracts showed less particle aggregation than BT and OT extracts due to the higher concentration of PPs/caffeine in GT extracts. Similarly, the surface area of the synthesized NPs was found to be the highest in GT extract, i.e., 5.8 m^2/g, than in OT and BT extracts, which were 5 and 2.6 m^2/g, respectively.

The formation of IONPs under various atmospheric conditions was also found to affect the innumerable physiochemical aspects of the synthesized NPs. Recently, Lin *et al.* [207] developed IONs by using GT extracts as a reducing agent under nitrogen (N_2) and oxygen (O_2) atmospheres, respectively. The spherical NPs synthesized under the N_2 atmosphere were found to be less aggregated and smaller in size (95 nm) than the O_2 atmosphere (167 nm) due to the capping of NPs in the non-N_2 atmosphere as observed by SEM. Also, the binding energy peaks

as exposed by X-ray Photoelectron Spectroscopy at 706 eV in N_2 and 530.7 and 532.8 eV in O_2 atmosphere confirmed the formation of Fe^0 and Fe-O, respectively.

Apart from GT leaf extracts, various researchers have explored the synthesis of IONPs using leaves of other plant extracts, as illustrated in Table 2.3. In a study by Makarov *et al.* stable IONPs were synthesized using *Rumex acetosa* and *Hordeum vulgare* plant leaf extracts. The biochemical characteristics of both the extracts, like pH, the concentration of protein, and reducing metabolites, were done, and it was found that plant extracts having low molecular weight components are suitable candidates for IONPs synthesis. IONPs synthesized by using *Rumex acetosa* extracts were well dispersed and 30-40 nm in diameter. In the case of IONPs prepared by using extracts of *Hordeum vulgare*, aggregation of particles was found within the initial 1 hour of reaction. The citrate buffer was used to make these NPs stable for upto 1 week after the synthesis. pH played an important role in terms of stability of the synthesized NPs, which were found to be more stable at a low pH, i.e., *R. acetosa* extract (pH 3.7) and *H. vulgare* extract (pH 5.8), as shown in Figure 2.4 [208].

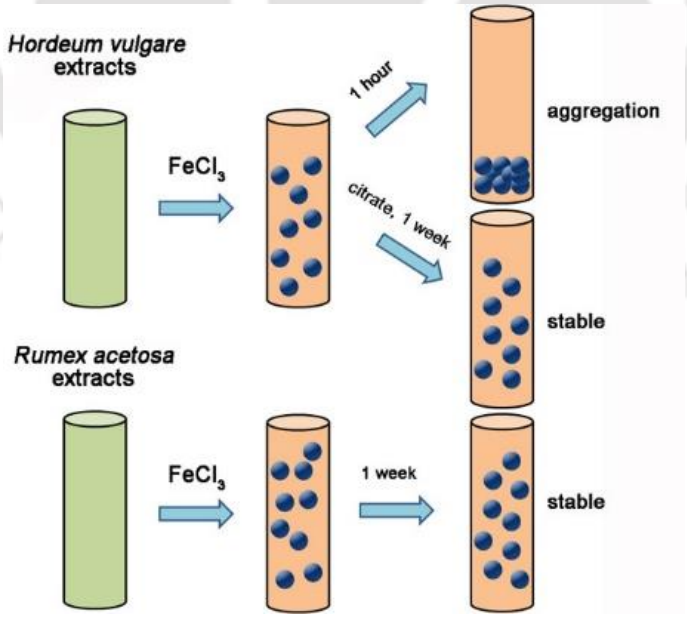

Figure 2.4: Stability of synthesized IONPs by using *R. acetosa* extract (pH 3.7) and *H. vulgare* extract (pH 5.8) extracts. Adapted and reprinted from Ref. [208].

Table 2.3: Influence of plant sources on the synthesis of various nZVI and IONPs.

S. No	Nanoparticles	Plant used	Morphology and size	Reference
1.	nZVI	*Camellia sinensis*	Spherical, 5 to 15 nm	[209]
2.	nZVI	Pomegranate, Mulberry and Cherry	Spherical, 10 to 30 nm	[210]
3.	nZVI	*Camellia sinensis*	Spherical, 70 nm	[211]
4.	Fe_3O_4	*Stevia*	Spherical, <25nm	[212]
5.	Fe_3O_4	Soya bean	Spherical, 8 nm	[213]
6.	Fe_3O_4	*Camellia sinensis*	Spherical, 40 - 60 nm	[214]
7.	Fe_3O_4	*Dolichos lablab L.*	Spherical, 12.5 nm	[215]
8.	Fe_3O_4	*Kappaphycus alvarezii*	Spherical, 16.5 nm	[216]
9.	Fe_3O_4	*Padina pavonica* (Linnaeus) and *Sargassum acinarium.*	Spherical, 10 to 19.5 nm and 21.6 to 27.4 nm	[217]
10.	Fe-PPs	*Eucalyptus tereticornis*	Cubic, 40-60 nm	[218]

Eslami *et al.* [219] developed nZVI using leaf extracts of *Myrtus communis* as a reducing agent for reducing Fe metal salts to form the desired NPs. The reduction of Fe(III) precursors under alkaline conditions formed nZVI due to the formation of hydrolyzed products of the tannin compound (Tellimagrandin II) present in the leaf extracts, as shown in Figure 2.5. These hydrolyzed products of the tannin compounds, i.e., glucose gallic acid and ellagic acid, tend to reduce the Fe(III) to Fe(II) and subsequently Fe^{2+} to Fe^0. The hydroxyl (-OH) and carbonyl (-C =O) groups present in the PPs acted like hard and soft ligands, respectively. The hard ligands (-OH) reduced the metal precursors, and consecutively, soft ligands (-C=O) capped the synthesized NPs as per the hard-soft acid-base (HSAB) theory. The microscopic images of nZVI found that NPs were spherical with a diameter ranging between 20 to 40 nm and surrounded by a transparent organic layer of phytochemicals to prevent the aggregation of particles. The capping of biomolecules from the leaves extract over nZVI was found to decrease its zeta potential value from -2.43 (uncoated nZVI) to -22.4 mV.

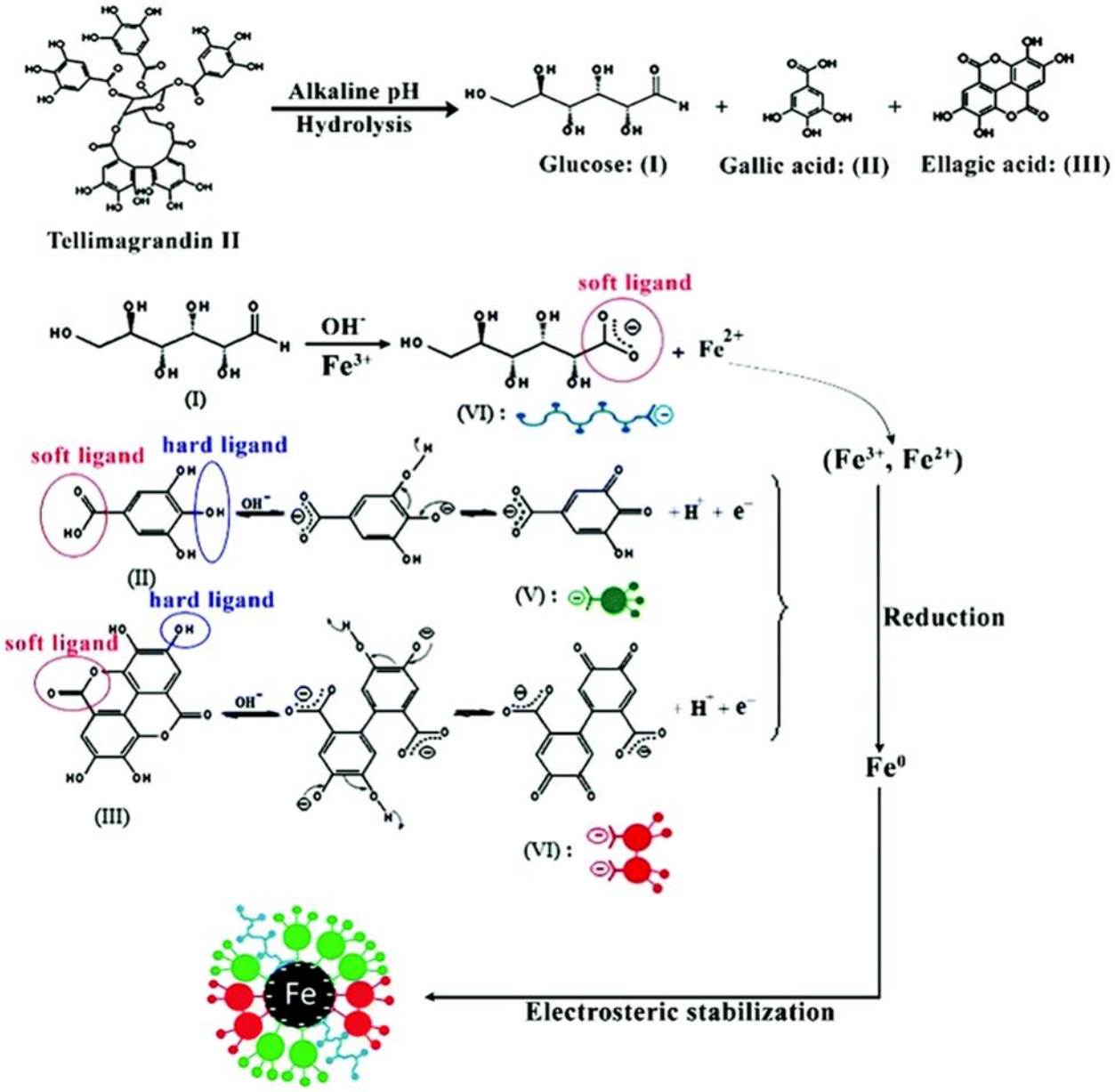

Figure 2.5: Reaction mechanism of hydrolyzable tannin-based reduction of Fe salt. Adapted and reprinted from Ref. [219].

2.5.2 IONPs using Microorganism

The application of microorganisms in synthesizing IONPs has attained considerable attention in recent years, mostly due to its several advantages over traditional chemical methods. There are various microbes, like bacteria, algae, and fungi, that are extensively employed for the synthesis of IONPs. The microorganism-based synthesis is classified into two categories: intracellular and extracellular. The intracellular process involves the uptake of

metal ions into microbial cells, leading to nanoparticle formation in the presence of biomacromolecules. The extracellular approach involves the reduction of precursors by enzymes, proteins, cell wall components, and other metabolites present in the culture medium to form nanoparticles [220]. Most of the studies employed the latter method for synthesizing IONPs. Different microorganisms like bacteria, fungi, and algae, which were reported for the synthesis of IONPs, are discussed below:

2.5.2.1 Bacterial-based synthesis

Nowadays, bacterial-based synthesis has been extensively used to produce IONPs due to its eco-friendly and sustainable nature [221]. Both gram-negative and gram-positive bacterial strains performed this approach of IONPs synthesis. Several researchers have employed bacteria as nano-scale production facilities for IONP synthesis [222]. Crespo *et al*. [223] reported the intracellular and extracellular synthesis of IONPs by utilizing gram-negative *E.coli* and *Pseudomonas aeruginosa* strains, respectively; for the intracellular activity, 15 mL of bacterial culture was incubated with different Fe metal salts, such as (1mM and 10 mM) $FeSO_4$, 1 mM $FeCl_3$, and 1 mM iron citrate ($C_{12}H_{18}Fe_3O_{14}$) at pH 6.5 for 2 days. Subsequently, for 30 min, the solutions were sonicated and centrifuged for 5 min at 8500 rpm. However, in the case of extracellular synthesis, the culture of bacteria was spun in a centrifuge, and resultant supernatant was mixed with Fe precursor salts, such as $FeSO_4$, $FeCl_3$, and iron citrate of varied concentrations (1 and 10 mM) at different pH (6.5 and 9). The average sizes of the produced IONPs ranged between 23-24 nm. In a separate study [223], *E.coli* was employed to synthesize IONPs. The IONPs synthesis included mixing the bacterial supernatant with 1 mM $FeSO_4$ for 48 h at a pH of 6.5 and temperature of 37°C. The produced spherical IONPs were found to have an average size of 18 ± 2 nm. Desai *et al*. [224] synthesized magnetic IONPs with an average size ranging from 10-20 nm using *Pseudomonas stutzeri* KDP_M2. The IONPs

synthesis involved a 96 h incubation of 100 mL bacterial culture supplemented with 0.5 mM ferric quinate ($C_{14}H_{19}FeO_{12}$) at pH 9 and temperature of 37°C.

Likewise, gram-positive bacterial strains have also been explored for the synthesis of IONPs. In a study by Daneshwar *et al*. [225], three gram-positive bacteria viz. *Bacillus pasteurii*, *Bacillus subtilis*, and *Bacillus licheniformis* were used to biosynthesise ammonia and bio-surfactant for IONPs production. Initially, bacterial cells were inoculated with Potato Dextrose Agar (PDA) media for 36 h at 35°C and 150 rpm. Subsequently, in broth medium, calcium chloride (40 g/L) and urea (30 g/L) were added and the flasks were placed back in the shaker incubator for an additional 96 h to produce ammonia through urease activities. Afterwards, the Fe precursors, 1 M $FeCl_2$ and $FeCl_3$, were added in a ratio of 1:2.5 (v/v) to the bacterial mediums for IONPs synthesis. The formed IONPs attained a rhombohedral structure in the cases of *Bacillus pasteurii* and *Bacillus subtilis* strains. Dynamic light scattering analysis revealed the sizes of synthesized IONPs as 37.4 nm, 53.5 nm, and 98.17 nm, using *Bacillus pasteurii*, *Bacillus subtilis*, and *Bacillus licheniformis* strains, respectively. Another group, Hajiali *et al*. [226], reported the synthesis of IONPs using a gram-positive strain of *Bacillus megaterium*. The grown bacterial culture of *Bacillus megaterium* was mixed in a ratio of 1:1 (v/v) with 0.1 M $FeSO_4$ at 25°C to produce IONPs. The diameter of synthesized spherical IONPs was found to be in the range of 20-30 nm. In a separate study [227], IONPs were synthesized using auxin produced from the bacterium supernatant of *Paenibacillus polymyxa*. The IONPs were synthesized by mixing auxin at a 50 µg/mL concentration with 2 mM $FeCl_3 \cdot 6H_2O$ over a water bath sonicator for 5 h at 45°C. The synthesized spherical IONPs exhibited an average diameter of 26.65 nm.

As mentioned above, the studies inferred the formation of stable and smaller-sized NPs at more extended incubation periods. The various functional groups like alkyl, hydroxyl, and amine are responsible for reducing and capping agents to form IONPs.

2.5.2.2 IONPs using Fungi

Heterotrophic eukaryotes like fungi are abundant throughout the biosphere, even in the most inhospitable conditions like deep-sea sediments, deserts, and highly salty areas [228]. Fungus has some extraordinary properties over other organisms like bacteria and algae. These benefits include the production of extracellular enzymes, a strong binding capability to cell walls, huge biomass-generating capacity, and the ability to utilize economical raw materials for growth [229]. Fungi are more environmentally viable, metal tolerant, and easy to scale up [230]. Therefore, nowadays, many researchers employ fungi to synthesize IONPs. Various metabolites, like polysaccharides, alkaloids, triterpenoids, fatty acids, vitamins, and minerals, bio-reduce metal precursor salts to nanoscale materials.

In a study by Chatterjee *et al*. [231], IONPs were produced using *Aspergillus niger BSC-1* of manglicolous origin. The fungus culture was incubated at 120 rpm for 10-12 days at 28°C. Consequently, fungal mycelia were separated utilizing the Whatman grade 1 filter paper and added to iron precursors of $FeCl_3.6H_2O$ and $FeSO_4.7H_2O$ in the ratio of 2:1 (v/v). Further, the prepared mixture was incubated under dark conditions for 3 h at 28°C for the formation of IONPs. The size of synthesized IONPs varied in the range of 20 - 40 nm. Mahanty *et al*. [232] synthesized IONPs using filamentous manglicolous fungi, namely STSP 27 (*Fusarium incarnatum*), STSP10 (*Trichoderma asperellum*), and STSP 19 (*Phialemoniopsis ocularis*). The fungal cell filtrates were mixed in a 2:1 molar ratio of Fe precursors ($FeCl_2$ and $FeCl_3$) solutions for 5 min, which prompted the formation of IONPs. The average diameters of synthesized IONPs were found to be 30.56 ± 8.68 nm, 25 ± 3.94 nm, and 13.13 ± 4.32 nm using the filtrates of *Fusarium incarnatum, Trichoderma asperellum*, and *Phialemoniopsis ocularis*, respectively.

Alamilla *et al*. [233] utilized the biomass of *Alternaria alternata* fungi to synthesize IONPs. The filament fungus was incubated at 30°C for 5 days at 150 rpm for the production of

biomass. Fe precursor ($FeSO_4$; 1mM) was added to this culture and incubated at 45°C for 3 days at 150 rpm for the formation of semi-oval and spheroid IONPs with sizes ranging between 10 to 80 nm. Mohamed *et al*. [234] utilized the biomass of *Alternaria alternata* fungus to produce IONPs. The fungal biomass was produced in a liquid medium at 28°C and 150 rpm for 72 h. Afterwards, the filtrate media was mixed with 1mM of Iron nitrate ($Fe(NO_3)_3$) for the synthesis of IONPs and again incubated at the above-mentioned conditions under dark. The synthesized cubical IONPs attained particle sizes in the range of 5.1-12.1 nm. In a separate study [235], the IONPs were synthesized using the biomass of fungi *Fusaium oxysporum*. The *Fusarium* biomass was incubated at 28° C and 180 rpm for 5 days. The obtained cellular-free extract was mixed with 1 mM $FeCl_3$ and allowed to incubate in the dark for an entire night at 28°C and180 rpm to facilitate the development of IONPs. The result showed the formation of spherical IONPs with particle sizes ranging between 2.5-20 nm.

2.5.2.3 Algal - based synthesis

Due to being rich in polymeric molecules, mainly polysaccharides, algae biologically reduce metal ions to produce flexible forms. Algal extracts typically contain a variety of ingredients, including minerals, proteins, carbohydrates, polyunsaturated fatty acids, and pigments (e.g., carotenoids, chlorophylls, and phycobilins). Other bioactive materials, such as antioxidants (tocopherols and polyphenols), also serve as stabilizing and reducing agents in the synthesis of IONPs. Owing to these combined properties, algae were applied as model organisms in the environmentally benign synthesis of IONPs.

Bhukal *et al*. [236] reported the synthesis of IONPs using *Spirulina* biomass. The washed *Spirulina* powder was added to 120 mL of deionized water, and a homogenous solution was formed. 1M $FeCl_3$ was added to this algal supernatant in a ratio of 1:1 (v/v) and mixed for 2 h at 75°C to synthesize IONPs. The synthesized IONPs have non-uniform particle structures

with an average size of 28.5 nm. El-kassas *et al*. [237] utilized two types of seaweed, viz. *Sargassum acinarium (Linnaeus)* and *Padina pavonica (Linnaeus) Thivy* Setchell 1933 were utilized for the production of IONPs. The synthesis of IONPs using both the algae was performed in two steps: first was algal extraction in which freeze-dried algal samples, approximately 1 g, were subjected to boiling in 100 mL of distilled water for 15 min with continuous stirring. Afterwards, the resulting extract was allowed to cool to room temperature and filtered. In the next step, the 0.1M $FeCl_3$ solution and filtered extract were mixed for 60 min at room temperature in a 1:1 (v/v) ratio to synthesize IONPs. The synthesized spherical IONPs from *P. pavonica* and *S. acinarium* extracts attained particle sizes in the range of 10-19.5 nm and 21.6-27.4 nm, respectively. The richness of diverse phyotchemical constituents in *P. pavonica* contributes to the formation of smaller-size IONPs in comparison to *S. acinarium.*

Marine algae have also been utilized to synthesize IONPs. In a study by Bensy *et al*. [238], IONPs were synthesized using the extract of marine algae *(Ulva lactuca)*. The algal extract and 0.1 M $FeCl_3$ were mixed in the 1:1 (v/v) ratio and allowed to stand for 2 h at room temperature. Thereafter, the formed suspension was dried at 40°C to produce IONPs. The size of the synthesized IONPs varied between 30-40 nm. Mashjoor *et al*. [239] used an aqueous extract from the green macroalgae *Ulva flexuosa* (wulfen) to synthesize IONPs by reducing a solution of $FeCl_3$/ $FeCl_2$ (2:1 M ratio) at 88°C along with drop-by-drop addition of 1 M NaOH to achieved pH between 8 to 11. The color of the mixture changed from light brownish-orange to black with time, signifying the formation of IONPs. The synthesized cubo-spherical IONPs had a particle size of 12.3 nm.

2.6. Adsorption of Cr(VI) onto green synthesized IONPs

The versatile chemical characteristics of green synthesized IONPs have achieved great attention in the field of Cr(VI) adsorption, as enlisted in Table 2.4. The PPs modified IONPs, incorporated either as stabilizing, capping, or reducing agents, have been widely explored in the field of Cr(VI) removal.

García *et al*. [240] performed an optimization study on the adsorption capacity of Cr(VI) using yerba mate (YM) extract fabricated Fe NPs. A higher removal (Q_m=1580 mg g^{-1}) occurred in the presence of a higher amount of PPs extract (rich in caffeine acid) due to their good reducing ability, in comparison to nZVI (Q_m=745 mg g^{-1}). However, it was observed that Cr(VI) reduction occurred within min of interacting with Fe^{2+}, causing it difficult to understand the involved adsorption kinetics as no traces of Cr(VI) were remained in the solution, i.e., established 100% removal. Zu *et al.* [241] also reported the effective removal (94.7%) of Cr(VI) at pH 5 by prepared green tea-mediated nZVI/Cu NPs. Likewise, Chrysochoou *et al.* [206] also reported maximum Cr removal at pH 3 using Green tea extract:2Fe ratio as the optimum concentration for the maximum removal efficiency.

Similar results were reported by Liu *et al*. [242] stating 100% removal of Cr(VI) by eucalyptus leaf extract synthesized Fe NPs when the ratio of polyphenol extract was twice that of NPs (i.e., 2:1 v/v). It was observed that at a higher PPs: NPs ratio (3:1), the overall Cr removal declined to 73.7% due to the overall reduction of the concentration of Fe^{3+} ions in the reaction mixture. In a similar way to decreasing the concentration of PPs to NPs (1.5:1), the overall Cr adsorption also declined to 58.2% due to the formation of larger-sized NPs. Interestingly, this study puts forward the impact of another parameter, the concentration of PPs extract in regulating the adsorption activity of the adsorbent. In addition, the extraction temperature affected the quality of PPs, which in turn varied the adsorption capacity. A ~100%

removal of Cr was observed when the extraction temperature was maintained at 80°C, which got significantly declined to 43.6% when extracted at 60°C.

The IONPs produced from pear peel extract were employed to adsorb Cr(VI) from a synthetic metal solution. The synthesized IONPs showed a remarkable 99.1% removal of Cr(VI) within a contact duration of 120 min. The prepared extract served dual roles as both stabilizing and capping agents for the formed IONPs. Fe^{2+} facilitated the reduction of Cr(VI) to Cr(III) through surface adsorption. At last, on the IONPs, Fe^{2+} and Cr(III) co-precipitate [11]. A similar study was done on Cr(VI) adsorption through IONPs synthesized using an extract of eucalyptus leaves. The surface complexation and co-precipitation were the predominant adsorption mechanisms responsible for a high Cr(VI) removal efficiency (98.9%) of IONPs [243].

Lingamdinne *et al.* [244] synthesized IONPs using seed extract of *Cnidiummonnieri (L.) Cuss* (CLC) was utilized for the individual removal of Cr(III) and Pb(II) from an aqueous solution. The synthesized IONPs exhibited maximum removal efficiency for Cr(III) and Pb(II) at pH 4.0 and a dosage of 0.5 g/L within 100 min. The Q_m values of IONPs for Cr(III) and Pb(II) removal were found to be 102.3 mg g^{-1} and 105.6 mg g^{-1}, respectively as per Langmuir isotherm. In another study by Sharma *et al.* [245], IONPs were synthesized using leaf extract of *Spilanthes acmella* for the removal of As(III), Co(II), Cd(II), and Cu(II) from aqueous solutions. The optimization of metal ions removal occurred at pH 7.0, with a dosage of 0.6 g/L for As(III) and Co(II) and 0.8 g/L for Cd(II) and Cu(II). The adsorption isotherm analysis showed that the Q_m were highest for As(III) (21.83 mg/g), followed by Co(II) (20.43 mg/g), Cu(II) (15.29 mg/g), and Cd(II) (13.54 mg/g), using the Langmuir isotherm model. A separate study by Idris *et al.* [246] synthesized IONPs using the aqueous stem bark extract of Prosopis Africana removed 100% of Cr and Zn, and 37% of Pb from tannery effluent at a 20% (v/v) dosage within 20 min. Mohanty *et al.* [10] utilized IONPs produced from manglicolous fungi

Aspergillus tubingensis (STSP 25) to effectively remove Pb(II), Ni(II), Cu(II), and Zn(II) from synthetic wastewater. The batch adsorption experiments demonstrated that at a pH of 6 and a temperature of 40°C, 1 g/L of IONPs dosage removed >90% of heavy metals from an aqueous matrix of 10 mg/L concentration.

Table 2.4: Performance of IONPs prepared using various extracts for Cr(VI) removal.

S. No.	Extracts	Size of IONPs (nm)	Optimized conditions	Q_m (mg g^{-1})	Removal %	Reference
1.	*S. jambos*(*L*) *Alston* leaf	5	pH-3.2, Dosage-0.2 mL, Initial concentration -50 mg/L, Contact time-90 min	699	100	[247]
2.	*Punica granatum* leaf	100-200	pH-2, Dosage-2 mL, Initial concentration -1000 mg/L, Contact time-60 min, Agitation speed-100 rpm	186	-	[248]
3.	*Eucalyptus* leaf	20-80	pH-5, Dosage-0.5 g/L, Initial concentration -15 mg/L, Contact time-30 min	149.3	60	[249]
4.	Peanut skin	25-77	pH-4.7, Dosage-2 g/L, Initial concentration -10 mg/L, Contact time – 1 min	-	100	[250]
5.	*Nephrolepis auriculata*	40-70	Dosage-1.5 mL, Initial concentration -50 mg/L, Contact time-90 min	-	98.01	[251]
6.	Green tea extract	40-80	pH-5, Dosage-20 g/L, Initial concentration -100 mg/L, Contact time-1440 min	66	-	[252]
7.	*Verbascum thapsus* leaf	-	pH-2, Dosage-1 g/L, Initial concentration -25 mg/L, Contact time-30 min	-	100	[253]
8.	*Eucalyptus globules* leaf extracts	50-80	Dosage-0.8 g/L, Initial concentration -200 mg/L, Contact time-30 min	5.47	98.1	[254]
9.	*Barberry* leaf	20-40	pH-2, Dosage-0.5 g/L, Initial concentration -50 mg/L, Contact time-60 min	-	100	[255]
10.	*Eucalyptus globulus* leaf	2.34 ± 0.53	pH-3, Dosage-5 mL, Initial concentration - 204.43 mg/L, Contact time-30 min	-	100	[256]

2.7. IONPs Impregnated Biopolymers for Cr(VI) adsorption

The removal of Cr(VI) through powdery IONPs from aqueous solution leads to the aggregation of NPs and also limit their reusability [257, 258]. These mentioned issues of IONPs can be tackled through various approaches like reducing their surface energy, tuning the synthesis method, and surface modification [134, 259]. In this regard, the surface of IONPs has been attached by different organic molecules/inorganic shells to prevent IONPs oxidation [260-263]. Functional groups like carboxylate, hydroxyl, and amine increased their stability, adsorption efficiency, and surface area for chelating metal ions from water/wastewater [144]. Therefore, in this regard, natural polymer chitosan has been mostly used as the matrix for the immobilization of IONPs via entrapment to form the desired composites for Cr(VI) removal [264, 265].

Chitosan (CS) is the second most abundant fiber derived from chitin. CS is attained by deacetylation of chitin, which is mainly found in crustacean shells, and there are plentiful waste shells from the food industry. CS contains 2-acetamido-2-deoxy- β-D-glucopyranose and 2-amino-2- deoxy-β-D-glucopyranose residues. For environment remediation purposes, CS is considered to be a low-cost, effective adsorbent A large amount of amino and hydroxyl functional groups present in the CS act as a coordination site and formed complexes with metal ions [266]. CS in various forms, such as spheres and films, were used for Cr(VI) adsorption [267]. Beads obtained from bio-resources like polysaccharide chitosan (CS) [268] are emerging as a potential adsorbent for environmental remediation.

Various researchers have studied the synergetic effect of IONPs and chitosan for heavy metal adsorption [269]. Composites of IONPs-chitosan were prepared in different structures like films, beads, etc. Recently, Neto *et al.* [270] developed a composite film of chitosan/CNTs/IONPs for Cr (VI) removal from a synthetic solution. The prepared composite has a varying concentration of all three materials, i.e., iron oxide, CNTs, and CS. The composite

with a concentration of 0.5 (w/w) of CS in CNTs/iron oxide found a Q_m of 477.30 mg g^{-1} at 40ºC for Cr(VI) removal from 100 mg/L of an aqueous solution. The removal of Cr(VI) was optimized at pH 4, with an adsorbent dose of 0.3 g/L and a contact time of 180 min. Lasheen *et al.*[271] also developed Fe_3O_4-chitosan films by casting approach and found to remove 92 % for Cr(VI) from 20 mg/L of an aqueous solution. The Q_m for Cr(VI) was reported as 116.2 mg g^{-1} per Langmuir isotherm. Magnetic beads of CS were also prepared by Huang *et al.* [156] using the cross-link method. The prepared beads were insoluble at various pH conditions of the solvent. Cr(VI) removal was optimized at pH 4 and a contact time of 80 min. The isotherm model was well fitted to Langmuir isotherm with a Q_m value of 69.4 mg g^{-1}. In a study by Ravi *et al.* [272], CS was coated with IONPs and found to remove 96.3 % of Cr(VI) from 150 mg/L of an aqueous solution. The removal of Cr (VI) was optimized at 5.32 and 80 min of pH and contact time, respectively. The isotherm of adsorption was well-fitted to the Langmuir isotherm model. Another study by Horst *et al.* [273] prepared magnetic nanocomposites composed of IONPs and chitosan, which were synthesized by co-precipitation of iron precursors and CS in a non-oxidizing environment. The prepared nanocomposites were used for Cr(VI) removal and found to have Q_m of 46 mg g^{-1} at pH 4 within 45 min from 100 mg/L of an aqueous solution. Also, the prepared composites were found to be excellent recyclable upto 8 cycles by losing 20% of its adsorption capacity in the last cycle. Shalaby *et al.* [274] coated IONPs with CS to remove Cr(VI) from 80 mg/L of metal concentration. The prepared coated structure was non-agglomerated with a spherical diameter of 13 nm as revealed by TEM micrographs. The synthesized structure removed 98 % of Cr(VI) at pH 2 within 100 min. The Q_m was reported to be 39.6 mg g^{-1} as per Langmuir isotherm. Therefore, from the above studies, it is clear that various composites of IONPs-chitosan have been found to remove Cr(VI) from synthetic solution.

2.8. Conclusions

IONPs have piqued the curiosity of researchers in water treatment due to their affinity for removing Cr(VI) from contaminated water. The production of IONPs using different synthesis techniques has raised concerns over their potential toxicity, expensive nature, and intricate processes. Consequently, scientists have been compelled to investigate other methods for the straightforward creation of these nanostructures. Hence, green synthesis provides an economically efficient, reliable, and commercially feasible approach to produce IONPs. Moreover, this approach offers a substantial yield and generates extraordinary structures of nanoparticles. The water contaminates Cr(VI) needs an environment-friendly adsorbent for its removal, which simultaneously does not cause any secondary pollution. Green synthesized IONPs have been identified as a viable candidate in this context.

2.9 Knowledge gap and thesis objectives

- Selectivity and adsorption capacity achieved by typical adsorbents are not adequate for large-scale applications
- Loss of adsorption capacity due to substrate ions leaching and cause of secondary pollution
- Nano-adsorbents used for water treatment suffer from high synthesis costs, lower adsorption capacity, and difficulty in adsorbent recovery
- Lack of investigation about the interaction of nano-adsorbent infused in composite beads with heavy metal ions to better understand the removal mechanism
- Scope for the development of recoverable and re-useable nano-adsorbents in an environmentally benign process

- Development of bio-based nano-adsorbents for the reduction of Cr(III) to Cr(VI) (decrease in toxicity) and simultaneous removal of Cr(III) and Cr(VI) is interest of environmental scientists

Based on the literature survey, it has been determined that Cr(VI) is an extremely toxic pollutant released in large quantities due to various anthropogenic and natural sources into the ground and water bodies. Additionally, we have determined that there is an apparent necessity to investigate affordable and eco-friendly adsorbents to remove hazardous Cr(VI) through adsorption. The extensive utilization of IONPs for Cr(VI) removal is evident from the existing collection of documents. However, shifting our attention towards innovative and environmentally-friendly methods for producing these nanoparticles is essential. Several studies have been conducted on the different techniques and procedures for synthesizing IONPs and their use in eliminating chromium. However, the utilization of bioinspired synthesized IONPs in chromium removal demonstrates a limited number of approaches and requires further research.

The tea plant (*Camellia sinensis var. assamica*) belongs to the theaceae family and is used for the production of tea beverages. This species is native to India's Assam area. It grows well in tropical climates and at low elevations [275]. More than half of India's tea is produced in Assam alone [276]. The extract of matured tea leaves (i.e., rejected leaves) emerges as a suitable stabilizing and reducing agent in green synthesis due to its high PPs content [277]. This doctoral study utilizes phytochemicals from matured tea (*Camellia sinensis var. Assamica*) leaves extract and polyphenols (tannic acid) to synthesize engineered IONPs for the removal of Cr(VI) from aqueous solutions. So, the objectives of this doctoral work are designed as given below:

- To develop a vegetal route for the synthesis of iron oxide nanoparticles (IONPs) by using *Camellia sinensis var. assamica* leaf extract for Cr(VI) adsorption
- To infuse IONPs into chitosan (CS) matrix for the formulation of reusable CS/IONPs composite adsorbents for Cr(VI) removal
- To develop tannic acid (TA) assisted IONPs/sodium alginate (Alg) composite adsorbent (Alg-TA-Fe) for simultaneous Cr(VI) uptake and antibacterial functionality
- To investigate CS/IONPs and Alg-TA-Fe beads in a continuous adsorption process for the decontamination of Cr(VI)

Chapter 3

Vegetal route for the synthesis of iron oxide nanoparticles (IONPs) by using *Camellia sinensis var. assamica* leaf extract for Cr(VI) decontamination and removal

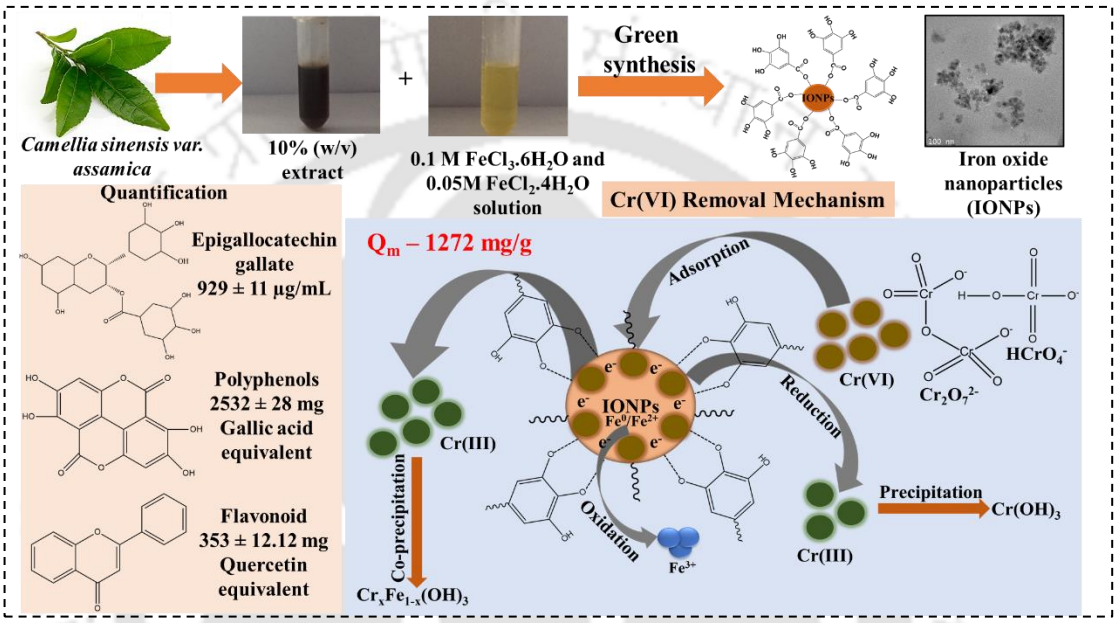

(Synthesis of iron oxide nanoparticles mediated by Camellia sinensis var. Assamica for Cr(VI) adsorption and detoxification. ***Aquib Jawed****, Animes K. Golder, Lalit M. Pandey (2023),* ***Bioresource Technology****, 376, 128816)*

Highlights

- Green synthesis of tea polyphenols-coated iron oxide nanoparticles (IONPs)
- Synthesis conditions optimization for IONPs through Response Surface Methodology
- Synthesized IONPs removed 96 % of Cr(VI) under optimized conditions
- Langmuir isotherm predicted the Cr(VI) adsorption capacity of 1272 mg g^{-1} for IONPs
- IONPs surface active sites act as an adsorption and reduction spots for Cr(VI)

This chapter aimed to develop an eco-friendly nanomaterial for the adsorption and detoxification of Cr(VI) in aqueous solution. Towards this goal, IONPs were synthesized using dried leaves extract of *Camellia sinensis var. assamica* for the removal of Cr(VI). The synthesis conditions (time, temperature, and iron precursors to leaf extract ratio (v/v)) of IONPs were optimized using Response Surface Methodology-Central Composite Design (RSM-CCD). The formed IONPs were characterized using various analytical techniques such as UV-Vis, FETEM, FTIR, XRD, EDS, etc. The process of Cr(VI) adsorption over IONPs was investigated through kinetic, thermodynamic, and isotherms studies. Furthermore, the adsorption mechanism was elucidated.

3.1. Introduction

As discussed in Chapter 2, IONPs were proven to be a potential candidate for Cr(VI) detoxification. Nevertheless, chemical synthesis of IONPs suffers drawbacks like the requirements of extravagant and toxic chemicals, such as organic solvents and $NaBH_4$, leading to secondary pollution. The quick oxidation and agglomeration of IONPs also restrict their usage [278].

Therefore, IONPs synthesis utilizing plant extracts has been endorsed nowadays because such processes avoid using noxious reducing agents. Several studies have documented the synthesis of IONPs through plant-based extracts made of *Eucalyptus* [243], *Rosa indica* [279], *Eucalyptus globules* [280], *Acacia catechu* [281], Green tea [12], and *Citrus limetta* [282]. These extracts are usually composed of polyphenols (PPs), flavonoids, and ascorbic acids that serve a dual role (reducing and stabilizing agent) in producing IONPs.

The green synthesized IONPs were also utilized for the removal of Cr(VI) from aqueous solution. Likewise, Hao *et al.* [12] synthesized core-shell IONPs through green tea extract showing 97.7% Cr(VI) removal within 60 min from 80 mg/L. They also reported a maximum

adsorption capacity (Q_m) value of 74 mg g^{-1}. Jin *et al.* [243] employed *eucalyptus* leaf extract to produce IONPs. At a pH of 4.2 and dosage of 0.8 g/L, IONPs removed 98.2% of Cr(VI) in 480 min from 10 mg/L aqueous solution and attained a Q_m value of 20.5 mg g^{-1}. Guo *et al.* [283] used grape seed extract to synthesize zero-valent iron NPs (nZVI). It resulted in 94.4% removal of Cr(VI) at a pH of 3 from 25 mg/L metal concentration. These studies revealed that green synthesized IONPs found to have a lower Q_m value which needs to be improved for their practical applications on an industrial scale.

Camellia sinensis var. assamica, a native species of Assam tea, belongs to the *theaceae* family, and it is widely used for tea beverage production in the Northeastern part of India. It grows well in tropical climates and at low elevations [275]. More than half of India's tea is produced in Assam alone. The extract of matured tea leaves (i.e., rejected leaves) emerges as a suitable stabilizing and reducing agent in green synthesis due to its high PPs content [277]. Catechin accounts for 60-80% of tea PPs [284]. The reduction potential (E° vs. Ag/AgCl electrode) of PPs in tea extract typically ranges from 0.3 to 0.8 V vs. Standard hydrogen electrode (SHE). On the other hand, E° of Fe^{3+} to Fe, Fe^{3+} to $Fe^{2+,}$ and Fe^{2+} to Fe are -0.036, 0.77, and -0.44 V vs. SHE [277], respectively. Therefore, tea extract could reduce Fe^{3+} forming IONPs. The extract of *Camellia sinensis var. assamica* has not been explored much for formulating IONPs. Recently, Xiao *et al.* [277] synthesized nZVI through leaves extract of *Camellia sinensis var. assamica (mast.) kitamura* via microwave extraction method and explored for the dye removal. Therefore, the use of *Camellia sinensis var. assamica* tea extract for IONPs synthesis and its application towards Cr(VI) removal is a prudent area of environmental researches.

Accordingly, in this Chapter, IONPs were synthesized using dried leaves extract of *Camellia sinensis var. assamica* for the adsorption and detoxification of Cr(VI) in aqueous solution. The effect of reaction time (30 - 150 min), temperature (25 - 85°C), and iron

precursors to leaf extract ratio (0.3 - 1 v/v) on the formation of IONPs was studied and optimized using RSM-CCD. The synthesized IONPs were characterized using various analytical techniques and investigated for Cr(VI) removal through batch adsorption test. A thorough equilibrium adsorption and thermodynamics study was carried out. The mechanism of Cr(VI) is postulated based on both solution and solid phase reactions.

3.2. Materials and Methods

3.2.1. Materials

Iron(II) chloride tetrahydrate ($FeCl_2.4H_2O$) (cat. no: A16327), iron(III) chloride hexahydrate ($FeCl_3.6H_2O$) (cat. no: A16231), and 1,1 -diphenyl-2 picrylhydrazyl (DPPH) (cat. no: 29128) were procured from Alfa Aesar, India. The chromium standard for Atomic absorption spectroscopy (AAS) (1000 mg/L, cat. no: 02733) from Sigma Aldrich, India, was utilized and then further diluted to lower concentrations of Cr(VI) to create the solutions for the batch adsorption studies. Folin-ciocalteu (cat. no: F9252) and epigallocatechin gallate (ECGC) (cat. no: E4143) were procured from Sigma Aldrich, India. 1,5-Diphenylcarbazide (DPC) (cat. no: GRM519), potassium ferricyanide (cat. no: GRM1034), di ammonium hydrogen phosphate (cat. no: GRM1102), pyrogallol (cat. no: GRM7444), potassium acetate (cat. no: GRM1091), sodium phosphate monobasic (cat. no: GRM3964), quercetin dihydrate (cat. no: RM6191), magnesium chloride (cat. no: GRM3922), sodium chloride (cat. no: GRM853), calcium chloride (cat. no: GRM534), magnesium sulphate heptahydrate (cat.no: GRM684), and sodium nitrate (cat. no: PCT0014) were purchased from Himedia, India. The experimental studies were performed in double distilled water (18 MΩ, Millipore system).

3.2.2 Preparation of *Camellia sinensis var. assamic* bio-extract

Fresh leaves of *Camellia sinensis var. assamica* were plucked from the tea garden located at the Indian Institute of Technology Guwahati, Assam. The bio-extract was prepared following the steps (Figure 3.1). First, leaves were washed to remove dust particles that adhered to them. It was then further air-dried at ambient temperature for a few days until the weight of dried leaves attained to a constant value. Dried tea leaves at a 10 % (w/v) of concentration were extracted in water over a water bath at 80℃ for 2 h. As time passes, the watery solution turns dark brown. Polyphenolic compounds in the extract caused this colour change. Further, the extract was vacuum-filtered after being cooled to room temperature. Afterwards, the filtered extract was centrifuged and stored at 4℃ until further usage.

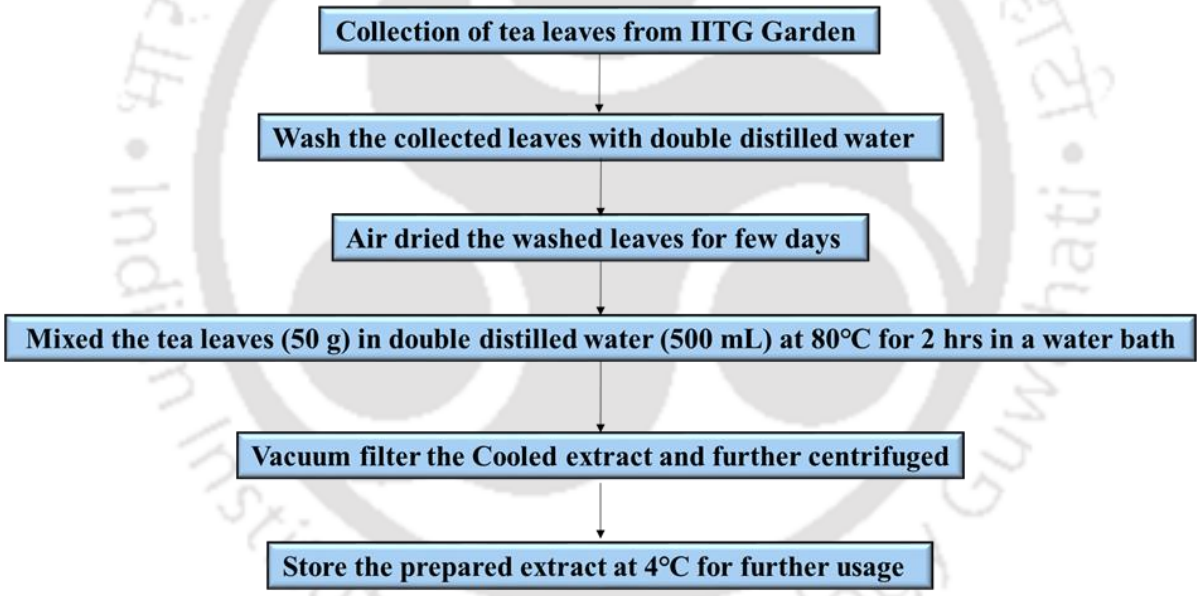

Figure 3.1: Schematic for the preparation of *Camellia sinenss var. assamica* bio-extract.

3.2.3 Phytochemical analysis of *camellia sinensis var. Assamica* leaves extract

3.2.3.1 Determination of ECGC

A ECGC stock solution of 1mg/mL was prepared in double distilled water (pH < 4.0). The prepared stock solution was then utilized to make the mixture of standards (10-50 µg/mL). Further, the calibration curves were plotted from the prepared diluted concentration of ECGC

in µg/mL. Either a 20 µL aliquot of the tea leaves extract or standard ECGC sample was injected into an HPLC system (Varian, Model: ProStar.210, USA), which was outfitted with a UV detector and a C18 column (Agilent TC-C18) that was set to run at 25°C. The current study used a mobile phase consisting of methanol (MeOH), water, and orthophosphoric acid in a 20:79.9:0.1 (v/v/v) ratio (isocratic mode) with a flow rate of 1 ml/min [285]. The scanning wavelength was set to 210 nm.

3.2.3.2 FC assay

Total polyphenolic content (TPC) of *Camellia sinenss var. assamica* leaves extract was determined using the FC method [286]. In a nutshell, 125 µL of tea leaves extract (10% w/v) and 500 µL of FC (10% v/v) reagent were mixed and maintained in the dark for 5 min before adding 375 µL of 10% (w/v) sodium carbonate. After another 60 min, the mixture was tested for absorbance at 765 nm. The calibration curve was used to compute the TPC, which is expressed in mg of gallic acid equivalent (GAE) per 100 g of dried tea leaves (DW).

3.2.3.3 DPPH assay

DPPH was used in the antioxidant assay that measures antioxidants ability to scavenge free radicals (SFR) by producing a deep violet color when a stable free radical is present [287]. When a DPPH solution comes into contact with a free radical scavenging agent, it turns brilliant yellow. *Camellia sinenss var. assamica* leaves extract or standard ascorbic acid concentrations (640 µL) of 2, 4, 6, and 8 (µg/mL) were added to the DPPH solution (1 mM). H^+ ion was released with the reaction between DPPH and an antioxidant resulting in a lower absorbance value at 515 nm. The DPPH activity was demonstrated in mg of ascorbic acid equivalent (AAE) per 100 g of DW.

3.2.3.4 Superoxide radical scavenging capacity (SRSC) assay (pyrogallol)

Camellia sinenss var. assamica extract was quantified for SRSC (pyrogallol) activity [288]. 25 mM pyrogallol (80 µL), Tris-HCl buffer (50 mM, pH 8.2, 560 µL), and sample (80 µL) were nurtured at 25°C for 5 min. Afterwards, to end the reaction, 8 mM HCl solution (80 µL) was put into the mixture. The wavelength for measuring the absorbance of the mixture was 420 nm. The positive control was 100-500 µg/mL of standard ascorbic acid. The value of SRSC is expressed in mg of AAE per 100 g of DW.

3.2.3.5 Total flavonoid content (TFC)

The TFC of *Camellia sinenss var. assamica* extract was quantified using the microplate method [289]. 200 µL volume of sample was added to 40 µL of potassium acetate [CH_3COOK], 520 µL of methanol, and 40 µL of aluminum nitrate [$Al(NO_3)_2.9H_2O$] (10% (w/v)). After allowing the mixture to sit for 40 min at room temperature, the absorbance was measured at 415 nm. The various concentrations (10-50 µg/mL) of standard quercetin dihydrate were used to prepare the calibration curve. The capture TFC value was expressed in quercetin equivalent (QE) per 100 g of DW.

3.2.3.6 Reducing power assay

Ferric reducing power (FRP) of *Camellia sinenss var. assamica* extract was adopted as stated elsewhere [289]. Briefly, 80 µL of the sample was combined with 40 µL of potassium ferricyanide (1% w/v) and 40 µL of sodium phosphate buffer (0.2 M, pH 6.6). The prepared samples were incubated at 50°C for 20 min. After that, 40 µL of tri-chloroacetic acid (10% w/v), 40 µL of double distilled water, and $FeCl_3$ (0.1% w/v) 20 µl were mixed into the incubated solution. Further, the absorbance was measured at 700 nm. The various concentrations (100-

500 µg/mL) of standard quercetin dihydrate were used to prepare the calibration curve. The FRP value was expressed in QE per 100 g of DW.

3.2.4 Synthesis of IONPs

The IONPs were synthesized using prepared bio-extract of *Camellia sinensis var. assamica* (Figure 3.2). In the synthesis process, 0.1 M $FeCl_3.6H_2O$ and 0.05M $FeCl_2.4H_2O$ (1:1, v/v) aqueous solution was mixed with *Camellia sinensis var. assamica* extract in the N_2 atmosphere as per the experimental details (Table 3.1). A strong black precipitate was observed, which signifies the production of IONPs. Further, the formed IONPs suspension was centrifuged for 20 min at 8000 rpm, and the neutral pH was maintained by several washes. After washing, the precipitate was dried in a vacuum oven at 60ºC for 24 h and grind in mortar/pestle to produce IONPs powder for further characterization and Cr(VI) removal studies.

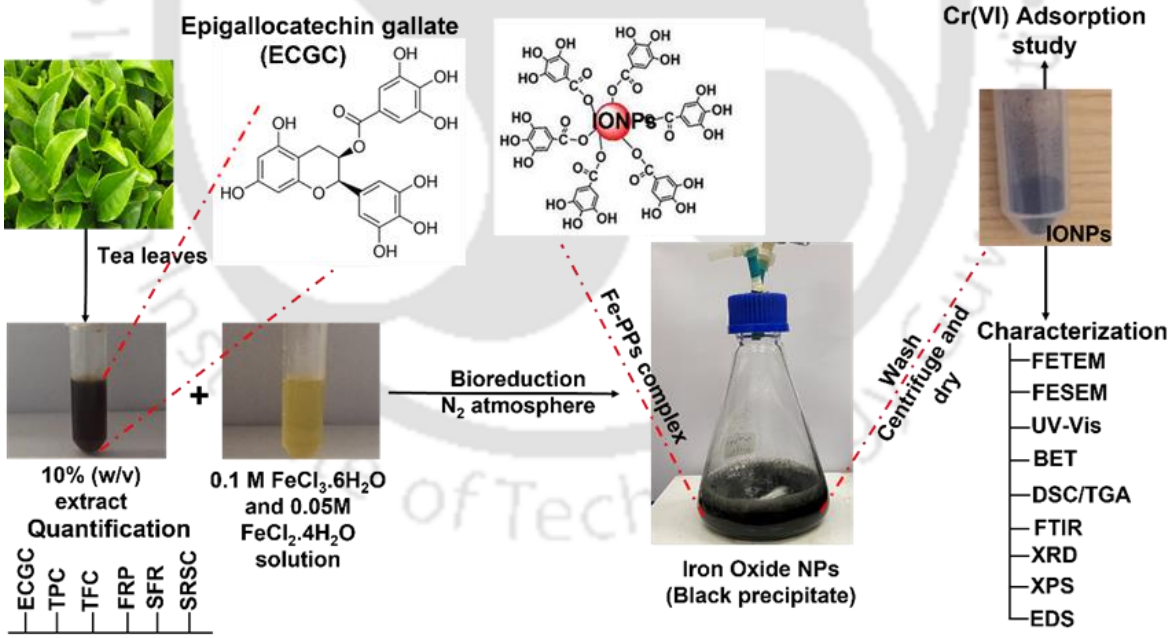

Figure 3.2: Schematic of IONPs synthesis steps using *Camellia sinensis var. assamica* leaves extract.

3.2.5 Optimization of IONPs formation through RSM

Three independent factors, namely, time (30-150 min), temperature (25-85°C), and Fe^{3+}-Fe^{2+}/tea leaves extract (v/v) (0.3-1) were investigated using the CCD to achieve IONPs of desired quality. The formation of IONPs was monitored by recording the optical absorbance at 277 nm. To predict the outcome, 20 sets of experiments were conducted based on the CCD. Further, the experimental data were also subjected to regression analysis using the ANOVA (analysis of variance).

3.2.6 Characterizations of IONPs

Ultraviolet–visible spectroscopy (UV-Vis) (Shimadzu, Model: UV-2600, Japan) was employed for the characterization of leaves extract, Fe precursors solution, and progress of IONPs formation in the wavelength ranging from 200 to 800 nm. High-resolution X-ray diffractometer (XRD) (Rigaku Technologies, Model: Smartlab, Japan) was utilized to analyze the crystal structure of the synthesized IONPs. Field emission scanning electron microscopy (FESEM) (Zeiss, Model: Sigma, Germany) and Field emission transmission electron microscope (FETEM) (JEOL, Model: 2100F, Japan) were employed to examine the shape and size of IONPs. Energy dispersive spectroscopy (EDS) (Zeiss, Model: Sigma, Germany) was captured for the elemental analysis. The presence of surface functional groups onto IONPs was investigated by Fourier transform infrared spectroscopy (FTIR) (PerkinElmer, Model: Spectrum two, USA). The specific surface area of IONPs was quantified through Brunauer-Emmett-Teller (BET) (Qunatchrome, Model: Autosorb-IQ MP, Austria). The thermal stability of IONPs was examined using a Differential scanning calorimetry (DSC) /Thermo Gravimetric analysis (TGA) System (Netzsch, Model: STA449F3A00, Germany). X-ray photoelectron spectroscopy (XPS) (Ulvac, Model: PHI 5000 VersaProbe III, Japan) utilizing Al kα (1486.6 eV) was also employed to determine the chemical state of IONPs and their alteration, if any,

after Cr(VI) adsorption. Further, particle size analyzer (Anton Paar, Model: LitesizerTM 500, Austria) was used to measure the zeta potential of the synthesized IONPs.

3.2.7 Batch adsorption study for Cr(VI) removal through synthesized IONPs

The procedure involved mixing 10 mL of 40 mg/L Cr(VI) solution with a series of flask contactors containing 0.1% (w/v) of IONPs, for 3 h agitation at 180 rpm in an incubator shaker (Scigenics, Model: Orbitek-LE, India). After an incubation period, the samples were centrifuged. The collected supernatant was mixed with DPC reagent at an appropriate dilution for the spectrophotometric analysis at λ = 543 nm to quantify dissolved Cr(VI) concentration [290]. The equilibrium adsorption capacity (q_e, mg g^{-1}) was examined using the adsorption experiments at different Cr(VI) concentrations, ranging from 40 to 375 mg/L (Eq. 3.1, [196]). Further, AAS (Variant, Model: Spectra AA240, USA) was utilized to compute the changes in concentration of Fe with and without a Cr(VI) solution.

$$q_e = \frac{(C_o - C_e) \times V}{m} \quad (3.1)$$

Where V denotes the volume (L) of the solution, C_o and C_e represent the initial and equilibrium concentrations of Cr(VI) (mg/L), and m states the mass of the IONPs used (g).

3.3 Results and discussion

3.3.1 Phytochemical analyses of bio-extract

The prepared extract of 10% (w/v) of *Camellia sinensis var. assamica* was quantified for ECGC, TPC, DPPH SFR antioxidant activity, SRSC, TFC and FRP. The concentration of ECGC in the leaves extract of *Camellia sinensis var. assamica* was found to be 929.2 ± 11 µg/mL (Figure 3.3). Further, the amount of TPC, DPPH antioxidant activity, SRSC, TFC, and FRP in the extract of *Camellia sinensis var. assamica* were estimated to be 2532 ± 28 mg GAE,

27.88 ± 8 mg AAE, 6718.51 ± 84.13 mg AAE, 353.44 ± 12.12 mg QE and 6755.55 ± 80.12 mg QE per 100 g on DW basis, respectively.

ECGC was one of the key component found in green tea leaves (*Camellia sinensis*), which accounts for its antioxidant properties [291]. Luo *et al.* [292] reported ECGC content of 1022.22 µg/mL in *Camellia sinensis* leaves extract of 2.7% (w/v) prepared at 85℃. It implies that *Camellia sinensis* contains a high concentration of ECGC compared to *Camellia sinensis var. assamica* prepared in the present work. The amount of TPC in the extract of *Camellia sinensis* was found to be 15200 ± 200 GAE per 100g DW which was on the higher side than *Camellia sinensis var. assamica* extract. However, Santos *et al.* [293] reported the maximum value of TPC 18284 ± 186 GAE per 100g DW for *Aspalathus linearis* extract. Also, in a separate study by Baba *et al.*, [286] the amount of TPC reported was 45 ± 1.70 mg GAE/g for the root extract of *Arisaema jacquemontii* at 60-65 ℃ in methanol for 3-4 h. This revealed that extraction in water as a solvent yielded more TPC content. The value of DPPH scavenging activity of *Camellia sinensis var. assamica* extract in mg AAE/ 100 g of DW reported by Armstrong *et al.* [294] was 98 times higher than the present work. This advocates that a lower extraction time was sufficient for the higher value of DPPH antioxidant activity. Further, the SRSC value of the prepared *Camellia sinensis var. assamica* extract was 76 times higher than the reported value of 88.51 ± 1.6 AAE per 100g DW [289]. It implies that *Camellia sinensis var. assamica* leaves extract could inhibit the generation of $O_2^{\cdot-}$ Which was formed during the oxidation of pyrogallol molecules [292]. In terms of TFC, a study by Baba *et al.* (2015) reported TFC in the root extract of *Arisaema jacquemontii* as 35 ± 2.20 mg rutin equivalents/g [286]. Further, in a separate study by Dehimat *et al*. [289] *Varthemia sericea* leaves extract was laden with a higher value of TFC (1843 ± 111 mg QE per 100 g DW). The FRP value for *Camellia sinensis* extract showed the maximum value of 9744 ± 280 mg AAE per 100g of DW due to

the presence of green tea catechin (ECGC). It could cause significant Fe^{3+} reduction for IONPs formation.

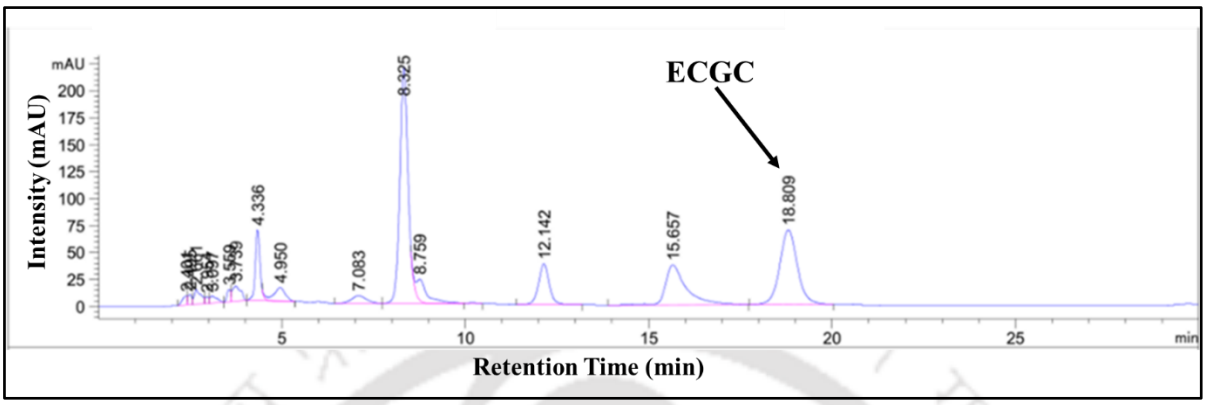

Figure 3.3: HPLC chromatogram of 10% (w/v) *Camellia sinenss var. assamica* leaves extract.

3.3.2 RSM-CCD optimization of synthesis conditions for the production of IONPs

Three independent variables, namely, reaction time (A, min), temperature (B, °C), and Fe^{2+}-Fe^{3+}/leaves extract ratio (v/v, C) affecting the IONPs formation, were selected for RSM-CCD. A, B, and C had lower/upper boundaries as 30/150, 25/85, and 0.3/1, respectively. The 20 experimental sets were created by the RSM software (Table 3.1). The absorbance value at 277 nm was selected as the model response, which was indicative of the presence of PPs forming IONPs.

$$\text{Absorbance at 277 nm} = 0.12 + 0.014A + 0.014B - 0.0095C + 0.0025B - 0.012AC - 0.0025BC + 0.008A^2 - 0.0025B^2 + 0.0027C^2 \quad (3.2)$$

A quadratic polynomial, Eq. 3.2, was fitted to the experimental response data. The experimental results were close to projected response values with the correlation coefficient (R^2) > 0.96. The model terms A, B, C, AC, and A^2 were considered significant with p-value < 0.05 after conducting an ANOVA analysis with the three independent variables (A, B, and C) and their interactions (AB, BC, AC, A^2, B^2, and C^2). The optimal synthesis conditions of IONPs

were found to be 48 min, 26°C, and 0.36 (v/v) Fe^{2+}-Fe^{+3}/leaves extract ratio. Figure 3.4 (a, b, and c) depicts the 3D response surface plots at the optimized conditions for the synthesis of IONPs. The absorbance value at the optimal conditions for IONPs synthesis was found to be 0.086 (Figure 3.5), which agreed with the predicted value of 0.085.

Table 3.1: Experimental and predicted values of Absorbance at 277 nm in relation to independent variables (pH, temperature and Fe^{2+}-Fe^{3+}/leaves extract ratio) in RSM-CCD runs.

S. No	Independent variables			Experimental result with absorbance at 277 nm	Predicted result with absorbance at 277 nm
	Time (min)	Temperature (°C)	Fe^{2+}-Fe^{3+}/leaves extract (v/v)		
1	54.3	37	0.44	0.1	0.09
2	125.6	37	0.44	0.15	0.15
3	54.3	72	0.44	0.13	0.13
4	125.6	72	0.44	0.19	0.18
5	54.3	37	0.86	0.11	0.11
6	125.6	37	0.86	0.11	0.11
7	54.3	72	0.86	0.13	0.13
8	125.6	72	0.86	0.14	0.13
9	30	55	0.65	0.12	0.12
10	150	55	0.65	0.16	0.17
11	90	25	0.65	0.09	0.09
12	90	85	0.65	0.13	0.14
13	90	55	0.3	0.14	0.15
14	90	55	1	0.11	0.11
15	90	55	0.65	0.12	0.12
16	90	55	0.65	0.13	0.12
17	90	55	0.65	0.12	0.12
18	90	55	0.65	0.12	0.12
19	90	55	0.65	0.12	0.12
20	90	55	0.65	0.12	0.12

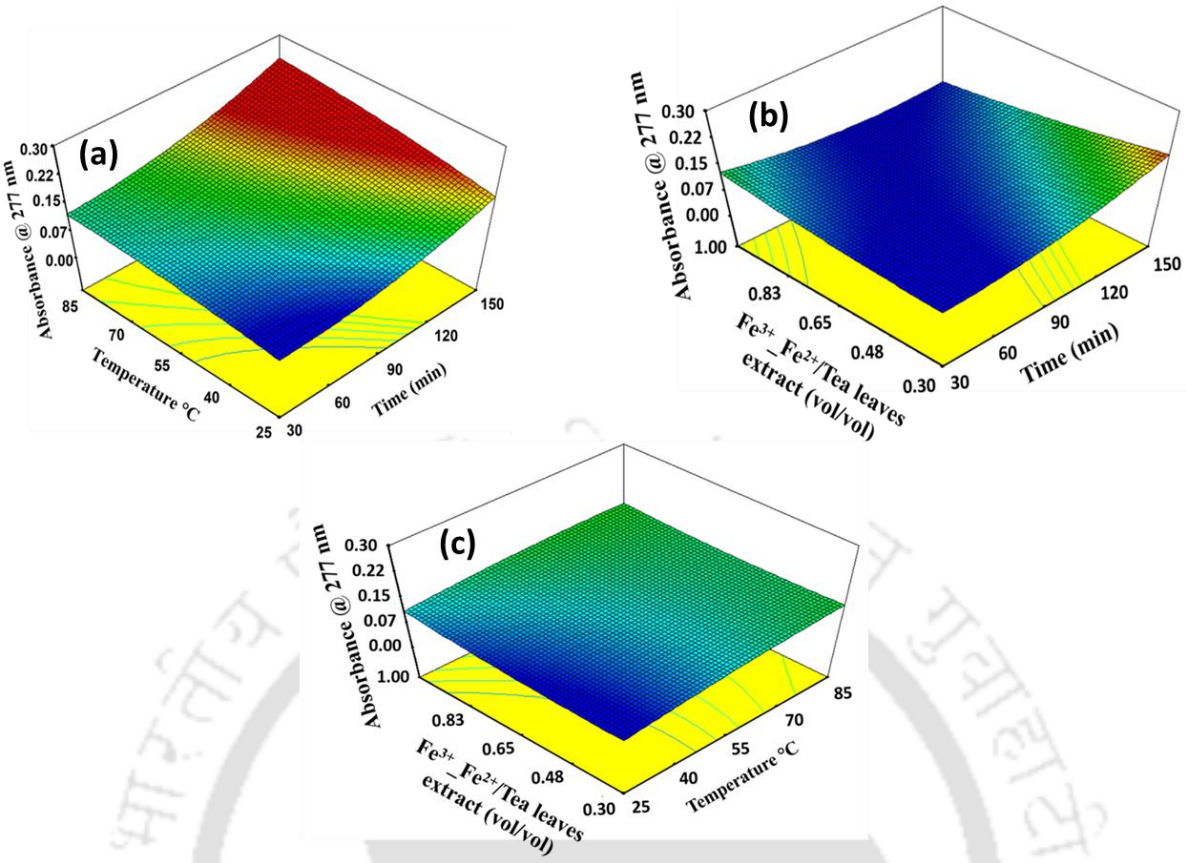

Figure 3.4. Plots of 3D response surface for absorbance at 277 nm for the independent parameters as Fe^{2+}-Fe^{3+}/leaves extract ratio (a), temperature (b), and time (c).

3.3.3 Characterization of synthesized IONPs

In order to characterize the synthesized IONPs, a variety of analytical techniques were employed. The spectra of UV–Vis absorption for Fe precursor, the aqueous leaf extract of *Camellia sinensis var. assamica*, and IONPs were performed in the spectral range from 200 – 800 nm (Figure 3.5). The tea extract showed two optical absorption bands at 210 and 277 nm, respectively. It infers the existence of catechins, tannins, flavonoids, and carbohydrates in the extract [295]. Moreover, the Fe precursor showed an absorption peak at 295 nm. Further, after mixing leaf extract and Fe precursor solution at the RSM optimized conditions, the formed IONPs showed an absorption band of tea extract at 277 nm with lower intensity, indicating the utilization of PPs during the synthesis of IONPs. Furthermore, the synthesized IONPs were

surrounded by charged organic molecules formed during iron reduction through aqueous leaf extract. Therefore, electrostatic repulsion ions also play a critical role in preventing further nanoparticle agglomeration [219].

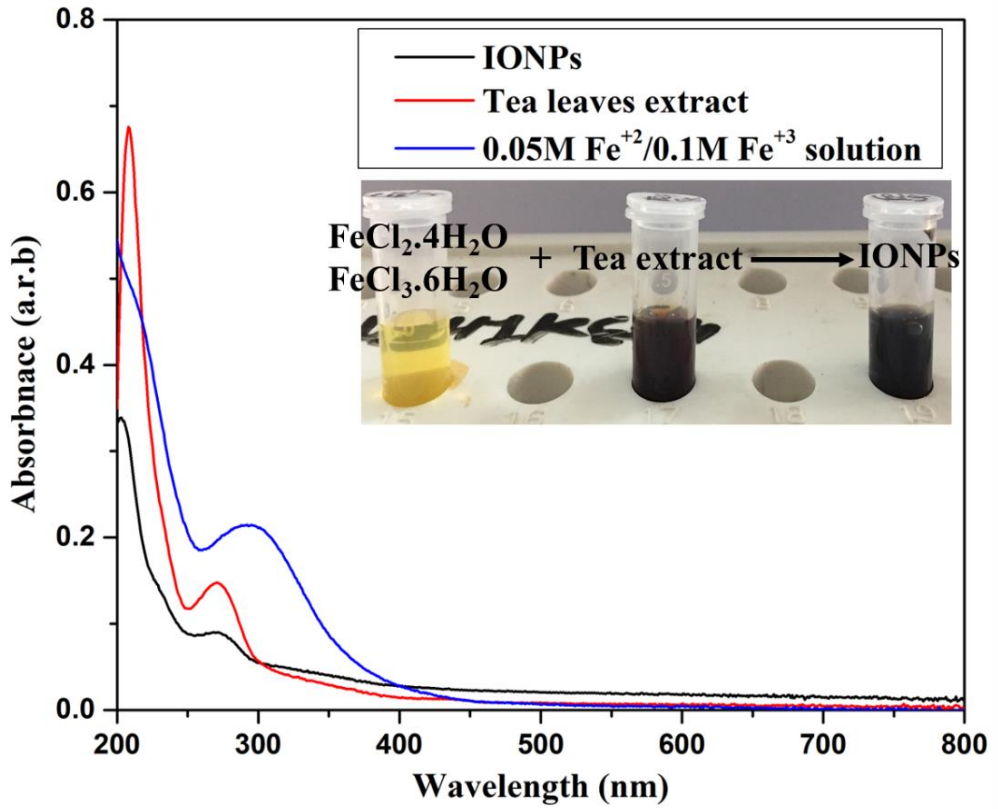

Figure 3.5: UV-Vis spectra of tea leaves extract, Fe precursor, and reaction product (IONPs) obtained from mixing of $FeCl_2.4H_2O$ and $FeCl_3.6H_2O$, at the optimized conditions from RSM-CCD design. The inset shows the photographic image of the $FeCl_2.4H_2O$ and $FeCl_3.6H_2O$ solution, tea extract and formed IONPs (from left to right).

Further, In the XRD pattern (Figure 3.6) of synthesized IONPs using aqueous tea leaf extract, lacked distinct diffraction peaks, implying that IONPs were largely amorphous due to the diverse composition of bio-extract. The bioextract was composed of organic components that capped IONPs, which attribute to the broad hump at around $2\theta = 25°$[250]. Also, the EDS pattern (Figure 3.7) exposed the presence of Fe, O, C, and Au elements. The contents of Fe and O in IONPs were found to be 21.64 and 27.23% by weight, respectively. Carbon showed the

highest content of 30.56% by weight, resulting from phytochemicals capped on the synthesized IONPs [277].

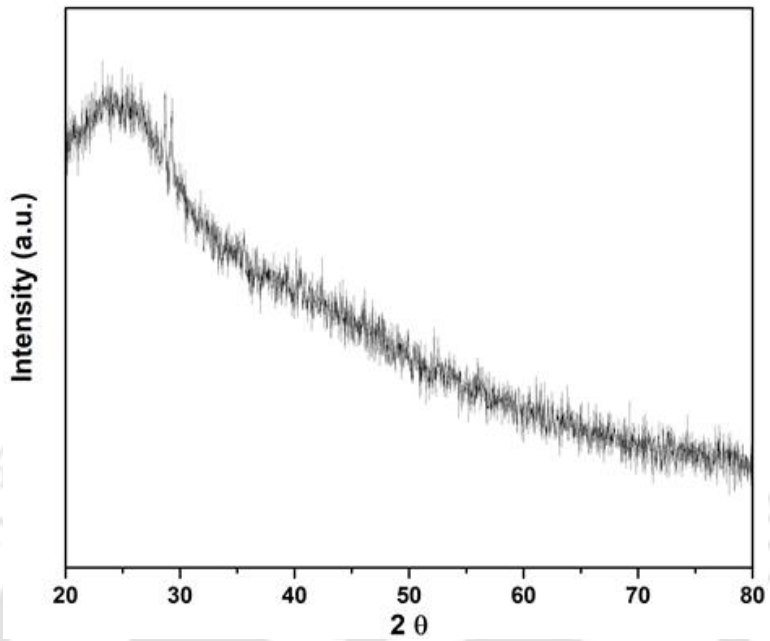

Figure 3.6: XRD patterns of IONPs synthesized using bio-extract of *Camellia sinensis var. assamica*.

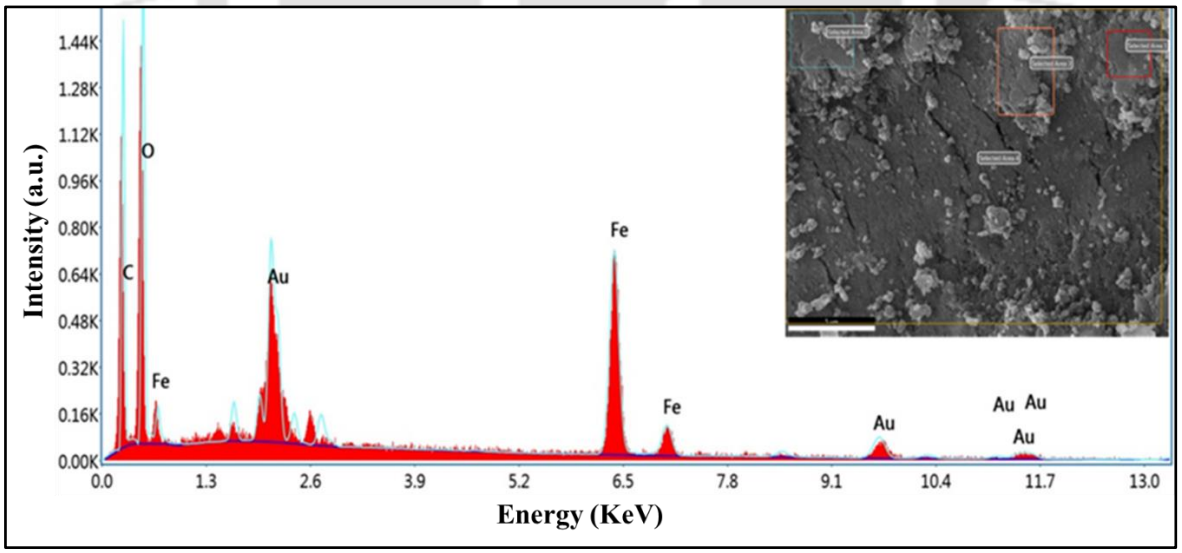

Figure 3.7: EDS spectrum of synthesized IONPs using bio-extract of *Camellia sinensis var. assamica.*

The FTIR spectra of the synthesized IONPs was done along with the prepared extract of *Camellia sinensis var. assamica* to find out the active functional groups (Figure 3.8) as listed in Table 3.2. In the FTIR spectrum of IONPs, robust peaks appeared at wavenumbers of 3359, 2932, 1621, 1365, 1079, 825, and 535 cm^{-1}. The band at 535 cm^{-1} was associated with the Fe-O bond vibration [296]. The hydroxyl (O-H) bond stretching from PPs was related to a wavenumber peak of 3359 cm^{-1} in IONPs, which was aroused from the extract of *Camellia sinensis var. assamica* [296]. The bands at 2932, 1621, and 1365 cm^{-1} resembled stretching and bending vibrations of C-H, C=O, [297] and C-H in alkanes [296] bond, respectively, which confirmed the capping of phytochemicals from the tea extract over synthesized IONPs. Further, the bands at 1097 and 825 cm^{-1} resonate with the stretching and bending vibrations of the C-O-C and C-H bonds, respectively [296]. The spectra of tea extract include peaks at wavenumbers of 3379, 2928, 1626, 1450, 1367, 1068, 822, and 611 cm^{-1}. The 3379 cm^{-1} wavenumber peak corresponded to robust vibration stretching in the O-H group present in *Camellia sinensis var. assamica* extract. The band at 2928 cm^{-1} was found to be associated with the C-H bond stretching. Further, the stretching of C=O bond represented the peak at 1626 cm^{-1} corresponding to catechins, PPs, and flavonoids present in the extract [298]. The C-C ring of aromatics stretching corresponded to the band at 1450 cm^{-1}. At 1367 and 1068 cm^{-1} bands were related to the bending of C-H plane vibration. Additionally, bands at 822 and 611 cm^{-1} resembled the bending of C-H in trans alkene [299].

Table 3.2: Wavenumber and corresponding functional groups identified in the FTIR spectra of *Camellia sinensis var. assamica* extract and synthesized IONPs.

Wavenumber (cm^{-1})	**Functional groups**
535	$Fe-O$
611	$C-H$ in trans alkene
1097	$C-O-C$
822, 825, 1068, 1365 and 1367	$C-H$ bending
1450	$C-C$
1621 and 1626	$C=O$
2928 and 2932	$C-H$ stretching
3359 and 3379	$O-H$

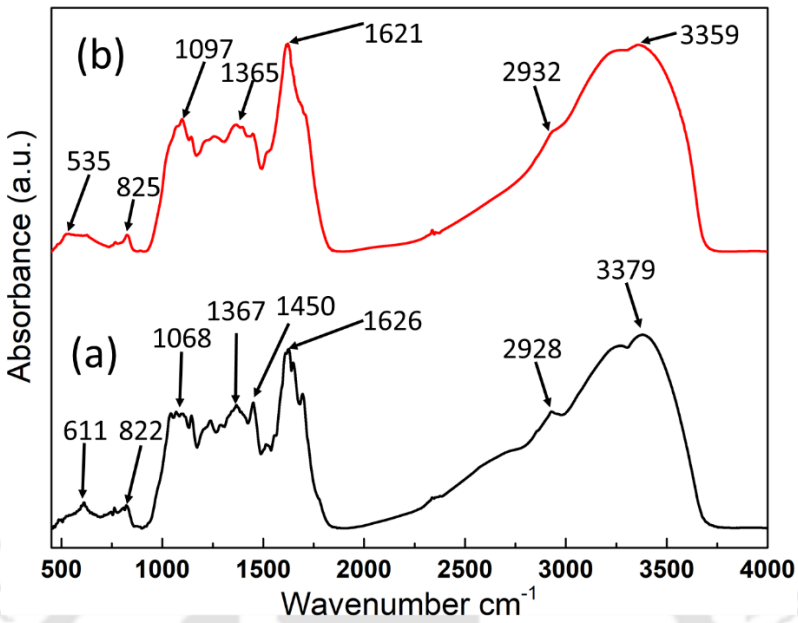

Figure 3.8: FTIR spectra of (a) *Camellia sinensis var. assamica.* extract and (b) synthesized IONPs.

Moreover, FETEM and FESEM analyses were done to look into the size and shape of as-synthesized IONPs. FETEM and FESEM images (Figure 3.9) revealed nearly spherical IONPs. The particles were well dispersed due to the surface capping of bio-analytes acting as stabilizing agents. The synthesized IONPs were found to have an average particle size of 21.33 ± 3 nm, as revealed by the histogram of the particle size distribution (PSD) from the FESEM micrograph. Further, from FETEM images, the average particle size was found to be 7.37 ± 1.8 nm. The D-spacing (0.20 nm) and lattice fringes of IONPs were visible in the HRTEM image at a 5 nm magnification scale. The selected area electron diffraction (SAED) pattern of IONPs reveals the irregular arrangement of scattered electrons (bright spots). Further, the spatial resolution of the SAED pattern demonstrates the amorphous nature of IONPs [300]. It supports the XRD analysis.

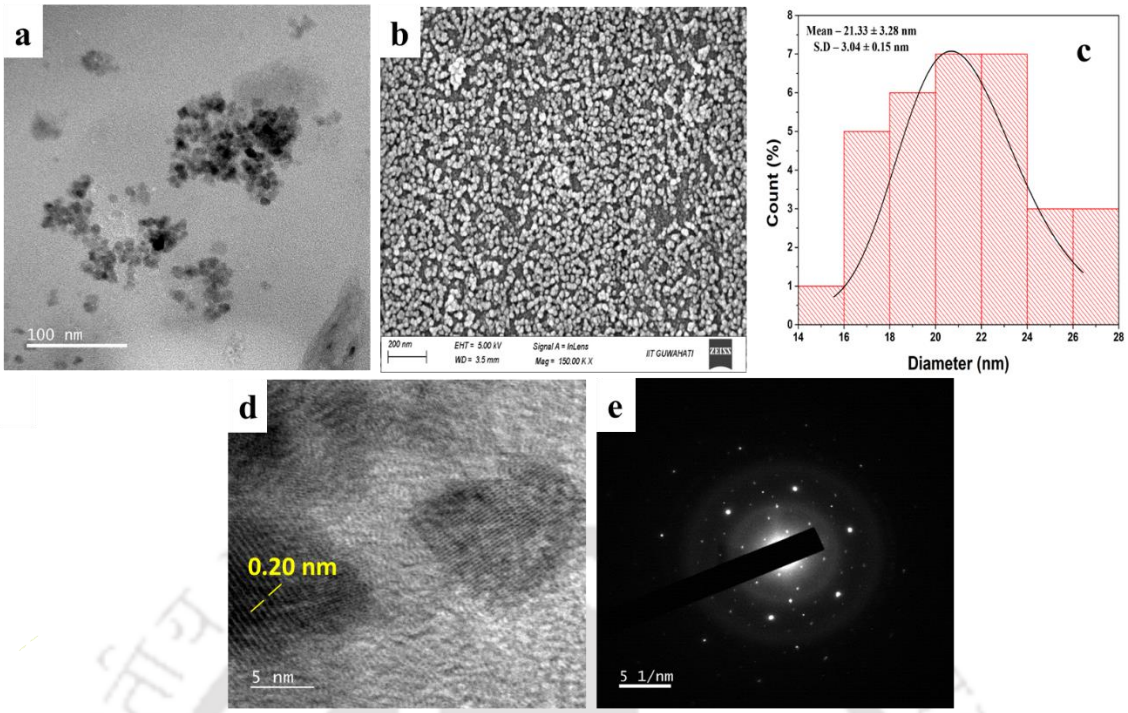

Figure 3.9: Synthesized IONPs using bio-extract of *Camellia sinensis var. assamica* (a) FETEM, (b) FESEM, (c) PSD, (d) HRTEM, and (e) SAED pattern.

The BET graph (Figure 3.10) reveals a Type IV adsorption-desorption isotherm of IONPs. It showed a clearly defined hysteresis loop, indicating the mesoporous nature of IONPs. The estimated diameter, surface area, and pore volume of IONPs were 37 nm, 18.27 m^2/g, and 0.17 cm^3/g, respectively. The hysteresis pattern demonstrated that condensation occurred roughly between 0.4 and 0.9 (P/P_0). The DSC/TGA (Figure 3.11) analysis showed the breakdown of IONPs started at about 250°C and subsequently at 380°C, which concluded at about 500°C, demonstrating that the sample was a form of iron oxide [301]. At a temperature above 800°C, the weight loss of IONPs (60%) was almost invariant. This reduction in weight loss from 0 - 800°C was due to the elimination of phytochemicals capping and water molecules present over the synthesized IONPs, reflecting the material thermal stability.

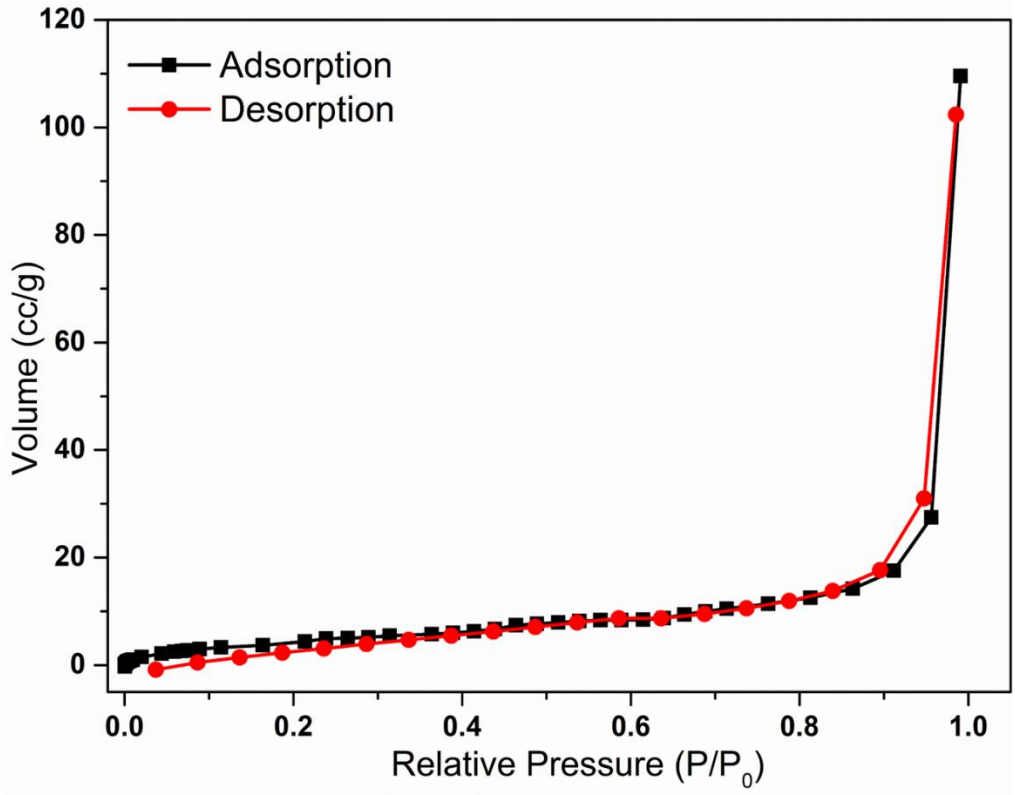

Figure 3.10: Nitrogen adsorption-desorption isotherms of IONPs synthesized using bio-extract of *Camellia sinensis var. assamica*.

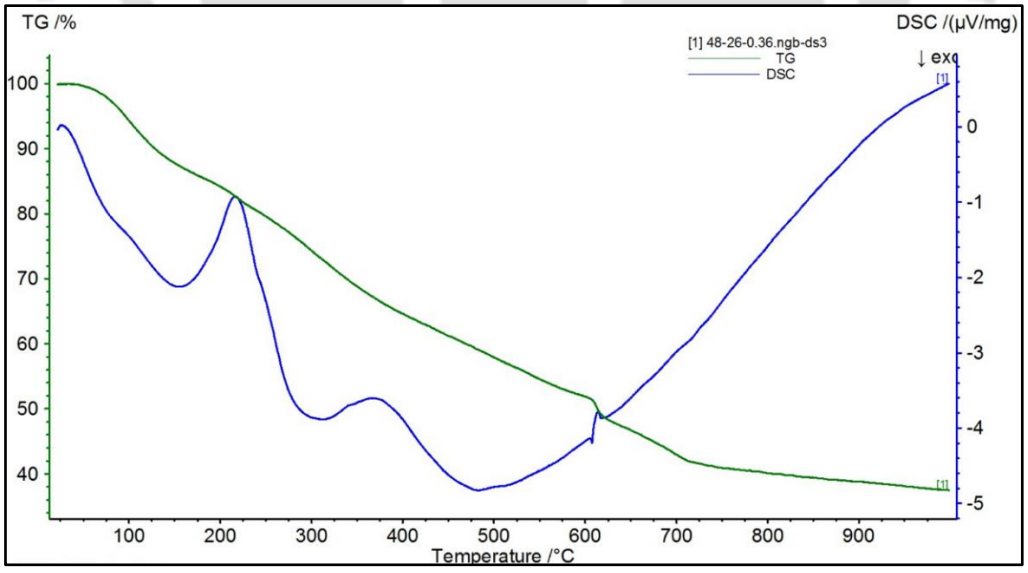

Figure 3.11: DSC/TGA plot of IONPs synthesized using bio-extract of *Camellia sinensis var. assamica*.

3.3.4 Cr(VI) removal using synthesized IONPs

3.3.4.1 Effect of pH and temperature

Both the pH and temperature of the environment have substantial effects on the adsorption process. Adsorption of Cr(VI) over the synthesized IONPs was investigated across a pH range of 2 to 10. At pH 2, the maximum q_e value of 38.19 mg g^{-1} was obtained (Figure 3.12(a)). The value of q_e was decreased from 38.19 to 9.52 mg g^{-1} with the rise in pH. Cr(VI) ions exist in an aqueous solution as H_2CrO_4, $HCrO_4^-$, CrO_4^{2-}, and $Cr_2O_7^{2-}$ based on pH values. Chromic acid (H_2CrO_4) was dominant at pH < 2. In the pH range from 2 to 6, hydrogen chromate ($HCrO_4^-$) and dichromate ($Cr_2O_7^{2-}$) ions were predominant. Above pH > 6, chromate ($CrO4^{2-}$) was found as a significant species of Cr(VI) [302].

Cr(VI) reductions under acidic and basic conditions in an aqueous solution were expressed in Eqs. 3.3 and 3.4, respectively.

$$Cr_2O_7^{2-} + 14H^+ + 6e^- \rightarrow 2Cr^{3+} + 7H_2O \quad (3.3)$$

$$CrO_4^{2-} + 4H_2O + 3e^- \rightarrow Cr(OH)_3 + 5OH^- \quad (3.4)$$

As seen in Eq. 3.3, the Cr(VI) species reduction occurred in acidic conditions, increases dissolved Cr(III) production. Whereas a basic pH increases Cr(III) hydroxide (Eq. 3.4). Therefore, Cr(VI) reduction to Cr(III) by IONPs was significant at pH 2 (Eqs. 3.5 and 3.6), and Fe^{2+} in IONPs was oxidized to Fe^{3+}.

$$Cr_2O_7^{2-} + 6Fe^{2+} + 14H^+ \rightarrow 2Cr^{3+} + 6Fe^{3+} + 7H_2O \quad (3.5)$$

$$HCrO_4^- + 7H^+ + 3Fe^{2+} \rightarrow 3Fe^{3+} + Cr^{3+} + 4H_2O \quad (3.6)$$

The release profile of Fe^{2+} and Fe^{3+} with (line and filled symbol) and without (line and unfilled symbol) Cr(VI) solution was shown in Figure 3.12(b). The Fe^{2+}concentration was decreased while there was an increase in Fe^{3+} concentration when IONPs were mixed with Cr(VI) solution. This shows the oxidation of Fe^{2+} to Fe^{3+} to reduce Cr(VI) ions as per Eqs. 3.5 and 3.6.

Zeta potential of as-synthesized IONPs was found to be -20.06 and -46.06 mV at pH values of 2 and 10, respectively (Figure 3.13), indicating a lower negative surface charge in acidic conditions. A better ionic contact between $Cr_2O_7^{2-}$ and $HCrO_4^-$ ions, and IONPs occurred when the pH value was below 6. This caused the deprotonation of IONPs and competition between OH^- and chromate ions. The improved interactions between Cr species and IONPs in the acidic environment led to the maximum removal of Cr(VI) (95.5%) at a pH value of 2.

Further, the effect of temperature on Cr(VI) removal over synthesized IONPs was examined. As shown in Figure 3.12(c), the q_e declined with the rise in temperature from 25 to 40°C due to weakened solute (IONPs) - solvent (Cr(VI)) interactions at higher temperatures. The active site of IONPs could chelate well with Cr species at lower temperatures, resulting in a stable structure [303]. It further indicated Cr(VI) removal using synthesized IONPs was exothermic. Based upon pH and temperature studies for Cr(VI) removal, further adsorption experiments were accomplished at pH 2 and a temperature of 25°C.

3.3.4.2 Effect of IONPs dosage and contact time

The effectiveness of Cr(VI) removal could be affected by the quantity of IONPs. Figure 3.12(d) depicts Cr(VI) removal % and q_e in mg g^{-1} at varying IONPs dosages (0.1 to 2 g/L) under optimized conditions of pH and temperature, as attained in Section 3.3.4.1. The Cr(VI) removal was enhanced from 54% at 0.1 g/L to 95.5 % at 1 g/L dosage of IONPs. Due to more active adsorption sites, the removal efficiency was enhanced with more amount of IONPs. The increase in q_e with increasing IONPs dosage was consistent with the earlier finding [304]. Further, q_e declined from 217 to 38 mg g^{-1} at a dosage of 0.1 and 1 g/L, respectively, due to unoccupied adsorption sites. Cr(VI) elimination percentage of more than 90 % above 0.5 g/L IONPs doses illustrates a high potential of the synthesized IONPs. There was no significant change in Cr(VI) removal observed above dosage of 0.75 g/L IONPs. Hence, further batch

adsorption tests were dosed at 0.75 g/L. As exposed from Figure 3.12(f), Cr(VI) removal increased considerably during the initial stage (upto 45 min). It might also be due to a significant concentration gradient of Cr(VI) and an abundance of vacant adsorption sites onto IONPs. Subsequently, as the contact period was lengthened, Cr(VI) adsorption over IONPs was deferred due to the depletion of Cr(VI) adsorption sites and their species. In 180 min, the adsorption equilibrium was established.

3.3.4.3 Effect of initial Cr(VI) concentration

To identify the most satisfactory conditions for Cr(VI) removal, its initial concentrations were varied from 40 to 450 mg/L. Figure 3.12(e) shows that q_e of 379.21 mg g^{-1} was saturated beyond the initial Cr(VI) concentration of 400 mg/L. This resulted from the complete occupation of adsorption sites at higher Cr(VI) concentrations which were left unoccupied at lower Cr(VI) concentrations [303]. Consequently, 40 mg/L was determined to be the optimal Cr(VI) concentration, achieving more than 95% Cr(VI) removal for further kinetics experiments. Furthermore, the adsorption capacity of IONPs when C_e value reached to 0.05 mg/L (permissible Cr(VI) limit in drinking water) from C_o (10 mg/L), denoted as q(0.05), was found to be 13.27 mg g^{-1}.

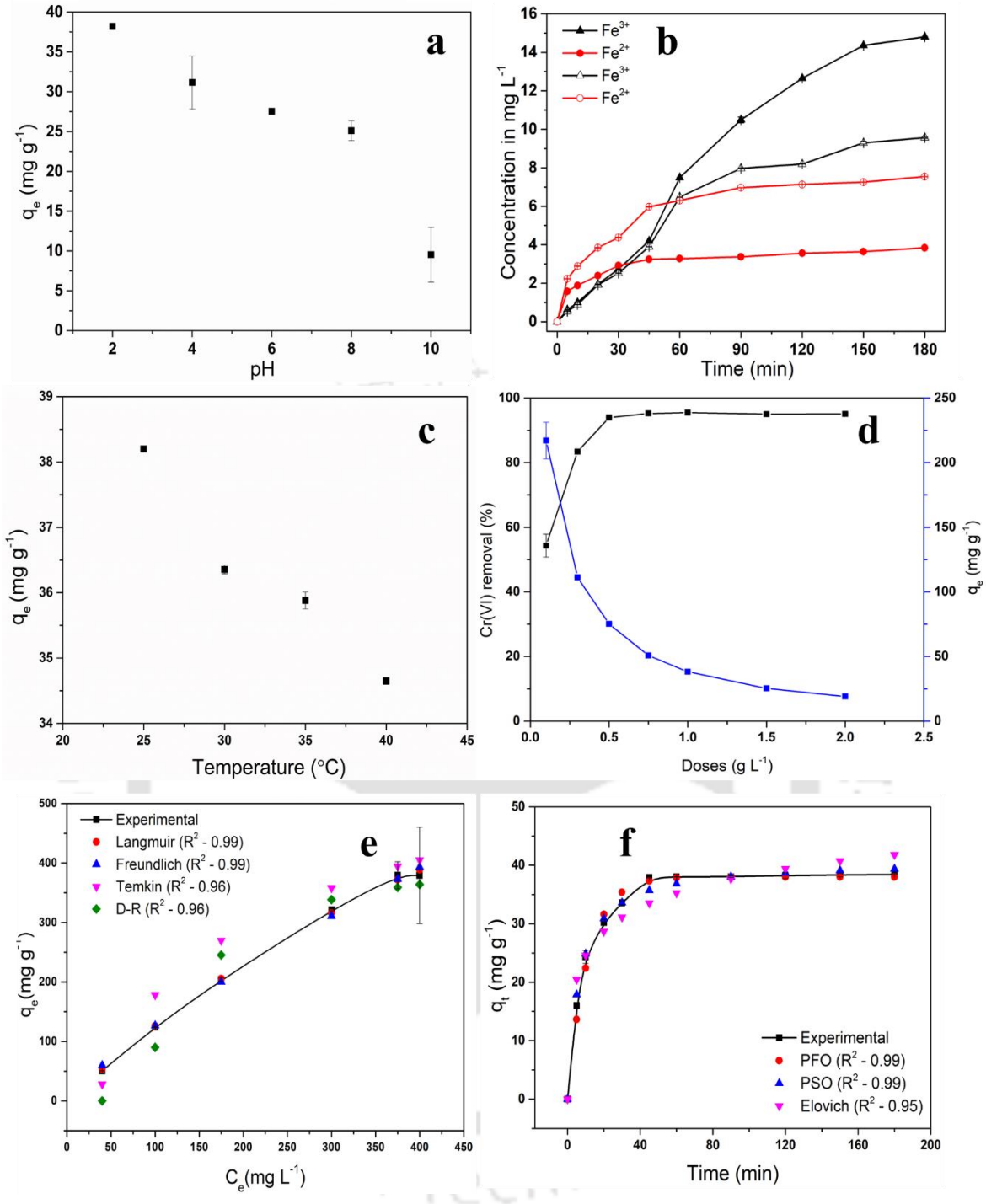

Figure 3.12: The influence of various parameters for the removal of Cr(VI) through synthesized IONPs. (a) Variation in q_e under different pH conditions (C_o – 40 mg/L and IONPs dosage - 1 g/L), (b) Fe^{2+} and Fe^{3+} release profile with (line and filled symbol) and without (line and unfilled symbol) Cr(VI) solution, (c) Effect of temperature on q_e (C_o – 40 mg/L, pH - 2, IONPs dosage - 1 g/L), (d) Effect of IONPs dosage on Cr(VI) removal % and q_e (C_o – 40 mg/L and pH - 2), (e) Effect of initial Cr(VI) concentration on q_e along with fitted adsorption isotherm

models (IONPs dosage - 0.75 g/L and pH - 2), and (f) Effect of contact time on q_t along with fitted adsorption kinetic models over experimental data (C_o – 40 mg/L, IONPs dosage - 0.75 g/L, pH - 2).

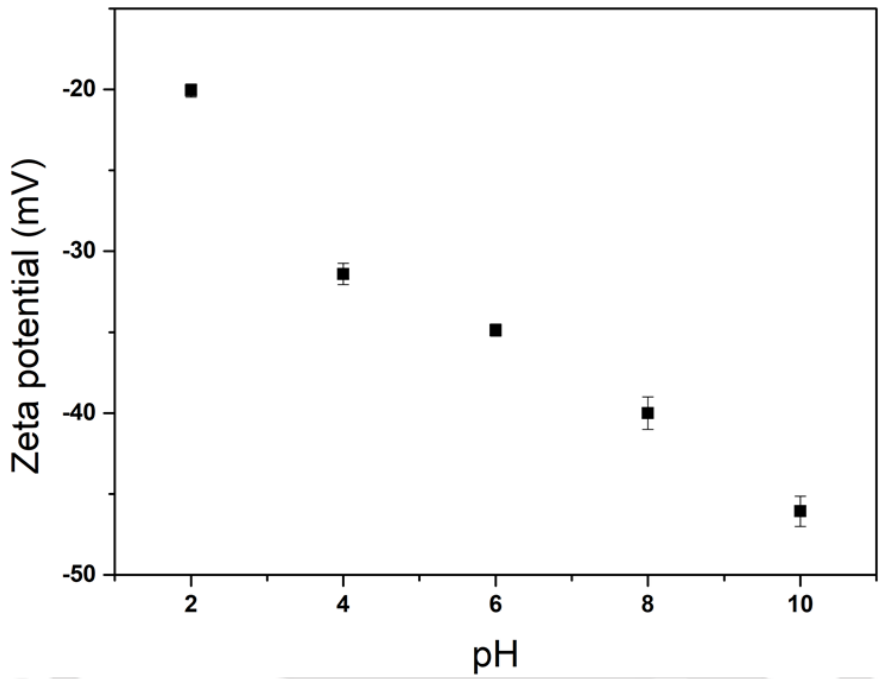

Figure 3.13: Zeta potential in mV of synthesized IONPs at various pH.

3.3.4.4 Effect of co-existing ions

The common interferents, namely, Na^+, Ca^{2+}, Cl^-, and NO^{3-} present in industrial and domestic wastewater could seriously affect Cr(VI) removal efficiency. According to earlier research [303], low concentrations (0 - 20 mM) of co-existing ions had no substantial influence on Cr(VI) removal. Consequently, our study aimed to identify the impact of high-concentration (50 mg/L) co-existing ions that could affect the elimination of Cr(VI) using IONPs. The effect of common cations (Na^+, $Ca^{2+,}$ and Mg^{2+}) and anions (Cl^-, SO_4^{2-}, PO_4^{3-}, and NO_3^-) on Cr(VI) removal (%) and q_e (mg g^{-1}) was evaluated (Figure 3.14). The study revealed no remarkable effect of co-existing ions, even up to 50 mg/L, on Cr(VI) removal efficiency. Further, as the

ratio of PO_4^{3-}/IONPs dosage was 0.06, there was no negative effects of PO_4^{3-} ions toward Cr(VI) removal efficiency. A similar observation was also reported in the literature [231].

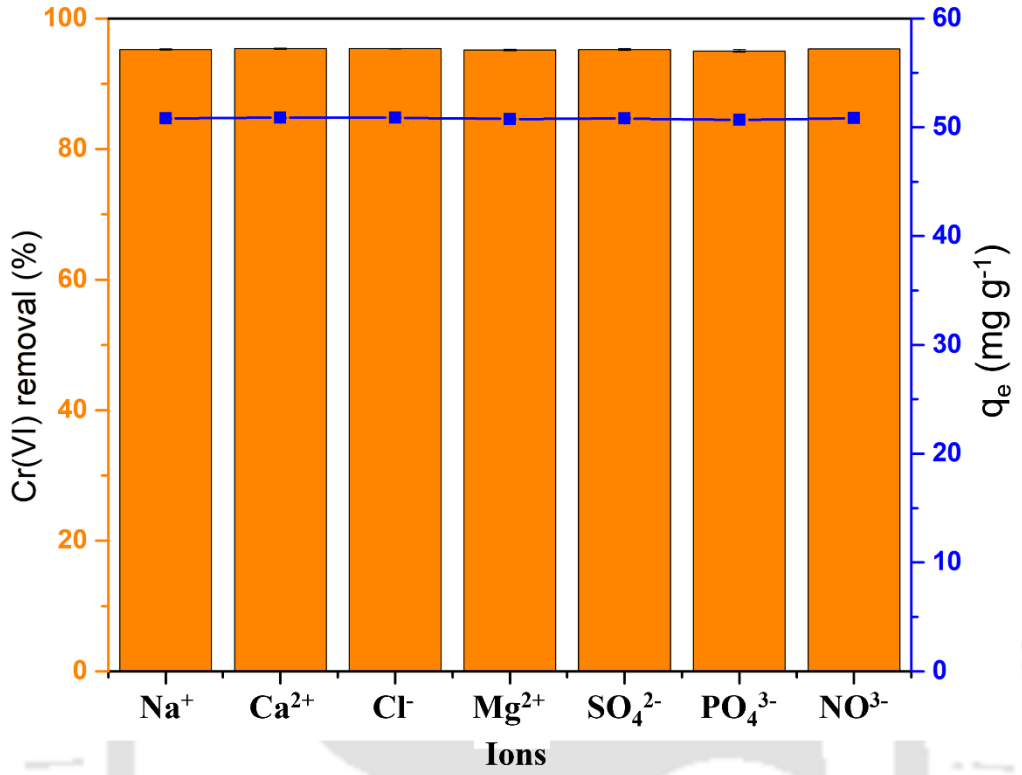

Figure 3.14: Effect of co-existing ions on Cr(VI) removal (%) and qe (mg g^{-1}) using IONPs (C_o – 40 mg/L, IONPs dosage - 0.75 g/L, pH - 2).

3.3.4.5 Thermodynamics study

The relations shown in Eqs. 3.7-3.9 were employed for the determination of thermodynamic variables, such as Gibbs free energy (G°), enthalpy (H°), and entropy (S°) of Cr(VI) adsorption onto IONPs [305].

$$\Delta G^{\circ} = -RT\ln K_C \quad (3.7)$$

$$\Delta G^{\circ} = \Delta H^{\circ} - T\Delta S^{\circ} \quad (3.8)$$

$$\ln K_C = \frac{\Delta S^{\circ}}{R} - \frac{\Delta H^{\circ}}{RT} \quad (3.9)$$

Where R stands for the gas constant (8.314 J mol^{-1} K), K_c (L g^{-1}) refers the distribution coefficient (q_e/C_0), and T represents adsorption temperature in Kelvin.

The intercept and slope of plot $\ln K_C$ vs 1/T curve (Figure 3.15) were used to determine ΔH° and ΔS°, respectively. Whereas, Eqs. 3.7 and 3.8 were used to calculate ΔG°. The Cr(VI) adsorption over the synthesized IONPs was found to be exothermic and spontaneous, as evidenced by the negative values of ΔH° (-3.68 KJ mol^{-1}) and ΔG° (-17 KJ mol^{-1}), respectively (Table 3.3). It also supports the negative effect of temperature on Cr(VI) removal, as discussed in section 3.4.1. ΔS° value was found to be 44.68 J mol^{-1} K^{-1}. It implies that the IONPs/liquid interface has a higher degree of randomness when Cr(VI) was adsorbed onto IONPs [306]. ΔH° values < 20 kJ mol^{-1} indicate physisorption, while values ranging from 80 to 200 kJ mol^{-1} imply a chemisorption process [307]. The ΔH° value showed that the adsorption of Cr(VI) over synthesized IONPs to be a physisorption process. Also, the value of ΔG° was about -17 kJ mol^{-1}. This further implied that Cr(VI) removal using IONPs was a spontaneous physiochemical adsorption process [303].

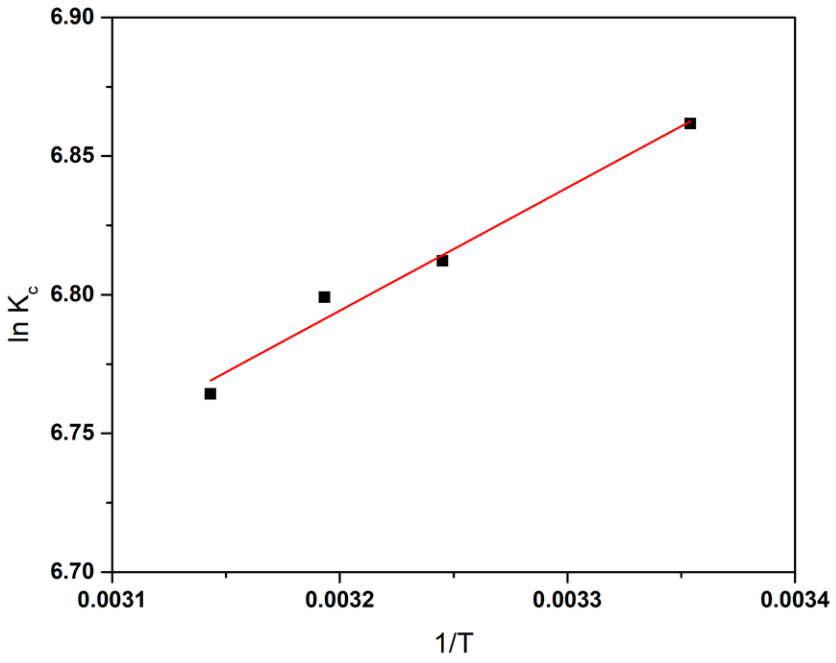

Figure 3.15: Linear fitting of distribution coefficient against temperature for Cr(VI) adsorption over synthesized IONPs.

Table 3.3: Thermodynamic variables for Cr(VI) adsorption over synthesized IONPs.

Temperature (K)	q_e (mg g^{-1})	ΔG (KJ mol^{-1})	ΔH (KJ mol^{-1})	ΔS (J mol^{-1} K^{-1})	R^2
298.15	38.20	-17	-3.68	44.68	0.97
310.15	37.65	-17.43			
313.15	35.88	-17.70			
318.15	34.65	-17.89			

3.3.4.6 Isotherms of Cr(VI) adsorption

The models of adsorption isotherm, namely Langmuir, Temkin, Dubinin- Radushkevich (D-R), and Freundlich, were engaged to study the nature of Cr(VI) adsorption at a fixed temperature of 298.15 K [196, 308]. The fitted adsorption isotherm models (q_e versus C_e) were shown in Figure 3.12(e) (represented by symbols). The adsorption isotherms and the associated fitted parameters with root mean square error (RMSE) values were enlisted in Table 3.4.

The Langmuir isotherm plot has an R^2 of 0.99. Q_m and K_L were calculated as 1272 mg g^{-1} and 0.001 L mg^{-1}, respectively. Based on the separation factor (R_L) value, adsorption can be: favorable ($0 < R_L < 1$), unfavorable ($R_L > 1$), linear ($R_L = 1$), and irreversible ($R_L = 0$) [309]. The R_L was found to be in the range of 0.69 - 0.95, implying a favorable process of Cr(VI) adsorption. The extent of multilayer adsorption well describes the Freundlich isotherm model. As per the nonlinear fitted expression of Freundlich isotherm (Table 3.4), n and K_F were determined as 1.22 and 2.95 (mg g^{-1}) (mg L^{-1})$^{1/n}$, respectively. Parameters of the Temkin isotherm i.e., b_T and A_T were determined as 16.47 J mol^{-1} and 0.0283 L mol^{-1}, respectively. The D-R isotherm parameters, β, and E were found to be 2.44×10^{-3} mol^2 J^{-2} and 14.31 KJ mol^{-1}, respectively. D-R isotherm did not fit the data well, having a relatively lower R^2 value of 0.96.

Based on the R^2 and RMSE values, the best-fit isotherm model was arranged as follows: Langmuir > Freundlich > D-R > Temkin. It implies that the adsorption of Cr(VI) by using synthesized IONPs takes place predominantly by forming a monolayer onto the surface of IONPs [12, 243]. The observed value of Q_m for Cr(VI) adsorption in this study (1272 mg g^{-1})

was compared (Table 3.6) with reported data of modified hydrochars and microbial-based synthesized IONPs. The Q_m value of the present work was found to be considerably higher as compared to other adsorbent for Cr(VI) removal. Also, modified hydrochars and microbial-based synthesized IONPs required more contact time to remove Cr(VI) than plant-based Iron nano adsorbent.

3.3.4.7 Cr(VI) adsorption kinetics

Figure 3.12(f) shows the kinetics of IONPs for the adsorption of Cr(VI). Within the first 45 min (Figure 3.12(f)), Cr(VI) adsorption was quite faster, and 95% Cr(VI) removal was accomplished owing to the presence of abundant vacant sites onto IONPs. Due to a decrease in readily accessible active sites, the adsorption rate slowed, and it plateaued after 180 min [11]. The non-linearized fitted kinetic models were illustrated in Figure 3.12(f). Elovich, pseudo-first-order (PFO), pseudo-second-order (PSO), and intra-particle diffusion (IPD) models were examined to study the kinetic behavior for the adsorption of Cr(VI) over IONPs. Figure 3.12(f) shows the fitted kinetic model's q_t (mg g^{-1}) values against time (represented by symbols). Further, the best-fitted model parameters with RMSE values were depicted in Table 3.5.

PSO model provided the best fit (Figure 2(f)) for Cr(VI) adsorption by using IONPs, with the lowest RMSE value (1.057) compared to the other three models. This indicates the process of Cr(VI) removal was controlled by Van der Waals forces (adsorptions) and electron transfer (reduction) [310]. Further, the rate constant values K_1, K_2, $K_{initial}$ [Initial 45 min], and K_{intra} [After 45 min] for PFO, PSO, and IPD models were found to be 0.09 min^{-1}, 0.004 g mg min^{-1}, 5.67 mg g^{-1} $min^{-0.5}$ and 0.075 mg g^{-1} $min^{-0.5}$, respectively. The fast adsorption kinetics ($K_{initial}$) was attained for Cr(VI) removal through as-synthesized IONPs within 45 min, which further

slowed down (K_{intra}) until equilibrium was achieved at 180 min representing the process of IPD (Figure 3.16).

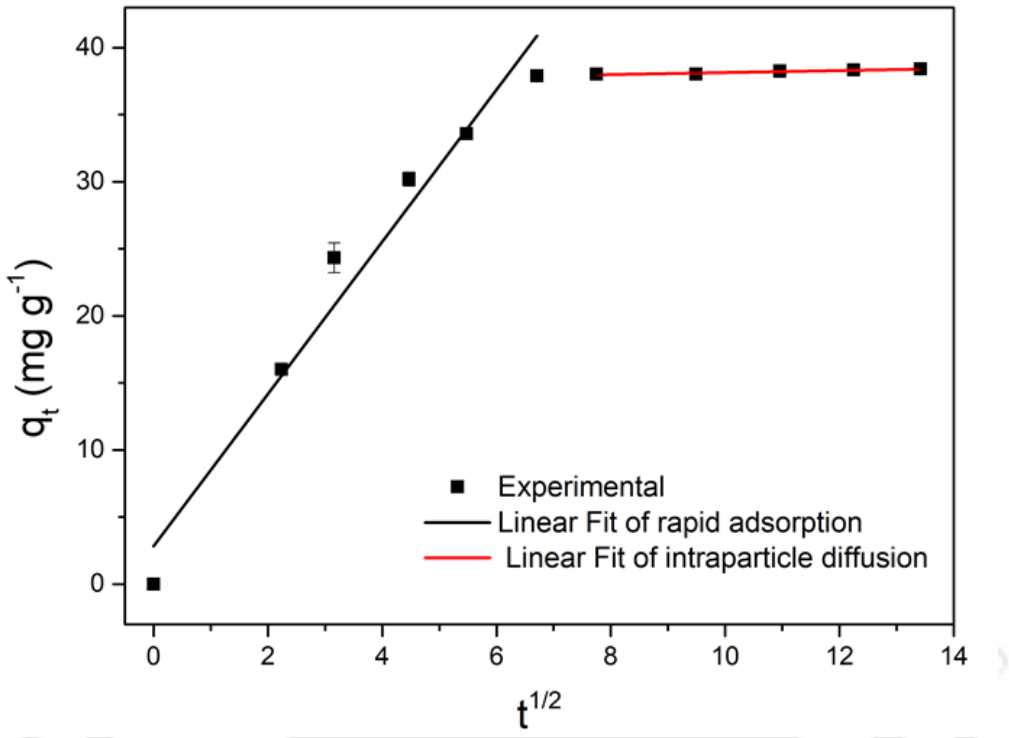

Figure 3.16: Linear fitted plot of Intraparticle diffusion analysis for Cr(VI) adsorption over synthesized IONPs.

Table 3.4: Adsorption isotherm models fitted parameters for Cr(VI) adsorption using IONPs at 298.15 K.

Isotherm model	Linear expression	Parameters	Value	RMSE
Langmuir	$\frac{C_e}{q_e} = \frac{1}{Q_m K_L} + \frac{C_e}{Q_m}$	Q_m (mg g^{-1})	1272	5.709
		K_L (L mg^{-1})	0.001	
		R_L	0.69 - 0.95	
		R^2	0.99	
Freundlich	$\log_{q_e} = \log_{K_F} + \frac{1}{n}\log_{C_e}$	n	1.22	8.656
		K_F (mg g^{-1})(mg $L^{-1})^{1/n}$	2.95	
		R^2	0.99	
Temkin	$q_e = \frac{R_T}{b_T}\ln(A_T) + \frac{R_T}{b_T}\ln(C_e)$	b_T (J mol^{-1})	15.13	40.824
		A_T (L g^{-1})	0.0296	
		R^2	0.96	
D-R	$\ln(q_e) = \ln(Q_m) - \beta\varepsilon^2$	β (mol^2 J^{-2})	2.44×10^{-3}	32.545

	$\varepsilon = RT\ln(1 + \frac{1}{C_e})$ $E = \frac{1}{\sqrt{2\beta}}$	E (KJ mol^{-1})	14.31	
		Q_m (mg g^{-1})	399.70	
		R^2	0.96	

Q_m: Maximum adsorption capacity; q_e: Equilibrium adsorption capacity; K_F: Freundlich constant; K_L: Langmuir constant; R_L: Separation factor; 1/n: adsorption intensity; β: sorption energy constant; E: mean free energy; A_T & b_T: Temkin constants

Table 3.5: Model fitted kinetic parameters for the adsorption of Cr(VI) over IONPs at a fixed initial concentration (C_e – 40 mg/L).

Model of kinetic	Linear expression	Parameters	Value	RMSE
PFO	$\ln[q_e - q_t] = lnq_e - K_1 t$	q_e (mg g^{-1})	38.03	1.174
		K_1 (min^{-1})	0.09	
		R^2	0.99	
PSO	$\frac{t}{q_t} = \left[\frac{1}{K_2 q_e^2}\right] + \frac{t}{q_e}$	q_e (mg g^{-1})	40.78	1.057
		K_2 (g mg min^{-1})	0.004	
		R^2	0.99	
Elovich	$q_t = \frac{1}{\beta}\ln(\alpha\beta) + \frac{1}{\beta}\ln(t)$	α (mg g min^{-1})	0.167	2.589
		β (g mg^{-1})	36.34	
		R^2	0.95	
IPD	$q_t = K_i t^{0.5} + C$	*Initial 45 min*		1.758
		$K_{initial}$ (mg g^{-1} $min^{-0.5}$)	5.67	
		C (mg g^{-1})	2.84	
		R^2	0.97	
		After 45 min		
		K_{intra} (mg g^{-1} $min^{-0.5}$)	0.075	
		C (mg g^{-1})	37.40	
		R^2	0.92	

K_1 and K_2: PFO and PSO constant; β: desorption constant; α: initial adsorption rate; K_i and C: IPD rate constant and intercept

Table 3.6: Reported optimized conditions and Qm values of Cr(VI) adsorption using green synthesized iron nano adsorbents.

Adsorbent	Optimized conditions					Q_m (mg g^{-1})	Ref.
	pH	Temperature (°C)	Initial Concentration (mg L^{-1})	Doses (g L^{-1})	Time (min)		
Pyrus sinkiangensis Yu pear peel extract – FeNPs	5	55	10	0.4	120	26.97	[11]
Rosa indica flower petal extract – FeONPs	7	25	20	0.5	100	16.39	[279]
Eucalyptus globules - nano-zero valent FeNPs	-	25	200	0.8	30	5.47	[280]
Acacia catechu leaf extract - $Fe(OH)_3$ NPs	2	25	50	1.5	120	29.5	[281]
Punica granatum leaf extract - Fe^0/Fe_3O^4 nanocomposite - modified cells of *Yarrowia lipolytica*	2	45	100	-	120	125	[248]
Camellia sinensis var. assamica leaf extract - IONPs	2	25	40	0.75	180	1272	This study

3.3.4.8 XPS analysis and Mechanism of Cr(VI) removal by IONPs

The synthesized IONPs were subjected to XPS analysis (Figure 3.17(a_1)). The XPS survey spectra of IONPs before and after Cr(VI) adsorption were analyzed. The high-resolution XPS spectrum was also investigated, in which the Fe, O, N and C peaks were visible before adsorption. The components were formed by deconvoluting the peaks. Two fitted peaks, corresponding to the OH^- and O-C=O [311] centers with binding energies of 531.25 and 532.87 eV, were present in the O1s high resolution spectrum of the IONPs profile (Figure 3.17 (a_2)). Prior to Cr(VI) adsorption over IONPs, the peak of OH^- in O1s shifts from 531.25 to 531.3 eV, while the O1s peaks of O-C=O remain unchanged (Figure 3.17 (a_3)). Three components

provided the best fit for the C1s spectrum, with 284.71, 286.28, and 288.50 eV peaks resembled C-C, C-H [311], C=O, and OH-C=O [312], respectively (Figure 3.17 (a_4)). The C1s peaks of C-H and C-C were unaffected by Cr(VI) adsorption, but OH-C=O was shifted from 288.5 to 288.45 eV and C=O from 286.28 to 286.24 eV, respectively (Figure 3.17 (a_5)). The C1s and O1s spectra reinforced the surface of IONPs due to the capping of *Camellia sinensis var. assamica* extract biomolecules. Further, three peaks were identified in the deconvoluted Fe2p spectrum of IONPs at 711.36, 716.54, and 724.9 eV, respectively (Figure 3.17 (a_6)). The characteristic peak from $Fe2p_{3/2}$ core level electrons at the Fe^{3+} octahedral site was shown by the major peak at 711.36 eV [312]. The carboxylate-iron bond was supported by a peak at 724.9 eV, which indicated the presence of Fe^{2+} species in the octahedral site [313]. The binding energy of 716.54 eV for $Fe2p_{3/2}$ with a weak shoulder corresponds to the $Fe^{2+}$of IONPs. The $Fe2_p$ peaks of $Fe2p_{3/2}$, Fe^{2+}, and $Fe2p_{1/2}$ at 710.65, 715.93, and 723.83 eV resulted from Cr(VI) adsorption (Figure 3.17 (a_7)). The Cr(VI) uptake onto IONPs was validated with the appearance of the peak of Cr2p in the after adsorption XPS spectra. The Cr2p spectrum deconvoluted into three peaks, i.e., 578.14, 582.66, and 586.81 eV, respectively, ascribed to $Cr(III)2p_{3/2}$, Cr^{6+} and $Cr(III)2p_{1/2}$ [314] (Figure 3.17 (a_8)). Based upon XPS analysis, the process of Cr(VI) removal occurred through surface adsorption along with the reduction of Cr(VI) to Cr(III) through synthesized IONPs.

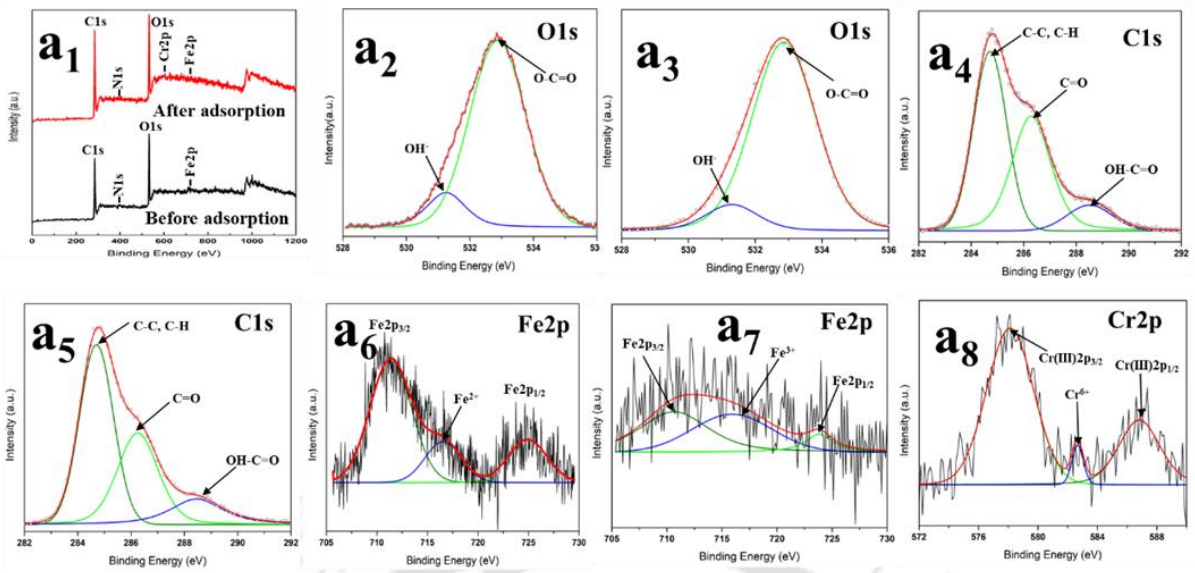

Figure 3.17: Synthesized IONPs XPS survey spectra (a_1) before and after Cr(VI) adsorption, high resolution spectrum (a_2 and a_3) O1s, (a_4 and a_5) C1s, (a_6 and a_7) Fe2p, (a_8) Cr2p.

Summarily, first, the Cr(VI) ions were adhered to the surface of IONPs. Cr(VI) could then interact with the surface active sites of IONPs, and some Cr(VI) species were reduced to Cr(III), releasing Fe^{3+}/Fe^{2+} ions, as evidenced by the XPS analysis. The possible routes of Cr(III) conversion from Cr(VI) and oxidation of Fe^0 to Fe^{2+} and Fe^{2+} to Fe^{3+} co-occurred [283]. Cr(III) was precipitated as $Cr(OH)_3$(s) with the increase in solution pH. It also could be co-precipitated in the presence of Fe(III), formed solid solution-like species such as $Cr_xFe_{1-x}(OH)_3$ [315]. However, the surface adherence of Cr species process was found to perform a dominant aspect in the removal process of Cr(VI) through synthesized IONPs.

3.4. Conclusions

In this study, IONPs were successfully synthesized by using leaf extract of *Camellia sinensis var. assamica*. A statistical approach was used to optimize IONPs synthesis condition, namely, time (30 - 150 min), temperature (25 - 85°C), and iron precursors to leaf extract ratio (0.3 - 1 v/v) by using RSM-CCD design. IONPs were examined for the removal of Cr(VI) in

an aqueous solution in a batch adsorption experiment at ambient condition. The optimal parameters to remove Cr(VI) were determined as pH 2, temperature of 25°C, and dosage of 0.75 g/L, respectively, and, 38.19 mg g^{-1} of IONPs adsorption capacity was achieved with an initial concentration of 40 mg/L. The Langmuir isotherm model could adequately represent the adsorption process with a Q_m value of 1272 mg g^{-1}. The presence of common cations (Na^+, Ca^{2+} and Mg^{2+}) and anions (Cl^-, SO_4^{2-}, PO_4^{3-}, NO_3^-) to the Cr(VI) solution, didn't show detrimental effect the Cr(VI) removal efficiency. Cr(VI) removal using IONPs was exothermic and spontaneous in nature. The kinetic of Cr(VI) uptake using IONPs well followed the pseudo-second order kinetic model. The recycle of IONPs should be explored. Consequently, IONPs can be considered affordable, reliable, and eco-friendly adsorbents for Cr(VI) removal from wastewater.

IONPs could detoxify Cr(VI) by reducing it to Cr(III) which was clearly supported by existence of Cr(III)$2p_{3/2}$ (578.14, eV) and Cr(III)$2p_{1/2}$ (586.81 eV) in X-ray photoelectron spectroscopic analysis. The mechanism for the removal of Cr(VI) includes adsorption and its reduction to Cr(III) along with Cr(III)/Fe(III) co-precipitation

Chapter 4

Entrapment of IONPs into chitosan (CS) matrix for the formulation of reusable CS/IONPs composite Cr(VI) adsorbents

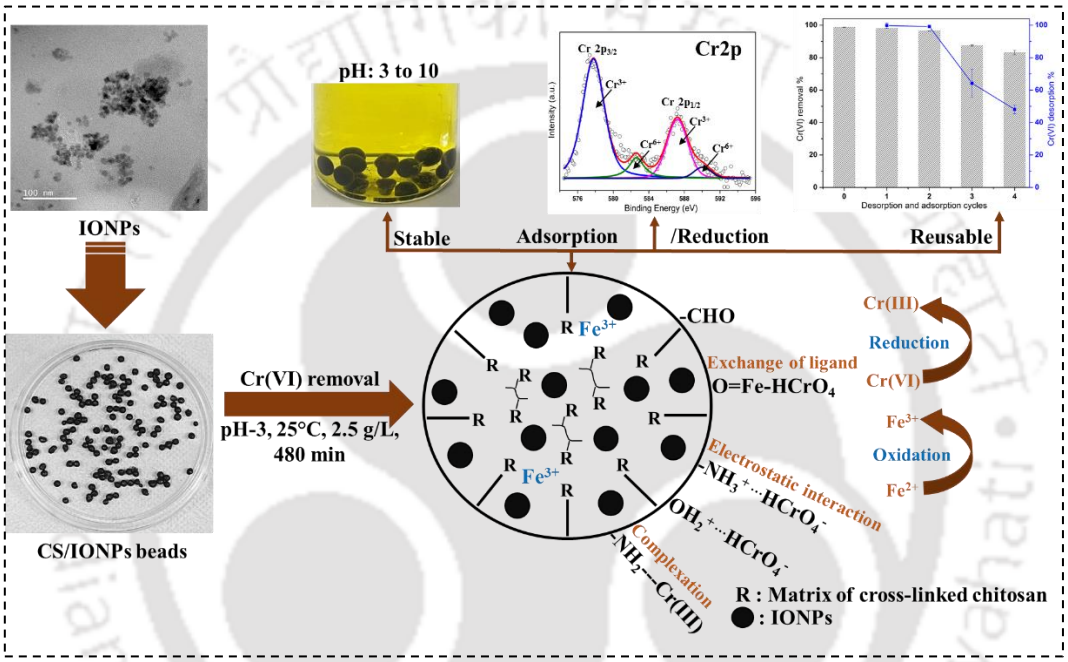

(Bio-based iron oxide nanoparticles forming bi-functional chitosan composite adsorbent for Cr(VI) decontamination. ***Aquib Jawed****, Animes K. Golder, Lalit M. Pandey (2024),* ***Chemical Engineering Journal****, 481, 148411)*

Highlights

- Bi-functional composite chitosan beads (CS/IONPs) developed for Cr(VI) removal
- CS/IONPs beads successfully achieved 99% removal of Cr(VI) at optimized condition
- Langmuir isotherm predicted the Cr(VI) adsorption capacity of 345 mg g^{-1} for CS/IONPs
- The beads were efficiently regenerated with NaOH solution and reused up to 4 cycles
- Cr species adsorbed and reduced by various surface and interior moieties of beads

In this Chapter, bio-based IONPs were immobilized and entrapped within the CS matrix to synthesize reusable bi-functional (adsorption/reduction) composite CS/IONPs adsorbent. The synthesized CS/IONPs beads were applied to remove Cr(VI) from the synthetic metallic solution. The influence of various environmental conditions, namely, pH, temperature, CS/IONPs dosage, initial Cr(VI) concentrations, and contact time, were studied and optimized. The isotherms, kinetics, and thermodynamics investigations were thoroughly performed. Moreover, several analytical methods such as EDS, FESEM, XPS, etc. were used to characterize the synthesized CS/IONPs adsorbent and also to understand Cr(VI) adsorption behavior. Finally, CS/IONPs adsorbent regeneration studies were carried out for Cr(VI) removal to explore its practical application.

4.1. Introduction

In Chapter 3, we reported synthesis of IONPs using *Camellia sinensis var. assamica* extract and applied them to remove Cr(VI) from water. With a Q_m of 1272 mg g^{-1}, the synthesized IONPs are an effective adsorbent for the removal of Cr(VI). However, due to their nano-scale dimensions and low magnetization, the synthesized IONPs pose a challenge for their separation from treated water, impeding their recycling applications. One potential approach to address this challenge involves the impregnation of synthesized IONPs into a polymer matrix and, further, cross-links them to form the structure of milli-scale adsorbent beads [15, 316, 317]. The control pore size in cross-linked polymer provides a suitable passage for the impregnating IONPs and allows the formation of a coarse adsorbent from the cross-linked reactions. In addition, selecting a suitable polymer matrix with particular functional groups can improve the removal efficacy of the synthesized IONPs by creating a synergistic effect. A commonly available amino polysaccharide, Chitosan (CS), composed of amine (NH_2) and hydroxyl (OH) groups for heavy metal ions scavenger, has been widely applied in the

treatment of Cr-polluted water [318]. Various reported literature adopted the in-situ and ex-situ chemically synthesized IONPs-impregnated CS sorbent for Cr(VI) removal [316, 319].

Recently, Li *et al.* [8] developed in-situ CS magnetic beads and applied them to treat a 50 mg/L synthetic metal solution of Cr(VI). The synthesized beads were determined to remove 99 % of Cr(VI) in 1200 min at a pH of 5. The Q_m value for CS magnetic beads was 293.46 mg g^{-1}. In another study, 99.25% of Cr(VI) was removed by in-situ synthesized composite adsorbent composed of CS/coconut shell activated carbon modified with iron from 25 mg/L synthetic metallic solution at pH 3 within 2880 min. The synthesized beads exhibited a reported Q_m value of 64.5 mg g^{-1} [320]. A separate study formed chemically synthesized IONPs in situ-impregnated CS beads for Cr(VI) removal from 20 mg/L aqueous solution. The synthesized beads were found to remove 75% of Cr(VI) at pH 5 within 600 min. The Q_m value for the formed beads was 69.8 mg g^{-1} [321].

Further, chemically synthesized Fe^0 NPs (nZVI) were added ex-situ in the CS matrix to form CS-nZVI beads to remove Cr(VI) from the aqueous solution. The synthesized CS-nZVI adsorbent attained a removal of 82% Cr(VI) from 20 mg/L solution at pH 6.4 in a time duration of 30 min [322]. However, the entrapment of green synthesized IONPs into the CS matrix has not been extensively investigated for Cr(VI) removal. This urges a demand for environment-friendly composite sorbent of CS for Cr(VI) removal. The ex-situ infusion of green synthesized IONPs in the CS matrix and, thus, forming beads for Cr(VI) removal is still a novel topic for environmental research. The encapsulation of green synthesized IONPs onto CS matrix creates a composite material with a composition combining organic and inorganic components. Such formed composite materials integrate the features of IONPs (adsorption and reduction) with the attributes of CS (complexation and ion-exchange). Therefore, the formed cross-linked combination of IONPs and CS composite adsorbent (CS/IONPs beads) is expected to

effectively couple the benefits of both materials, resulting in a highly effective composite adsorbent for Cr(VI) removal.

Accordingly, in this Chapter, CS/IONPs beads were prepared through the ex-situ infusion of green synthesized IONPs in the CS matrix. The cross-linking of the CS/IONPs mixture to form spherical beads was performed in sodium tripolyphosphate (STPP) solution to make the whole synthesis process environment-friendly [323, 324]. However, to be best of our understanding, there have been no prior investigations performed on the adsorption of Cr(VI) onto CS/IONPs beads, containing IONPs synthesized using leaf extract of *Camellia sinensis var. Assamica*. The specific novelty of the present research includes the assessment of the synthesized CS/IONPs beads to decontaminate harmful contaminant Cr(VI) from an aqueous solution along with its productive regeneration. The influence of various environmental conditions, namely, pH, temperature, CS/IONPs dosage, initial Cr(VI) concentrations, and contact time were studied and optimized. Furthermore, a comprehensive analysis was conducted to ascertain the adsorption efficacy of the CS/IONPs adsorbent concerning the elimination of Cr(VI). The isotherms, kinetics, and thermodynamics investigations were thoroughly performed. Moreover, several analytical methods were used to characterize the synthesized CS/IONPs adsorbent and to understand Cr(VI) adsorption behaviour. Finally, the regeneration studies of used CS/IONPs adsorbent were performed and tested for Cr(VI) removal to evaluate their practical applicability.

4.2. Materials and Methods

4.2.1 Materials

Chitosan (cat. no: GRM9358; degree of deacetylation: ≥ 75%), acetic acid glacial (AA) (cat. no: AS001), 1,5-diphenylcarbazide (DPC) (cat. no: GRM519), magnesium chloride (cat. no: GRM3922), sodium chloride (cat. no: GRM853), sodium phosphate monobasic (cat. no:

GRM3964), calcium chloride (cat. no: GRM534), sodium nitrate (cat. no: PCT0014) and magnesium sulphate heptahydrate (cat. no: GRM684) were purchased from Himedia, India. Sodium tripolyphosphate (cat. no: 85124) was purchased from Sisco research laboratories Pvt. Ltd. Cr standard solution (1000 mg/L, cat. no: 02733) supplied and prepared from Ammonium dichromate by Sigma Aldrich, India, was diluted to lower Cr(VI) concentrations with deionized water to make working solutions for batch adsorption studies. The experimental studies utilized double distilled water that was obtained from a Millipore system (Mili-Q) with a resistivity of 18 MΩ.

4.2.2 Synthesis of CS/IONPs adsorbent

In Chapter 3, we used an aqueous extract of *Camellia sinensis var. assamica* to synthesize IONPs. These IONPs were utilized in this Chapter for the formation of CS/IONPs beads. For the synthesis of beads, first, 2% (w/v) CS was dissolved in 1% (v/v) AA, and then 0.25% (w/v) IONPs were added to the mixture while it was stirred continuously (200 rpm) at room temperature. The resulting mixture was frequently swirled for 24 h. Subsequently, the obtained solution was dropped into a solution of STPP (1% (w/v)) through a syringe to produce spherical CS/IONPs beads (Scheme 4.1), which were aged for 12 h in the same solution for hardening. The hardened CS/IONPs beads were rinsed multiple times with double distilled water unless the pH was neutralized. The same procedure was followed to synthesize bare CS beads without including IONPs. For further characterization, the synthesized CS and CS/IONPs beads were freeze-dried. Cr(VI) removal experiments were performed through wet beads (CS/IONPs and CS) dosed in numbers according to the evaluated dry weight of each synthesized beads.

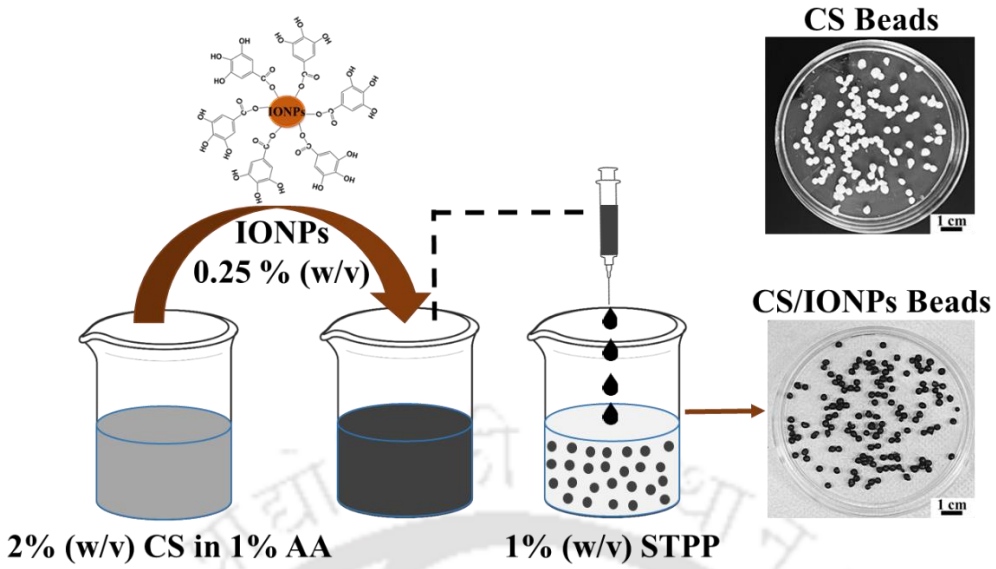

Scheme 4.1. Adopted protocol of CS and CS/IONPs beads synthesis.

4.2.3 Characterization of synthesized beads

Fourier transform infrared (FT-IR) spectrometer (PerkinElmer, Model: Spectrum two, USA) recorded the pertinent functional groups on CS/IONPs beads within the wavenumber from 4000 to 400 cm^{-1}. The synthesized beads were analyzed using a high-resolution X-ray diffractometer (XRD) (Rigaku Technologies, Model: Smartlab, Japan) system. The elemental composition of the formed beads was evaluated using an X-ray photoelectron spectroscopy (XPS) instrument (Ulvac, Model: PHI 5000 VersaProbe III, Japan), with Al k (1486.6 eV) as the excitation source. The morphological changes of the synthesized CS beads after IONPs infusion were examined using Field emission scanning electron microscopy (FESEM) (Zeiss, Model: Sigma, Germany). Energy dispersive spectroscopy (EDS) (Zeiss, Model: Sigma, Germany) was engaged with synthesized beads for elemental analysis. The particle size analyzer (Anton Paar, Model: Litesizer^{TM} 500, Austria) was used to measure the surface charge in mV of the formed beads at various pH values (3, 4, 6, 8, 10). CS and CS/IONPs beads thermal stability was inspected using Differential scanning calorimetry (Netzsch, Model: STA449F3A00, Germany) with a Thermo Gravimetric analysis (TGA) System. The surface

area of both the synthesized beads was determined using the Brunauer-Emmette-Teller (BET) instrument (Qunatchrome, Model: Autosorb-IQ MP, Austria). The mechanical strength of CS and CS/IONPs beads in various pH (3, 6, 10) of double distilled water was analyzed in an Electro-Mechanical Universal Testing Machine (ZwickRoell, Model: Z005TNProline, Germany). It was expressed in terms of the force (N) value used for the breakdown of a bead under uniaxial compression.

4.2.4 Removal of Cr(VI) using synthesized CS/IONPs beads in batch adsorption

The experimental procedure involves conducting batch experiments in 30 mL glass bottles at a starting pH of 3.0 and temperature of 25°C unless stated otherwise. CS/IONPs beads (0.25% w/v) were stirred in 150 mg/L Cr(VI) initial concentration for 8 h in a shaker incubator (Scigenics, Model: Orbitek-LE, India) at 180 rpm. Following the incubation period, the samples underwent centrifugation, resulting in the supernatant extraction. Further, to evaluate dissolved Cr(VI) concentration, the recovered supernatant was diluted with DPC reagent and measured spectrophotometrically at 543 nm. Using Atomic emission spectroscopy (Agilent, Model: MP-AES - 4210, USA), the concentrations of total chromium (Cr(tot)) and Fe were measured in the solution. Cr(III) concentration in the aqueous phase was calculated from the difference between Cr(tot) and Cr(VI) concentrations.

A series of batch adsorption studies were carried out to assess the adsorption efficacy of synthesized CS/IONPs beads. These experiments involved the assessment of the effect of pH (3-10), temperature (25-45°C), CS/IONPs beads doses (0.5-3 g/L), co-existing ions (Na^{+}, Ca^{2+}, Mg^{2+}, PO_4^{3-}, SO_4^{2-}, NO_3^{-}, Cl^{-}), adsorption isotherms (25 - 900 mg/L), and adsorption kinetics (30 - 480 min) studies. pH of the solutions was adjusted with HCl and NaOH solutions. The equilibrium adsorption capacity (q_e, mg g^{-1}) and Cr(VI) removal % were calculated as per the following relations (Eqs. 3.1, Chapter 3 and 4.1).

$$\text{Cr(VI) removal } \% = \frac{(C_o - C_e)}{C_o} \times 100 \quad (4.1)$$

Herein, C_0 (mg/L) and Ce (mg/L) represent the initial Cr(VI) concentration and the residual Cr(VI) concentration in the aqueous phase after reaching adsorption equilibrium.

4.2.5 Reusability studies of synthesized CS/IONPs beads

Conducting reusability studies is crucial for determining the practical applicability of an adsorbent. The Cr(VI) desorption experiments were carried out in accordance with the previously described approach, with minor alterations [316, 325]. The Cr(VI) loaded CS/IONPs beads were agitated in a 30 mL glass contactor with 10 mL of 1M NaOH at 180 rpm and 25°C for a duration of 4 h. As stated earlier, the concentration of Cr(VI) in the post-desorbed supernatant was determined. The desorbed CS/IONPs beads were then washed in deionized water and allowed to dry. Following the washing procedure, the CS/IONPs beads were subsequently revived into a fresh 150 mg/L Cr(VI) solution for the purpose of conducting further adsorption study, as outlined in Section 2.4. A total of four sequential desorption/adsorption cycles were performed to investigate the CS/IONPs reusability for Cr(VI) removal.

4.3. Results and Discussion

4.3.1 Characterization of synthesized beads

The synthesized beads of CS and CS/IONPs as depicted in Scheme 4.1 were spherical with diameters calculated as 5.2 ± 0.38 and 5.1 ± 0.74 mm, respectively. The physical appearance of CS/IONPs was black due to the infusion of IONPs (Scheme 4.1), whereas the CS beads looked white (Scheme 4.1). The preparation procedure of CS beads involved using CS powder containing functional groups, including hydroxyl (-OH) and amine ($-NH_2$) and carbon chains. As a result, the CS beads include C, N, and O (Figures 4.1(a) and 4.2(a)).

Further, after IONPs infusion in CS, the gelated Fe in the CS matrix appeared in the EDS spectrum (Figure 4.2(b)) and image mapping (Figure 4.1(b)). Moreover, upon the reaction of Cr(VI) with CS/IONPs beads, the mapping (Figure 4.1(c)) and EDS spectrum (Figure 4.3) displayed the presence of Cr peaks and surface coverage, revealing Cr adsorption over the formed beads.

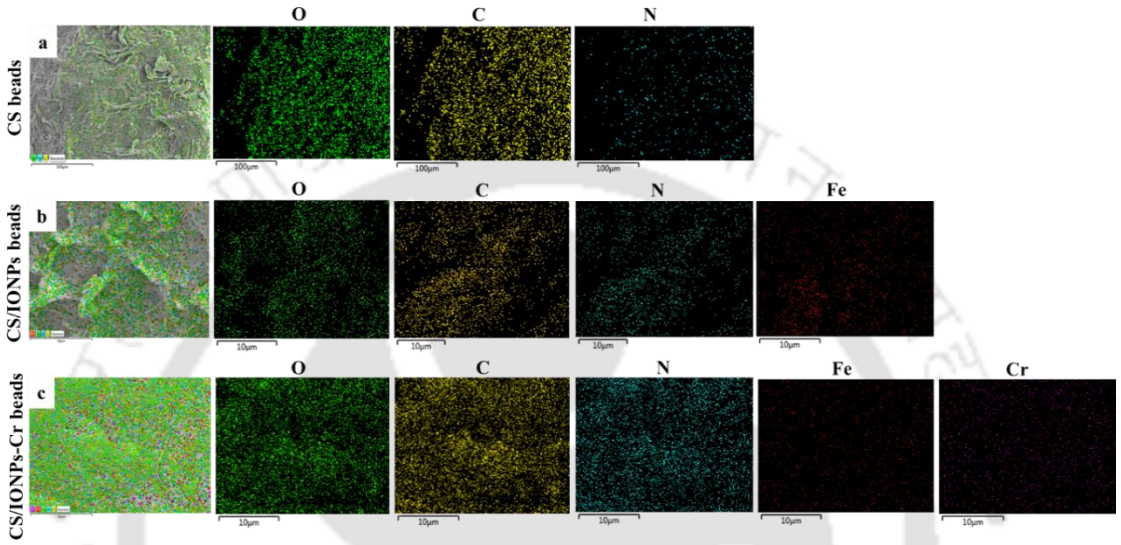

Figure 4.1: EDS mapping of (a) CS beads, (b) Fresh CS/IONPs beads, and (c) Used CS/IONPs beads after Cr(VI) adsorption. (O – Oxygen, C – Carbon, N – Nitrogen, Fe – Iron, Cr – Chromium)

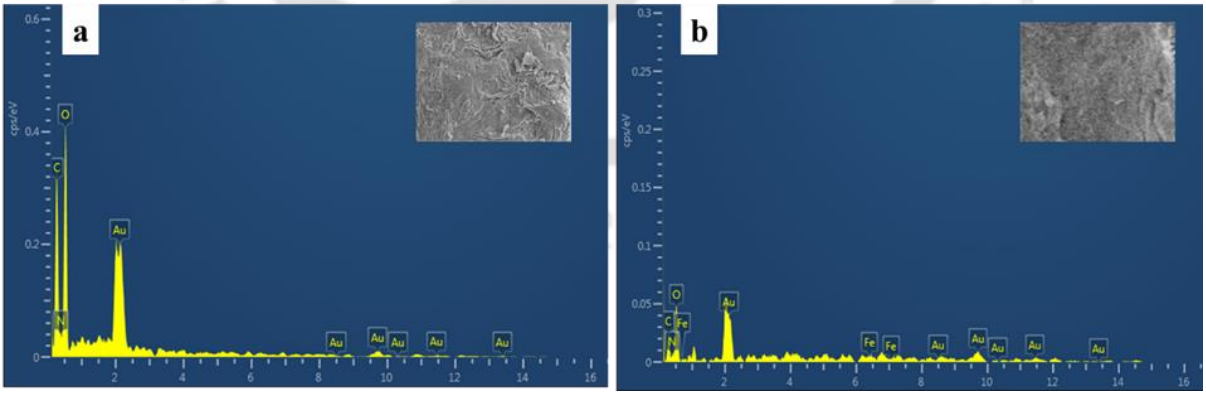

Figure 4.2: EDS spectra of synthesized (a) CS and (b) CS/IONPs beads.

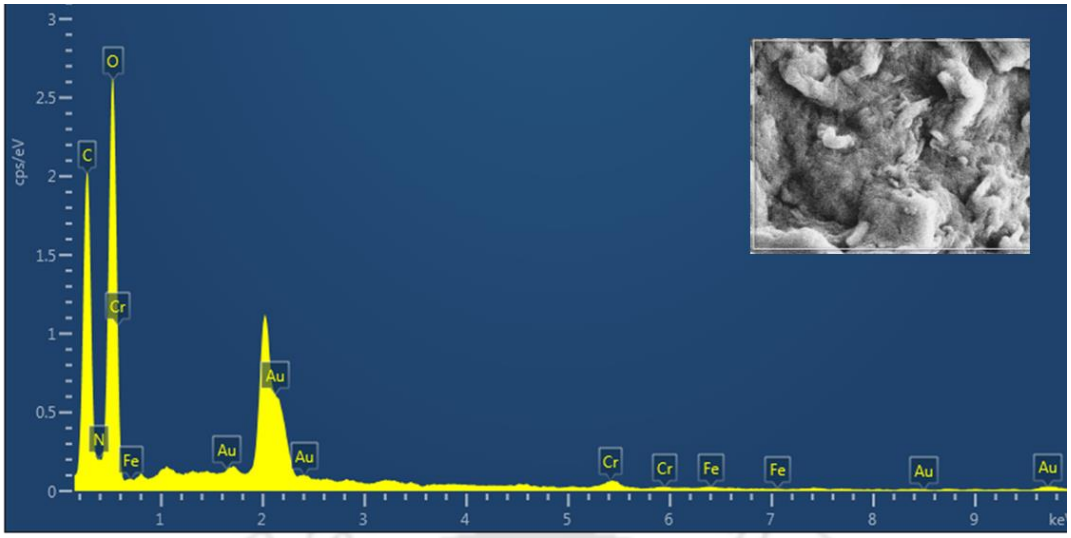

Figure 4.3: EDS spectrum of used CS/IONPs beads after Cr(VI) adsorption.

The lower magnification view of CS (Figure 4.4(a)) and CS/IONPs (Figure 4.4(b)) beads exhibited a resemblance and provided a visual representation of the desiccated circular surface of the produced beads. The FESEM images of the formed bead's outer, inner, and cross-section surfaces were also captured to reveal the morphological changes between CS (Figures 4.4(c), 4.4(e), and 4.4(g)) and CS/IONPs (Figures 4.4(d), 4.4(f), and 4.4(h)) beads. The CS beads exhibited a smooth outer surface (Figure 4.4(c)), whereas the CS/IONPs (Figure 4.4(d)) variant displayed a rough surface with minor cracks. The inner surface of CS beads (Figure 4.4(e)) showed a pattern of cross-linked CS aggregates. However, following the infusion of IONPs (Figure 4.4(f)), the inner portion displayed gelated and uniformly distributed IONPs in the CS matrix. This distribution in the CS matrix was infused with various Fe (Fe^{2+} and Fe^{3+}) species in IONPs. The cross-section micrographs revealed heterogeneous and undulated surfaces for CS (Figure 4.4(g)) and CS/IONPs (Figure 4.4(h)) beads, respectively. Following the adsorption of Cr(VI), circular and rough surfaces of CS (Figures 4.5(a) and 4.5(b)) and CS/IONPs beads (Figures 4.5(c) and 4.5(d)), respectively, were observed from FESEM micrographs.

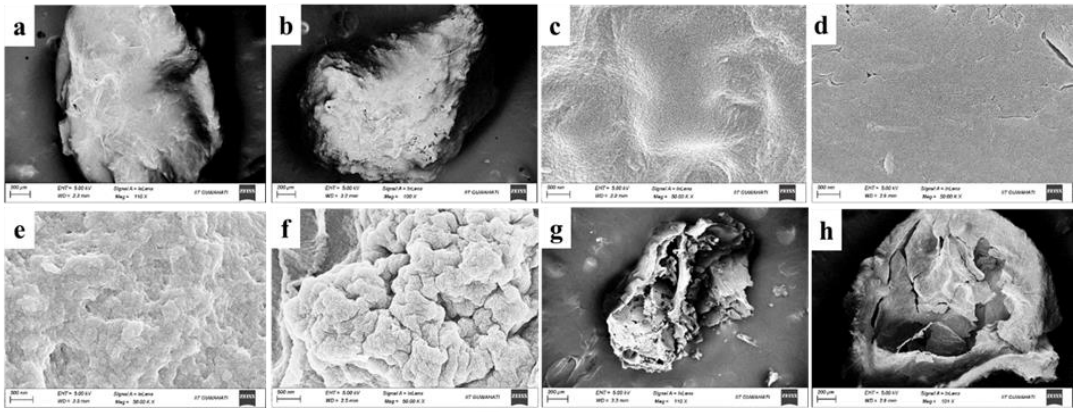

Figure 4.4: FESEM micrographs (a and b) Top view, (c and d) Outer, (e and f) Inside, (g and h) Cross-section of synthesized CS and CS/IONPs beads, respectively.

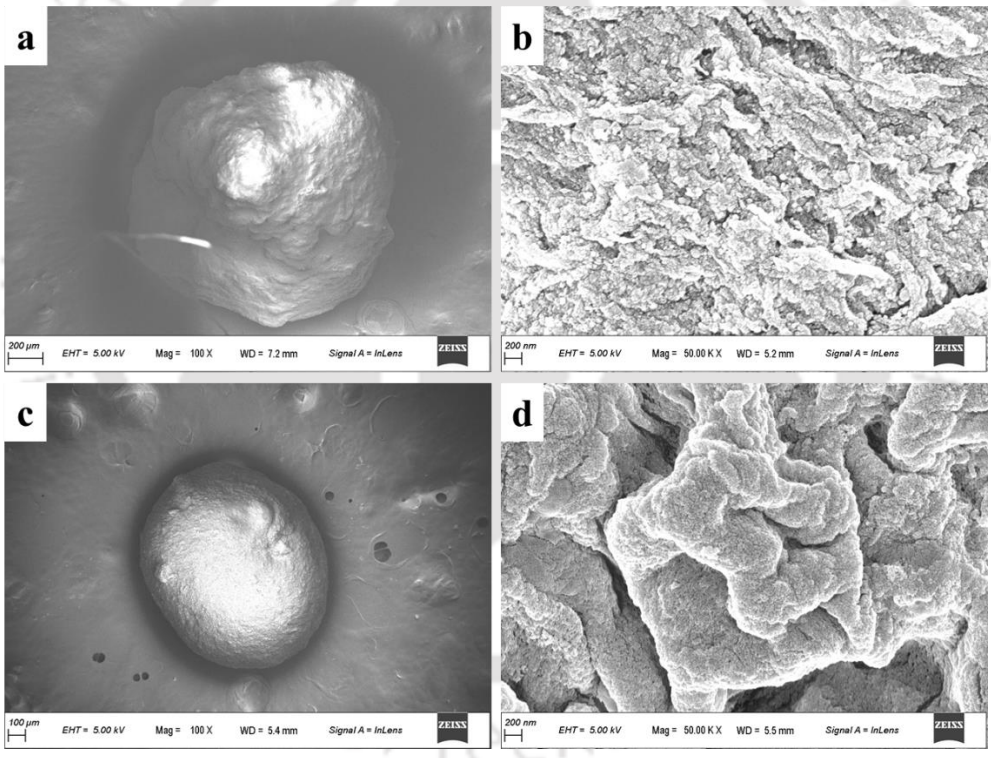

Figure 4.5: FESEM micrographs (a and c) Lower (100X) and (b and d) Higher (50 KX) magnifications of CS and CS/IONPs beads, respectively, after Cr(VI) adsorption.

Figure 4.6(a) displays the XRD patterns of the original CS powder, CS, and CS/IONPs beads. The CS powder exhibited distinct peaks at 9.7° and 19.5° on the 2θ scale, which is attributed to crystals forms I and forms II in CS structure and revealed the existence of CS

hydrophilic groups [325, 326]. However, two more broad humps at 30.12° and 41° also appeared in CS powder, representing an amorphous carbon structure. After the formation of CS beads, crystal forms 1 peak disappeared, and forms II shifted to 19°. The broad hump in CS powder at 30.12 ° formed a distinct peak at 30.3° in CS beads, and another hump moved to 40.3°. The CS/IONPs beads showed a similar trend as CS beads, with a broad hump at 30.19° and narrow humps at 18.74° and 40.95°, respectively. The disappearance and shift of crystal forms I and forms II peaks, respectively in CS/IONPs beads might be due to the chelation of Fe^{3+} with the CS hydrophilic group ($-NH_2$) [316].

The N_2 adsorption-desorption isotherm study was conducted to determine the BET area of synthesized CS and CS/IONPs beads at 77 K by plotting the adsorbed quantity (cm^3/g) against relative pressure (P/Po) as shown in Figure 4.6(b). The plotted N_2 adsorption-desorption isotherms of both CS and CS/IONPs beads exhibited a Type IV isotherm pattern and an H4 hysteresis loop [327, 328]. The specific BET surface area (S_{BET}) of CS and CS/IONPs beads were found to be 25.42 and 63.67 m^2/g, respectively. This increase in S_{BET} of CS/IONPs beads confirmed the successful inclusion of IONPs in CS matrix with enhanced porosity. The average pore diameter of CS beads was determined to be 6.62 nm, while for CS/IONPs beads, it was found to be 11.65 nm. The total pore volume of CS was determined to be 0.04 cm^3/g, whereas for CS/IONPs beads it was estimated as 0.18 cm^3/g. This indicates that the inclusion of IONPs in CS matrix may improve the adsorptive properties by enabling easy access for Cr(VI) ions within the pores. Moreover, after Cr(VI) adsorption (Figure 4.7), the S_{BET}, pore diameter, and pore volume of the used CS/IONPs beads were reduced to 8 m^2/g, 4.92 nm, and 0.045 cm^3/g, respectively as compared to pre-adsorbed beads. The decrement in the surface area of used CS/IONPs beads reveals the occupancy of Cr(VI) species inside the mesopores of CS/IONPs beads [329]. These findings illustrate that the adsorption of Cr(VI) occurs both on the surface of the synthesized CS/IONPs beads and within their mesopores [330].

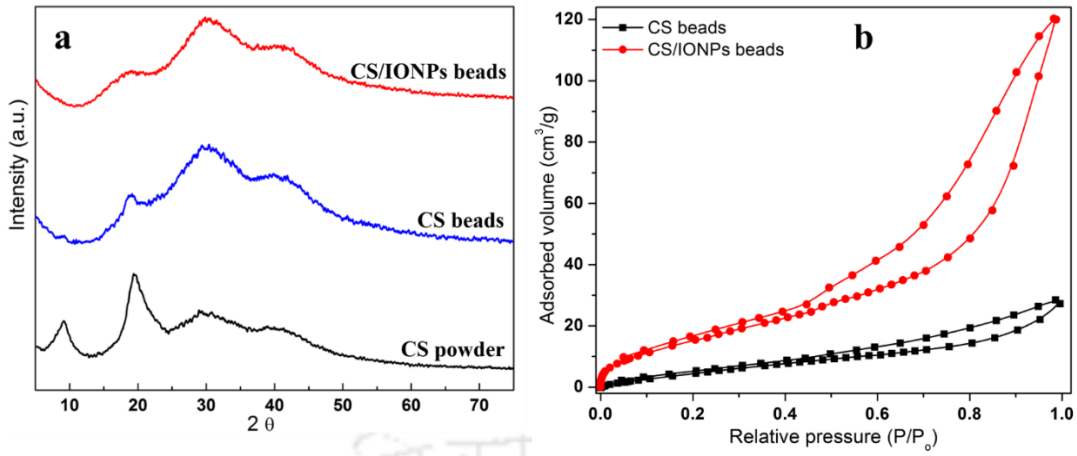

Figure 4.6: (a) XRD spectra of CS powder, CS beads, and CS CS/IONPs beads and (b) Nitrogen adsorption/desorption isotherms of synthesized CS and CS CS/IONPs beads.

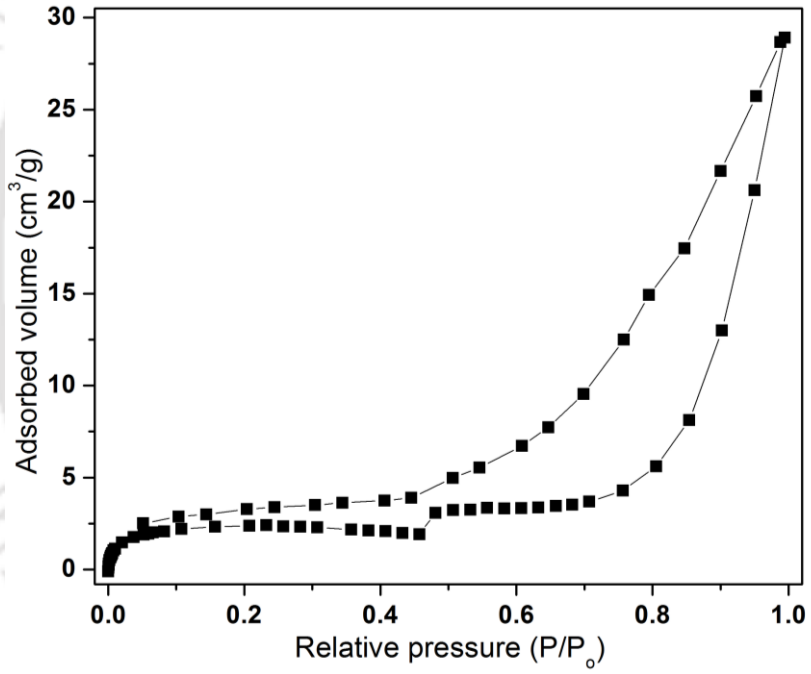

Figure 4.7: Nitrogen adsorption/desorption isotherms of synthesized CS CS/IONPs beads after Cr(VI) adsorption.

The thermal stability of the CS and CS/IONPs beads was analyzed using TGA (Figure 4.8). According to TGA curves, the CS and CS/IONPs beads experienced a weight loss of 16% at 200°C, followed by a weight loss of 50 and 51% at 400°C, respectively. This observed % weight loss was caused due to the evaporation of physically adsorbed water molecules and the

decomposition of CS [325]. Upon reaching the termination temperature of the TGA experiment (800°C), the final % weight losses were 68 and 64% for CS and CS/IONPs beads, respectively. The weight reduction was ascribed to the complete degradation of the CS backbone under high-temperature conditions and dihydroxylation of Fe oxides [321]. The TGA curves were also compared to evaluate the difference between the CS and CS/IONPs beads. The analysis indicated no apparent difference between the two types of beads (CS and CS/IONPs) until the temperature reached 200°C. It was observed that the initial decomposition rate of the CS beads was higher as compared to CS/IONPs. After that, at 800°C, CS beads (68%) had more mass loss than CS/IONPs beads (64%). This demonstrates that the addition of IONPs reduced the amount of weight loss of CS at elevated temperatures. This may occur due to the bonds between IONPs and chains of CS molecules, which increases the decomposition temperature [325]. Consequently, CS/IONPs beads can be considered stable up to 200°C and suitably applied for water treatment at normal temperature.

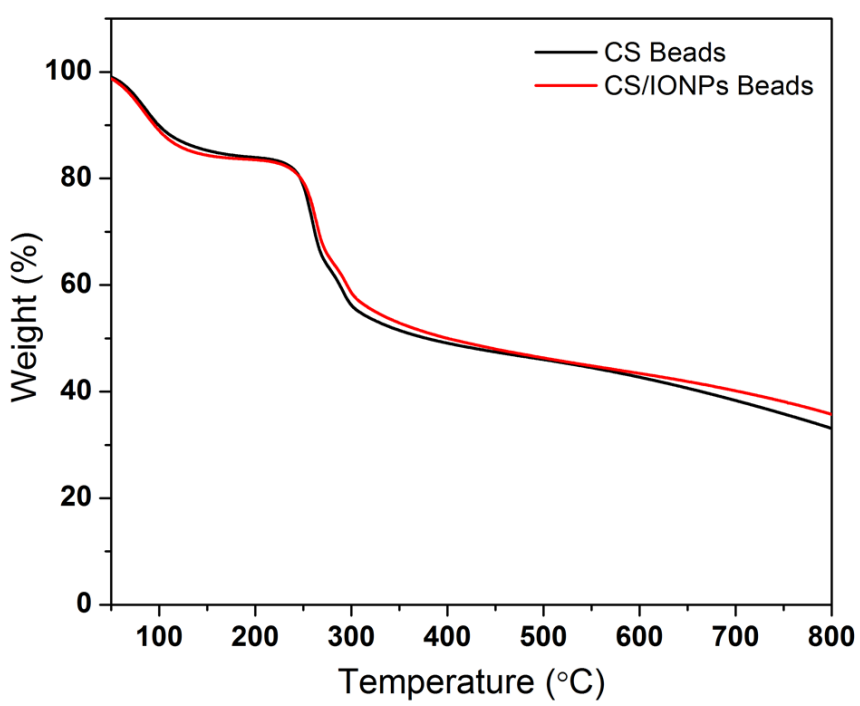

Figure 4.8: TGA profile of synthesized CS and CS CS/IONPs beads.

The mechanical strength of synthesized CS and CS/IONPs beads in various pH (3, 6, 10) solutions was expressed in terms of compressive force (N) for the breakdown of a bead as shown in Figure 4.9. When compared to bare CS beads, the CS/IONPs could withstand 54% more compressive force at all pH conditions, for its breakdown (Figure 4.9). This revealed the enhancement of mechanical strength in the CS beads through the inclusion of nanomaterials, which is also supported by previous studies [331, 332].

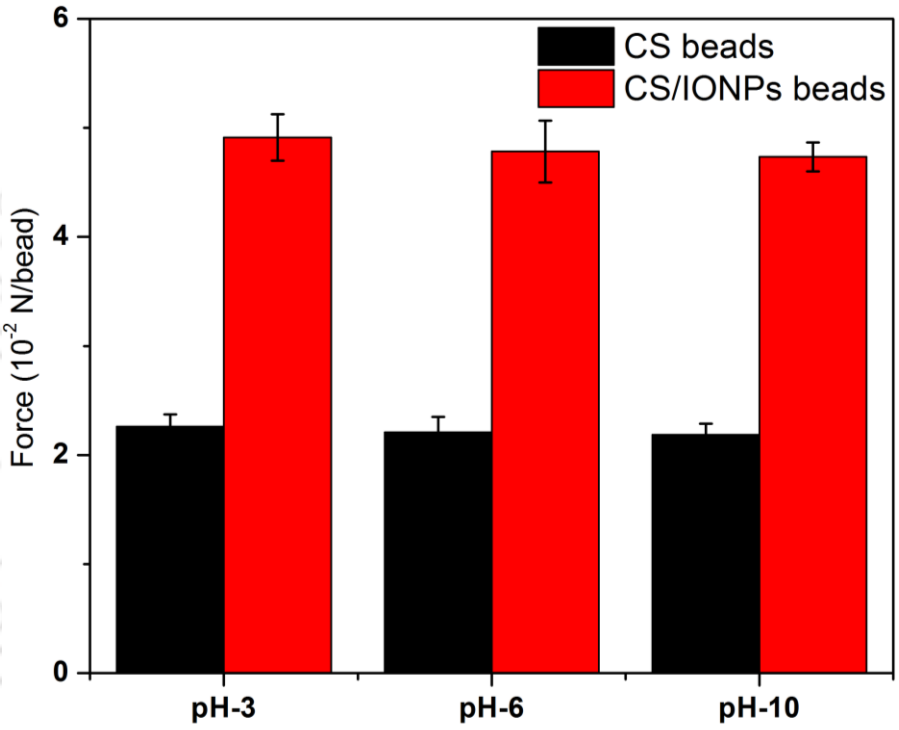

Figure 4.9: Mechanical strength of synthesized CS and CS CS/IONPs beads at various pH conditions of double distilled water.

4.3.2 Removal of Cr(VI) through synthesized CS/IONPs beads

4.3.2.1 Effect of pH and temperature

Cr(VI) ions exist in various forms in an aqueous solution, including chromate (CrO_4^{2-}), hydrogen chromate ($HCrO_4^-$), and dichromate ($Cr_2O_7^{2-}$), depending upon the solution pH. At a pH range of 2-6, the predemoninat Cr(VI) species are $HCrO_4^-$ and $Cr_2O_7^{2-}$. While CrO_4^{2-}

becomes the dominating species at pH > 6. The initial pH was adjusted between 3 and 10 for Cr(VI) solution for the current adsorption studies. The amount of Cr(VI) adsorbed to CS/IONPs beads depends on the pH. q_e value was maximum (58.56 mg g^{-1}) at an initial pH 3 (Figure 4.10(a)). On the other hand, the bare CS beads showed only 24 mg g^{-1} removal (Figure 4.11) at the similar pH. This postulates that IONPs infused in the CS matrix were key candidates responsible for the adsorption and reduction (Eqs. 4.6 and 4.7) of Cr(VI) species in the aqueous solution. The results are line with the investigations made in Chapter 3. Moreover, the zeta potential magnitude was more positive in the case of CS/IONPs (52.77 mV) than CS (41.63 mV) beads at pH 3 (Figure 4.12). Further, the -NH_2 and –OH functional groups on CS/IONPs beads were also protonated in acidic solutions (pH<4) [333]. This led to enhanced electrostatic interactions compared to CS beads between protonated CS/IONPs beads functional groups and Cr(VI) species in acidic conditions (pH 3) (Eqs. 4.2-4.7).

$$R - NH_2 + H^+ \rightarrow R - NH_3^+ \quad (4.2)$$

$$R - NH_3^+ + HCrO_4^- \rightarrow R - NH_3^+ \ldots . HCrO_4^- \quad (4.3)$$

$$R - OH + H^+ \rightarrow R - OH_2^+ \quad (4.4)$$

$$R - OH_2^+ + HCrO_4^- \rightarrow R - OH_2^+ \ldots . HCrO_4^- \quad (4.5)$$

$$HCrO_4^- + 7H^+ + 3Fe^{2+} \rightarrow 3Fe^{3+} + Cr^{3+} + 4H_2O \quad (4.6)$$

$$Cr_2O_7^{2-} + 14H^+ + 6Fe^{2+} \rightarrow 6Fe^{3+} + 2Cr^{3+} + 7H_2O \quad (4.7)$$

Therefore, IONPs reduction affinity and electrostatic interactions of protonated functional groups (-NH_2 and -OH) in CS/IONPs beads at pH 3 were responsible for maximum Cr(VI) removal. Further, increased pH decreased the q_e from 58.56 to 4.54 mg g^{-1}. This was due to decrement in surface charge (5.83mV, pH 10) (Figure 4.12) and deprotonation of the positively charged (-NH_2, and –OH) groups over CS/IONPs beads occurred at high pH due to low H^+ ions concentration. This causes an electrostatic repulsion between the negatively charged Cr species and the synthesized CS/IONPs beads.

Figure 4.10(b) depicts how temperature influences Cr(VI) removal. Low temperature showed a better Cr(VI) removal from the aqueous solution. Specifically, the q_e was increased from 27.63 to 58.56 mg g^{-1} as the temperature dropped from 45 to 25°C. The observed phenomenon can be ascribed to the weaker interactions of solute (CS/IONPs beads) – solvent (Cr(VI solution)) at elevated temperatures. Moreover, the active sites of CS/IONPs beads exhibited stronger chelation with Cr species at reduced temperatures and formed a stable structure [334].

4.3.2.2 Influence of CS/IONPs beads dosage and contact time

Figure 4.10(c) illustrates the relationship between the dosage of CS/IONPs in g/L and the percentage of Cr(VI) removal and q_e in mg g^{-1}. Cr(VI) removal % was higher with increased CS/IONPs beads doses and achieved a plateau at 3g/L dosage. This trend started from 31% to 99% at 0.5 and 3 g/L CS/IONPs beads dosages, respectively. However, at 2.5 g/L dosage, the Cr(VI) removal (Figure 4.10(c)) reached the plateau. As active adsorption sites increased, Cr(VI) removal efficiency increased when more CS/IONPs beads were dosed into the Cr(VI) solution. The earlier finding also supports the correlation between escalated adsorbent (CS/IONPs) dosage and enhanced Cr(VI) removal [323]. However, due to unoccupied adsorption sites, q_e was decreased from 92 to 49 mg g^{-1} at 0.5 and 3 g/L dosages of CS/IONPs beads, respectively. As illustrated in Figure 4.10d, the removal of Cr(VI) exhibited a significant increase during the initial stage, up to 300 min. The observed phenomenon could be attributed to the concentration declivity of Cr(VI) and a surplus of unoccupied adhesion spots over CS/IONPs beads [335]. The prolonged contact time exhausted the Cr(VI) adsorption sites, which further delayed Cr(VI) adsorption on CS/IONPs beads. Meanwhile, the adsorption equilibrium was achieved within 480 min.

4.3.2.3 Effect of initial Cr(VI) concentration

A range of initial concentrations was tested to determine optimal conditions for removing Cr(VI), ranging from 25 to 900 mg/L (Figure 4.10(e)). Moreover, despite the increase in q_e value, the removal % was reduced as the initial Cr(VI) concentration climbed. This reduction in Cr(VI) removal % was due to the inverse relation between Cr(VI) removal % and C_o as depicted in Eqs. 4.1. On the other hand, q_e values were found to be increased with a rise in Cr(VI) concentrations. This observed phenomenon was ascribed to the saturation in adsorption spots of CS/IONPs beads at elevated Cr(VI) concentrations, which were left vacant at lower concentrations [336]. As a result, 150 mg/L was established as an optimal concentration of Cr(VI) for further kinetics tests, attaining more than 95% Cr(VI) elimination.

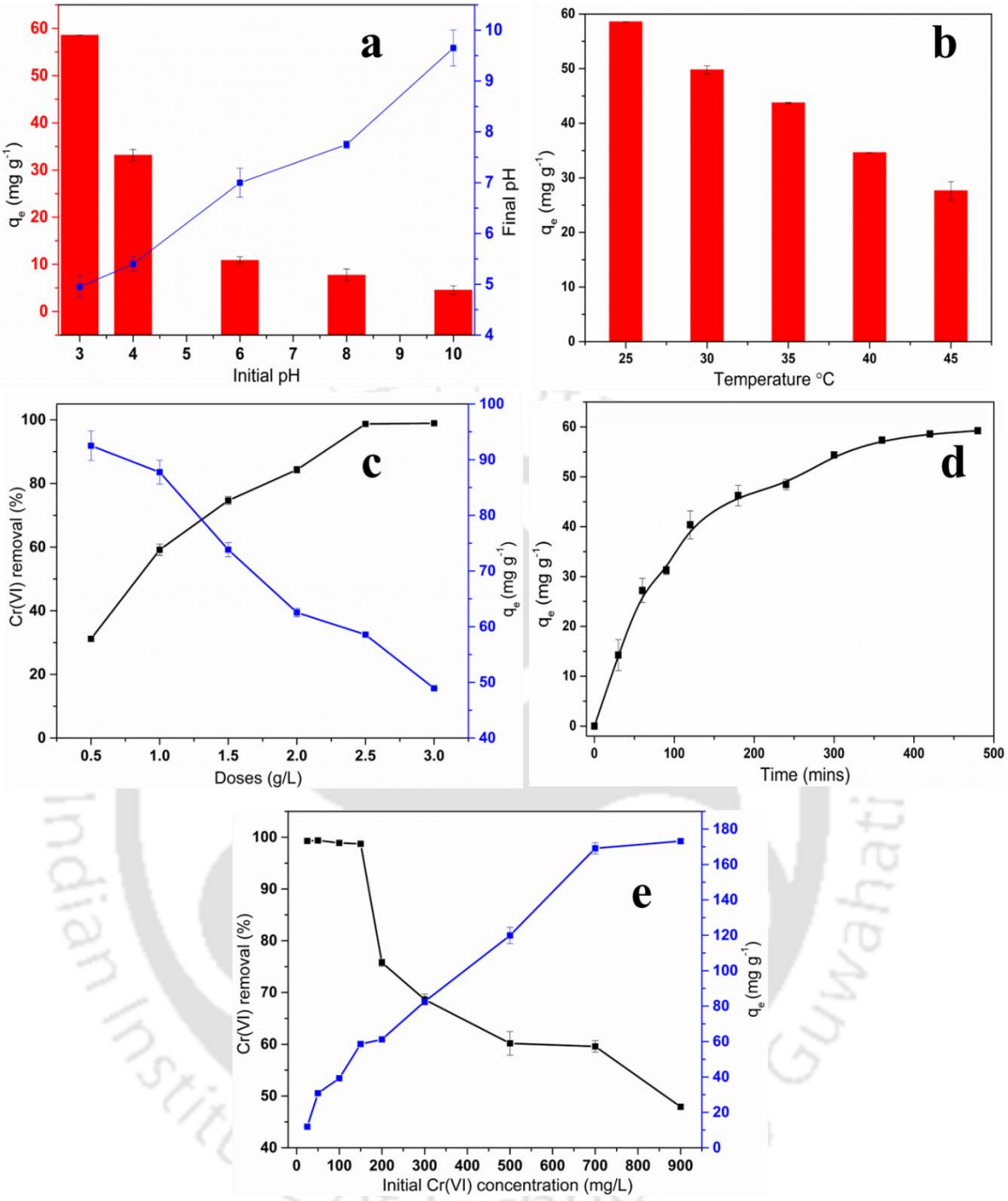

Figure 4.10: Effect of (a) pH (C_o - 150 mg/L and CS/IONPs dosage - 2.5 g/L), (b) temperature (C_o - 150 mg/L, CS/IONPs beads dosage - 2.5 g/L, pH - 3), (c) dosage (C_o - 150 mg/L and pH - 3), (d) time (C_o - 150 mg/L, CS/IONPs beads dosage - 2.5 g/L, pH - 3), and (e) initial Cr(VI) concentration (CS/IONPs beads dosage - 2.5 g/L and pH - 3) on Cr(VI) removal through synthesized CS/IONPs beads.

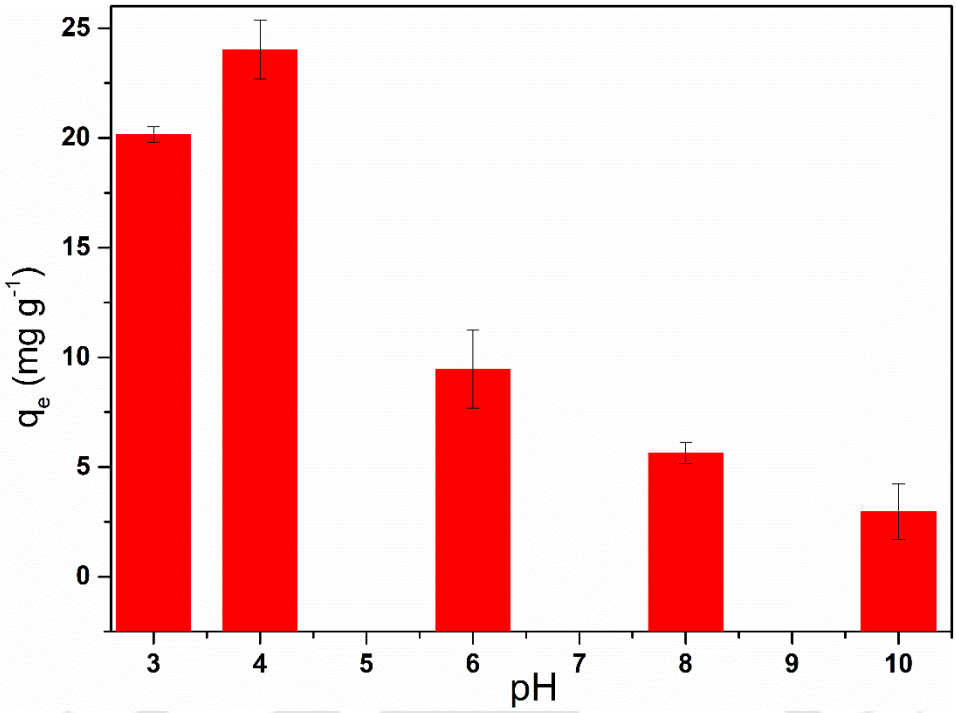

Figure 4.11: Effect of pH on q_e using bare CS beads (C_o - 150 mg/L and CS beads dosage - 2.5 g/L).

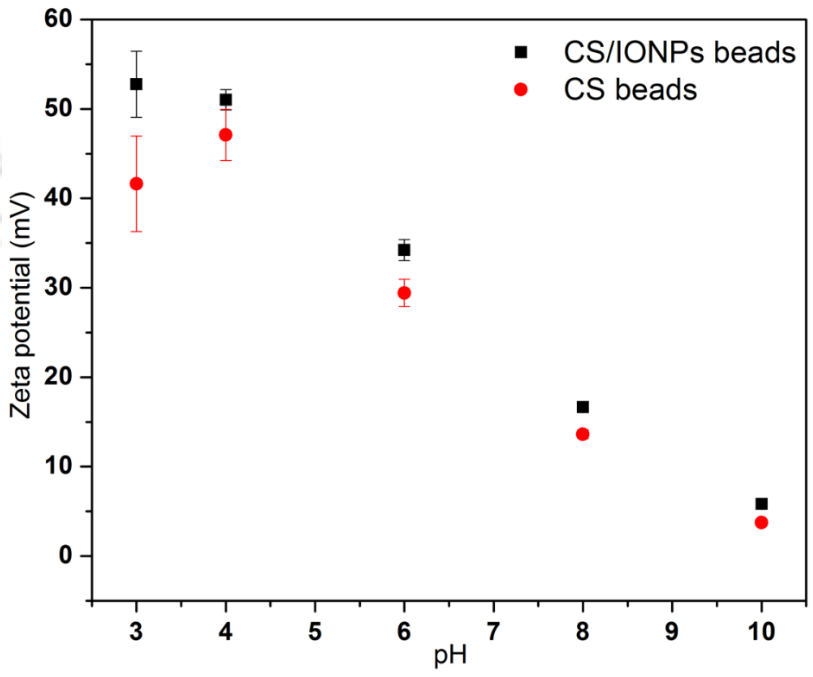

Figure 4.12: Variation of zeta potential of CS and CS/IONPs beads measured at different pH.

4.3.2.4 Effect of co-existing ions

The efficacy of the synthesized adsorbent (CS/IONPs beads) in removing Cr(VI) from contaminated water may be hindered by co-existing ions. In this regard, several cations (Na^+, Ca^{2+}, Mg^{2+}) and anions (PO_4^{3-}, SO_4^{2-}, NO_3^-, Cl^-) were individually introduced into the aqueous Cr(VI) solution at a concentration of 1 and 10 mM, respectively (Figure 4.13). The ionic strength (I) of co-existing ions was evaluated as $I = \frac{\sum C_i z^2}{2}$ [337]. C_i and z donated the concentration of co-existing ions (mol/L) and charge, respectively. The I values follow the trend as $Ca^{2+} > Mg^{2+} > Na^+$ for cations while $PO_4^{3-} > SO_4^{2-} > NO_3^- > Cl^-$ in the case of anions. The removal efficacy of Cr(VI) was not significantly altered by the inclusion of co-existing cations due to electrostatic repulsion between the positively charged CS/IONPs adsorbent and cations at lower pH. The lowest q_e value was observed in the case of a higher concentration of Ca^{2+} ions because of the high I value compared to other cations. Due to the lower affinity and I value of NO_3^- and Cl^- as compared to other co-existing anions (PO_4^{3-} and SO_4^{2-}), they were found to have less influence on the adsorption capacity of CS/IONPs beads [335]. The competitive effects of PO_4^{3-} and SO_4^{2-} for Cr(VI) elimination were significant. The strength of these effects was increased with an increase in the I value of anions. This was due to the identical tetrahedral structure of PO_4^{3-}, SO_4^{2-}, and Cr(VI) species ($HCrO_4^-$) [316]. Consequently, PO_4^{3-} and SO_4^{2-} competed with Cr species to access the adsorption sites over CS/IONPs beads. The IONPs composed of Fe^{3+} species of Fe and PO_4^{3-} ions tend to form complexes with Fe^{3+} species at low pH values, reducing the efficacy of Cr(VI) removal [336]. The observed results were consistent with previous research on the effect of co-existing ions on Cr(VI) removal using similar adsorbents [320].

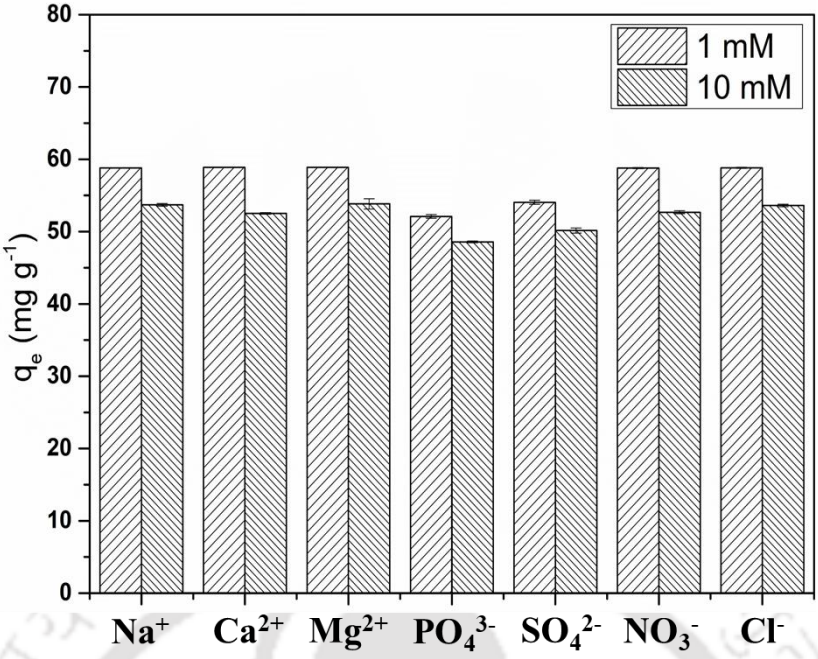

Figure 4.13: Effect of co-existing ions on q_e (C_o - 150 mg/L, CS/IONPs beads dosage - 2.5 g/L, pH - 3).

4.3.2.5 Thermodynamics study

The thermodynamic variables for Cr(VI) adsorption through CS/IONPs beads were determined at various temperatures (298, 303, 308, 313, and 318 K). Eqs. 3.7-3.9 (Chapter 3) were employed to calculate the three thermodynamic parameters, namely, Gibbs free energy (ΔG), enthalpy (ΔH), and entropy (ΔS) change of Cr(VI) removal [338-340].

The various thermodynamic parameters as calculated from the linearized fitting of Figure 4.14. The slope and intercept values of Figure 4.14 were employed to quantify the magnitude of ΔH and ΔS, respectively. Afterwards, the computed ΔH and ΔS values were equated in Eq. 3.8 (Chapter 3) to evaluate the magnitude of ΔG. The spontaneous occurrence of Cr(VI) adsorption through CS/IONPs beads was indicated through negative magnitudes of ΔG at different temperatures. As the temperature increased, the negative magnitude of ΔG values dropped (14.8 to 13.8 KJ mol^{-1}), indicating that low temperatures favoured Cr(VI) adsorption using prepared CS/IONPs beads, as described in Section 3.2.1 (Chapter 3). Cr(VI) adsorption was facilitated mainly by electrostatic interaction (physisorption), as indicated by values of

$\Delta G<20$ KJ mol^{-1} [333]. The negative value of ΔH (-29.35 KJ mol^{-1}) advocated that Cr(VI) removal through CS/IONPs beads was an exothermic process. The magnitude of ΔS was estimated to be -48.55 J mol^{-1} K^{-1}. This indicated a decrease in randomness at the CS/IONPs beads/liquid interface upon Cr(VI) adsorption onto the beads [321].

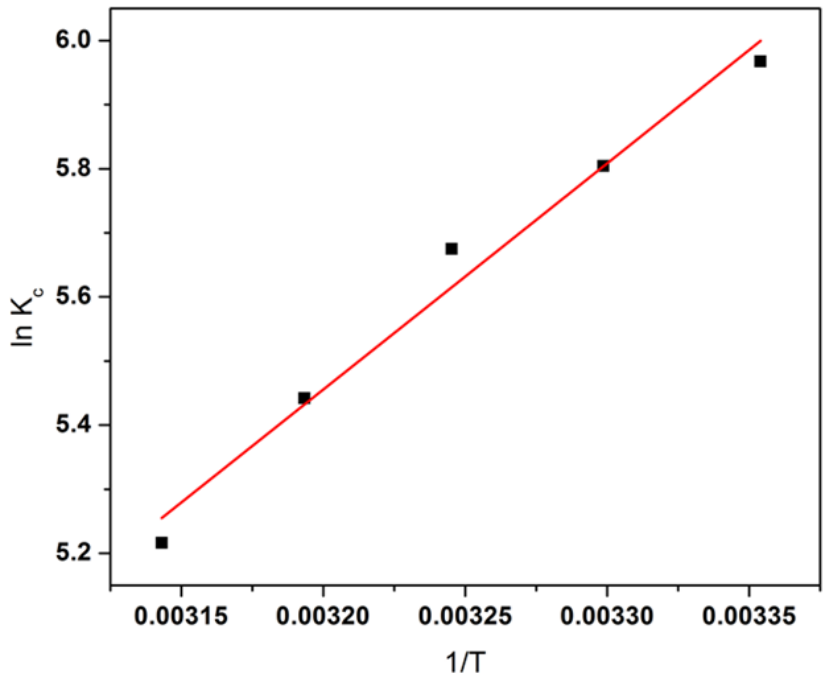

Figure 4.14: Linear correlation between distribution coefficient and inverse of adsorption temperature for Cr(VI) elimination over synthesized CS/IONPs beads.

4.3.2.6 Adsorption kinetics

It is important to look into the kinetics of Cr(VI) adsorption through CS/IONPs beads to design an adsorption system properly. The kinetics of CS/IONPs beads for Cr(VI) adsorption are illustrated in Figure 4.15a. Cr(VI) adsorption was much faster in the first 300 min (Figure 4.15a, symbols show experimental data points) and attained 90% removal owing to abundant empty sites on CS/IONPs beads. The adsorption rate decelerated and reached a plateau at 480 min due to reduced active sites.

To gain additional insight into the adsorption process, four frequently employed kinetic models were utilized to interpret the kinetics data, namely, pseudo-first-order (PFO), pseudo-second-order (PSO), Elovich, and intra-particle diffusion (IPD) models. The graph in Figure 4.15a displays the q_t (mg g^{-1}) values obtained from the fitted kinetic models plotted against time (min), represented by the fitted lines. Table 4.1 shows the model parameters of the fitted models to the experimental data and their corresponding root mean square error (RMSE) and correlation coefficient (R^2) values.

As depicted in Table 4.1, the PSO model exhibited the lowest RMSE value of 1.301 compared to the other three models. However, the estimated fitted value of q_e (73.40 mg g^{-1}) significantly deviated from the experimental value (58.56 mg g^{-1}). In contrast, the PFO model demonstrated an RMSE value of 1.588 and a fitted q_e value of 58.67 mg g^{-1} close to the experimental q_e value of 58.56 mg g^{-1}. Hence, Cr(VI) adsorption kinetics using CS/IONPs beads followed the PFO model. It corroborates that Cr(VI) adsorption onto the CS/IONPs beads was primarily driven by physisorption [341-343]. The rate constants for PFO (K_1) and PSO (K_2) models were determined to be 0.009 min^{-1} and 0.00012 g mg min^{-1}, respectively. Also, the R^2 values for both the PFO and PSO kinetic models were calculated as 0.99. The parameters α and β of Elovich model were calculated as 0.972 mg g min^{-1} and 0.052 g mg^{-1}, respectively with an R^2 value of 0.98. Further, the Weber-Morris model fitted results (Figure 4.16) indicate that Cr(VI) adsorption onto CS/IONPs beads occurred in stages. Initially, a fast adsorption process happened on the surface of CS/IONPs beads, which was then succeeded by diffusion through the pores of the beads (up to 300 min). As the active sites and pores were saturated by that time (300 min), the adsorption process then moved to the interior pores of beads, i.e., IPD, which continued up to 480 min. The values of rate constants for IPD, specifically $K_{initial}$ (<300 min) and K_{intra} (>300 min), were calculated as 3.22 mg g^{-1} $min^{0.5}$

(R^2=0.97) and 0.425 mg g^{-1} $min^{0.5}$ (R^2=0.96), respectively. The comparatively higher value of $K_{initial}$ to K_{intra} indicated a more rapid adsorption rate during the initial phases of Cr(VI).

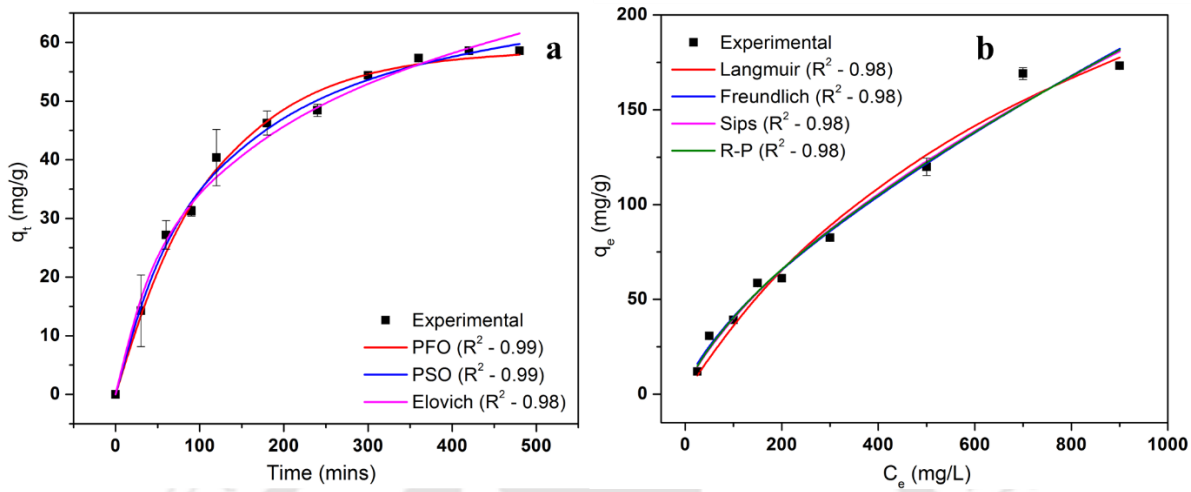

Figure 4.15: Non-linearized fitting of adsorption (a) Kinetics and (b) Isotherms models.

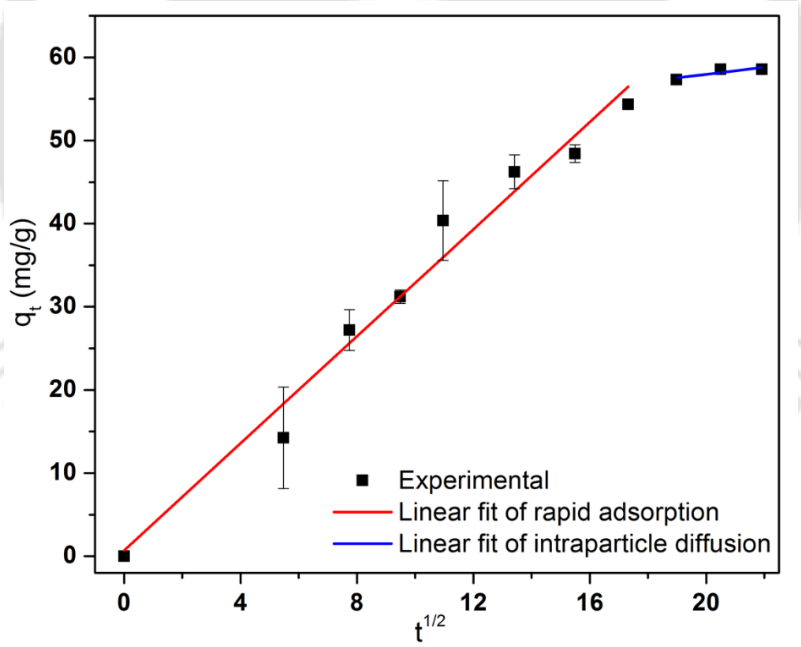

Figure 4.16: Linear fit to the experimental data using intraparticle diffusion model of Cr(VI) adsorption on synthesized CS/IONPs beads.

4.3.2.7 Adsorption isotherm

The adsorption isotherms may reveal interaction processes involved in Cr(VI) removal by CS/IONPs beads. The Q_m value of CS/IONPs beads can be obtained from an isotherm plot,

providing insight into the adsorption performance. Adsorption isotherm models, specifically, Langmuir, Redlich-Peterson (R-P), Sips, and Freundlich, were employed at 298.15 K. Figure 4.15b shows the derived adsorption isotherm models (q_e against C_e) (indicated by lines). Table 4.2 presents the adsorption isotherms models equation, fitted parameters, R^2, and RMSE values. Langmuir isotherm graph yielded Q_m, $K_{L,}$ and R^2 values as 345.53 mg g^{-1}, 1.1×10^{-3} L mg^{-1}, and 0.98, respectively. The value of the separation factor (R_L) varied between 0.49-0.97, indicating a favorable Cr(VI) adsorption system [305]. Freundlich isotherm model constitutes a suitable model to represent multilayer adsorption. Freundlich isotherm is expressed in a non-linear form (Table 4.2), exhibiting n, K_F, and R^2 of 1.47, 1.82 (mg g^{-1}) (mg $L^{-1})^{1/n}$, and 0.98, respectively. The Sips and R-P model is a hybrid model that involves characteristics of both Langmuir and Freundlich models. The Sips isotherm parameters, specifically q_{max}, Ks, and ns, were calculated to be 478.08 mg g^{-1}, 1.16×10^{-3} L $mg^{-1,}$ and 0.92, respectively. Further, the parameters associated with the R-P model, namely K_{RP}, $\alpha_{RP,}$ and g, were determined as 1.64 L g^{-1}, 0.5 (L $mg^{-1})^{g}$, and 0.39, respectively. The R^2 values of both (Sips and R-P) isotherm models were determined to be 0.98.

The isotherm models were evaluated based on their RMSE values, as listed in Table 4.2. Sips model showed the lowest RMSE value (6.554), followed by R-P, Freundlich, and Langmuir models, in that order. This demonstrates that heterogeneous active sites over CS/IONPs beads were involved in the adsorption of Cr(VI) [344]. Also, the heterogeneity exponent (n_S) value of Cr(VI) removal through CS/IONPs beads was not equal to unity (Table 4.2), which confirms the occurrence of heterogeneous adsorption [345]. This heterogeneity was due to various active components such as IONPs, $-NH_2$, and -OH on the surface of CS/IONPs beads. However, most of the utilized CS based adsorbents co-related well with Langmuir isotherm model for Cr(VI) adsorption [318, 346-348]. In contrast, the fitted outcomes of the Langmuir equation were used for assessing the Q_m. The computed Q_m of CS/IONPs beads for

Cr(VI) removal was substantial, reaching 345.53 mg g^{-1} at pH 3 and 25 °C, as shown in Tables 4.2. Table 4.3 compares the achieved Q_m value as calculated from Langmuir isotherm of synthesized CS/IONPs beads to those of other CS-based adsorbents at the optimized removal conditions. Looking into some of the reported literature (Table 3), bare CS in powdery and flake forms does not have much Q_m value for Cr(VI) adsorption. However, CS-based composite (aerogel/hydrogel) achieved a higher adsorbed mass of Cr(VI) over them than its powdered form. Further, a higher Q_m value was attained in the case of CS-based beads, which suggested beads form as a suitable composite adsorbent of CS as compared to other forms. The achieved Q_m value (345.53 mg g^{-1}) of CS/IONPs beads in the present study was relatively higher than those of other CS-based beads adsorbent.

Table 4.1: Parameters for PFO, PSO, Elovich, and IPD kinetic models for the removal of 150 mg/L Cr(VI) using CS/IONPs beads.

Kinetic model	Non-Linear expression	Parameters	Value	RMSE
PFO	$q_t = q_e(1 - e^{-K_1 t})$	q_e (mg g^{-1})	58.67	1.588
		K_1 (min^{-1}) × 10^{-3}	9	
		R^2	0.99	
PSO	$q_t = \frac{K_2 q_e^2 t}{1 + K_2 q_e^2 t}$	q_e (mg g^{-1})	73.40	1.301
		K_2 (g mg min^{-1}) × 10^{-4}	1.2	
		R^2	0.99	
Elovich	$q_t = \frac{1}{\beta}\mathrm{Ln}(\alpha\beta t)$	α (mg g min^{-1})	0.972	1.914
		β (g mg^{-1})	0.052	
		R^2	0.98	
IPD	$q_t = K_i t^{0.5} + C$	Initial 300 min		2.211
		$K_{initial}$ (mg g^{-1} $min^{-0.5}$)	3.22	
		C (mg g^{-1})	0.69	
		R^2	0.97	
		After 300 min		
		K_{intra} (mg g^{-1} $min^{-0.5}$)	0.425	
		C (mg g^{-1})	49.46	
		R^2	0.96	

[The constants K_1 and K_2 represent the PFO and PSO, respectively. The desorption constant was denoted by β, whereas the initial adsorption rate was denoted by α. The rate constant (K_i) and intercept (C) were domains of IPD.]

Table 4.2: Parameters of adsorption isotherm models for Cr(VI) adsorption onto CS/IONPs beads.

Isotherm model	Non-Linear expression	Parameters	Value	RMSE
Langmuir	$q_e = \frac{Q_m K_L C_e}{(1 + K_L C_e)}$	Q_m (mg g^{-1})	345.53	7.650
		K_L (L mg^{-1}) × 10^{-3}	1.1	
		R_L	0.49 - 0.97	
		R^2	0.98	
Freundlich	$q_e = K_F C_e^{\frac{1}{n}}$	n	1.47	6.895
		K_F (mg g^{-1})(mg L^{-1})$^{1/n}$	1.82	
		R^2	0.98	
Sips	$q_e = \frac{q_{max} K_S C_e^{n_s}}{1 + K_S C_e^{n_s}}$	q_{max} (mg g^{-1})	478.08	6.554
		K_S (L mg^{-1}) × 10^{-3}	1.16	
		n_S	0.92	
		R^2	0.98	
R-P	$q_e = \frac{K_{RP} C_e}{1 + \alpha_{RP} C_e^g}$	K_{RP} (L g^{-1})	1.64	6.865
		α_{RP} (L mg^{-1})^g	0.5	
		g	0.4	
		R^2	0.98	

[K_F- Freundlich constant, K_L-Langmuir constant, R_L-separation factor, n- adsorption intensity, q_{max} - maximum adsorbed amount, K_s and n_s- Sips constants and, K_{RP}, α_{RP} and g- R-P constants

Table 4.3: Reported Q_m values and optimum conditions for Cr(VI) removal using CS-based adsorbents.

Adsorbent	Optimized conditions					Cr(VI) removal (%)	Q_m (mg g^{-1})	Regeneration cycles	Anti-interference	Source
	Initial pH	Temperature (°C)	Doses (g/L)	Contact time (min)	Initial Cr(VI) concentration (mg/L)					
CS powder	4	20	0.1	240	0.5	94.7	35.6	-	Cl^-, SO_4^{2-}	[349]
CS flakes	3	30	13	180	30	-	22.09	-	-	[318]

CS-doped multiwalled carbon nanotubes	2	-	-	60	-	-	26.14	-	-	[350]
CS-based hydrogel	4.5	25	0.83	3000	100	94.72	73.14	-	-	[351]
CS oligosaccharide hydrogel	3	30	0.5	100	100	-	148.1	5	-	[352]
CS-graphene oxide (GO)/ carboxymethyl Cellulose composite aerogel	-	25	0.1	2880	0.58	-	127.4	5	-	[353]
CS-modified magnetic bamboo biochar	3	25	2.5	1440	300	>90	127	5	Na^{+}, Ca^{2+}, Fe^{3+}, Cl^{-}, SO_4^{2-}, PO_4^{3-}	[354]
FeS-CS-biochar composite	2	25	0.2	360	500	100	88.18	5	Cl^{-}, SO_4^{2-}	[355]
Polyethyleneimine-activated carbon-Fe_3O_4-CS/polyvinyl alcohol beads	6	29	1	30	-	98	199.8	5	-	[356]
Fe_2O_3-GO/CS beads	2	45	0.9	3000	80	94.3	141.50	5	Ca^{2+}, Mg^{2+}, Zn^{2+}, NO^{3-}, Cl^{-}, SO_4^{2-}, PO_4^{3-},	[342]
CS/IONPs beads	**3**	**25**	**2.5**	**480**	**150**	**98.71**	**345.53**	4	Na^{+}, Ca^{2+}, Mg^{2+}, PO_4^{3-}, SO_4^{2-}, NO_3^{-}, Cl^{-}	**This study**

4.3.2.8 Mechanism of Cr(VI) removal

The mechanisms behind the removal of Cr(VI) through CS/IONPs beads were investigated through analytical techniques of XPS (Figure 4.17) and FTIR (Figure 4.18(a)), respectively. Figure 4.17 displays the XPS spectra obtained before and after Cr(VI) adsorption. The presence of the Cr2p spectrum in the Cr-loaded CS/IONPs beads advocates (Figure 4.17a) the removal of Cr(VI). The XPS spectra of C1s (Figures 4.17b and 4.17c) revealed the presence of three distinct peaks at binding energies (BE) of 284.5, 286.1, and 288.4 eV. These peaks were attributed to C–C, C–N, and C=O functional groups [316, 357]. This observation revealed the possible existence of CS groups, such as $–NH_2$ and -OH, in CS/IONPs beads. The oxidation of the n–OH group facilitated the removal of Cr(VI) [316] and thus promoted Cr(VI) removal efficiency through CS/IONPs beads. Moreover, in the case of CS/IONPs beads deconvoluted N1s spectra (Figure 4.17d), two peaks were found at 400.9 and 402.8 eV, which were assigned to $-NH_2$, and -NH- of CS, respectively [321]. After Cr(VI) adsorption (Figure 4.17e), the $–NH_2$ functional group peak was shifted, which validated their participation in Cr species removal. Further, protonation of $–NH_2$ to NH_3^+ was confirmed through a deconvoluted peak (Figure 6e) at 402 eV [320]. The peaks at 532 and 533.9 eV of O1s in CS/IONPs beads (Figure 4.17f) were ascribed to C-OH and -O-C-O, respectively [316, 320, 358]. After Cr(VI) adsorption (Figure 4.17g), the deconvoluted peak of C-OH was shifted to 532.6 eV, while the peak for -O-C-O remained unchanged. This proposed that C-OH groups were involved in Cr(VI) removal through CS/IONPS beads. Prior to Cr(VI) adsorption (Figure 4.17h), the BE peaks at 709.2, 712.4, and 721.2 eV were associated with Fe^{2+} and Fe^{3+} in CS/IONPs beads, respectively [320]. However, after adsorption of Cr(VI) (Figure 4.17i), the Fe^{2+} peak disappeared (oxidized to Fe^{3+}), and Fe^{3+} peaks were shifted to higher BE (713.2 and 723.2 eV), along with additional peaks aroused for Fe^{3+} at 710.3 and 715.4 eV, respectively [359]. These findings demonstrated that Cr(VI) adsorption through CS/IONPs beads involves Fe^{2+} and Fe^{3+}. Furthermore, the

deconvoluted peaks in the Cr2p spectrum (Figure 4.17j) at BE of 577.7 and 587.2 eV corresponded to Cr(III) [316, 360], signifying the reduction of Cr(VI). The peaks observed at 582.6 and 590 eV were attributed to Cr(VI) [361], which advocated the adsorption of Cr(VI) occurred through CS/IONPs beads. Cr(III) also could be removed by co-precipitation with Fe(III), forming a solid solution-like species.

The stretched vibrations of O-H and N-H (Figure 4.18(a)) caused the broad band between 3300 - 3450 cm^{-1} observed in CS/IONPs beads [316]. The methyl (-CH_3) and methylene (-CH_2) groups C-H stretched vibration in CS were assigned to the band at 2929 cm^{-1} [321]. The -NH_2 groups bending was observed to the bands at 1640 and 1565 cm^{-1} [362]. The band at 1565 cm^{-1} became weaker and broader in the spectrum of Cr(VI) adsorbed CS/IONPs beads, which could be ascribed to the formation of a complex between -NH_2 and Cr(III) [316]. The -CH_2 bending was associated with a robust 1383 cm^{-1} band [363]. At 1315 cm^{-1}, the absorption band corresponded to amide III (C-N stretching) [364]. The secondary alcohol groups' C-O signals were observed at 1068 and 1162 cm^{-1} [321]. The iron oxides in CS/IONPs beads corresponded to the bands with wavenumbers of 709, 892, and 535 cm^{-1} [316, 365]. Further, these bands were weakened after Cr(VI) adsorption (CS/IONPs-Cr beads), which was attributed as a result of secondary alcohol groups chelated with Fe^{3+} [321]. These observations imply that IONPs in CS/IONPs beads were implicated in Cr(VI) removal.

To facilitate a more comprehensive examination of Cr(VI) ions removal mechanism, differences in Cr species concentrations, comprising Cr(VI), Cr(III), and Cr(tot), were also observed over the contact time (480 min) of Cr(VI) removal through CS/IONPs beads (Figure 4.18(b)). During the first 300 min of contact time, Cr(tot) concentration decreased significantly before levelling off at a plateau (480 min). The observed fast rise in Cr(III) concentration suggested a significant quantity of Cr(VI) species reduced through reaction with Fe^{2+} ions (Eqs. 4.6 and 4.7) during the initial stages of Cr(VI) removal. Afterwards, CS/IONPs active sites

quickly re-adsorbed the produced Cr(III) ions, leading to a plateau for Cr(III) concentrations. Nevertheless, Cr(III) adsorption over CS/IONPs beads reached saturation within 300 min. As a result, the steady reduction reaction of Cr(VI) to Cr(III) led to an increase in the concentrations of Cr(III) from 300 min, ultimately reaching nearly the saturation concentration of 34 mg/L at intitial pH 3.

Furthermore, Cr(tot) concentration exhibited a notable decline following a similar pattern as Cr(VI). This observation suggests that during the contact period of 480 min, more significant Cr(VI) ions underwent adsorption onto the CS/IONPs beads surface rather than being condensed to Cr(III). According to the above explanations, Cr(VI) removal mechanisms through CS/IONPs beads involved adsorption and reduction of Cr species through various surface and interior moieties of the formed beads, as described in Figure 4.19.

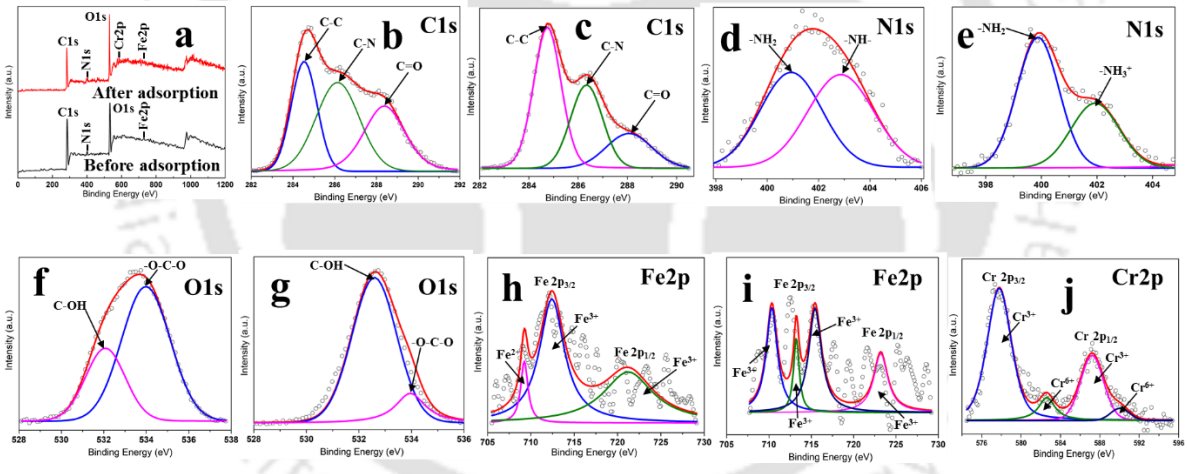

Figure 4.17: (a) XPS survey spectra of fresh and used CS/IONPs beads, deconvoluted XPS high-resolution spectrum for (b and c) C1s, (d and e) N1s, (f and g) O1s, (h and i) Fe2p and (j) Cr2p.

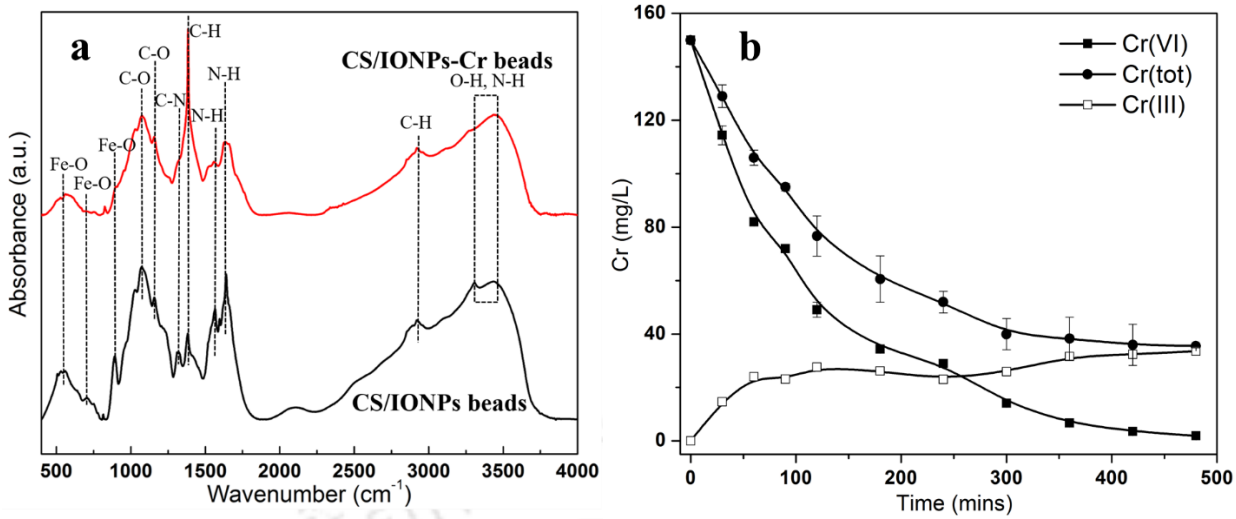

Figure 4.18 (a) FTIR spectra of CS/IONPs and after Cr(VI) adsorption (CS/IONPs-Cr) beads and (b) Measured Cr(tot), Cr(VI), and Cr(III) concentrations within a contact period of 480 min of Cr(VI) species with CS/IONPs beads.

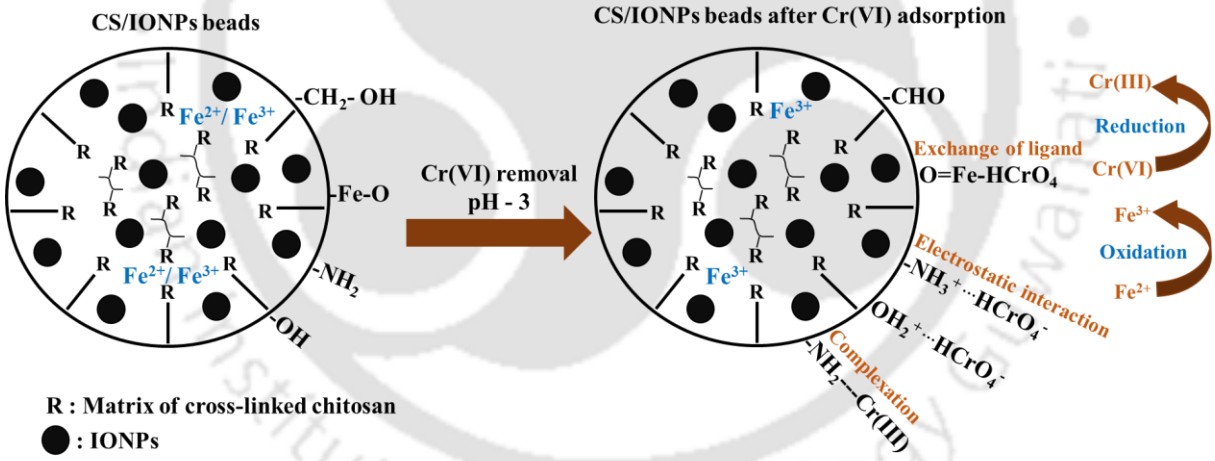

Figure 4.19: The proposed Cr(VI) elimination approach uses synthesized CS/IONPs beads.

4.3.2.9 Reusability of CS/IONPs beads

The ability of a saturated adsorbent to be well regenerated and reused impacts its practical usefulness. The present investigation involves the assessment of Cr(VI) desorption using NaOH solution for four successive cycles. The findings indicate that the removal % remained consistent (98 %) for up to two cycles but dropped to 83 % in the final (4^{th}) adsorption cycle

(Figure 4.20). The desorption of Cr(VI) was about 99.8% up to two desorption cycles. It started to decline with more desorption/adsorption cycles and reached 48 % in the 4th desorption cycle (Figure 4.20).

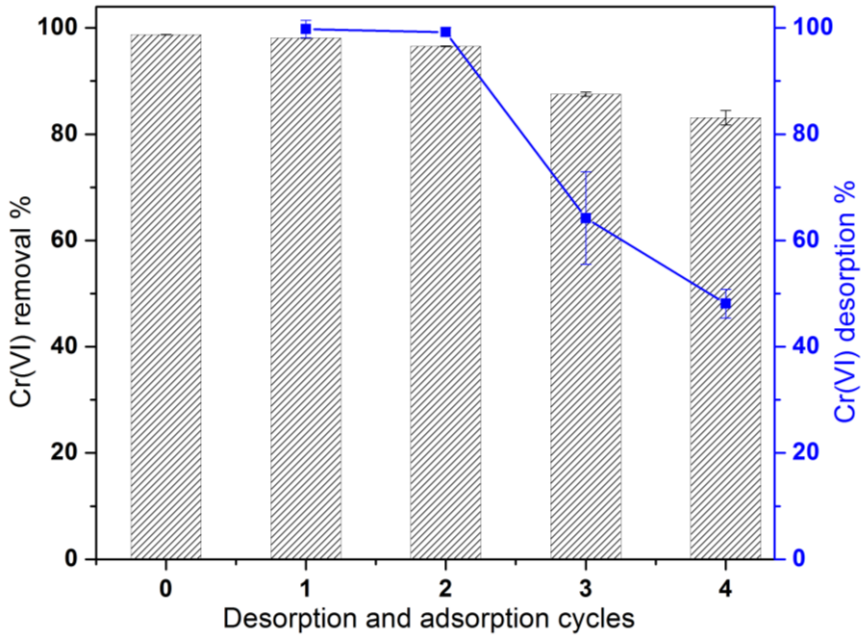

Figure 4.20: Variations in Cr(VI) removal and desorption % during four cycles of repeated adsorption and desorption of CS/IONPs beads in aqueous solution (C_o - 150 mg/L, CS/IONPs beads dosage - 2.5 g/L, pH - 3, Desorbing agent - 1M NaOH).

All elements (O, C, N, and Fe) except Cr were present in EDS image mapping of used CS/IONPs beads (Figure 4.21). It indicates complete desorption of Cr(VI) ions from the beads in NaOH solution up to two desorption cycles. The conversion of Cr(VI) to Cr(III) also declined beyond two desorption/adsorption cycles (Figure 4.22). The incomplete desorption of Cr(VI) species from CS/IONPs beads resulted in the unrecoverable occupation of adsorptive sites over the beads and decreased the adsorbent (CS/IONPs beads) and adsorbate (Cr(VI)) interactions [325] after the first two desorption/adsorption cycles. As a consequence, the removal percentage of Cr(VI) was reduced in subsequent adsorption cycles.

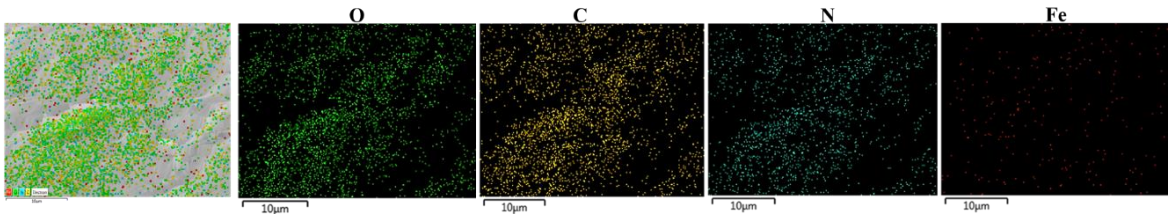

Figure 4.21: EDS image mapping of reused CS/IONPs beads after Cr(VI) adsorption (O – Oxygen, C – Carbon, N – Nitrogen, Fe – Iron).

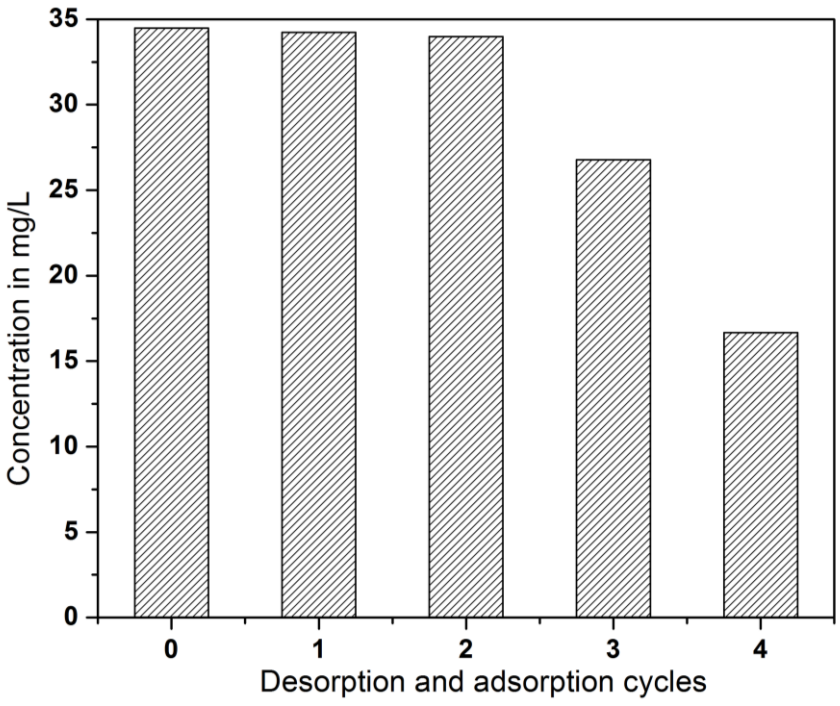

Figure 4.22: Variation in Cr(III) concentrations in aqueous solution during four cycles of repeated adsorption and desorption of CS/IONPs beads.

Also, the changes in C1s, O1s and N1s signals (Figure 4.17c, 4.17e and 4.17g) of CS/IONPs beads after Cr(VI) adsorption exposed the partial oxidation of adsorbent beads [366]. This passivation contributed towards progressive degradation of the CS/IONPs beads during subsequent adsorption cycles, which decreased the Cr(VI) removal efficacy upon its reusability (Figure 4.20). Figure 4.23 reveals that a very small amount of iron (<0.55 mg/L) was leached from IONPs into the aqueous solution during subsequent adsorption cycles and

followed a decreased trend, with the lowest in the last (4^{th}) cycle. It implies that the IONPs remained closely packed in the CS matrix during subsequent cycles of Cr(VI) adsorption through CS/IONPs beads. These findings suggest that CS/IONPs beads can undergo facile regeneration using NaOH. Therefore, CS/IONPs beads are regarded as a suitable adsorbent candidate for removing Cr(VI) in real applications.

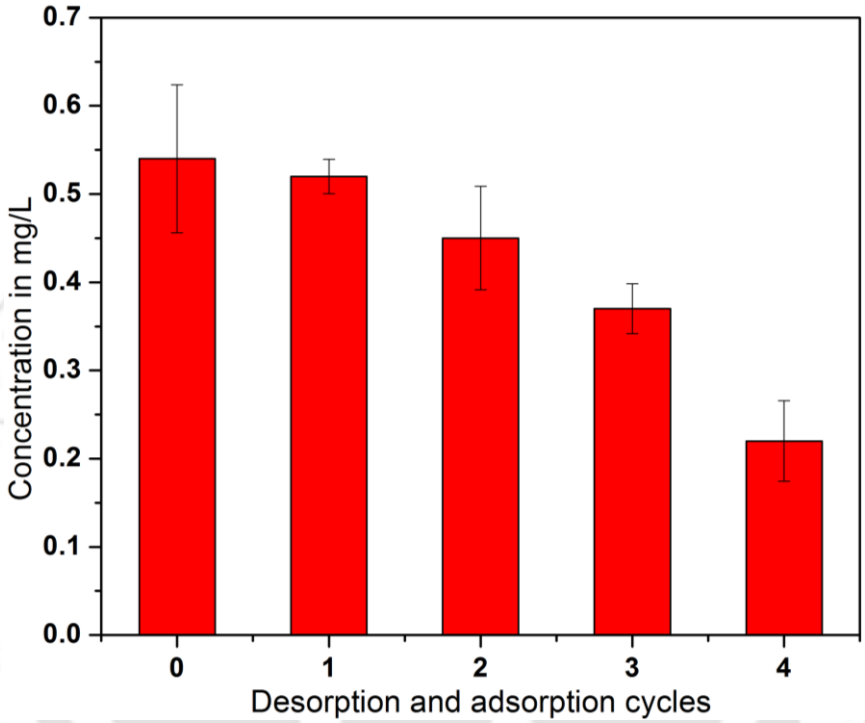

Figure 4.23: Variation in Fe concentration in aqueous solution during four cycles of repeated adsorption and desorption of CS/IONPs beads.

4.4. Conclusions

In the present investigation, bio-based IONPs were immobilized and entrapped within the CS matrix to synthesize reusable bi-functional composite CS/IONPs adsorbent. The stability of CS/IONPs beads was significantly affected by the pH of the aqueous solution, and composite beads were found to be stable above pH≥3. The used CS/IONPs adsorbent retained its morphological and structural attributes after 4 cycles of reusability tests. CS/IONPs exhibited a maximum 58.56 mg g^{-1} adsorption capacity at the optimized initial pH of 3, CS/IONPs dose

of 2.5 g/L, and temperature of 25°C with an initial Cr(VI) concentration of 150 mg/L. Co-existing cations (Na^{+}, Ca^{2+}, Mg^{2+}) did not significantly affect Cr(VI) adsorption capacity; however, PO_4^{3-} and SO_4^{2-} anions interfered with Cr(VI) adsorption owing to complexation with Fe^{3+} species in CS/IONPs. Langmuir isotherm suggests that CS/IONPs composite beads could adsorb as high as 345 mg Cr(VI)/g CS/IONPs. The change in Gibbs free energy, heat of adsorption, and entropy of Cr(VI) adsorption was found to be -14.8 to -13.18 KJ mol^{-1}, -29.35 KJ mol^{-1}, and -48.55 J mol^{-1} K^{-1}, respectively.

Cr(VI) species were removed by electrostatic interactions between protonated NH_3^{+} and OH_2^{+} functional groups of CS/IONPs beads. Fe(II) and Fe(III) synergized Cr(VI) removal through Cr(VI) reduction to Cr(III) and Cr(III)/Fe(III) co-precipitation along with Cr(III) surface complexation with the $–NH_2$ group. CS/IONPs beads exhibited a gradual decay in Cr(VI) removal within 5 cycles of adsorption, and a decrease of 15.7% in Cr(VI) removal was observed using the re-used adsorbent. Therefore, CS/IONPs are a potential bi-functional composite adsorbent for Cr(VI) removal and Cr(VI) detoxification to Cr(III).

A significant difference in Cr(VI) adsorption efficacy was observed when comparing CS/IONPs beads to the synthesized IONPs. The IONPs exhibited 3.68 times greater Q_m values, along with rate constants K_1 and K_2, which were 10 and 33.33 times higher than the CS/IONPs beads, respectively. However, Fe dissolution was significantly more in IONPs than CS/IONPs beads. Further, the CS/IONPs beads were found to have a BET surface area 3.48 times more than that of the IONPs. Moreover, the lower concentrations of PO_4^{3-} and SO_4^{2-} in aqueous solution greatly impacted the Cr(VI) removal efficiency of CS/IONPs beads compared to IONPs.

Chapter 5

Tannic acid (TA) assisted formation of IONPs/sodium alginate (Alg) composite adsorbent (Alg-TA-Fe) for Cr(VI) removal and antibacterial functionality

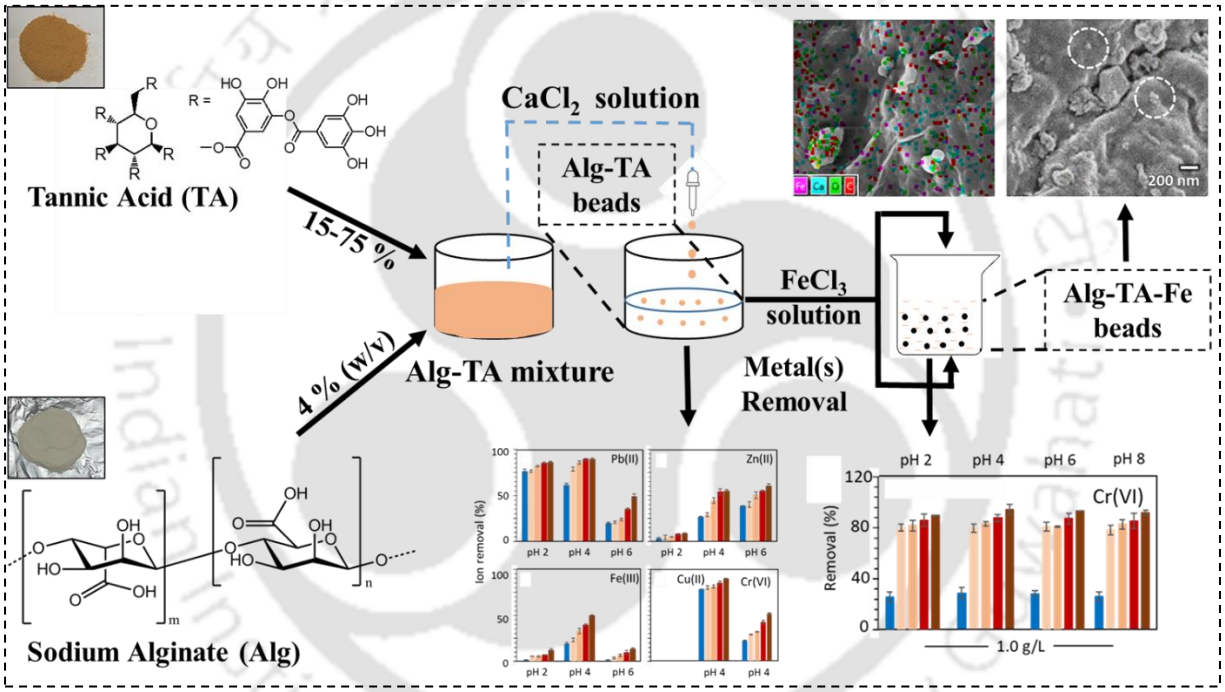

Highlights

- Composite adsorbent (Alg-TA and Alg-TA-Fe) beads developed for metal(s) removal
- Ability of Alg-TA beads to remove metal(s) increased with increasing TA incorporation
- IONPs formed within Alg-TA75 beads enhanced Cr(VI) removal efficiency by 86.23%
- Alg-TA75-Fe beads showed *E.coli* and *E.hirea* growth inhibition of 74% and 85%
- Higher amount of TA enhanced the stability of the synthesized Alg-TA-Fe beads

In this Chapter, novel and environment-benign beads were prepared by incorporating tannic acid (TA) and ferric ions (Fe(III)) into an alginate (Alg) hydrogel to enhance its Cr(VI) sorption properties and antimicrobial performance. Firstly, we synthesized Alg beads with varied (15-75%) TA content. These synthesized Alg-TA (15-75) beads were applied for the individual removal of Pb(II), Zn(II), Cu(II), Fe(III), and Cr(VI) from aqueous solution. Furthermore, we used the Alg-TA (15-75) beads to form IONPs. The modified Alg-TA (15-75)-Fe beads were then employed for enhanced Cr(VI) removal from the aqueous solution. The influence of various Cr(VI) removal conditions, namely, pH, Alg-TA (15-75)-Fe beads dosage, and initial Cr(VI) concentrations, were studied. Moreover, the synthesized Alg-TA and Alg-TA-Fe beads' antibacterial performance was tested over *Escherichia coli* (*E.coli*) and *Enterococcus hirea* (*E.hirea*), respectively.

5.1. Introduction

In Chapter 4, the preparation of CS/IONPs beads was described, and applied to remove Cr(VI) from the aqueous solution. In this Chapter, another biopolymer, i.e., alginate (Alg), was utilized to form the metal sorbent beads along with antibacterial functionality. Alg is a hydrophilic polysaccharide linear binary copolymer composed of (1-4)-linked β-d-mannuronic acid (M) and α-l-guluronic acid (G) residues as monomers, constituting M-, G-, and MG-sequential blocks. The use of Alg hydrogels is in demand due to its porous network structure, rapid swelling behavior, charge over the surface, and functional group attached [367]. Recently, Alg was extracted from *Laminaria digitata*, and hydrogels of alginate-acrylamide were formed through a polymerization technique for Pb(II) removal from an aqueous solution [368]. In a separate study by Qu *et al.*, [369] urea formaldehyde was grafted onto Alg beads to enhance the porosity and stability of the formed beads for the removal of Pb(II), Cu(II), and Cd(II), respectively, from aqueous solution. The metals, pathogens, and dyes present in the

wastewater were also disinfected by encapsulating Alg beads with zinc oxide NPs [370]. This postulates that several modifications on Alg beads can be used as an adsorbent to remove heavy metals and pathogens from the wastewater.

The key active agent in the synthesis of metal NPs is polyphenols (PPs), i.e., tannic acid (TA), which are readily present in various parts of plants (e.g., tea, red grape) like leaf, seed, stem, and root [200, 201]. Catechol groups in TA can bind over surfaces through both covalent and non-covalent interactions [371]. Routinely, PPs are used by plants for their defense against ultraviolet radiation and pathogens present in the surrounding atmosphere. Green tea PPs extract primarily comprises 4 catechins: epigallocatechin gallate (EGCG), epigallocatechin, epicatechin gallate, and epicatechin. EGCG accounts for roughly 50-80% of overall catechins [202]. Graphene oxide (GO) was reduced with EGCG by Liao *et al.* [372] creating reduced GO (rGO). In order to retain the flavonoid structure, EGCG was converted to galloyl-derived orthoquinone via nucleophilic addition of epoxide, which then reduces GO to rGO. There has been a lot of work done in recent years to create novel polymer adsorbents with extraordinary adsorption capacities at a low cost [373-375]. In a study by Ucer *et al.* [376], the adsorption of Cu(II), Cd(II), Zn(II), Mn(II), and Fe(III), respectively, was achieved through TA-coated activated carbon. The highest affinity of metal adsorption was achieved for Cu(II) with a % removal of 65.5 at pH 5.4. In another study by Zou *et al.* [377], adsorption of Pb(II) ions was done through TA@Zr and found to have a Q_m of 100 mg g^{-1} as per Langmuir isotherm. Zing *et al.* [378] prepared double crosslinked Fe^{3+}-TA-HCHO polymer for the removal of Pb(II), Hg(II), and As(III), respectively, from synthetic metal solutions. The Q_m values for Pb(II) and Hg(II) removal through synthesized Fe^{3+}-TA-HCHO were reported as 819.67 and 699.3 mg g^{-1}, respectively. Further, a TA-rGO composite was developed by Cheng *et al.* [379] for Cr(VI) removal with a Q_m value of 179.22 mg g^{-1}. When applied to graphene sheets, TA inhibits the formation of aggregates by dampening the hydrophobic stacking interactions between

individual sheets. The coordination polymer of Fe^{3+}-TA, as reported by Ejima *et al.* [380] was prepared by a one-pot fabrication approach. The method required no unique tools, and the regents employed were both economical and environmentally friendly. Motivated by polyphenols' remarkable anti-inflammatory properties. The functionalized film of TA was developed by Yang *et al.* [381] to create a simple and effective chemical strategy for the acquisition of circulating tumor cells without tagging. Also, Zhang *et al.* [382] created a polypropylene separator coated with a TA/Fe^{3+} complex to slow the shuttle effect of polysulfides in lithium-sulfur batteries. Fe^{3+}-TA polymers tend to disassemble in acidic conditions due to the strong pH dependence of their coordination, thereby restricting the usefulness of the promising materials [380]. Therefore, it is crucial to create a study and adaptable TA-based material.

Accordingly, in this Chapter, environment-benign beads of Alg with varied (15-75%) TA content were prepared by using the polymerization technique. The synthesized Alg-TA (15-75) beads were characterized for weight, size, polymer content, and swelling ratio, respectively. The synthesized beads of Alg-TA (15-75) were applied to remove Pb(II), Zn(II), Cu(II), Fe(III), and Cr(VI) from aqueous solution. Further, the synthesized beads of Alg-TA (15-75) were dipped in Fe precursor solution to form IONPs within them and thus formed novel Alg-TA (15-75) -Fe beads. These formed beads of Alg-TA (15-75)-Fe were used to enhance Cr(VI) removal from the aqueous solution. To the best of our knowledge, this is the first time Alg-TA -Fe beads have been synthesized and used in environmental cleanup. Furthermore, several analytical methods were used to characterize both the synthesized beads of Alg-TA and Alg-TA-Fe. The influence of various Cr(VI) removal conditions, namely, pH, Alg-TA (15-75)-Fe dosage, and initial Cr(VI) concentrations, were studied and optimized. Moreover, the antibacterial performance of the synthesized beads (Alg-TA and Alg-TA-Fe) was also tested on *E.coli* and *E.hirea* pathogenic bacterial strains.

5.2. Materials and Methods

5.2.1 Materials

Tannic acid (cat. no: A17022) was bought from Alfa Aesar, UK. Sodium alginate (cas. no: 9005-38-3), copper (II) sulfate (cas. no: 7758-98-7) ($CuSO_4$), and calcium chloride (cas. no: 10043-52-4) were procured from Thermo Fisher Scientific, UK. Lead (II) nitrate (cat. no: 228621) $Pb(NO_3)_2$) and zinc (II) chloride (cat. no: 208086) ($ZnCl_2$) were purchased from Sigma-Aldrich, UK. 1,5-Diphenylcarbazide (DPC) (cat. no: GRM519) and ferric chloride anhydrous ($FeCl_3$) (cat. no: GRM1379) were purchased from Himedia, India. The chromium standard for atomic absorption spectroscopy (AAS) (1000 ppm), purchased from Sigma-Aldrich (cat. no: 02733), was diluted and used for Cr absorption experiments. Double distilled water (18 MΩ, Millipore) was used throughout the experiments.

5.2.2 Synthesis of Alg, Alg-TA and Alg-TA-Fe beads

Hydrogel beads were prepared by crosslinking a mixture of Alg and TA with calcium chloride solution by adapting a protocol reported in the literature [195, 383]. First, a thick solution of as-bought 4% (w/v) Alg was prepared in double distilled water (>1 h orbital shaker). Then 15-75% of TA (w/w with respect to Alg) was mixed into Alg solution and stirred until a homogeneous mixture was obtained. The Alg-TA mixture was then either pipetted into 3.5 % $CaCl_2$ solution (w/v) to form hydrogel Alg-TA beads or poured into a mold containing the $CaCl_2$ solution to form bulk samples for visual inspection and mechanical testing. To obtain the dry weight of hydrogel beads and to perform further physical characterization, including measurement of metal ion adsorption, beads were lyophilized (18 h), and then oven-dried (4 d). To induce iron particle formation, the Alg-TA beads were immersed in 0.1 M $FeCl_3$ solution (i.e. 5.58 g/L Fe^{3+}) for 30 min and then rinsed with water to form Alg-TA-Fe beads. A color

change indicating Fe_xO_y particle formation can be seen within 5-10 min. The control beads, i.e., only Alg beads dipped in $FeCl_3$ solution, were also prepared and denoted as Alg-Fe.

5.2.3 Characterization of synthesized Alg, Alg-TA and Alg-TA-Fe beads

The synthesized Alg-TA-Fe beads were imaged using a Field-Emission Scanning Electron Microscope (FESEM) (Zeiss, Model: Sigma, Germany) operated at 3 kV. Elemental mapping of Alg-TA-Fe bead surfaces was achieved using Energy dispersive spectroscopy (EDS) (Zeiss, Model: Sigma, Germany) installed in the SEM. The bead surfaces were also examined with X-ray photoelectron spectroscopy (XPS) (Ulvac, Model: PHI 5000 VersaProbe III, Japan) conducted using Al Kα X-rays, with a take-off angle of 45°. The measurements were performed under low energy electron and Ar^+ surface charge correction. A pass energy of 23.5 eV was used for high-resolution scans, while a pass energy of 117.4 eV was used for survey spectra. The binding energy (BE) of the primary C1s peak at 284.8 eV (C-C/C-H) was employed to compensate for specimen charging during data acquisition. The high-resolution scan BE data was further compensated for during peak fitting to be consistent with the main C1s C-O peak of the alginate material. A Shirley background was used in all high-resolution peak fittings, and Gaussian peak components of equal width were assumed for each type of peak (O1s, C1s, Fe2p, Fe2p satellite). BE fittings were further constrained within a range of chemical shifts reported for each bonding environment in the literature. Fourier transform infrared (FT-IR) spectrometer (PerkinElmer, Model: Spectrum two, USA) recorded the pertinent functional groups on the synthesized TA powder, Alg and Alg-TA (15-75) beads within the wavenumber from 4000 to 400 cm^{-1}. Further, the sizes of the prepared Alg and Alg-TA beads were determined by using Image J analysis. The wet, over-dried, and lyophilized weights of the synthesized Alg and Alg-TA (15-75) beads were also reported. The Universal Testing Machine (Instron, Model: 5944, USA) was employed to conduct the mechanical testing of the

synthesized larger hydrogel samples of Alg and Alg-TA (15-75), respectively. Furthermore, the swelling ratio of the synthesized Alg and Alg-TA (15-75) was calculated using the following Eq. 5.1 [384]. Where W_T and W_d represent the wet and dry weight of the formed Alg and Alg-TA beads in g, respectively.

$$\text{Swelling ratio} = \frac{W_t - W_d}{W_t} \quad (5.1)$$

5.2.4 Batch adsorption studies through synthesized Alg, Alg-TA and Alg-TA-Fe beads

The batch adsorption experiments were carried out for Pb(II), Cu(II), Zn(II), Fe(III), and Cr(VI) ions, respectively, from synthetic wastewater samples. Briefly, 1 g/L of lyophilized beads (Alg and Alg-TA (15-75)) were taken and mixed with C_o of Pb(II), Cu(II), Fe(III), and Zn(II) of 50 mg/L in glass vials and were agitated at a speed of 180 rpm and temperature of 25ºC in a shaker incubator (Scigenics, Orbitek-LE) for 12 h. The effects of various pH (2.0, 4.0, and 6.0) were explored to obtain the optimal pH condition for Pb(II), Zn(II), and Fe(III) removal, respectively, through Alg and Alg-TA (15-75) beads. The removal of Cu(II) and Cr(VI) using synthesized beads of Alg and Alg-TA (15-75) beads was performed at a constant pH of 4. Further, the synthesized Alg-TA (15-75)-Fe beads were applied to remove Cr(VI) from 20 mg/L aqueous solution. In addition, the effect of various pH, adsorbent dosage, and initial concentration were also studied in the range from 2.0 to 8.0, 1 to 2 g/L, and 20 to 150 mg/L, respectively, were explored to obtain the optimal removal conditions. Moreover, the adsorption isotherm studies were also performed on the synthesized beads Alg, Alg-TA (15-75), and Alg-TA (15-75)-Fe beads, respectively. Inductively coupled plasma mass spectrometry (Agilent, Model: 7700 series, USA) was used to measure the concentrations of metal ions (Pb(II), Cu(II), Fe(III), and Zn(II)), respectively, in the solution during adsorption experiments. Further, DPC reagent was utilized to determine the concentration of dissolved Cr(VI) by measuring absorbance at λ = 543 nm in a spectrophotometer [290]. The adsorption

capacity (q_e, mg g^{-1}) and removal % of metal ions were determined by using Eq. 3.1 (Chapter 3) and Eq. 4.1 (Chapter 4), respectively. Moreover, Langmuir and Freundlich isotherm expressions as already stated in Chapter 3 were equated to determine the adsorption isotherm parameters of the synthesized beads.

5.2.5 Antibacterial studies of the synthesized Alg, Alg-TA, Alg-Fe and Alg-TA-Fe beads

The antibacterial performance of the synthesized Alg, Alg-TA (15-75), Alg-Fe, and Alg-TA (15-75)-Fe beads was done by using both broth dilution and zone of inhibition (ZOI). The beads were tested for *Escherichia coli* (*E. coli*, MTCC 1610) and *Enterococcus hirea* (*E. hirea*, MTCC 3612) bacteria, respectively. The bacteria were grown in fresh Luria Broth media, and optical density (O.D.) at 600 nm was adjusted to 0.025, which resembles 10^7 CFU/mL. The prepared cultures of the bacteria were incubated with Alg, Alg-TA (15-75), Alg-Fe, and Alg-TA (15-75)-Fe beads at a dosage of 0.05 and 0.1 % (w/v), respectively, in a sterile 50 mL falcon's tube for 12 h at 37°C. After the incubation period, the O.D. 600 nm values were measured for different sets of concentrations of beads. Further, in the ZOI method, samples of Alg, Alg-TA (15-55), Alg-Fe, and Alg-TA (15-75)-Fe beads were put over the Mueller Hinton agar (MHA) grown bacteria (*E.coli* and *E.hirea)* plates for 12 h at 37°C. After incubation, the images of MHA plates were captured, and ZOI was measured using Image J software.

5.3. Results and Discussion

5.3.1 Alg-TA bead formation and characterization

Figure 5.1(a) illustrates the facile procedure of producing Alg-TA beads, adapted from the literature [385] simply by mixing TA powder into a sodium alginate solution and then pipetting drops of this mixture into a $CaCl_2$ solution for gelation. The hydrated Alg-TA beads, through the entire range of 15-75% TA incorporation, mostly retain the color of pure Alg beads

when initially prepared (Figure 5.1(b) and Figure 5.2(a)), and they acquire a brown tint after drying (Figure 5.2(b)). Roughly spherical beads may be formed up to 55% TA incorporation (Alg-TA-55) (Figure 5.1(c)), while higher TA resulted in more viscous Alg-TA mixtures that more easily gel into shapes influenced by the pipetting process (Figure 5.1(d)). Larger hydrogel sample may also be prepared by pouring Alg-TA pre-gelation mixtures into suitable molds filled with $CaCl_2$ solution (Figure 5.2(c)).

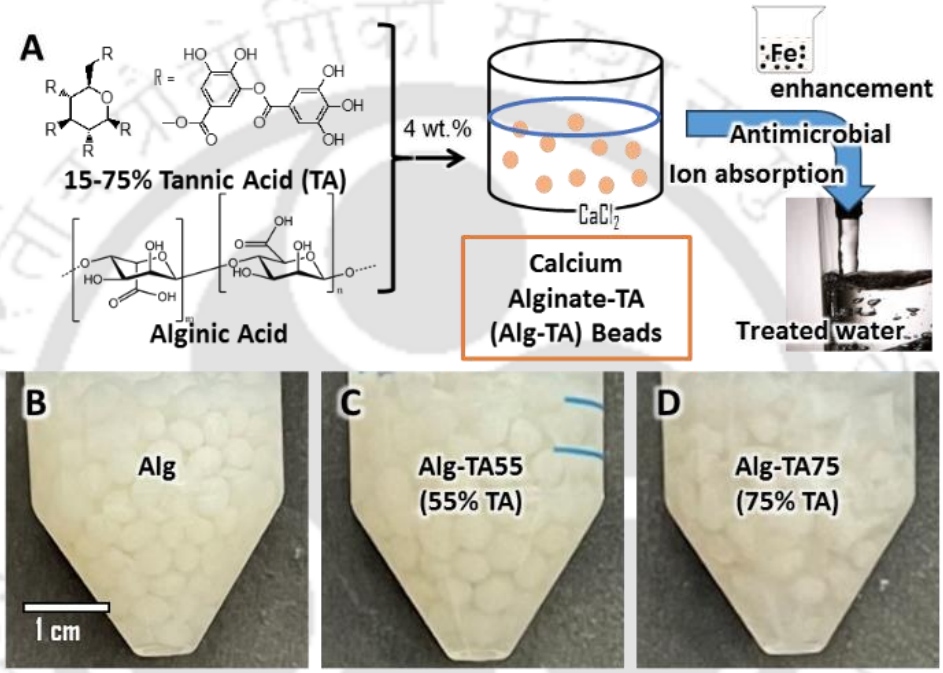

Figure 5.1: Schematic of hydrogel adsorbent bead preparation (A) and examples of wet beads of unfunctionalized 4% Alg (w/v) (B), and Alg-TA55 beads with 45:55 Alg:TA content (C) and Alg-TA75 beads with 25:75 Alg:TA content.

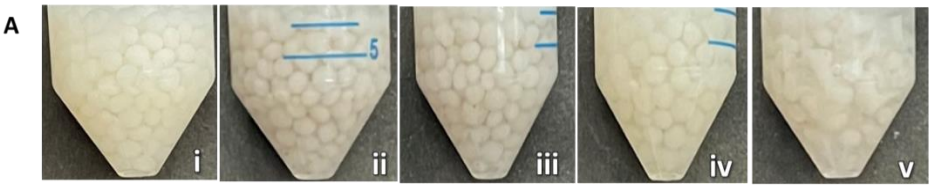

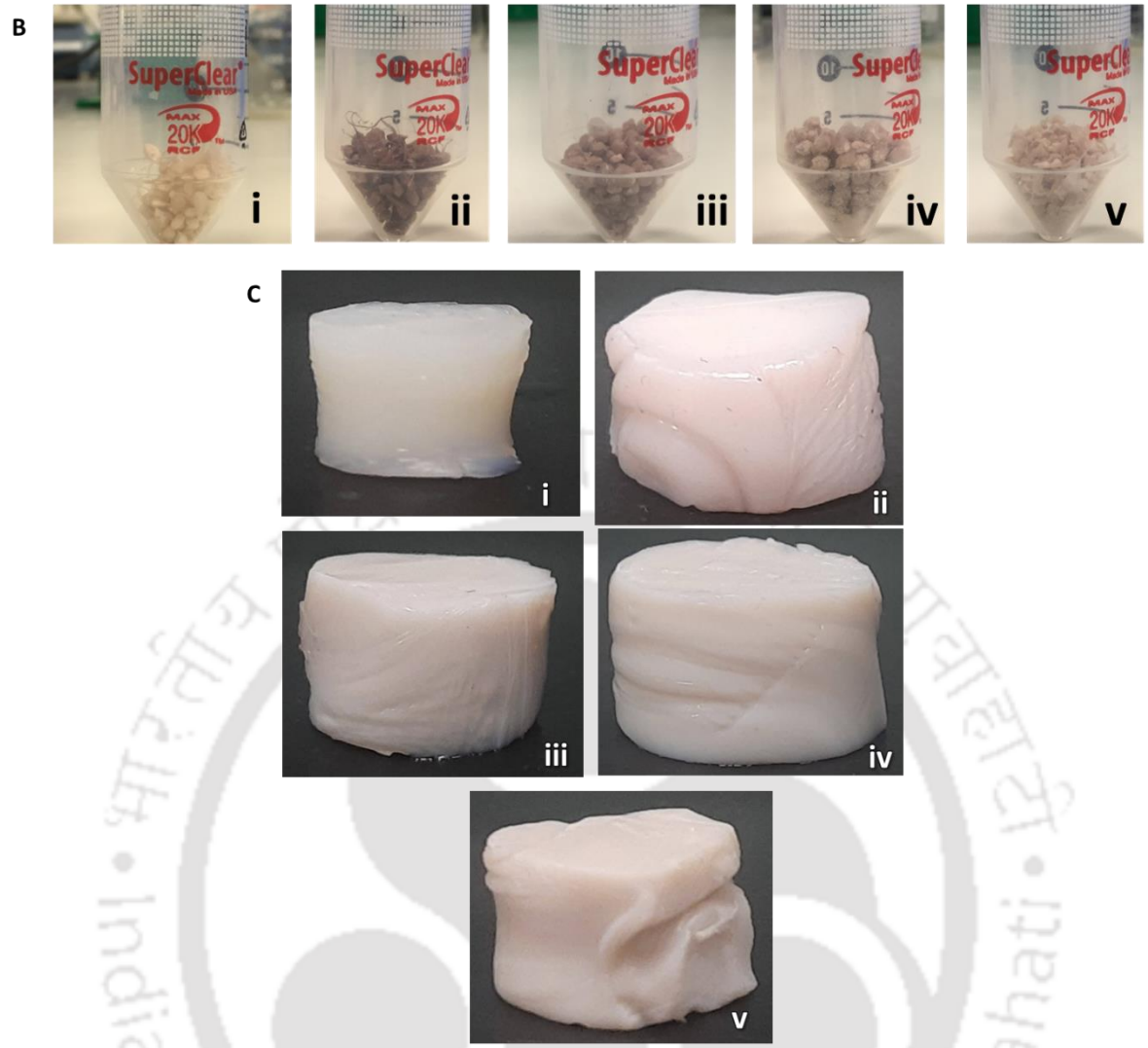

Figure 5.2: (A) Wet Alg beads (i) and (ii-v) Alg-TA beads with 15, 35, 55 and 75% of TA. (B) Dried Alg beads (i) and (ii-v) Alg-TA beads with 15, 35, 55 and 75% of TA. (C) Larger hydrogel samples molded from the 50 mL Falcon tubes of Alg (i) and (ii-v) Alg-TA gels with 15, 35, 55 and 75% of TA.

ATR-FTIR characterization of dried Alg-TA beads (Figures 5.3 and 5.4(a)) shows clear absorption bands expected for both alginate and TA, demonstrating actual TA incorporation from the pre-gelation mixture. In fact, based on the increases in peak areas for absorption bands expected for TA between 1153~1700 cm^{-1} when increasing amounts of TA were added (and corresponding decreases in alginate bands between 950~1153 cm^{-1}), we inferred that the actual TA: alginate ratio in the gel (Figure 5.3 inset) tended to be higher than the pre-gelation Alg-

TA mixture for lower TA additions (e.g., 25% TA incorporated at 15% added). TA incorporation became roughly proportional to the amount added at TA content above ~50%. The exact IR peak positions were also observed to shift gradually with the amount of TA added, possibly indicating specific chemical interactions during the gelation process.

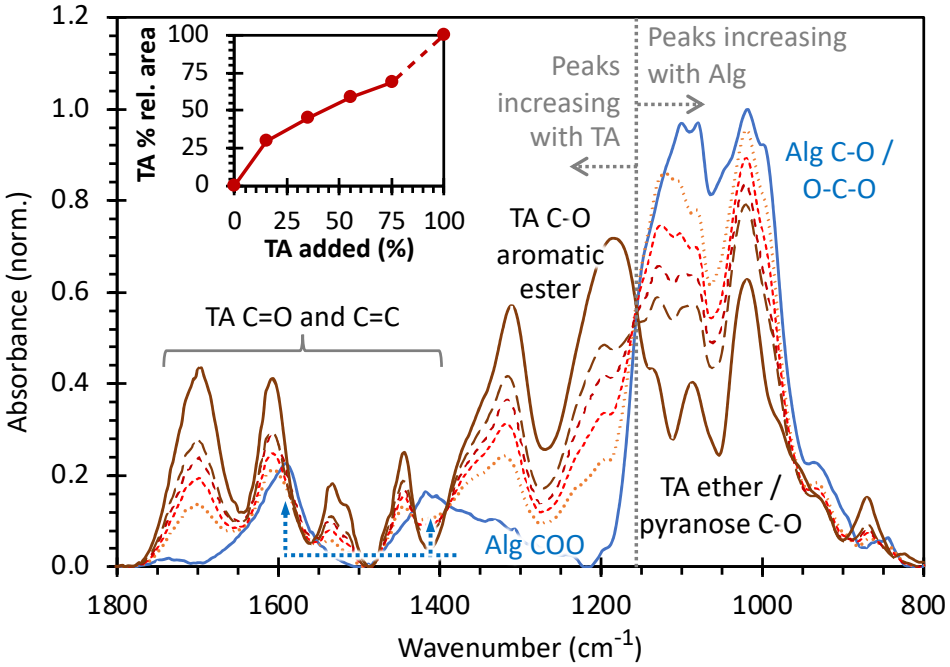

Figure 5.3: Main IR absorption bands of Alg-TA beads spanning 800-1800 cm^{-1} compared with the unfunctionalized Alg bead and neat TA powder as measured by ATR-FTIR. The full spectra from 650-4000 cm^{-1} is shown in Figure 5.4(a). The inset plots TA incorporation against the weight percentage of TA added during hydrogel preparation, as indicated by the relative absorbance increases in TA-associated peaks from 1153-1800 cm^{-1}. The same trend is also indicated by the relative decreases in Alg-associated absorbances below 1180 cm^{-1} (Figure 5.4(b)).

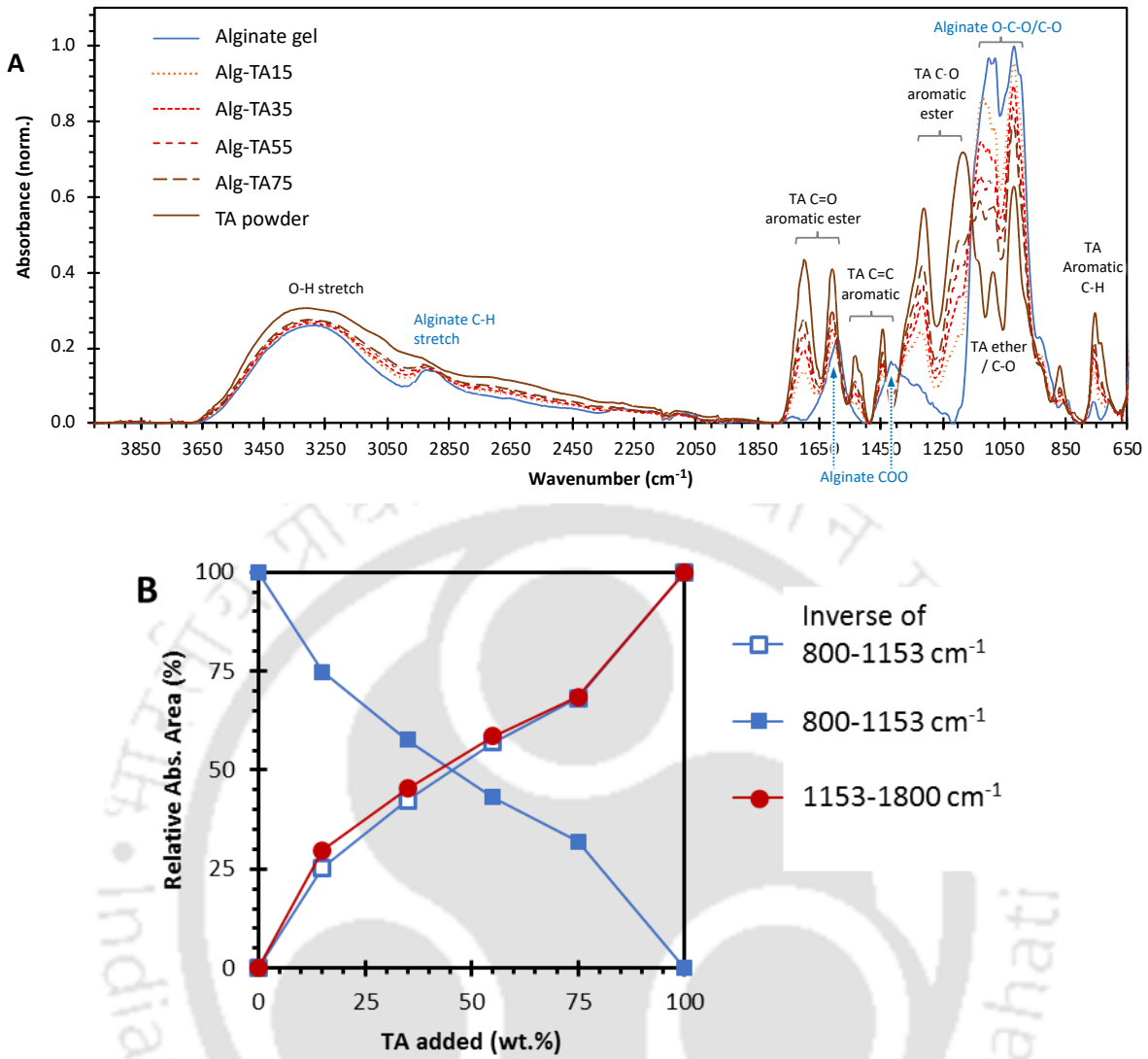

Figure 5.4: (A) FTIR absorbance spectra of Alg gel, TA powder, and Alg-TA with 15, 35, 55, and 75% of TA. (B) Relative absorbance peak area (%) basis variations in wavenumber regions (800-1153 cm^{-1} and 1153-1800 cm^{-1}) of Alg-TA with 0, 15, 35, 55, 75 and 100% of TA.

Figure 5.5 compares the sizes, weights, volumes, and swelling ratio of Alg-TA hydrogel beads. The wet and dry weights of the beads were measured (Figure 5.5(a)) in order to obtain the swelling ratio (Figure 5.5(b)). To obtain higher weighing accuracy, especially for dried beads, 5-10 beads were weighed together, and their averaged weights were reported. Interestingly, while actual TA content on the beads increased with TA addition (Figure 5.3), the wet and dry weights, and hence the swelling ratio, initially remained similar to pure Alg

beads at 15% TA added (Alg-TA-15 beads). With further increases in TA incorporation, the dry weight decreased systematically by more than 10-fold between 15% and 75% TA, but the wet weight remained roughly similar up to 55% TA. Thus, the swelling ratio increased from ca. 20-times for Alg-TA-15 beads (similar to native Alg) to ~70-times for Alg-TA-75.

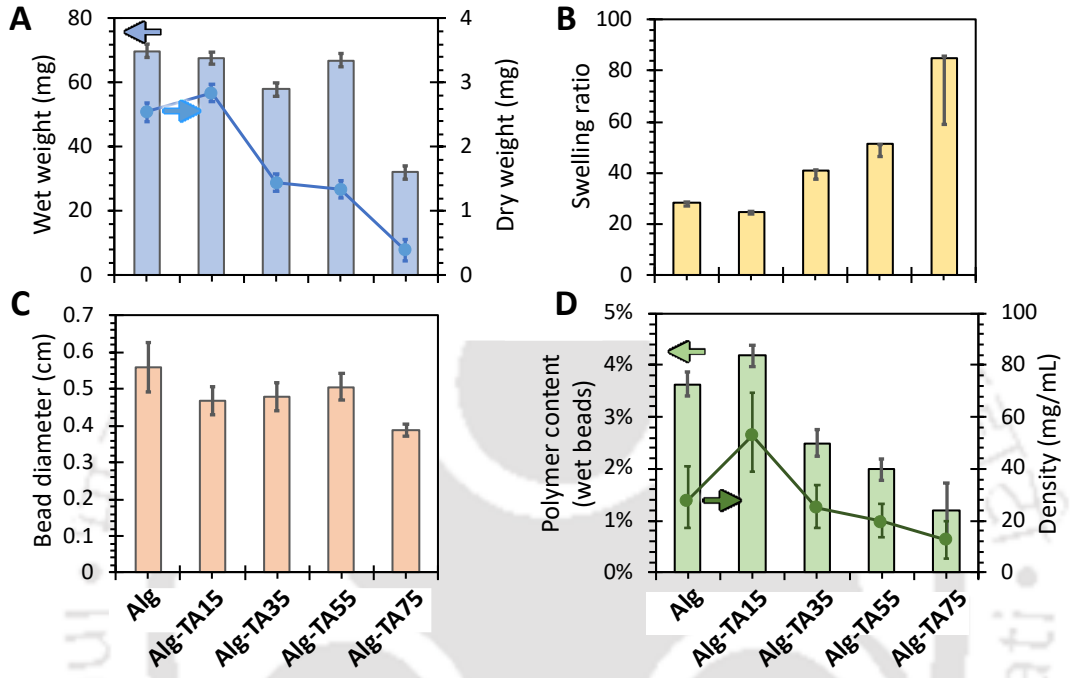

Figure 5.5: (A) Average wet and dry weights of Alg-TA beads with increasing TA content. (B) The average diameters of the same beads measured from image analysis. (C) The weight percentage of Alg+TA material within each bead type calculated from the wet and dry weights. (D) Corresponding swelling ratio of beads of increasing TA content.

At the same time, the size of swollen beads, controlled by the preparation drop volume and the viscosity of the pre-gelation mixture, was roughly similar across Alg-TA-15, Alg-TA-35 and Alg-TA-55 before dropping somewhat for Alg-TA-75 (average diameter ~0.5 cm compared to ~0.4 cm; Figure 5.5(c)). Thus, overall, higher TA incorporation enabled formation of beads of similar sizes with lower polymer densities (Figure 5.5(d)). Since TA molecules are too small to crosslink into a hydrogel themselves (MW < 1711 depending on the number of galloyl groups), [386] our observations indicate the strong ability of TA to bind with alginate

polymer chains, in line with our previous report on the superior binding ability of TA on cellulose, another polysaccharide [387]. Indeed, compressive mechanical testing of wet hydrogel samples further indicated only a ~20% drop in toughness as TA content increased to 75% (Figure 5.6), despite the 4-times reduction of polymer weight content from 4% to 1% (Figure 5.5(d)), and similar elastic moduli for all levels of TA incorporation.

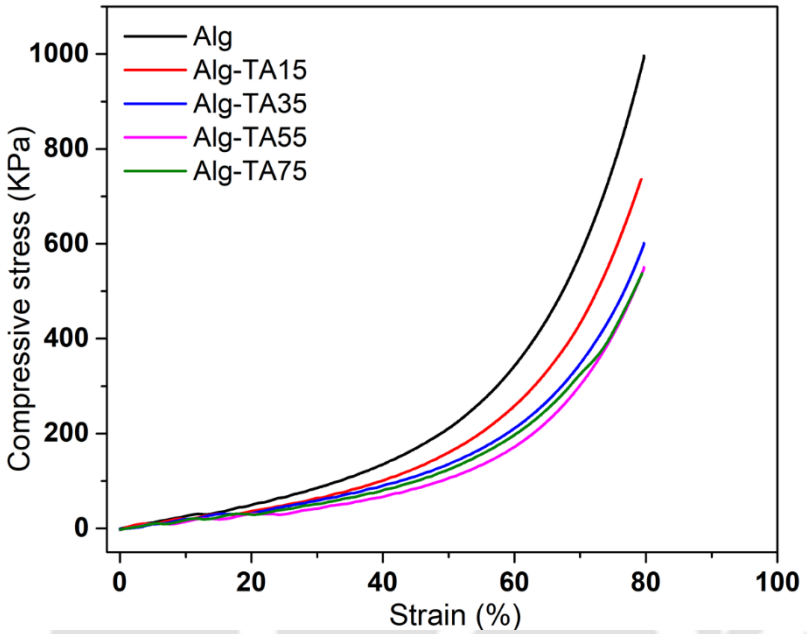

Figure 5.6: Stress versus strain plot of Alg and Alg-TA with 15, 35, 55 and 75% of TA hydrogel samples at a loading rate of 1 mm/min.

5.3.2 Effect of TA incorporation on sorption

The ability of Alg-TA beads to remove some potential toxic heavy metal ion pollutants typically found in contaminated water/wastewater [388, 389] is shown in Figure 5.7. Sorptions of Pb(II), Zn(II), and Fe(III) at an initial ion concentration (C_0) of 50 mg/L (i.e., 50 ppm) and loading of 1 g/L (i.e., 1 g dried beads per liter of solution) were evaluated over pH 2 to 6 (Figures 5.7(a)-5.7(c)) while, as example, sorptions of Cu(II) and Cr(VI) were tested at pH 4 (Figure 5.7(d)). Additional sorption isotherms for the Alg, Alg-TA-35 and Alg-TA-55 beads were measured across a wide range of C_0 = 0.05-500 mg/L at pH 4 and analyzed with Langmuir

(Figure 5.8) and Freundlich fittings (Figure 5.9) for Pb(II), Zn(II), and Cu(II) to further evaluate the adsorption capacity (fitting parameters shown in Tables 5.1(a)-5.1(d)). Higher pH was not tested because of ion precipitation [390]. The chosen C_0 = 50 mg/L, relatively high compared to the safety limits [391-393], was chosen to help highlight the differences between pure alginate and the enhanced Alg-TA beads.

It is clear from Figure 5.7 that the ability of the Alg-TA beads to remove ions increased with increasing TA incorporation under the conditions tested. For example, the Alg-TA 75 beads were able to remove a maximum of 98% Pb(II) at pH 4 (q_e = 49 mg g^{-1}) and 67% Zn(II) at pH 6 (q_e = 38 mg g^{-1}), while amounts of removal by the pure Alg beads were roughly 75% lower at these pH conditions. Moreover, while the pH response of ion removal differed variously depending on the ion type, TA incorporation can nonetheless be seen to improve sorption/removal especially in cases where the performance of the pure alginate beads was poor. For example, the percentage removal for alginate only beads were all below 25% for Pb(II) at pH 6 (Figure 5.7a) and for Zn(II), Fe(III), Cu(II), and Cr(VI) at pH 4 (Figures 5.7(b)-5.7(d)), but the sorption performance at least doubled as TA incorporation increased successively to 75%.

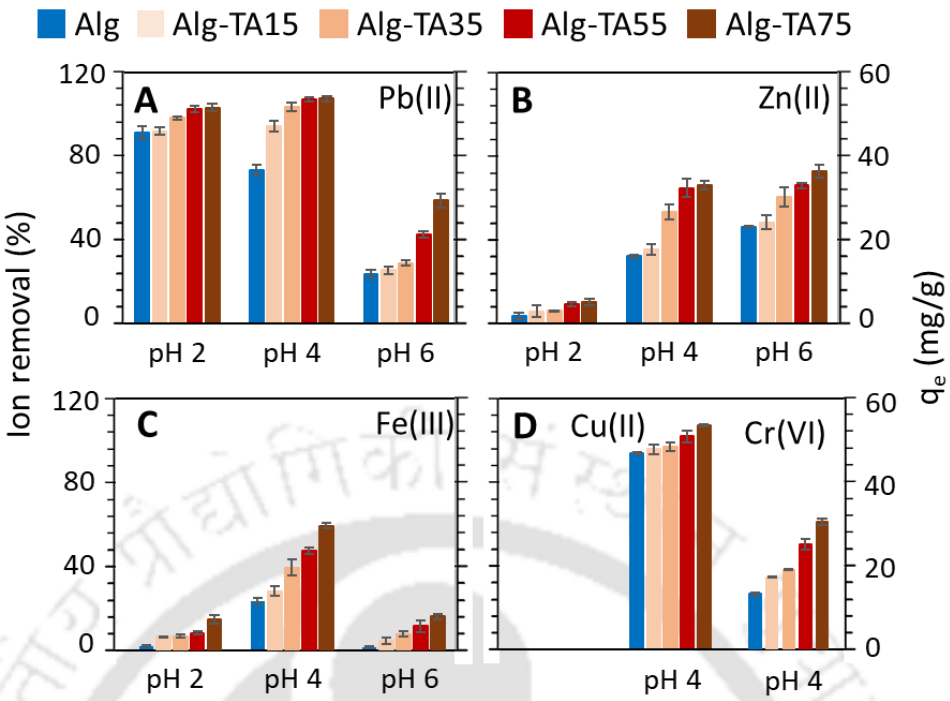

Figure 5.7: Bulk measurements of ion removal from aqueous salt solutions using alginate beads with different levels of TA incorporation. The effect of pH is studied for Pb(II) (A), Zn(II) (B) and Fe(III) (C) sorption from an initial ion concentration of 20 mg/L (i.e., 20 ppm). (D) Corresponding measurements at pH 4 for Cu(II) and Cr(VI). Additional measurements at higher initial ion concentrations and corresponding model fittings are shown in Figures 5.8 and 5.9.

The enhancement of metal binding with increasing TA incorporation is expected from the various natural functions of polyphenols, e.g., binding of cations as ion nutrients and to enable antioxidant properties involving metal ion redox chemistry [394-396] which can be active even at the acidic pH range of our measurements [397, 398]. The mannuronic and guluronic acids of alginate have pKa's of 3.4 and 3.7, respectively, [399] and hence, the polysaccharide component of the Alg-TA hydrogel should be uncharged at pH 2 and increasingly negatively charged above pH ~3. TA is chemically complex (pK_a ~ 6 - 8.5) but is expected to be largely uncharged under our conditions, as half-dissociation is expected only at pH 7.8 [400]. In the case of Zn(II), therefore, electrostatic interactions driven by alginate could

have contributed to the overall increase in sorption as pH increased from pH 2 to 6. On the other hand, the decrease in overall sorption for Pb(II) and Fe(III) as pH increased from pH 4 to 6 may be due to other properties of these cations (e.g., the low solubility of Fe(III) above pH 4 may have interfered with the results) [401].

Sorption isotherm measurements show that the amounts of ions removed (q_e) by Alg-TA-55 beads at the highest C_0 tested (500 mg/L) was ca. 340 mg g^{-1} for Pb(II), 120 mg g^{-1} for Zn(II), and 165 mg g^{-1} for Cu(II) (Figure 5.8). At the same time, although Langmuir fittings for Pb(II) and Zn(II) appear to be reasonable fits (Figures 5.8(b) and 5.8(d)), it is clear from the trends of the raw data (Figures 5.8(a) and 5.8(c)), that the sorption capacities of the hydrogels have not been reached, as the amounts of ions removed (q_e) are still increasing rapidly with the equilibrium concentration of ions remaining in the solutions (C_e). The Cu(II) data could be well fitted by Langmuir isotherms (Figures 5.8(e) and 5.8(f)), potentially supporting the model's single molecular adsorption per interaction site mechanism, [196] and the fitted Q_m are 143 mg/g, 164 mg/g and 167 mg/g for the Alg, Alg-TA-35 and Alg-TA-55 samples, respectively (Table 5.1).

For Pb(II) and Zn(II), the empirical Freundlich fitting could be reasonably applied to describe the data at lower and higher C_0 regimes separately (fittings for higher q_e and C_e shown in Figure 5.8). While the Zn(II) data show very similar behavior between Alg and the Alg-TA beads, the large enhancements for Pb(II) removal shown by Alg-TA beads could be consistent with multilayer adsorption or the presence of interaction sites with heterogeneous affinities that can be fitted by Freundlich isotherms [196, 402]. Overall, our results demonstrate sorption/removal across a larger panel of ions than previously reported for these Alg-TA hydrogels conveniently prepared entirely from all natural biomolecules, and we show that the removal performance of these materials to at least match the properties of various previously reported synthetic adsorbents [402-404].

Table 5.1: Fitted parameters (A) Q_m and (C) Langmuir constant (K_L) for Langmuir and (B) adsorption intensity (n) and (D) Freundlich constant (K_F) for Freundlich adsorption isotherm models for metal(s) ion (Pb(II), Zn(II) and Cu(II)) adsorption onto Alg and Alg-TA with 35 and 55% of TA, respectively.

A

Fitted Q_m (mg g^{-1})	Alg	Alg-TA35	Alg-TA55
Pb(II)	322.58	322.60	333.33
Zn(II)	370.37	277.77	200
Cu(II)	142.85	163.93	166.66

B

Fitted $^1/_n$	Alg	Alg-TA35	Alg-TA55
Pb(II)	0.28	0.20	0.19
Zn(II)	0.63	0.49	0.44
Cu(II)	0.32	0.28	0.27

C

Fitted $K_L \times 10^{-3}$ (L mg^{-1})	Alg	Alg-TA35	Alg-TA55
Pb(II)	8.85	48.66	142.18
Zn(II)	1.10	1.87	3.60
Cu(II)	30.81	21.73	89.55

D

Fitted K_F (mg g^{-1})(mg L^{-1})$^{1/n}$	Alg	Alg-TA35	Alg-TA55
Pb(II)	47	100	121
Zn(II)	2.5	5.9	8.0
Cu(II)	23	28	35

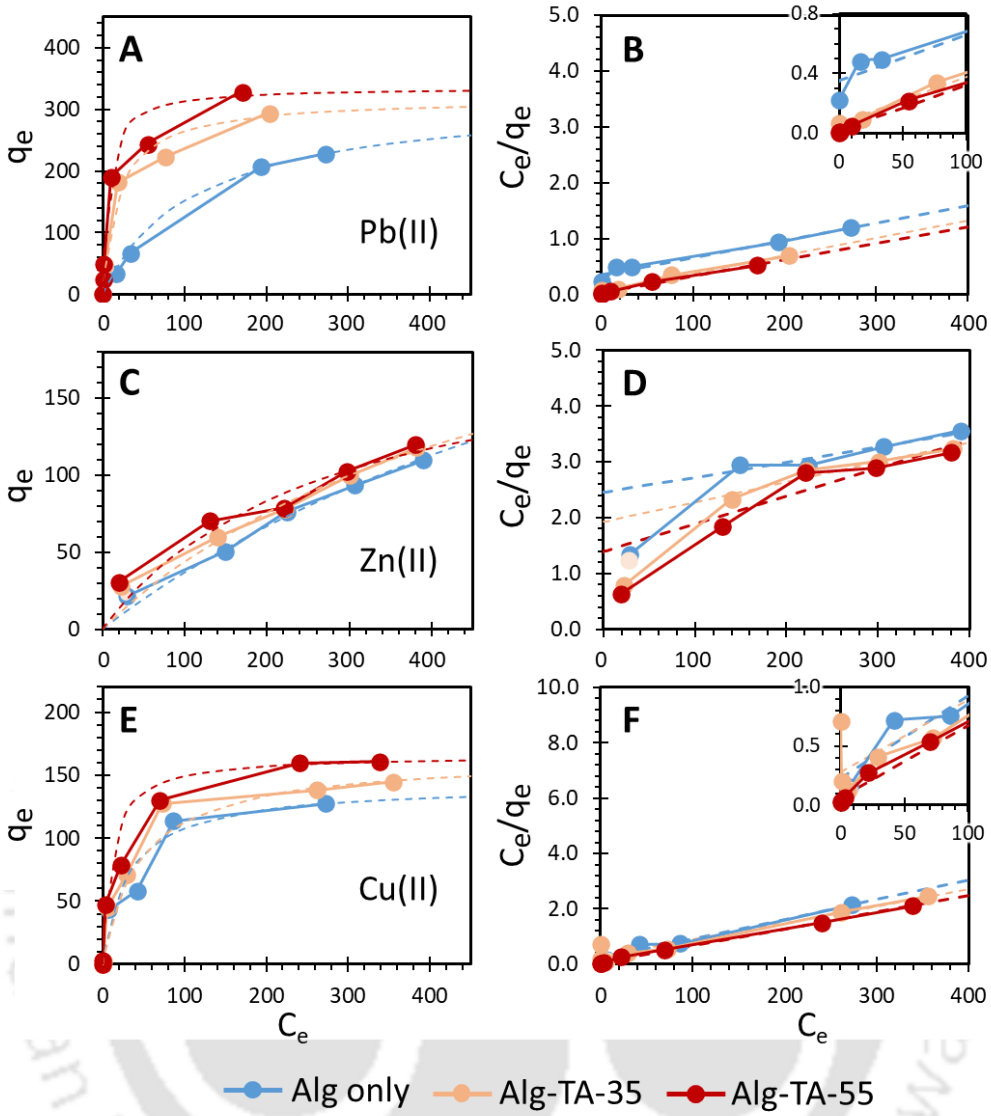

Figure 5.8: Raw data and Langmuir isotherm fitted plot for the adsorption of (A) and (B) Pb(II), (C) and (D) Zn(II), (E) and (F) Cu(II) through synthesized Alg only and Alg-TA with 35 and 55% of TA beads, respectively.

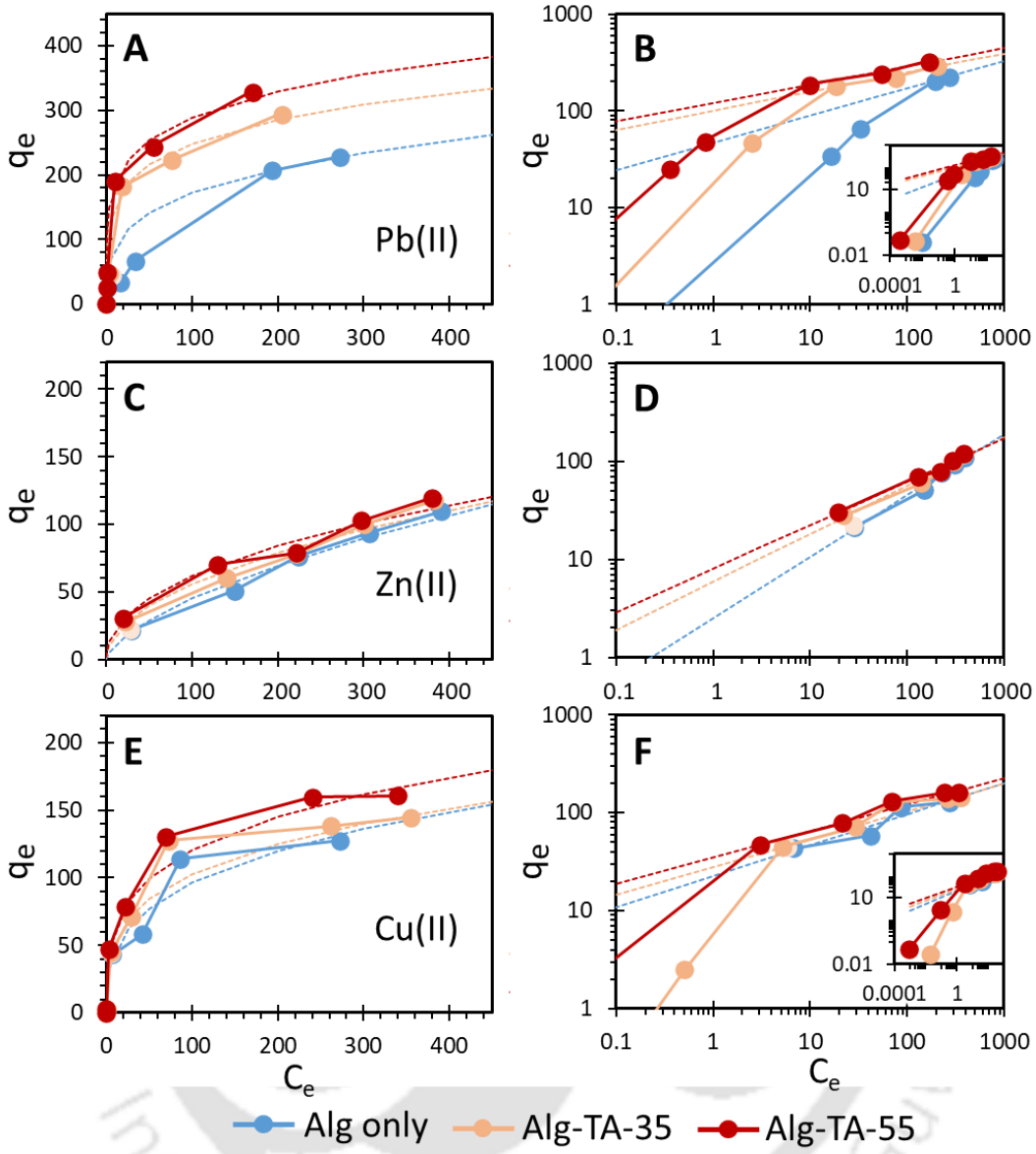

Figure 5.9: Raw data and Freundlich isotherm fitted plot for the adsorption of (A) and (B) Pb(II), (C) and (D) Zn(II), (E) and (F) Cu(II) through synthesized Alg only and Alg-TA with 35 and 75% of TA beads, respectively.

5.3.3 Characterization of Alg-TA-Fe beads

In previous chapters 3 and 4, it was indicated that IONPs synthesized by raw plant part extract were effective in the adsorption of Cr(VI). Moreover, as introduced earlier, TA has an intrinsic antimicrobial effect. Therefore, given the present results demonstrating significantly

more Fe ion sorption by Alg-TA than pure alginate gel beads (Figure 5.6(c)), we were motivated to investigate the potential synergy in Cr(VI) sorption and antimicrobial activity by combining Fe and TA within an alginate hydrogel system.

To maximize the potential effect, we prepared Fe incorporated Alg-TA beads (i.e., Alg-TA-Fe beads) using a high concentration of Fe ions (100 mM $FeCl_3$; see section 5.2.2) far in excess of the acid and galloyl groups present in the hydrogel. While pure alginate beads also incubated in the $FeCl_3$ preparation solution as controls appear indistinguishable from beads without Fe (Figure 5.10(a)), all our Alg-TA beads with TA compositions from 15% to 75% quickly turned a deep black in color after a short incubation (<30 min) (resulting beads designated as Alg-TA15-Fe through Alg-TA75-Fe) (Figure 5.10(b)). Thus, there is a clear change induced by the chemistry of the TA. Cross sections and outer surfaces of very large samples prepared also show a homogenous black coloration (Figures 5.10(c) and 5.10(d)), suggesting that the process responsible for the color change had initiated homogeneously throughout the Alg-TA hydrogel matrix and the colorant likely did not have to be transported/diffused into the gels.

To gain a better chemical understanding, we performed SEM EDS and XPS analysis on the Alg-TA55-Fe and Alg-Fe beads as examples. A black coloration could potentially be the absorption of Fe complexes or an optical scattering effect of Fe or IONP formation induced by TA, a polyphenol. SEM imaging with EDS mapping showed that both the interior and exterior of the gels appeared morphologically similar (Figures 5.10(e) and 5.10(f)), with some sparsely distributed microscale particulates as well as 20-200 nm nanoparticle features. Although the spatial resolution of our EDS analysis (~3 μm for the 15 keV electron beam used) was not high enough to directly characterize the NPs, the elemental mapping indicated a relatively uniform distribution of Fe and O elements across both the exterior surface (Figure 5.10(e)) and cross-sectional interior of the beads (Figure 5.11). Therefore, the larger micro-

features do not appear to be salt or Fe deposits, and there are too few nanostructures to explain the homogeneity of the Fe or O content. Thus, the Fe present could be directly coordinated with the alginate acid or TA galloyl groups, or any Fe or IONPs formed would be smaller than the resolution limit of our SEM imaging (<20 nm).

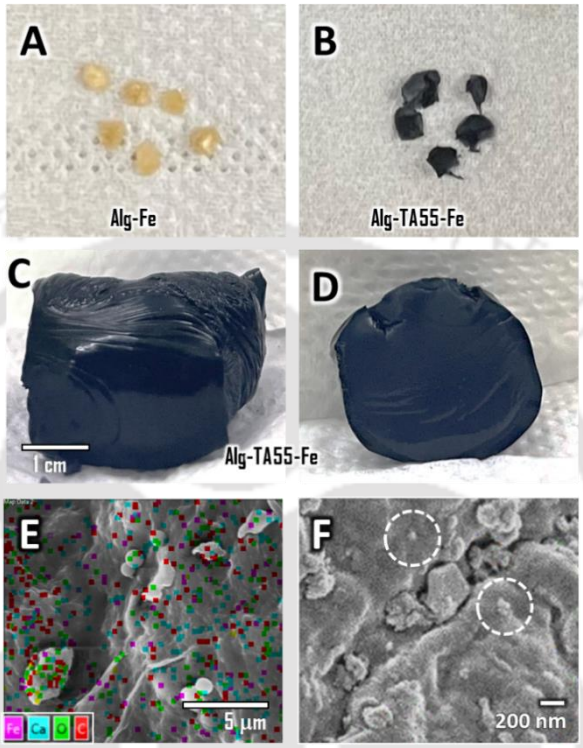

Figure 5.10: Alg-Fe beads (A) have no special coloration. The Alg-TA55-Fe bead is dramatically darkened (B), as are Alg-TA-Fe samples at all other levels of TA incorporated. The darkening is uniform on both the external surface (C) and across a cut section (D) even for large-sized samples. SEM-EDS characterization of Alg-TA55-Fe (E) shows the Fe content (purple overlay) is relatively uniform regardless of surface features, same as for other elements detected. Higher resolution FE-SEM imaging (F) of a Alg-TA55-Fe bead cross-section suggests a distribution of NPs within the hydrogel after Fe sorption (two NPs-like features highlighted as examples).

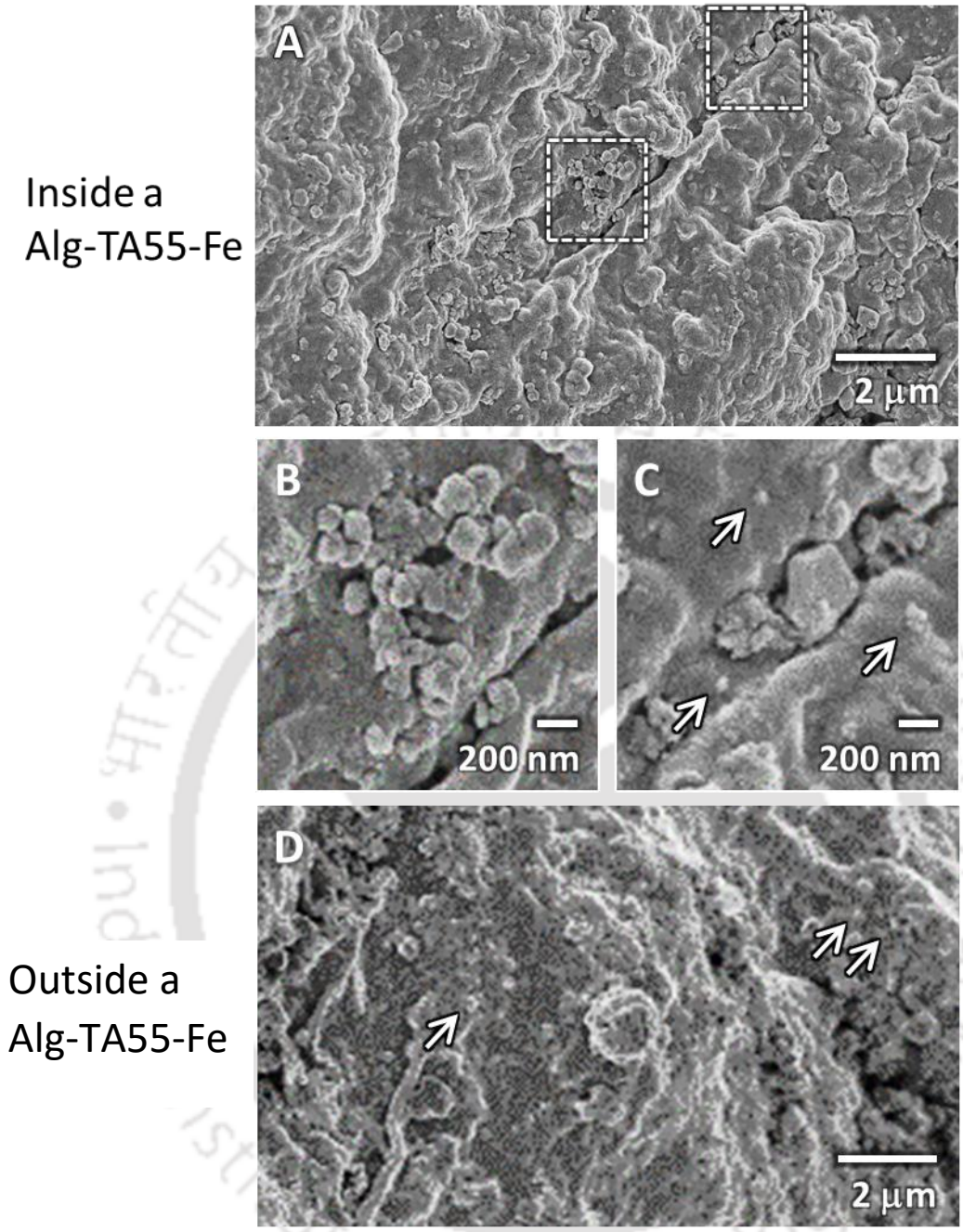

Figure 5.11: FESEM micrographs of Alg-TA55-Fe bead inside/cross-section (A) and zoomed-in views (B and C), as well as a micrograph of the external surface (D).

EDS analysis of Fe elemental composition had large uncertainties because of corresponding uncertainties in the amounts of C, O and Ca determined due to overlapping X-ray lines (Figure 5.12). XPS survey scans also produced relatively small Fe peaks sometimes near the background (Figure 5.13). On the other hand, well resolved Fe2p peaks and their

chemical shifts were measured in high resolution scans of both the Alg-Fe and Alg-TA55-Fe samples, with Alg-TA55-Fe exhibiting a roughly 3 times higher intensity (Figure 5.14a). Therefore, the highly visible change in coloration (Figures 5.10(a) and 5.10(b)) of Alg-TA-Fe samples but not for Alg-Fe could be due to a significant chemical change induced by TA. Peak fitting differentiated at least 3 sets of chemical shifted peaks in both samples. Notwithstanding the difference in peak intensities (i.e., 3-times higher Fe incorporated in Alg-TA55-Fe), the main difference between the samples is a clear peak component at a chemical shift of 706.6 eV with TA present that accounts for ca. 20% of the Fe present (Figure 5.14(b)).

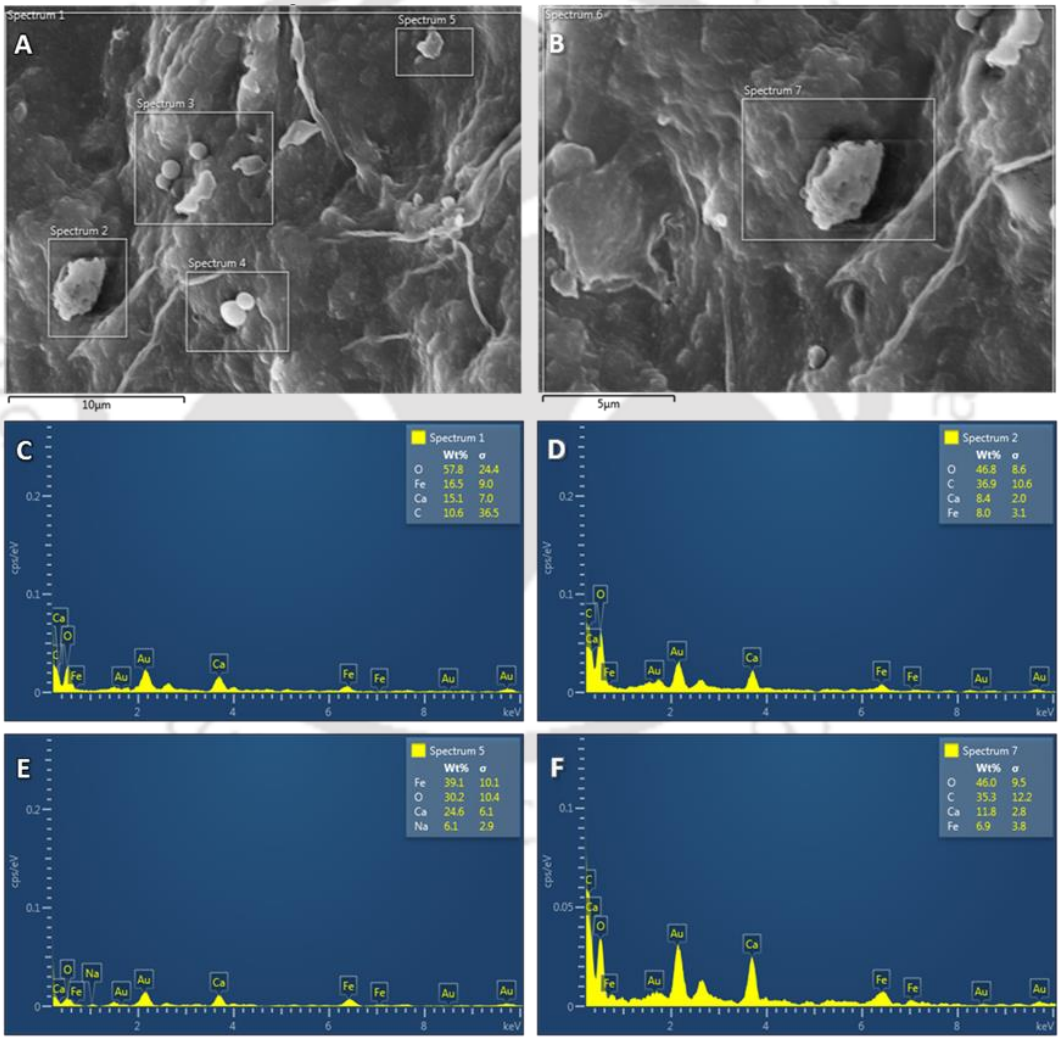

Figure 5.12: SEM-EDS of cutted Alg-TA55-Fe bead (A) micrograph, (C), (D) and (E) spectrums at lower scale (10 µm), and (B) micrograph and (F) spectra at higher scale (5 µm), respectively.

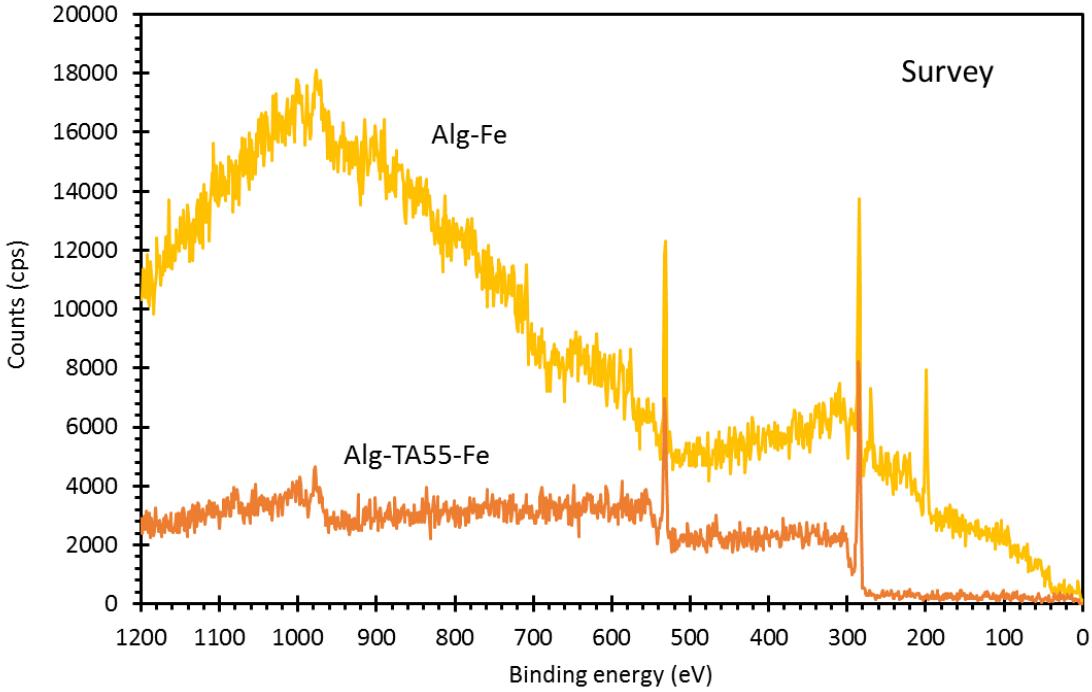

Figure 5.13: XPS survey spectra's of Alg-Fe and Alg-TA55-Fe beads.

This relatively low BE corresponds to metallic Fe(0), and would be consistent with the well-known ability of polyphenols to reduce metal salts [405, 406]. The Fe(0) component of the Alg-Fe sample is small and could simply be fluctuations in the background. We can further distinguish this Fe(0) material from a peak component with a chemical shift of ~708.5 eV consistent with coordination to organic groups [407] (e.g., alginic acids or TA phenols) (Figure 5.14b), accounting for ~50% and ~70% of Fe content in the Alg-TA55-Fe and Alg-Fe samples, respectively. The remaining peak component at ~711.1 eV for both samples is consistent with either Fe_2O_3 (e.g., oxidized from Fe(0)) or $FeCl_3$ (e.g., unwashed salts from sample preparation). These assignments and fitted intensities are further corroborated by chemical shifts in O1s and C1s chemical shift analyses corresponding to acid and galloyl group Fe coordination or salts (Figures 5.15 and 5.16). Thus, the alginic acid component in both samples with and without TA likely was responsible for a majority of Fe uptake (at the high Fe^{3+} concentration used for preparing samples), while the TA component apparently was able to produce Fe(0) possibly in the form of NPs, some of which could be oxidized to Fe_2O_3.

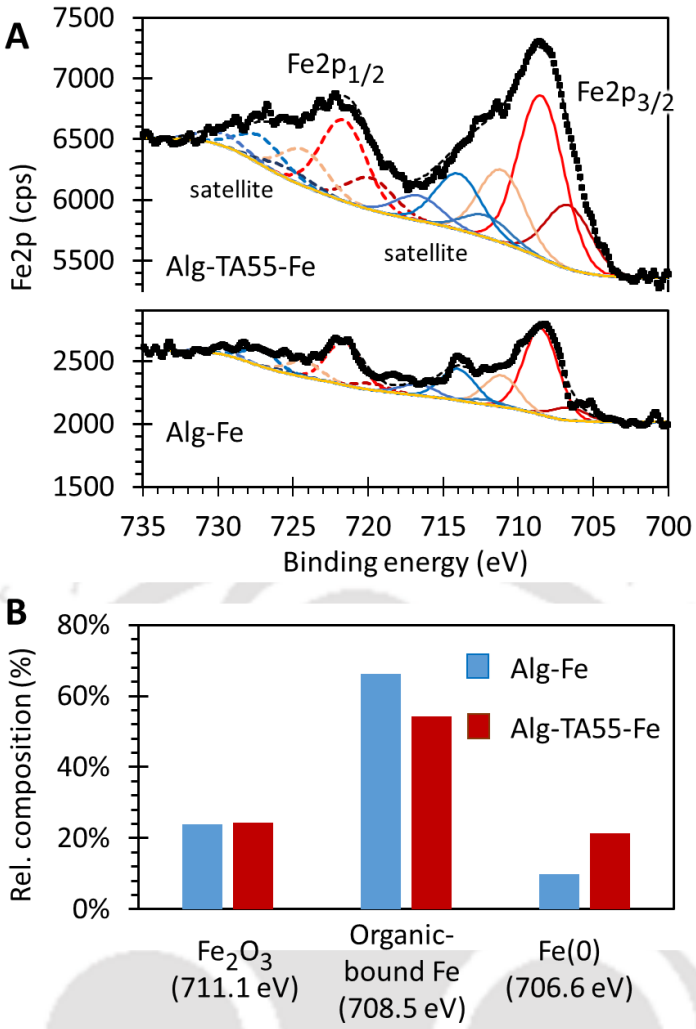

Figure 5.14: (A) XPS Fe2p spectra of Alg-Fe and Alg-TA55-Fe samples. The fitted binding energies (BEs) of the assigned principal $Fe2p_{3/2}$ peak components and their relative intensities/compositions are shown in (B). The BEs and areas of all peak components are shown in Table 5.2.

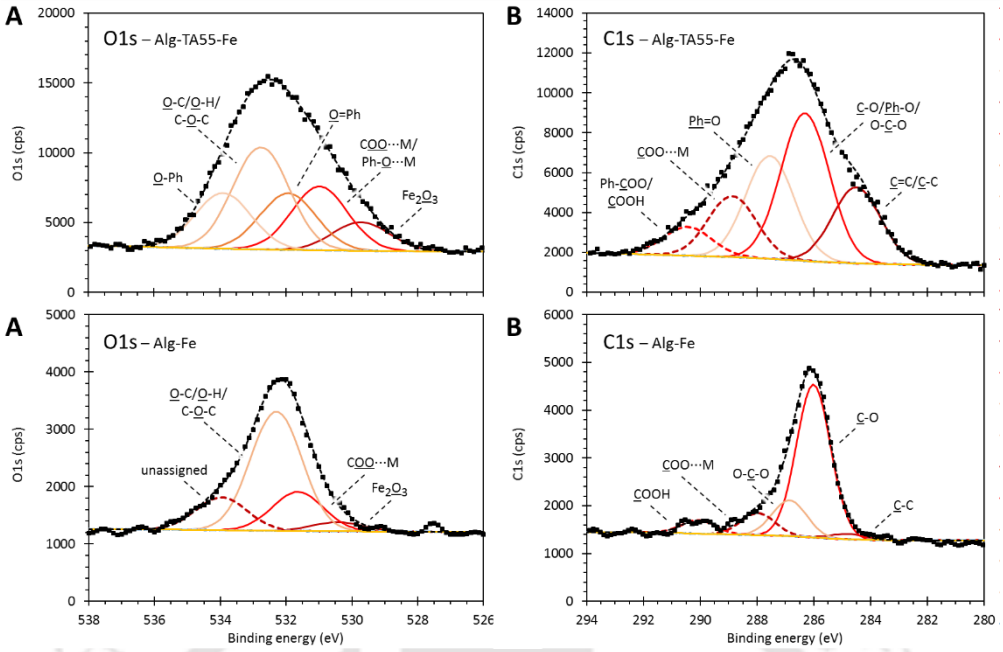

Figure 5.15: XPS high resolution spectra's (A) O1s and (B) C1s of Alg-TA55-Fe and Alg-Fe beads, respectively.

Table 5.2: Enlisted various Fe species binding energy (eV) and their corresponding areas (eV-cps) as revealed from deconvoluted XPS Fe2p high resolution spectra's of Alg-Fe and Alg-TA55-Fe beads, respectively.

Fitted Fe2p binding energy (BE/eV)	Fe[0] ($2p_{3/2}$)	Fe..COO^- or Fe..O-Ph ($2p_{3/2}$)	Fe_2O_3 ($2p_{3/2}$)	Fe[0] ($2p_{1/2}$)	Fe..COO- ($2p_{1/2}$)	Fe_2O_3 ($2p_{1/2}$)
Alg-Fe	706.6	708.5	711.1	719.7	721.6	724.3
Alg-TA55-Fe	706.7	708.5	711.1	719.8	721.6	724.3

Fitted Fe2p area (eV-cps)	Fe[0] ($2p_{3/2}$)	Fe..COO- ($2p_{3/2}$)	Fe_2O_3 ($2p_{3/2}$)	Fe[0] ($2p_{1/2}$)	Fe..COO- ($2p_{1/2}$)	Fe_2O_3 ($2p_{1/2}$)
Alg-Fe	293	1974	712	147	987	356
Alg-TA55-Fe	1987	5068	2268	994	2534	1134

Additional fitting characteristics	FWHM (eV)	Satellite FWHM (eV)	Satellite BE distance (eV)	$2p_{3/2}$ to satellite intensity ratio
Alg-Fe	3.9	4.0	5.5	3.1
Alg-TA55-Fe	2.6	2.8	5.5	2.8

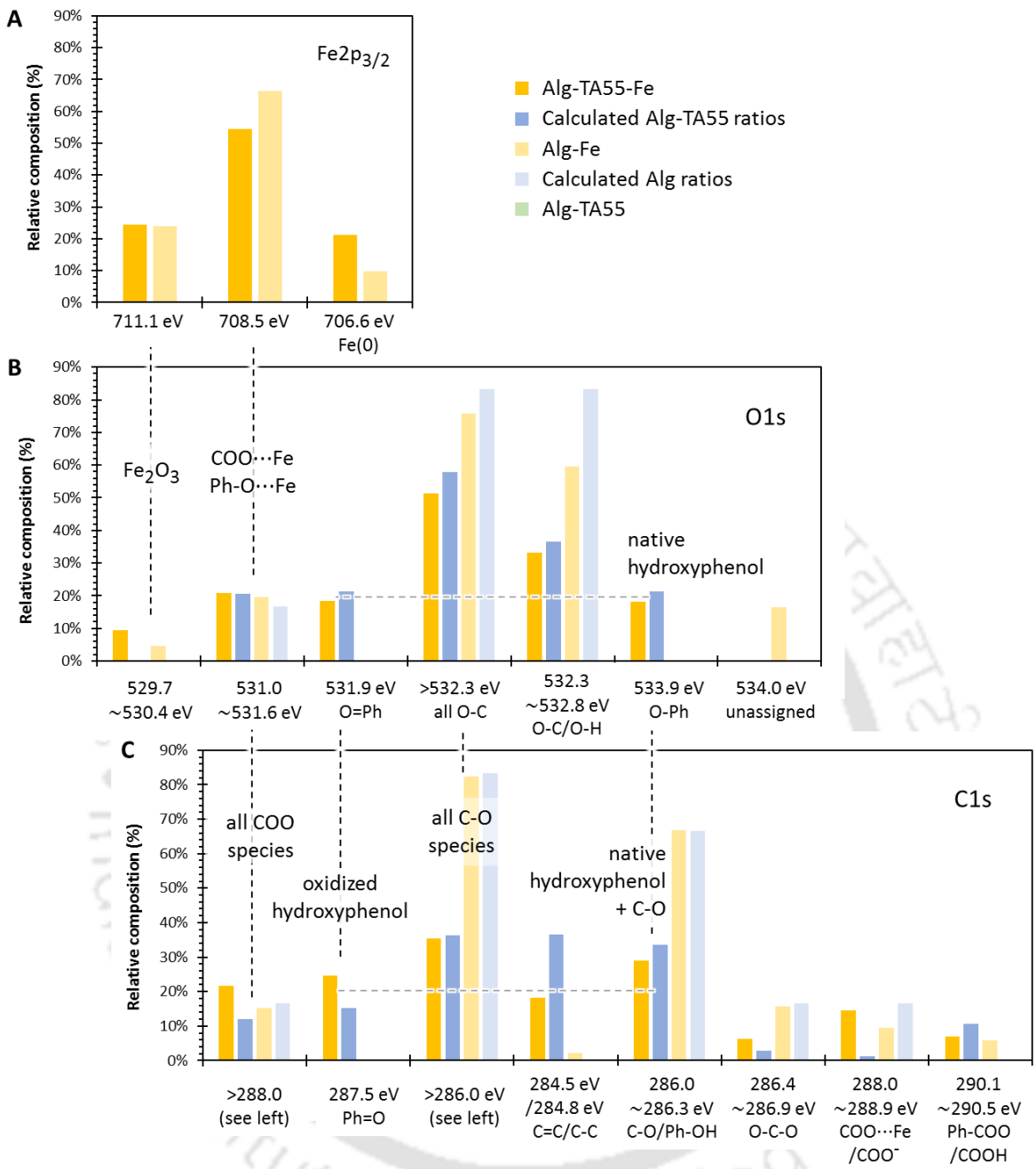

Figure 5.16: Calculated relative elemental composition in % from high resolution spectra's (A) $Fe2p_{3/2}$, (B) O1s and (C) C1s of Alg-TA55-Fe bead.

5.3.4 Adsorption of Cr(VI) by Alg-TA-Fe Beads

We characterized the removal of hexavalent chromium Cr(VI) by the Alg-TA-Fe beads (Figure 5.17) following the same procedures as earlier experiments using Alg-TA beads without Fe (Figure 5.7). Cr(VI) solutions could be prepared without precipitation over pH 2 to

8 under our conditions, and we performed our sorption measurements over this range. A dramatic increase in Cr(VI) removal can be observed using beads incorporating both TA and Fe, with roughly 3-times higher sorption for Alg-TA-Fe vs. Alg-Fe beads in the main experiments using 1 g/L beads in Cr(VI) solution, while the effect of pH is relatively small (Figure 5.17(a)). For example, at pH 4, removal using Alg-Fe was only ~30%, compared with 82~94% sorption for the entire range of Alg-TA15-Fe to Alg-TA75-Fe beads, with sorption increasing systematically with the amount of TA added. The data for other pH measurements were similar.

The large jump in sorption from the Alg-Fe to Alg-TA15-Fe beads and the systematic increase as more TA is added both indicate a fundamentally different mechanism of Cr(VI) binding induced by the TA incorporated. Given the significant increase in actual TA incorporated with increasing amounts of TA added to the bead preparation (Figure 5.3), the small corresponding increase in Cr(VI) sorption may indicate that most of the additional TA is bound with the alginate or has formed crosslinked polyphenol components that do not exhibit free trihydroxyl phenol groups for Fe or Cr(VI) binding. The 3-times higher Cr(VI) sorption with TA addition is incidentally similar to the increase of Fe incorporation from the Alg-Fe to the Alg-TA55-Fe bead as characterized by XPS (Figure 5.14). Moreover, our earlier data using Alg-TA beads without Fe^{3+} incorporation produced only roughly half as much Cr(VI) sorption (e.g., only 51.5 % removal using Alg-TA75 at pH 4, Figure 5.6(d)). Therefore, the Cr(VI) sorption enhancement is not directly due to ion binding to TA but is a result of Cr(VI) binding to the material produced by TA-induced Fe incorporation, i.e., a synergistic effect.

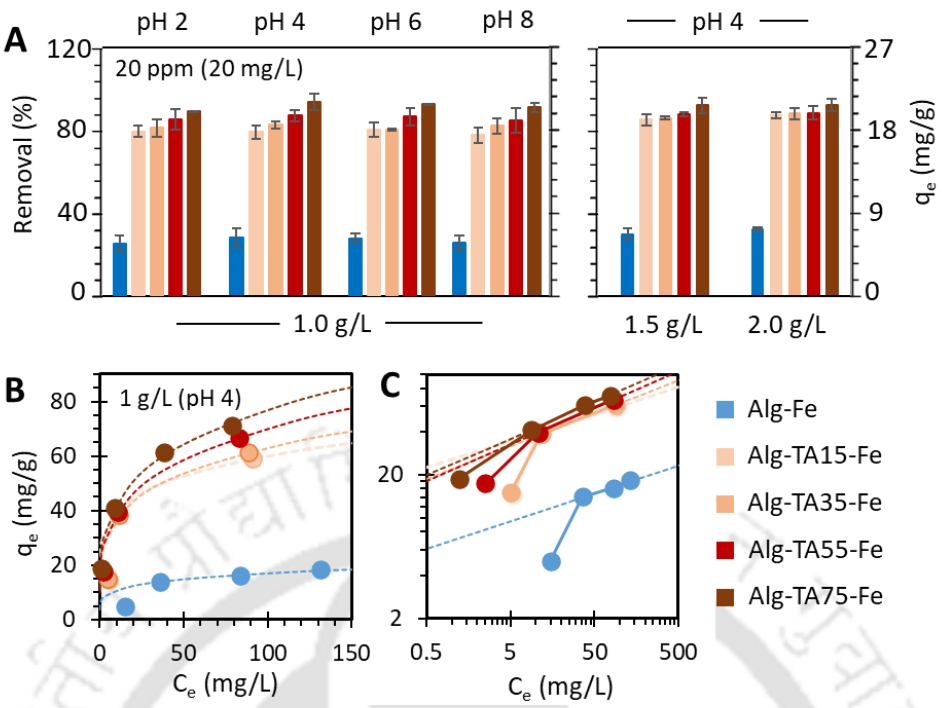

Figure 5.17: (A) Percentages of Cr(VI) ion removal using 1 g of Fe-incorporated Alg-TA beads with 15-75% TA content per liter of 20 mg/L aqueous solution (i.e., 1 g/L loading), at a pH ranging from 2 to 8. Measurements at high 1.5 g/L and 2 g/L loading were also made for comparison. (B) Additional measurements made at higher initial Cr(VI) concentrations up to 150 mg/L plotted with Freundlich isotherm fitting. (C) Corresponding log-log plot of the data shown in (B). Langmuir and Freundlich isotherm fittings are shown in Figure 5.18. Freundlich parameters are shown in Tables 5.3.

We further investigated Cr(VI) removal at higher bead loadings and at various Cr(VI) concentrations to obtain the sorption isotherms (Figures 5.17(a)-right, 5.17(b) and 5.17(c)). As the bead concentration doubled from the previous 1 g/L to 2 g/L, the amount of Cr(VI) removal (at pH 4) was observed to increase more at lower TA contents (e.g., for Alg-TA15-Fe, removal increased from ~82% to ~90%, while for Alg-TA75-Fe beads, removal increased only from ~94% to ~95%). Overall, however, the lack of complete removal indicated that Cr(VI) sorption was limited by simultaneous ion desorption (i.e., an equilibrium effect). Along these lines, the sorption isotherms measured indicated that the beads could take up additional Cr(VI) as its

concentration increased from 20 mg/L to 150 mg/L and beyond (Figure 5.17(b)). Fitting of the data also indicates a slightly higher slope for TA-incorporated beads (Figure 5.17(c) and Table 5.3), corroborating the possibility of a different mode of Cr(VI) sorption on hydrogels with Fe(0) captured (see previous section). Additional FESEM imaging (Figure 5.19) did not reveal any obvious difference in surface (inside and outside) of Alg-TA75-Fe beads after Cr(VI) adsorption, indicating that the mechanism was molecular or at least nanoscale.

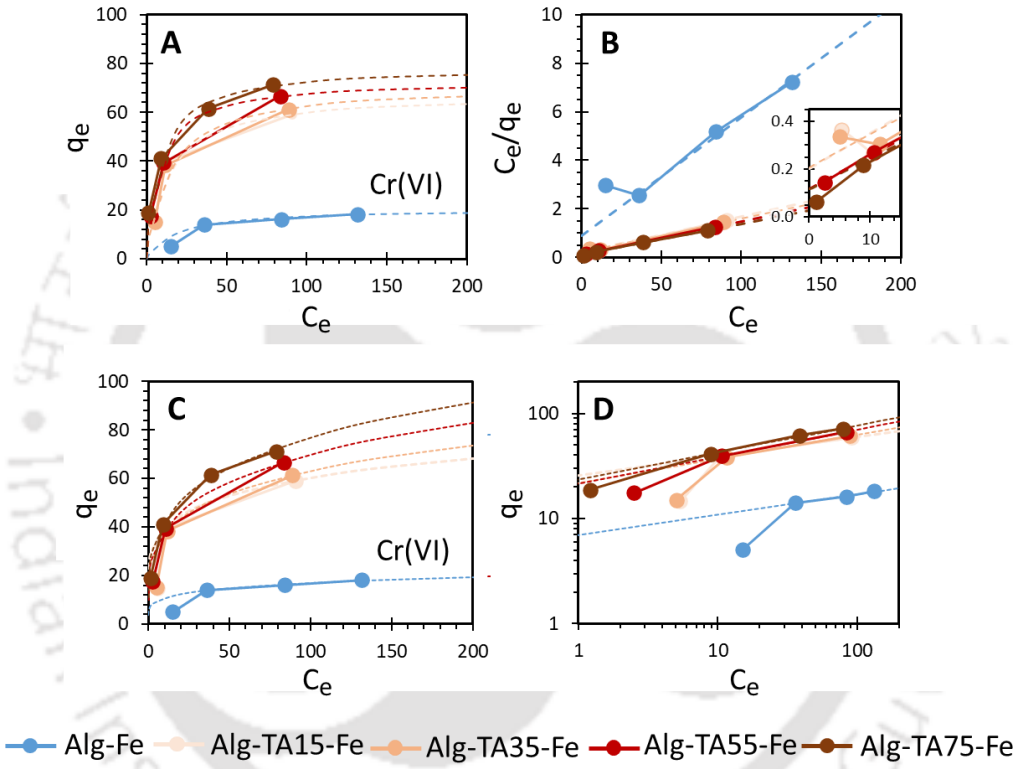

Figure 5.18: (A) and (C) Raw data, (B) Langmuir and (D) Freundlich isotherm for Cr(VI) adsorption through synthesized Alg-Fe and Alg-TA-Fe with 15, 35, 55 and 75% of TA, respectively.

Table 5.3: Langmuir and Freundlich isotherms fitted model parameters of Alg-Fe and Alg-TA-Fe with 15, 35, 55 and 75% of TA, respectively for Cr(VI) adsorption.

Cr(VI)	Alg-Fe	Alg-TA15-Fe	Alg-TA35-Fe	Alg-TA55-Fe	Alg-TA75-Fe
Fitted Q_m (mg g^{-1})	20.51	68.21	71.67	73.42	78.86
Fitted K_L (L mg^{-1})	0.054	0.072	0.067	0.116	0.109

Fitted K_F ((mg g^{-1}) (mg L^{-1})$^{1/n}$)	7.0	25.5	21.8	21.5	23.7
Fitted 1/n	0.19	0.19	0.23	0.26	0.26

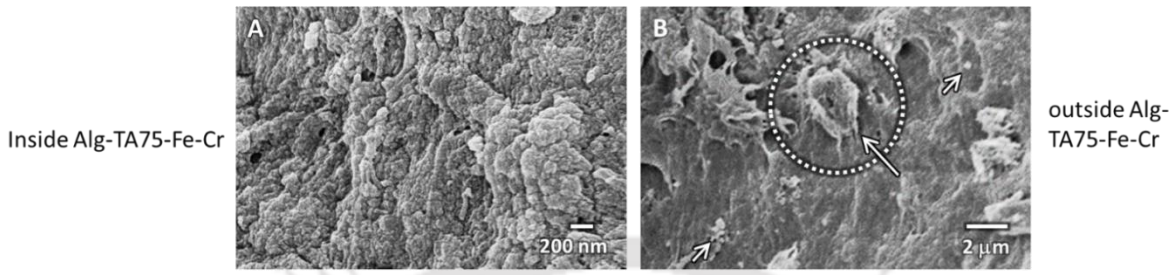

Figure 5.19: FESEM micrographs of Alg-TA75-Fe bead cross-section (A) and external surface (B) after Cr(VI) adsorption.

5.3.5 Enhancements of antibacterial activity by TA and Fe incorporation

We investigated the antibacterial activity of our Alg-TA-Fe hydrogel beads because water treatment materials possessing antimicrobial activity are advantageous in extending their convenient storage and enabling their use over extended durations, especially in the case of contaminated water sources already laden with bacteria, e.g., domestic wastewater. Biofouling of the material may potentially not only alter its performance and become a health and safety concern, but it may also lead to secondary fouling of nearby equipment surfaces and cause further problems downstream [408]. The fouling of membranes utilized for water filtration processes includes organic/inorganic/biofouling/colloidal fouling issues that affect the overall efficiency of its practical applicability. Biofouling is of significant concern as it accounts for more than 45% of all fouling issues mentioned [409]. This may especially be an issue for naturally derived materials that may potentially be a nutrient for microbes [410, 411]. Following established protocols, we evaluated both the zone of inhibition (ZOI) due to the surface contact of our beads on agar culture plates and the inhibition of bacterial growth in

cultures incubated with our beads. Pathogens typically occurring in environmental waters, i.e. *E. coli* and *E. hirea*, were chosen to evaluate the antibacterial activity of the synthesized beads.

Figure 5.20(a) visually shows the results of our ZOI measurements and compares the effects of bead samples with and without TA (data of Alg compared with Alg-TA35 and Alg-TA55 as examples), as well as compares the further effect of incorporating Fe. The quantitative ZOI measured for all samples tested, from Alg-TA15 to Alg-TA55 without Fe, and from Alg-TA15 to Alg-TA75, are further plotted in Figures 5.20(b) and 5.20(c). From the images shown (Figure 5.20(a)), it is clear that the pure alginate gel has no antimicrobial effect. In fact, alginate gels have been used as an inoculant carrier of bacteria [411]. In comparison, ZOIs can be observed around both the Alg-TA35 and Alg-TA55 beads placed on agar plates inoculated with *E.coli* and *E.hirea* (i.e., darkened areas around the beads at the center of the images; a ring outlining the ZOI may or may not be obvious depending on lighting conditions). TA is a well-known natural antimicrobial, [412] and Figure 5.20b further illustrates this effect by showing an extension of the ZOI from roughly 4 mm to 5.5 mm, with the ZOI being 0.5 to 1 mm longer for *E.coli* than for *E.hirea*, as the TA content increases from Alg-TA15 to Alg-TA55.

When Fe is incorporated, there is a moderate extension of the ZOIs at corresponding levels of TA, with the ZOI extending from roughly 4.5 mm for Alg-TA15-Fe to 6.5 mm for Alg-TA55-Fe (Figure 5.20(c)). Moreover, the ZOI further extends to roughly 7.5 mm at the highest TA content (Alg-TA75-Fe), and Alg-Fe beads were also observed to induce a ZOI, although this was smaller than for the Alg-TA15-Fe beads. Recent reports indicate that iron coatings, as well as IONPs, may exhibit an antibacterial effect, with various antimicrobial mechanisms being proposed or investigated, such as a reduction of bacterial membrane integrity by Fe ions that can enhance antimicrobial uptake and the generation of reactive oxygen species from the excited electrons of Fe NPs, which further causes oxidative stress and damages the DNA [413-415]. While the exact antimicrobial mechanism of Fe ions is still under

investigation, our present ZOI results imply that biofouling of the Alg-TA and Alg-TA-Fe beads themselves is unlikely and that our materials actually release TA and Fe ions as active antimicrobial species. This may confer additional anti-biofouling effects in a water treatment system, which we investigate in our bacterial culture studies.

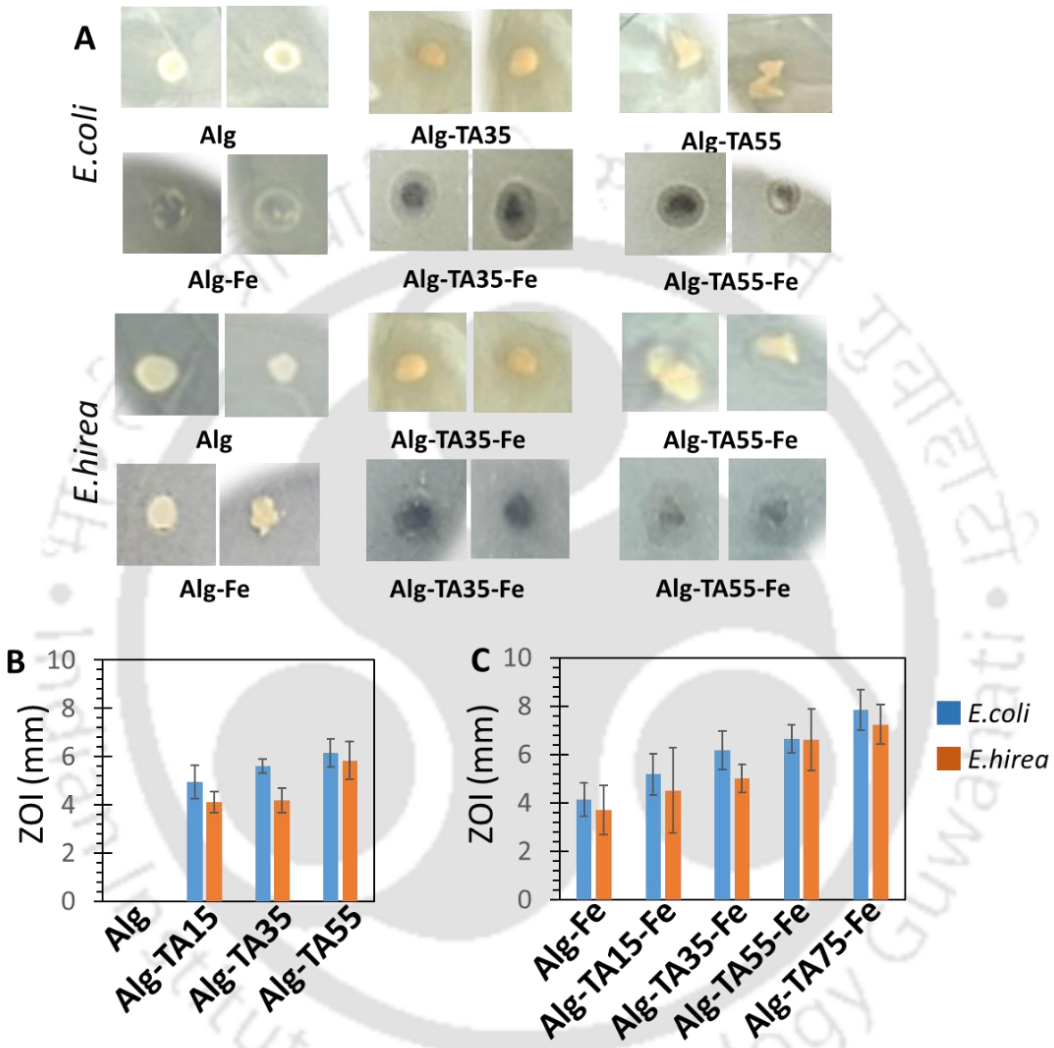

Figure 5.20: Photographs of the zone of inhibition (ZOI) of *E.coli* and *E.hirea*, respectively (A) cultured on agar plates around a hydrogel bead. The corresponding quantitative ZOI's measured for beads with increasing TA without (B) and with pre-sorbed Fe (C) in the beads.

As with the ZOI study, we observed negligible growth inhibition of *E. coli* and *E. hirea* bacterial growth when we immersed pure alginate beads in the culture broths as a negative

control (Figure 5.21). Unlike the ZOI results, the addition of Fe in Alg-Fe did not produce a significant inhibition. Since any released antimicrobial agent would be diluted much more significantly throughout the volume of the culture broth than around the surface of the bead in the ZOI assay, it appears that the amount of Fe ion that can be released from the alginate beads is small.

In contrast, with TA incorporated in our hydrogel beads at increasingly higher levels, bacterial growth inhibition was observed to be increasingly hindered. While the overall inhibition was small for *E. coli* (Figure 5.21(a)), a large enhancement of the antibacterial properties was observed with further Fe incorporation (Figure 5.21(b)). There was also a step increase in inhibition when the number of beads "loaded" in the culture flask doubled from 0.05% w/v to 0.1% w/v (i.e., from 0.5 g/L to 1 g/L). For example, while 19% inhibition was observed for Alg-TA75 at 0.1% w/v loading (Figure 5.21(a)), the combination of TA and Fe incorporation brings the inhibition up to 74% for the corresponding Alg-TA75-Fe beads (Figure 5.21(b)). This enhancement (i.e., ca. 3.9-times between Alg-TA75 and Alg-TA75-Fe) was much larger than anticipated from the ZOI results. Since earlier characterization indicated a few times higher Fe incorporation in the presence of TA in the beads (Figure 5.14), the larger contrast in performance between Alg-Fe and Alg-TA-Fe could be corroborating the large dilution of the released TA/Fe ions in the volume of the culture broth.

Analogous trends were observed in the case of *E. hirea* culture, and in fact, significant inhibition was already observed even without Fe incorporation (ca. 62% inhibition for Alg-TA75 at 0.1% w/v loading) (Figure 5.21(c)). Because of this already significant inhibition under our culture conditions, the further enhancement of activity with TA-induced Fe incorporation was not as dramatic (e.g., a maximum of 85% inhibition for the corresponding Alg-TA75-Fe beads) (Figure 5.21(d)).

Overall, the culture inhibition results demonstrate a synergistic action between TA and TA-Fe incorporation. Indeed, the lack of inhibition by the Alg control shows that neither the alginate material nor the physical surface of the beads can confer activity (e.g., by adhering or otherwise sequestering the cells, as in some other systems). Moreover, the step change in inhibition after doubling the bead load confirms the activities of both the Alg-TA and Alg-TA-Fe hydrogels, and the increasing trend of inhibition with the increasing incorporation of TA gives further evidence that TA is the fundamental causative agent leading to the change in antimicrobial properties.

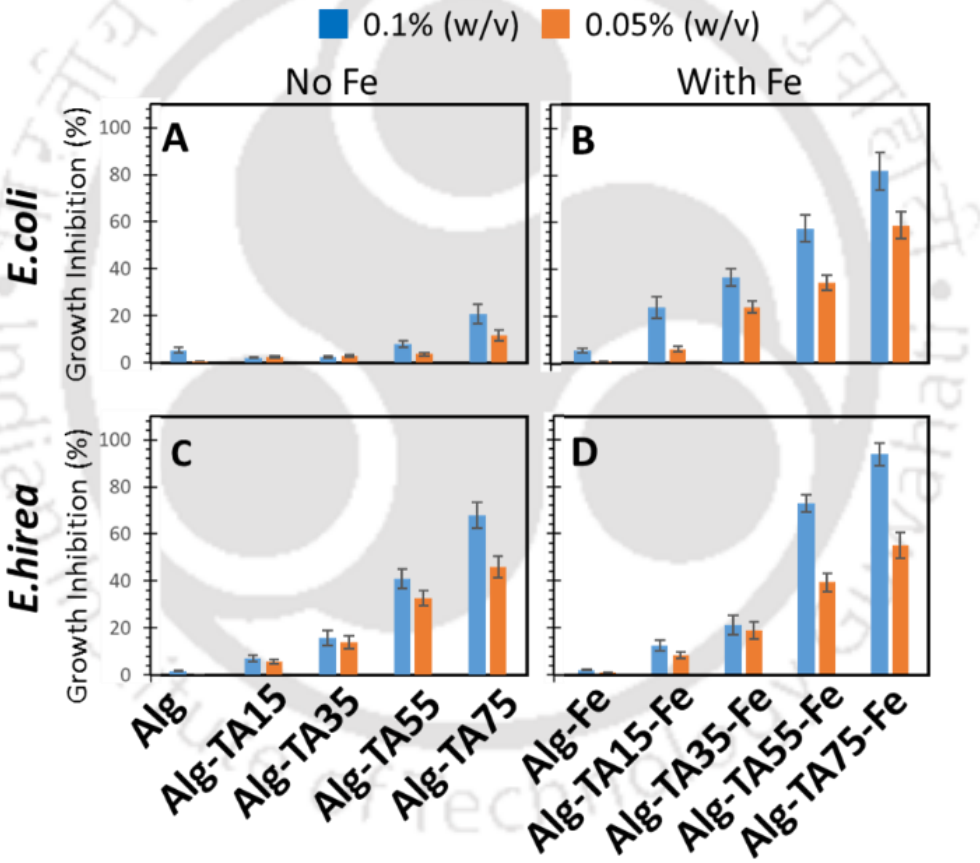

Figure 5.21: Growth inhibition of *E.coli* using Alg and Alg-TA beads, without (A) and with Fe (B), when suspended together with the bacteria in the culture broth. Corresponding inhibition of *E.hirea* growth without (C) and with Fe (D). Two bead loadings (0.05% and 0.1%) were tested.

5.3.6 Stability of Alg-TA and Alg-TA-Fe beads

The synthesized beads should maintain their stability under the harsh conditions of the buffer. We therefore tested whether the TA-incorporated hydrogel may be degraded/dissolved at harsh pH environments, specifically at both acidic (pH 2) and basic (pH 10) conditions. The synthesized Alg-TA35 and Alg-TA55 beads were found to be stable at pH 2 and 10 (Figures 5.22(a) and 5.22(c)), respectively. In the case of Alg-TA35-Fe, the beads were stable at pH 2 (Figure 5.22 (b)) however, we observed a darkening of the pH 10 basic test solution (Figure 5.22(d)), which we interpreted as the dissolution or release of the Fe ion/particle component. On the other hand, this instability was resolved at a higher level of TA corporation; the test solution remained clear in the presence of Alg-TA55-Fe (Figure 5.22(d)). This suggests that a higher amount of TA enhanced the stability of the synthesized beads, corroborating our mechanical test results (Figure 5.6).

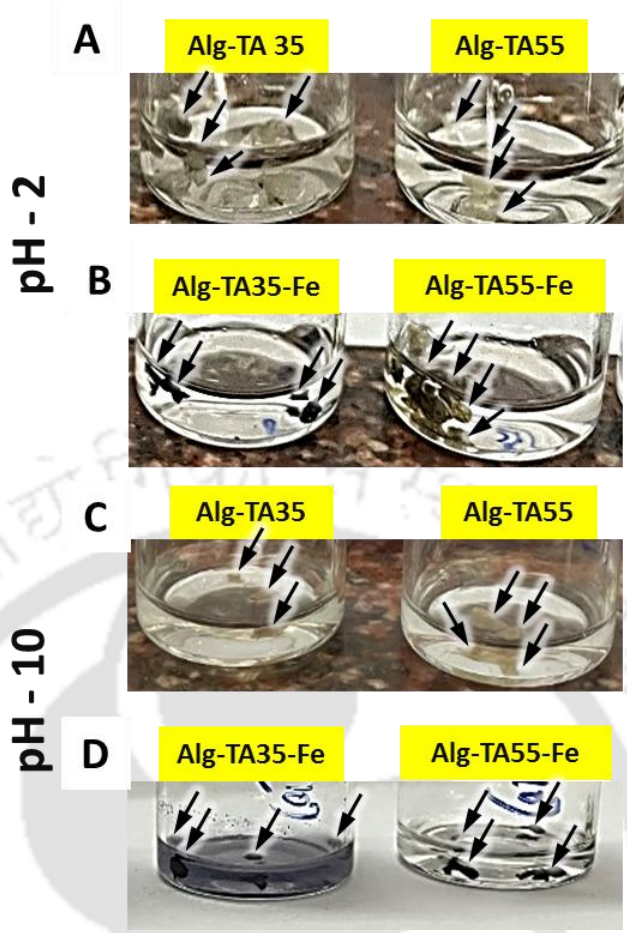

Figure 5.22: Photograph observations of Alg-TA35 and Alg-TA55 beads, without (A) and with (B) pre-sorbed Fe, stored at pH 2. Corresponding observations after storage at pH 10 for beads without (C) and with (D) pre-sorbed Fe. Arrows highlight the location of the beads.

5.4. Conclusions

The work in this chapter focuses on Alg, Alg-TA (15-75), Alg-Fe, and Alg-TA (15-75)-Fe beads preparation and their application for the removal of heavy metal ions from an aqueous solution. The trend of metal adsorption increased with higher amounts of TA content in Alg. The maximum removal % values of 98, 98, 67, 59, and 51 were found for Pb(II), Cu(II), Zn(II), Fe(III), and Cr(VI), respectively, through Alg-TA75 beads at a dosage of 1 g/L and pH of 4 for Pb(II), Cu(II), Fe(III), and Cr(VI), and 6 for Zn(II) ions, respectively. Furthermore, the Alg-TA (15-75) beads were used to form Fe complexes or IONPs throughout them. XPS

spectroscopy analysis indicated that most Fe ions were chemisorbed, but the Alg-TA matrix may have formed IONPs. Thus, the formed novel Alg-TA (15-75)-Fe beads showed enhanced antibacterial performance and Cr(VI) removal from aqueous solution compared to Alg-TA (15-75) beads. The adsorption parameters for Cr(VI) removal through synthesized Alg-TA (15-75)-Fe beads were optimized at pH-4, and a dosage of 1 g/L, respectively. A maximum Cr(VI) removal of 95 % was achieved through Alg-TA75-Fe beads from 20 mg/L aqueous solution. Synergistic antibacterial activity of TA and the IONPs was observed towards *E.coli* and *E.hirea* strains. The antibacterial performance was enhanced by up to 4-fold for *E. hirea* based on bacteria plating experiments for Alg-TA75-Fe beads. Also, the ZOI values of Alg-TA-Fe beads were higher than bare Alg and Alg-TA beads, respectively. The stability studies reveal that the synthesized beads of Alg-TA were more stable than Alg-TA-Fe in both acidic and basic conditions, respectively. Overall, based on the performance, the synthesized Alg-TA and Alg-TA-Fe beads were found to be optimal candidates for water remediation applications.

The synthesized Alg-TA75-Fe demonstrated a lower Cr(VI) adsorption efficiency than CS/IONPs beads and IONPs. The CS/IONPs beads and IONPs exhibited Q_m values of 4.38 and 16.12 times greater than those of Alg-TA75-Fe beads, respectively. Furthermore, it was observed that Fe ions were released into the aqueous solution from both CS/IONPs beads and IONPs. However, in the case of Alg-TA-Fe beads, with higher TA content, it successfully prevented the dissolution of Fe ions.

Chapter 6

Potential of CS/IONPs and Alg-TA-Fe beads in a continuous adsorption process for the decontamination of Cr(VI)

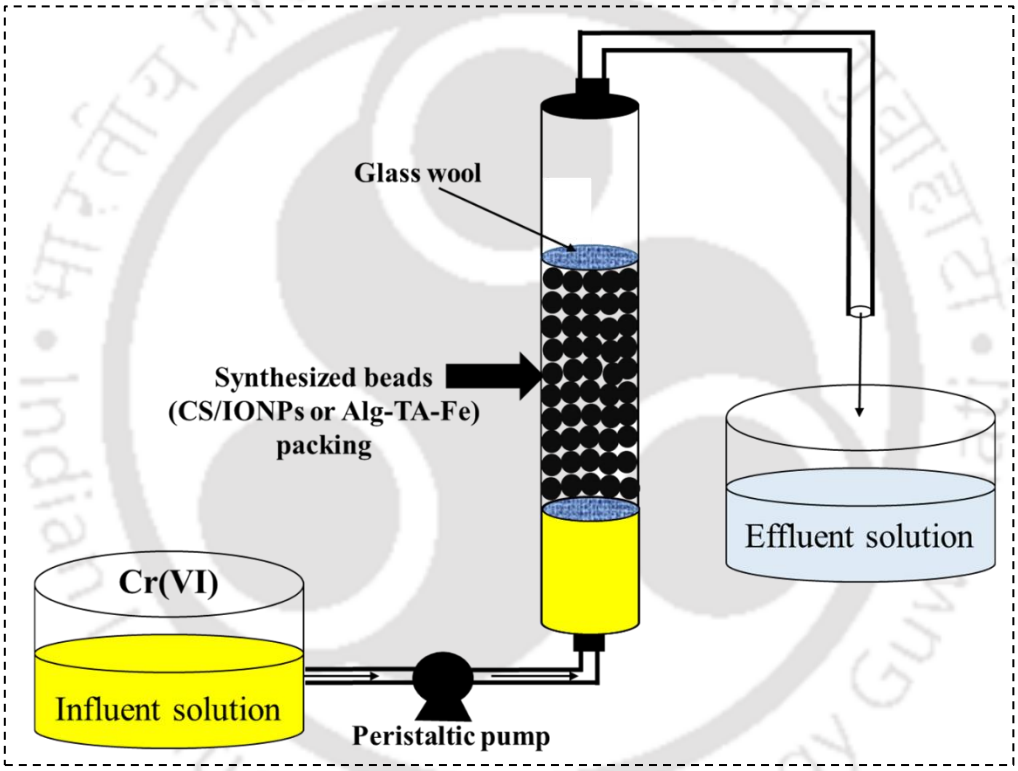

Highlights

- Cr(VI) elimination using CS/IONPs and Alg-TA55-Fe beads in continuous mode
- Increasing packed bed height from 5 to 15 cm enhances Cr(VI) removal efficiency
- CS/IONPs showed higher efficiency for Cr(VI) removal compared to Alg-TA55-Fe
- Breakthrough models well interpreted experimental breakthrough profiles
- Beads regeneration was successful with NaOH solution and reused for up to 2 cycles

In this chapter, the synthesized beads of CS/IONPs and Alg-TA55-Fe as demonstrated in Chapters 4 and 5 were subsequently employed as the adsorbent materials in a fixed-bed adsorption column for the removal of Cr(VI) from the synthetic metal solution. The impact of bed depth and influent flow rate on the performance of both types (CS/IONPs and Alg-TA55-Fe) of composite beads was investigated with a fixed concentration of Cr(VI). The Yoon-Nelson, Clark, Thomas, Bohart-Adams, and Bed Depth Service Time models were employed to analyze the breakthrough profiles of Cr(VI) adsorption. Further, the practical applicability of used CS/IONPs and Alg-TA55-Fe beads after Cr(VI) adsorption was assessed through regeneration and Cr(VI) re-adsorption tests.

6.1. Introduction

Environmental scientists are deeply concerned about the presence and widespread occurrence of Cr(VI) due to its toxicity and the resulting consequences on both human health and the ecological balance of our environment [416]. As discussed in Chapter 2, Cr could enter into surface waters through various means, including natural occurrences like the erosion of rocks and volcanic eruptions. Industrial operations like dye production, electroplating treatments, leather tanning, and paper manufacturing contribute to the release of Cr into environments [417]. In aquatic environments, Cr mainly exists in two distinct oxidation states, Cr(VI) and Cr(III). The Cr(VI) species are more toxic than the Cr(III) species by a factor of 100, imparting highly harmful effects on biological systems [418]. The Cr(VI) species have been recognized as potent carcinogens and mutagens, posing significant risks to the health and functionality of living organisms [419]. Hence, it is imperative to implement an efficient treatment method for Cr(VI) removal before its releases into aquatic environments.

Nevertheless, the use of powdered IONPs as demonstrated in Chapter 3 for water treatment processes often leads to agglomeration issues. Many contemporary studies also have relied on green-synthesized powdered IONPs, typically restricting their application to batch

experiments. For instance, *Catha edulis* leaf extract was utilized to produce IONPs, which were subsequently employed to remove Cr(VI) from an aqueous solution. At a pH of 5 and a dosage of 1 g/L, IONPs could remove 98.6 % Cr(VI) from a 20 mg/L Cr(VI) concentration solution in 60 min [420]. In a separate study, *yerba mate* leaf extract was utilized to synthesize IONPs for removing Cr(VI). IONPs showed complete removal of Cr(VI) from an aqueous solution with an initial Cr(VI) concentration of 15.6 mg/L at a pH of 3 within 20 min [240]. Another research group employed green tea extract to produce zero-valent iron NPs (nZVI) and applied them for Cr(VI) removal. nZVI could effectively reduce 92.8% Cr(VI) from a rich solution (100 mg/L) in 60 min [421]. On the other hand, fixed-bed adsorption processes are commonly employed for industrial applications. The use of powdered IONPs in such systems is problematic due to their tendency to cause clogging. Additionally, the separation of powdered IONPs from treated water is quite challenging [422]. The granulation of adsorbents by incorporating powdered IONPs into a supportive matrix is a realistic solution to overcome these challenges [321].

In this chapter, we utilized synthesized CS/IONPs and Alg-TA55-Fe composite beads in a fixed-bed adsorption column to effectively remove Cr(VI). The study investigated the impact of different column parameters, specifically bed heights (5, 10, and 15 cm) and flow rates (1, 2, and 3 mL/min). The Yoon-Nelson, Clark, Thomas, Bohart-Adams, and Bed Depth Service Time models were employed to analyze the breakthrough profiles of Cr(VI) adsorption. In addition, the practical usability of CS/IONPs and Alg-TA55-Fe beads was evaluated by conducting regeneration and Cr(VI) re-adsorption tests.

6.2. Materials and methods

6.2.1 Chemicals

The chemicals required for the formation of CS/IONPs and Alg-TA55-Fe beads are already documented in Chapters 4 (Section 4.2.1) and 5 (Section 5.2.1), respectively.

6.2.2 Synthesis of CS/IONPs and Alg-TA55-Fe composite beads

The synthesis methodology of CS/IONPs and Alg-TA55-Fe beads are also documented in Chapters 4 (Section 4.2.2) and 5 (Section 5.2.2), respectively.

6.2.3 Fixed bed adsorption studies using CS/IONPs and Alg-TA-Fe beads

Continuous fixed-bed column adsorption experiments were conducted to remove Cr(VI) using synthesized beads (CS/IONPs and Alg-TA55-Fe) in a custom glass column with a height (H) of 32 cm and internal diameter (D) of 1.6 cm. The column was packed with wet beads (either CS/IONPs or Alg-TA55-Fe) and sealed with glass wool at both ends to ensure uninterrupted flow during the fixed-bed tests (illustrated in graphical abstract). To prevent channeling within the column, the Cr(VI) solution (influent) was pumped upward using a peristaltic pump (MICLINS, Model: PP-20EX, India). The effluent solution was analyzed to determine the Cr(VI) concentration (C_t) in a UV-Vis spectrophotometer at 543 nm using the DPC reagent method.

Based on the batch adsorption studies, it was found that pH values of 3 (Section 4.3.2.1, Chapter 4) and 4 (Section 5.3.4, Chapter 5) were optimal for maximum Cr(VI) removal using CS/IONPs and Alg-TA55-Fe beads, respectively. Subsequently, these pH values were fixed for the Cr(VI) influent solution for the column studies using CS/IONPs and Alg-TA55-Fe beads. In India, groundwater typically contains Cr(VI) in concentrations ranging from 1 to 12.3 mg/L [423-426]. Therefore, for the column studies, an elevated initial influent Cr(VI) concentration (C_o) of 20 mg/L was chosen. The experimental investigations were carried out at a fixed temperature of 25 °C. The peristaltic pump was used to maintain the flow rates (Q=1, 2, and 3 mL/min) [427] at a constant bed height (Z) of 5 cm. Further, the influence of Z (5, 10, and 15 cm) on Cr(VI) removal was studied at a fixed Q of 1 mL/min [428].

6.2.4 Assessment of the breakthrough curve

The efficiency of CS/IONPs and Alg-TA55-Fe beads for removing Cr(VI) was carried out through breakthrough curve analysis, a relationship between the ratio (C_t/C_0) and time. The shape and duration of the breakthrough curve are critical factors for understanding the behavior of the column and play a vital role in optimizing the overall operational design to enhance effectiveness.

The selection of column breakthrough time (t_b) occurs in instances where the concentration of C_t is found to be ≤0.05 mg/L [429], and the saturation time (t_s) is established at which C_t reaches 95% (19 mg/L) of C_0 [430]. The effluent volume (V_{eff}, L) leaving the column can be calculated as in Eq. 6.1 [431]. Here, Q represents the flow rate (L/h) and t_e denotes the column exhaustion time in h. The quantity of Cr(VI) at time t (h) in the column is represented by $q_{in,t}$ (mg) and calculated using Eq. 6.2. The quantity of unadsorbed Cr(VI) ($q_{out,t}$, mg) at a given time, t, was determined by multiplying the integral of the dimensionless quantity by C_0, and Q as given by Eq. 6.3. The quantity of Cr(VI) adsorbed onto the column was expressed as $q_{ads,t}$ in mg as in Eq. 6.4.

$$V_{eff} = Q \times t_e \tag{6.1}$$

$$q_{in,t} = C_0 Q\, t \tag{6.2}$$

$$q_{out,t} = C_O Q \int_0^t \left(\frac{C_t}{C_0}\right) dt \tag{6.3}$$

$$q_{ads,t} = q_{in,t} - q_{out,t} \tag{6.4}$$

Cr(VI) removal % achieved using the synthesized beads is expressed by Eq. 6.5. Eq. 6.6 relates the equilibrium metal adsorption capacity (q_{eq}) of the column as $q_{ads,t}$ per g of adsorbent (M) at the end of t_e. The empty bed contact time (EBCT, min) and empty bed volume (EBV) of the column are described by Eqs. 6.7 and 6.8, respectively.

$$\text{Cr(VI) removal \%} = \frac{q_{ads,t}}{q_{in,t}} \times 100 \tag{6.5}$$

$$q_{eq} = \frac{q_{ads,t}}{M} \quad (6.6)$$

$$EBCT = \frac{\text{Bed volume (mL)}}{\text{Q (mL/min)}} \quad (6.7)$$

$$EBV = \pi \times \left(\frac{D}{2}\right)^2 \times H \quad (6.8)$$

6.2.5 Column regeneration studies

Desorption experiments were carried out in the same column to recover adsorbed Cr(VI) and reuse the desorbed beads (CS/IONPs and Alg-TA55-Fe) for further adsorption studies. At first, Cr(VI) ions were adsorbed onto CS/IONPs and Alg-TA55-Fe beads until the column reached saturation by introducing a 20 mg/L Cr(VI) solution at Q=1 mL/min and Z=5 cm. After that, the saturated beads were regenerated by eluting with 1 M NaOH for CS/IONPs and 0.5 M NaOH for Alg-TA55-Fe beads [325, 432]. Following the alkali elution, the bed was thoroughly rinsed with deionized water until the pH of the washed effluent stabilized at 7.0. The column was again fed with fresh 20 mg/L of Cr (VI) influent solution for further adsorption study using CS/IONPs and Alg-TA55-Fe beads under the previously mentioned conditions. This process was repeated for a total of 3 adsorption cycles, and after each cycle, desorption was performed to assess the breakthrough parameters of the used CS/IONPs and Alg-TA55-Fe beads.

6.3. Results and Discussion

6.3.1 Breakthrough analysis

6.3.1.1 Effect of the influent solution flow rate on Cr(VI) adsorption

The analysis of the flow rate is important in designing an adsorption column with a fixed bed height. Figures 6.1(a) and 6.1(b) illustrate the breakthrough curves of Cr(VI) adsorption for CS/IONPs and Alg-TA55-Fe beads at 3 different Q (1, 2, and 3 mL/min) with a constant C_o of 20 mg/L and Z of 5 cm. As Q increased, there was a noticeable decrease in the time (h)

required to reach the breakthrough point (Table 6.1). In particular, t_b for CS/IONPs and Alg-TA55-Fe beads drops from 5 to 1.5 h and 0.75 to 0.37 h, respectively, as Q increased from 1 to 3 mL/min. The decline in t_b can be attributed to increased Cr(VI) mobility in the mass transfer zone, which led to a shorter time to reach the breakthrough concentration [432]. The q_{eq} was also lowered (Table 6.1) at higher Q due to insufficient Cr(VI) residence time in the column [433]. Further, the EBCT was also found to be higher at lower Q values (Table 6.1) for both CS/IONPs and Alg-TA55-Fe beads. This implies that higher Q resulted in an earlier column saturation (Figures 6.1(a) and 6.1(b)), as the adsorption front rapidly reached the top of the column [428]. Moreover, the adsorption efficiency of CS/IONPs beads was greater than Alg-TA55-Fe beads for Cr(VI) removal due to longer t_b values (Table 6.1). These findings are well aligned with previous studies in the literature [428, 434].

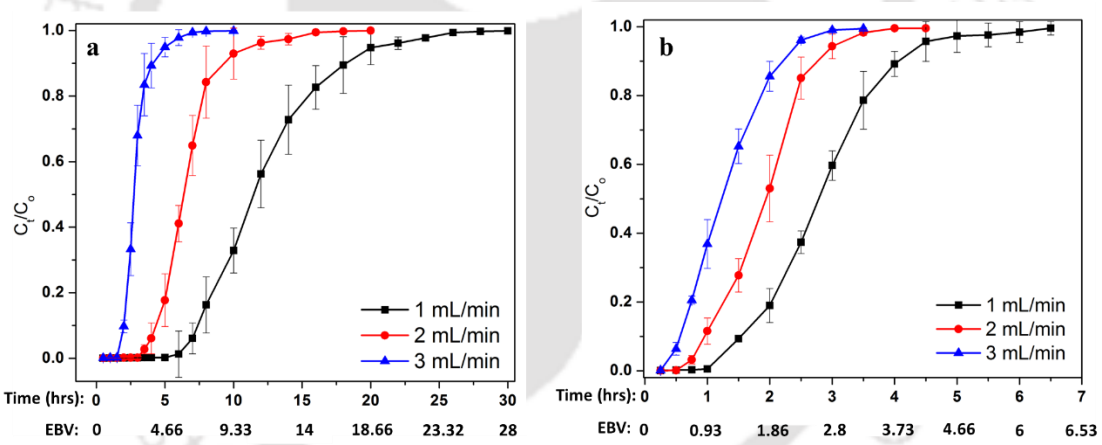

Figure 6.1: Breakthrough curves for Cr(VI) adsorption onto (a) CS/IONPs and (b) Alg-TA-Fe beads at different flow rates (Q) (Z – 5 cm, C_0 – 20 mg/L, pH – 3 and 4 for CS/IONPs and Alg-TA55-Fe beads, respectively).

6.3.1.2 Effect of synthesized beads bed height

The impact of varying bed height (Z) on the adsorption of Cr(VI) from a solution with an initial concentration of 20 mg/L was studied at a flow rate (Q) of 1 mL/min. Both CS/IONPs and Alg-TA55-Fe beads were tested at different bed heights of 5, 10, and 15 cm. The

corresponding breakthrough curves are presented in Figures 6.2(a) and 6.2(b). An increase in Z to 15 cm resulted in longer t_b and t_s values for both CS/IONPs (Figure 6.2(a)) and Alg-TA55-Fe (Figure 6.2(b)) beads, as depicted in Table 6.1. V_{eff} also exhibited a direct correlation (Table 6.1) with Z, indicating that the increase in V_{eff} was attributed to the extended contact time between the influent Cr(VI) and the adsorbent. The results (Figures 6.2(a) and 6.2(b)) show that the changes in Z resulted in a slight modification both in the gradient and shape of the breakthrough curve. Initially, there was a rapid uptake of Cr(VI), but after t_b, Cr(VI) concentration in the effluent increased rapidly. In fact, the column saturation reached earlier in the lower Z (5 and 10 cm) compared to the higher bed depth (15 cm) for both CS/IONPs and Alg-TA55-Fe beads (Figure 6.2). The highest Cr(VI) removal (%) values (Table 6.1) were observed for Z=15 cm at a Q of 1 mL/min for both CS/IONPs and Alg-TA55-Fe beads. This phenomenon can be attributed to the larger surface area of the adsorbent beads with a higher bed height, resulting in more available adsorption sites for Cr(VI) removal [434]. Further, CS/IONPs beads demonstrated higher Cr(VI) adsorption efficiency than Alg-TA55-Fe beads due to longer t_b and higher q_{eq} values.

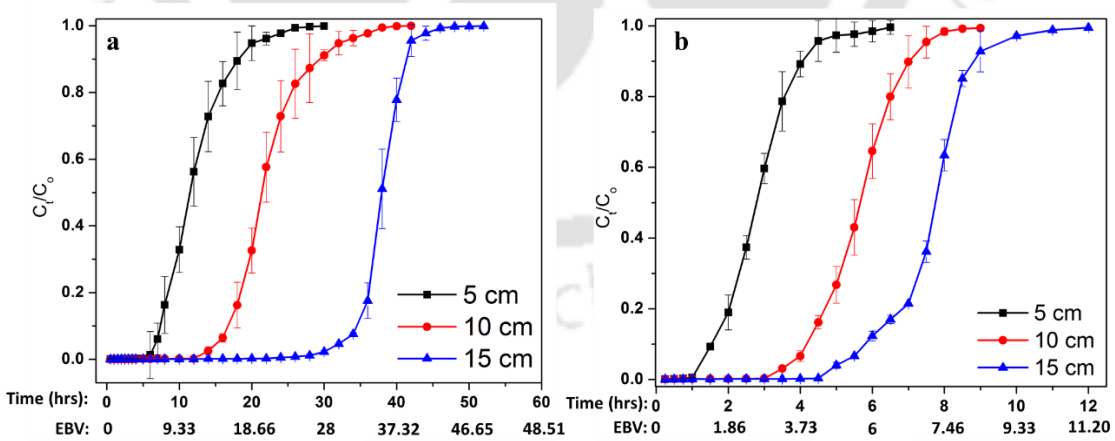

Figure 6.2: Breakthrough curves for Cr(VI) adsorption onto (a) CS/IONPs and (b) Alg-TA-Fe beads at different bed heights (Z) (Q – 1 mL/min, C_0 – 20 mg/L, pH – 3 and 4 for CS/IONPs and Alg-TA55-Fe beads, respectively).

Table 6.1: Cr(VI) elimination parameters evaluated from breakthrough curves analysis for the synthesized beads utilized in a fixed-bed adsorption column.

Beads	Z (cm)	Q (mL/min)	Cr(VI) removal (%)	q_{eq} (mg g^{-1})	t_b (h)	t_s (h)	V_{eff} (L)	EBCT (min)
CS/IONPs	5	1	24.7	391.9	5	20	1.8	10.0
	5	2	22.9	368.1	3	10	2.4	5.0
	5	3	16.5	260.5	1.5	5	1.8	3.4
	10	1	31.6	388.4	12	32	2.52	20.1
	15	1	53.0	384.9	22	42	3.12	30.1
Alg-TA55-Fe	5	1	21.5	60	0.75	4.5	0.39	10.0
	5	2	21.4	57.9	0.62	3	0.54	5.0
	5	3	19.3	54	0.37	2.5	0.63	3.4
	10	1	39.2	58.13	3	7.5	0.54	20.1
	15	1	49.2	55.05	4.5	9	0.72	30.1

6.3.2 Breakthrough curve modeling

To assess the breakthrough behaviors of Cr(VI) adsorption using the synthesized CS/IONPs and Alg-TA55-Fe beads, theoretical kinetic models, namely, Bohart-Adams, Thomas, Yoon-Nelson, and Clark, and a semi-empirical model known as Bed Depth Service Time (BDST) were tested. These model equations were applied to establish a correlation between the data fitted by the models and the experimental data [435].

6.3.2.1 Bohart - Adams model

The correlation between the ratio of C_t to C_0 and the progression of time in a continuous adsorption column was described by a fundamental equation developed by Bohart and Adams [436]. This model is based on surface reaction theory and postulates that the attainment of adsorption equilibrium in a continuous system is not an instantaneous process. The rate of adsorption is linearly related to two key factors: the residual efficiency of the adsorbent and the concentration of the pollutant being adsorbed. The linear expression of the model is as follows (Eq. 6.9).

$$\ln\left(\frac{C_t}{C_o}\right) = K_{BA}C_0t - K_{BA}N_0\left(\frac{Z}{U_0}\right) \quad (6.9)$$

In this equation, K_{BA} represents the Bohart-Adams rate constant, which is measured in L/mg/h. U_0 represents the linear velocity in cm/min, and N_0 denotes the saturation concentration (mg/L). Figures 6.3 and 6.4 depict the simulation of experimental breakthrough curves using the Bohart-Adams model, specifically about the parameters Q and Z for CS/IONPS and Alg-TA55-Fe beads, respectively. The entire range of variable t was considered throughout the breakthrough curve. Table 6.2 demonstrates that K_{AB} values increase with increasing Q (1 to 3 mL/min) while they decrease with increasing Z (5 to 10 cm) for both CS/IONPs and Alg-TA55-Fe beads. These observations suggest that the kinetics of Cr(VI) adsorption were primarily governed by the prevalence of external mass transfer [417, 437].

6.3.2.2 Yoon-Nelson model

This model states that the reduction in the adsorption rate for individual adsorbate molecules is directly linked to the probabilities of both adsorbate-adsorption and breakthrough occurring within the adsorbent material [438]. The linear expression of the Yoon-Nelson model is depicted in Eq. 6.10.

$$\ln\left(\frac{C_t}{C_o - C_t}\right) = K_{YN}t - \tau K_{YN} \quad (6.10)$$

Where τ represents the temporal duration required for 50% adsorbate breakthrough (min). K_{YN} denotes the Yoon-Nelson rate constant (min). The values of k_{YN} and τ were determined from the fitted plots, as shown in Figures 6.3 and 6.4 for CS/IONPs and Alg-TA55-Fe beads, respectively. The values of τ were found to be decreased at higher Q for both CS/IONPs and Alg-TA55-Fe beads (Table 6.2). This decrease can be attributed to the faster achievement of breakthroughs due to the reduced EBCT (Table 6.1) [431]. A direct relationship (Table 6.2) was found between Q and K_{YN} in both the cases of synthesized beads (CS/IONPs and Alg-TA55-Fe). Further, an increase in Z (5 to 15 cm) for both CS/IONPs and Alg-TA55-Fe beads

indicated a longer column saturation time as depicted from higher τ values (Table 6.2). The τ values closely correspond to the experimental times needed for a 50% Cr(VI) breakthrough across all experimental conditions. Figures 6.3 and 6.4 depict the nonlinear fits of the experimental data concerning Q and Z to the Yoon-Nelson model for CS/IONPS and Alg-TA55-Fe beads, respectively. The patterns exhibited by the fitted curves indicate that the model could accurately describe the experimental data.

6.3.2.3 Clark model

The Clark model is developed based on principles of mass transfer principles in conjunction with the Freundlich isotherm [439]. The linear expression of the Clark model is shown in Eq. 6.11.

$$\ln\left(\left(\frac{C_t}{C_0}\right)^{n-1}\right) = (-\mathrm{rt} + \ln A) \quad (6.11)$$

Here, A and r (min^{-1}) represent the Clark model constants, and n represents the Freundlich parameter. Figures 6.3 and 6.4 show the fitted Clark model to the experimental data for Cr(VI) adsorption onto synthesized CS/IONPs and Alg-TA55-Fe beads at different Q and Z values. It can be observed that an increase in Z from 5 to 10 cm leads to a drop in the values of r for both CS/IONPs and Alg-TA55-Fe beads (Table 6.2). This decrease was caused by an increase in the number of accessible adsorbent sites, which influences the mass transfer rate [439-441]. Conversely, a noticeable positive correlation was noted between the increased r-value with the rise in Q (1 to 3 mL/min) for both CS/IONPs and Alg-TA55-Fe beads. The experimental outcomes and data regression analysis indicate that the Clark model exhibits a strong correlation in capturing the effects of Z and Q for Cr(VI) removal using the synthesized beads.

6.3.2.4 Thomas model

The Thomas model was developed to describe adsorption processes that are not controlled by external or internal diffusion limitations [442],[443]. The model considers that the adsorption rate is governed by the interaction between unoccupied adsorption sites and the adsorbate without considering Intraparticle mass transfer resistance. The linear form of Thomas's model is depicted in Eq. 6.12.

$$\ln\left(\frac{C_0}{C_t} - 1\right) = \frac{K_{TH} q_0 m}{Q} - K_{th} C_0 t \quad (6.12)$$

The parameter, K_{TH} represents the Thomas rate constant (L/mg/h), variable q_0 denotes the quantity of Cr(VI) adsorbed per g of beads, and m represents the mass of the absorbent (g). The values of K_{th} and q_0 were determined from the fitted plot, as shown in Figures 6.3 and 6.4 for CS/IONPs and Alg-TA55-Fe beads, respectively. The experimental data exhibited a strong agreement (correlation coefficients>0.99) with the Thomas model for all experimental data of Cr(VI) adsorption using CS/IONPs and Alg-TA55-Fe beads. However, the expected q_0 values from the model (presented in Table 6.2), do not agree with the computed q_{eq} values using both CS/IONPs and Alg-TA55-Fe beads, as depicted in Table 6.1. For both CS/IONPs and Alg-TA55-Fe beads, it was observed (Table 6.2) that K_{th} values decreased when Z increased from 5 to 10 cm. Furthermore, an increase in Q from 1 to 3 mL/min corresponded to an increase and decrease in K_{th} and q_0 values for both CS/IONPs and Alg-TA55-Fe beads, respectively. Thus, lower Q and higher Z enhance Cr(VI) removal (%) over synthesized CS/IONPs and Alg-TA55-Fe beads.

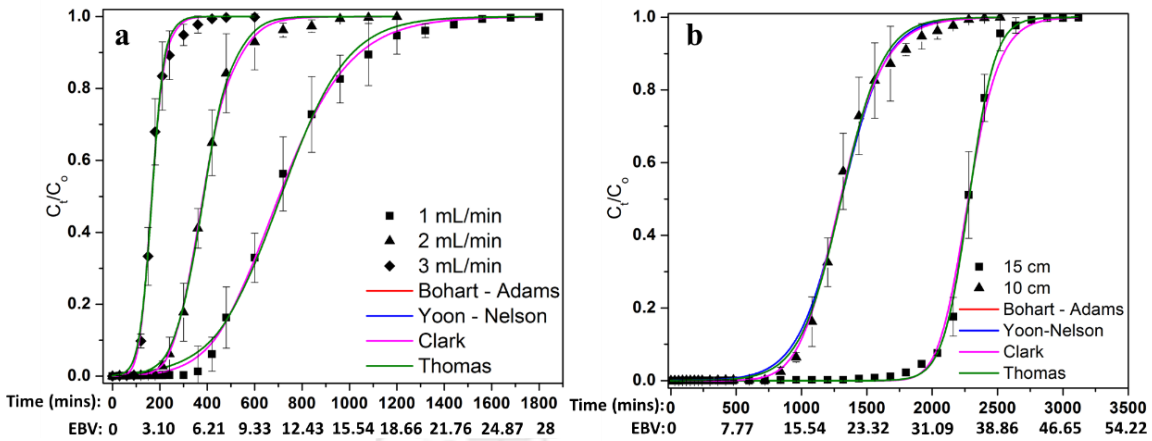

Figure 6.3: Fitted breakthrough curves in various adsorption models for Cr(VI) removal using CS/IONPs beads at different (a) Q at a fixed Z of 5 cm and (b) Z at a fixed Q of 1 mL/min.

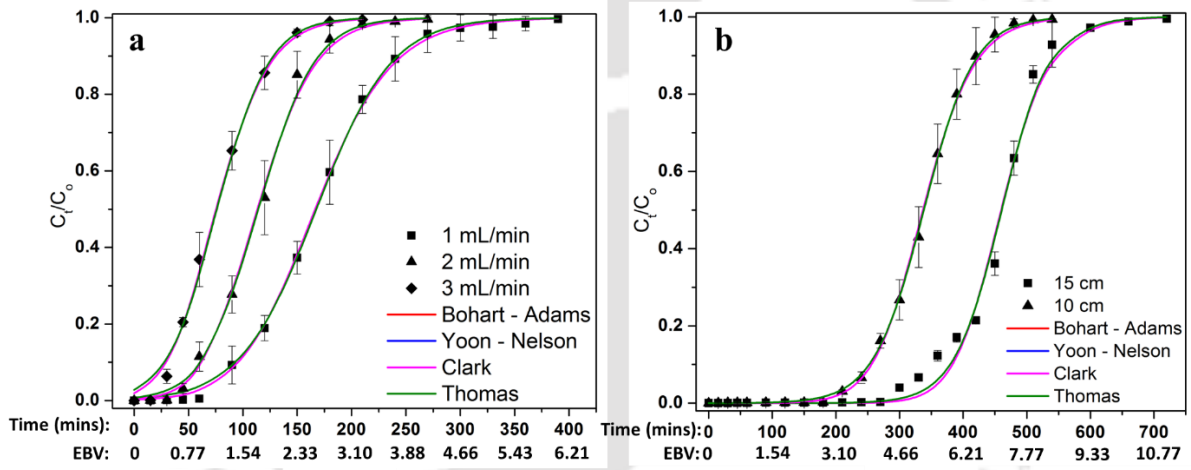

Figure 6.4: Fitted breakthrough curves in various adsorption models for Cr(VI) removal using Alg-TA55-Fe beads at different (a) Q at a fixed Z of 5 cm and (b) Z at a fixed Q of 1 mL/min.

Table 6.2: Breakthrough curve models fitted parameters.

Beads	Q (mL/min)	Z (cm)	Bohart - Adams			Yoon - Nelson			Clark			Thomas		
			$K_{BA}\times10^{-3}$ (L/min/g)	N_0 (mg/L)	R^2	$K_{YN}\times10^{-3}$ (min^{-1})	τ (min)	R^2	A	$r\times10^{-3}$ (min^{-1})	R^2	$K_{TH}\times10^{-2}$ (L/h/mg)	q_0 (mg g^{-1})	R^2
CS/IONPs	1	5	0.37	8.42	0.99	7	710.3	0.99	31.1	6	0.99	2.27	77.00	0.99
	2	5	0.9	4.55	0.99	17	384.78	0.99	99.38	14	0.99	5.34	71.02	0.99
	3	5	2.1	1.97	0.99	42.2	166.65	0.99	133.16	34	0.99	12.6	50	0.99
	1	10	0.3	7.73	0.99	6.5	1305.51	0.99	489.66	5.4	0.99	1.96	54.97	0.99
	1	15	0.5	9.01	0.99	11.3	2281.75	0.99	28962.24	8	0.99	3.33	38.02	0.99
Alg-TA55-Fe	1	5	1.5	1.98	0.99	30.8	167.64	0.99	53.23	27.1	0.99	9.24	22.84	0.99
	2	5	2.1	1.35	0.99	43.3	114.22	0.99	42.17	37.8	0.99	13	16.76	0.99
	3	5	2.3	0.9	0.99	46.75	75.88	0.99	12.71	41.21	0.99	21	15.17	0.99
	1	10	1.3	2	0.99	26.5	338.14	0.99	1612.20	23.54	0.99	8.4	9.66	0.99
	1	15	1.4	1.81	0.94	28.2	460.68	0.99	56255.73	24.9	0.88	7.9	7.08	0.99

6.3.2.5 BDST model

The performance of the adsorption column depends upon its capacity to deliver safe treated water over an extended period. The BDST model was employed to estimate the column service time for a specific Z for both CS/IONPs (Figure 6.5(a)) and Alg-TA55-Fe (Figure 6.5(b)) beads. This model assumes that the adsorption rate is controlled by the interaction between the adsorbate and the unused adsorbent within the column bed [428, 431]. This model was first proposed by Bohart and Adams and later improved by Hutchins [444]. The model (Eq. 6.13) is based on a linear relation between the variables Z and t_b in a continuous fixed-bed column of adsorption.

$$t_b = \frac{N_0 Z}{C_0 U_0} - \frac{1}{K_B C_0} \ln\left(\frac{C_0}{C_t} - 1\right) \quad (6.13)$$

In this equation, N_0 represents the adsorption capacity (mg/L) of the synthesized beads (CS/IONPs and Alg-TA55-Fe), and K_B is the rate constant (L/min/g). The N_0 values (Table 6.3) imply that CS/IONPs beads are more efficient in removing Cr(VI) compared to Alg-TA55-Fe beads.

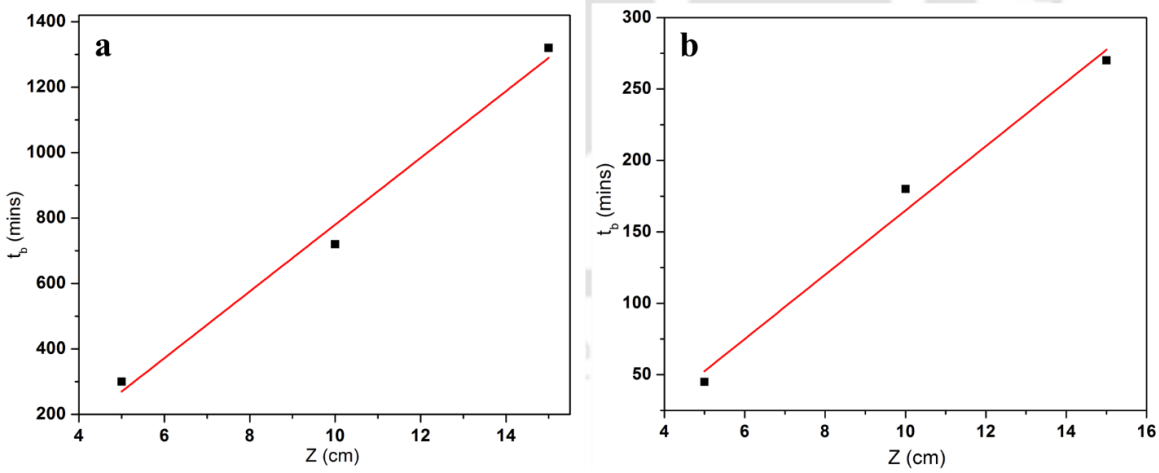

Figure 6.5: BDST for (a) CS/IONPs and (b) Alg-TA55-Fe beads for adsorption of Cr(VI) from aqueous solution.

Table 6.3: BDST model fitted parameters for the synthesized beads.

Beads	N_0 (mg/L)	$K_B \times 10^{-3}$ (L/min/mg)	R^2
CS/IONPs	6.04	0.61	0.99
Alg-TA55-Fe	1.33	2.45	0.98

The effectiveness of CS/IONPs and Alg-TA55-Fe beads in Cr(VI) sorption was assessed by comparing them to other adsorbents used for removing Cr(VI) in fixed bed columns. The results are presented in Table 6.4. The CS/IONPs beads demonstrated a competitive performance of Cr(VI) uptake which is evident from an equilibrium uptake capacity of 391.9 m g^{-1}. Alg-TA55-Fe outperformed most of the adsorbents reported in the literature for removing Cr(VI) in continuous mode of operation.

Table 6.4: Performance parameters and equilibrium adsorption capacity of various adsorbents utilized for the removal of Cr(VI) in fixed bed adsorption column.

Adsorbents	C_o (mg/L)	Q (mL/min)	Z (cm)	pH	q_{eq} (mg g^{-1})	Source
CS flakes	10	5	20	3	130.12	[445]
CS-Fe^0 NPs	-	0.12	-	6	32	[446]
CS-modified magnetic carbon nanotube Fe beads	30	1	8	4	1.52	[447]
CS beads impregnated with nano-γ-Al_2O_3	20	0.25	1.5	3	158.33	[448]
nZVI immobilized alginate beads	10	0.5	18	7	320.66	[449]
SA/phosphorus tetramethyl methyl sulfate biocomposite beads	5	3	1.5	3	331.18	[450]
Core-shell/bead-like alginate@polyethylenimine (PEI)-1.5 composites	50	1	10	2	309.19	[432]
Cellulose@PEI aerogel beads	50	1	8	2	119.46	[451]
Titanium(IV) oxide NPs	32	1	4	2	12.94	[452]
Imidazole functionalized adsorbent	50	1	-	2.6	102	[453]
CS/IONPs beads	**20**	**1**	**5**	**3**	**391.9**	**This study**
Alg-TA55-Fe beads	**20**	**1**	**5**	**4**	**60**	

6.3.3 Regeneration studies of CS/IONPs and Alg-TA55-Fe beads

The reusability of the adsorbent is important for practical applications for the removal of toxic pollutants from wastewater. The desorption of Cr(VI) from the Alg-TA55-Fe and CS/IONPs beads was conducted using 0.5 M and 1 M NaOH solutions, respectively. The breakthrough curves are shown in Figure 6.6(a) (CS/IONPs) and Figure 6.6(b) (Alg-TA55-Fe) for the re-adsorption of Cr(VI) using regenerated beads. Cr(VI) removal efficiency was decreased from 24.75 to 8.61% for CS/IONPs beads, while in the case of Alg-TA55-Fe beads, it was reduced to 9.86 from 21.5 % after the second cycle in comparison to the fresh beads (after 1st adsorption cycle). This suggests that the Cr(VI) adsorption process in a continuous flow system may require an extended regeneration period. In addition, t_b, t_s, and the calculated values of q_{eq} were decreased notably (Table 6.5) for both CS/IONPs and Alg-TA55-Fe beads upon reuse. This implies that the synthesized CS/IONPs and Alg-TA55-Fe beads exhibit good recoverability [437].

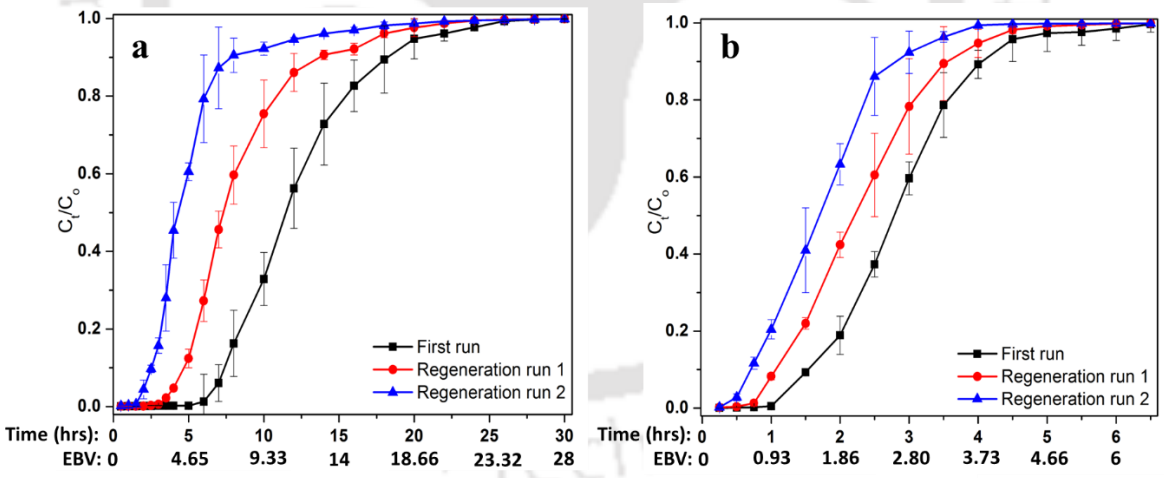

Figure 6.6: Fixed-bed column regeneration profiles for Cr(VI) adsorption: (a) CS/IONPs, and (b) Alg-TA55-Fe beads.

Table 6.5: Breakthrough curve parameters for the used CS/IONPs and Alg-TA55-Fe beads.

Beads	Run	Cr(VI) removal (%)	q_{eq} (mg g^{-1})	t_b (h)	t_s (h)
CS/IONPs	First	24.75	391.91	5	20
	Regeneration run 1	15.86	251.35	2.25	16.5
	Regeneration run 2	8.61	136.43	0.75	12.5
Alg-TA55-Fe	First	21.5	60	0.75	4.5
	Regeneration run 1	15.3	42.68	0.3	4
	Regeneration run 2	9.86	27.51	0.25	3

6.4 Conclusions

The current work successfully reports on the removal of Cr(VI) using green synthesized CS/IONPs and Alg-TA55-Fe beads in a continuous adsorption column. The breakthrough point reaches rapidly and leads to lower Cr(VI) removal at lower bed heights (Z) and higher flow rates (Q) for both CS/IONPs and Alg-TA55-Fe beads. In particular, increasing Z from 5 to 15 cm enhances the t_b values by 4.4 and 6 times for CS/IONPs and Alg-TA55-Fe beads, respectively. CS/IONPs were more efficient for removing Cr(VI) compared to Alg-TA55-Fe beads, as evidenced by higher q_{eq} values of 6.53 times for CS/IONPs than Alg-TA55-Fe beads. The mathematical models, namely Clarke, Thomas, Yoon-Nelson, BDST, and Bohart-Adams, could satisfactorily fit and interpret the experimental breakthrough profiles of Cr(VI) adsorption over CS/IONPs and Alg-TA55-Fe beads. Both types of beads are regenerated using an alkali solution and reused for Cr(VI) re-adsorption up to two regeneration cycles, and showed a decrease in Cr(VI) removal by 65.21 and 54.13% from 1st regeneration run for CS/IONPs and Alg-TA55-Fe beads, respectively. These findings indicate that green synthesized CS/IONPs and Alg-TA55-Fe beads have the potential for effectively eliminating Cr(VI) from aqueous solutions, making them suitable for various industrial applications.

Chapter 7

Overall conclusions and recommendations of future studies

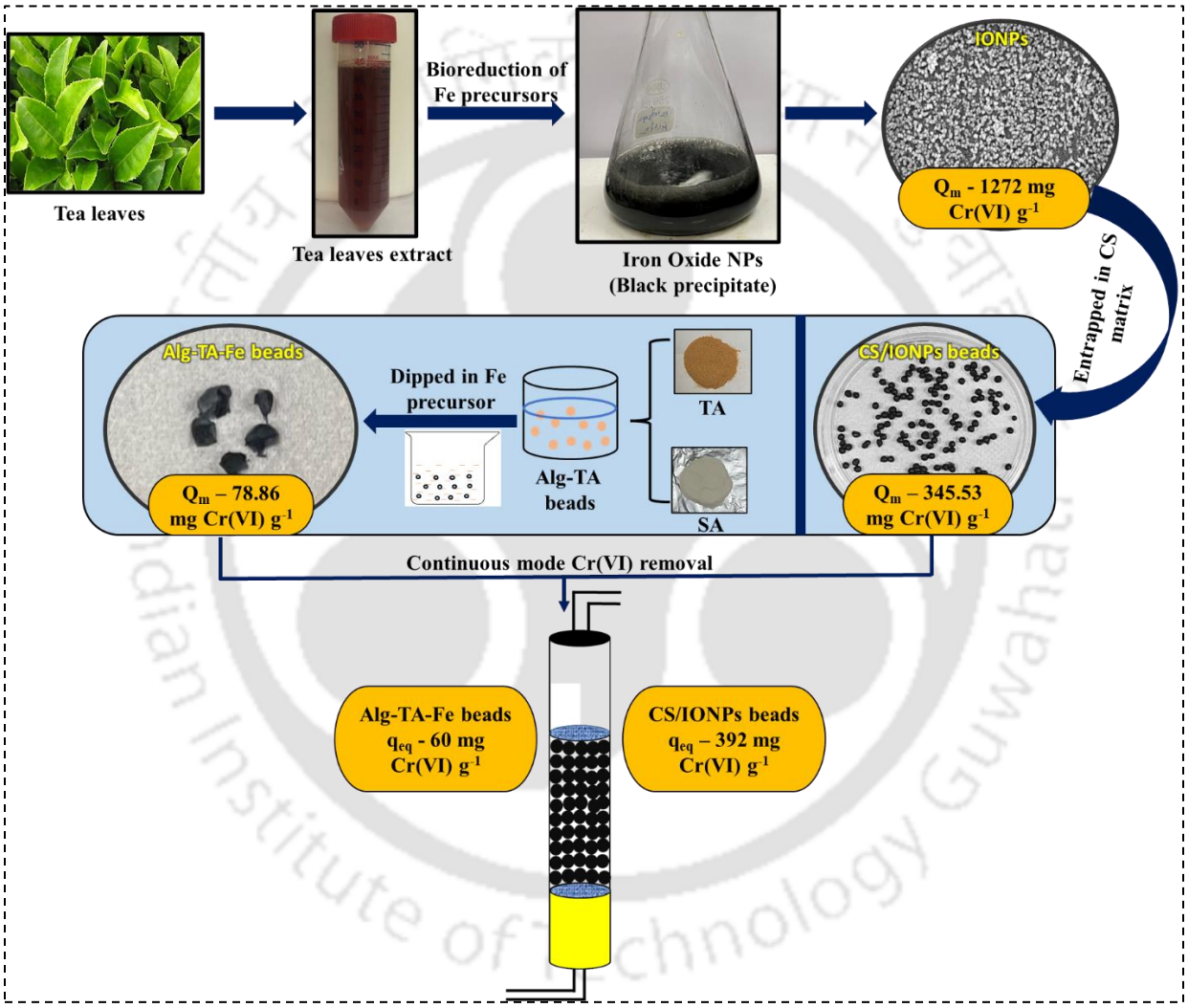

This chapter provides an overview of the key findings from the entire doctoral work. In addition, the recommendations for future research direction are also offered in light of the current study experience.

7.1. Conclusions

Given the depletion of water sources and rising water pollution, there is a notable focus and emphasis on wastewater recycling to remove contaminants. Hexavalent chromium, a confirmed Category A carcinogen, is being utilized and discharged substantially due to human urban and industrial activities. Adsorption is a simple, environmentally friendly, cost-effective technique and requires minimal or no use of chemicals. This present study explicitly investigates the elimination of hexavalent chromium from synthetic wastewater using IONPs and their composites through adsorption.

In this adsorption study, the green synthesized IONPs using *Camellia sinensis var. assamica* leaf extract was explored for Cr(VI) removal as a cheap, effective, and eco-friendly adsorbent. The RSM-CCD was applied for the optimization of IONPs synthesis conditions (time, temperature, and iron precursors to leaf extract ratio). The adsorption process followed a pseudo-second-order kinetic model and Langmuir adsorption isotherm, with a remarkably higher Q_m of 1272 mg g^{-1} of IONPs. The adsorption process was described as spontaneous and exothermic. The proposed mechanism behind Cr(VI) removal and detoxification involved adsorption and its reduction to Cr(III), followed by Cr(III)/Fe(III) co-precipitation.

Similarly, reusable and bi-functional (adsorption/reduction) CS beads (CS/IONPs) were developed for Cr(VI) removal. A removal of 98.71% Cr(VI) was achieved by CS/IONPs adsorbent at the optimized pH of 3, CS/IONPs dose of 2.5 g/L, and temperature of 25°C with an initial Cr(VI) concentration of 150 mg/L. The Cr(VI) adsorption was not significantly affected by co-existing cations, whereas anions (PO_4^{3-} and SO_4^{2-}) suppressed the Cr(VI) removal efficiency by 18% and 15.32%, respectively, at an individual ionic concentration of 10 mM. The Cr(VI) removal process was spontaneous and exothermic and followed the pseudo-first-order kinetic. CS/IONPs

composite beads could adsorb a maximum of 345.53 mg Cr(VI) per g of CS/IONPs beads as determined by Langmuir isotherm. The used CS/IONPs beads could be regenerated using NaOH for the initial 4 cycles, but about 15.7% of active sites were reduced afterward. Cr(VI) removal involves electrostatic interaction, Cr(VI) reduction to Cr(III), Cr(III) adsorption, Cr(III) surface complexation through abundant $–NH_2$ group, and Cr(III) co-precipitation with Fe(III).

Simultaneously, the simple preparation of multifunctional beads based on Alg and TA that have a unique combination of metal(s) removal, antimicrobial, and metal particle generation. The beads can reduce Fe salt to form IONPs within them. Thus, formed novel Alg-TA-Fe beads displayed enhanced antibacterial activity and adsorption of Cr(VI) from an aqueous solution. A maximum Cr(VI) removal of 95 % was achieved through Alg-TA75-Fe beads from 20 mg/L aqueous solution. Synergistic antibacterial activity of TA and the Fe particles was observed. The ZOI was also found to be higher for Alg-TA (15-75)-Fe beads than bare Alg-TA (15-75). The antibacterial performance was enhanced by up to 4-fold for *E. hirea* based on bacteria plating experiments for Alg-TA75-Fe beads. The synthesized beads exhibited excellent performance as an adsorbent for removing Cr(VI) and pathogens from aqueous solutions.

Concurrently, continuous column studies were conducted by preparing a packed bed of CS/IONPs and Alg-TA55-Fe beads for Cr(VI) removal. The study investigated the impact of different column parameters, specifically Z (5, 10, and 15 cm) and Q (1, 2, and 3 mL/min). The column exhaustion time exhibits a direct correlation with Z and a declined correlation with Q. In particular, t_b for CS/IONPs and Alg-TA55-Fe beads drops from 5 to 1.5 h and 0.75 to 0.37 h, respectively, as Q increased from 1 to 3 mL/min. However, increasing Z from 5 to 15 cm enhances the t_b values by 4.4 and 6 times for CS/IONPs and Alg-TA55-Fe beads, respectively. The efficiency of CS/IONPs in removing Cr(VI) was superior to that of Alg-TA55-Fe beads, as

indicated by the significantly higher q_{eq} values of 6.53 times for CS/IONPs compared to Alg-TA55-Fe beads. The adsorption data was well fitted to various known fixed-bed adsorption models, including the Yoon-Nelson, Thomas, Adams-Bohart, Clark, and Bed Depth Service Time models, with correlation coefficients, $R^2 \geq 0.94$. The column was regenerated by eluting the used CS/IONPs and Alg-TA55-Fe beads using NaOH solution after Cr(VI) adsorption. Two regeneration cycles were conducted in the same column for Cr(VI) re-adsorption performance, and CS/IONPs beads outperformed Alg-TA55-Fe beads for Cr(VI) re-adsorption, exhibiting longer t_b and higher q_{eq} values.

7.2. Recommendations for future work

Adsorption has shown potential in eliminating several metal pollutants from contaminated water, including hexavalent chromium. Hexavalent chromium removal has been investigated using natural and synthetic adsorbents, including the ones that have been the focus of our research. Our investigation of environmentally friendly synthesized IONPs nanoadsorbents and their composites leads to the conclusion that these particles hold significant promise for effectively treating a wide range of contaminants such as dyes, heavy metals, etc., including hexavalent chromium. The prospects of the current work are as follows:

7.2.1 Attempts have been undertaken to create nanomaterials through the imitation of bio based synthesis, employing natural bio-extracts. However, the specific roles of each phytochemical have yet to be understood

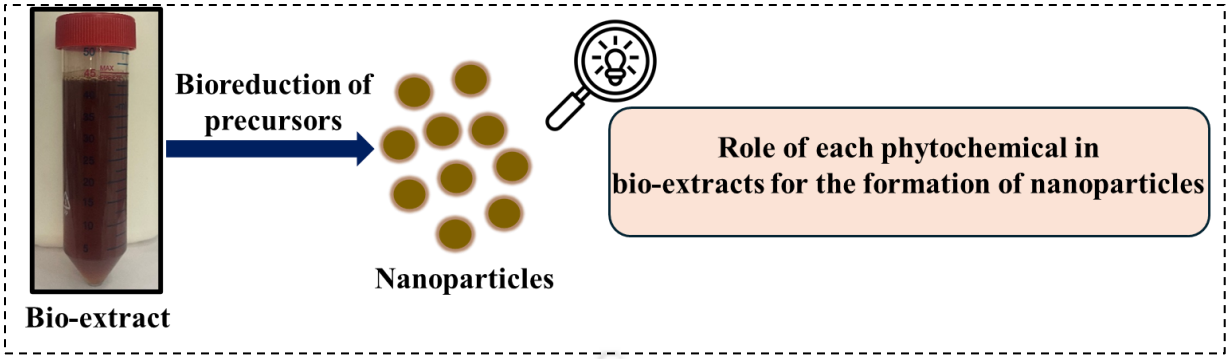

Researchers have created nanomaterials by utilizing natural bio-extracts through green synthesis method. These methods use the natural characteristics of phytochemicals present in plants extract as a reducing agent to facilitate the production of nanoparticles, providing an environmentally friendly and sustainable alternative to traditional chemical techniques. Despite some progress in this field, the specific functions of each phytochemical in the synthesis process remain largely unexplored. Gaining insight into the role of these natural compounds in the formation, functionalization, and stabilization of nanoparticles is essential for improving the synthesis methods and boosting the characteristics of the final synthesized product (nanomaterials). In this regard, additional investigation is necessary to elucidate the precise functions performed by various phytochemicals, potentially leading to the advancement of more efficient and tailored synthesis methodologies.

7.2.2 Newly explored adsorbents can undergo testing for the adsorption of other heavy metals, and pigmenting agents, either separately or in combination and/or from synthetic/industrial wastewater

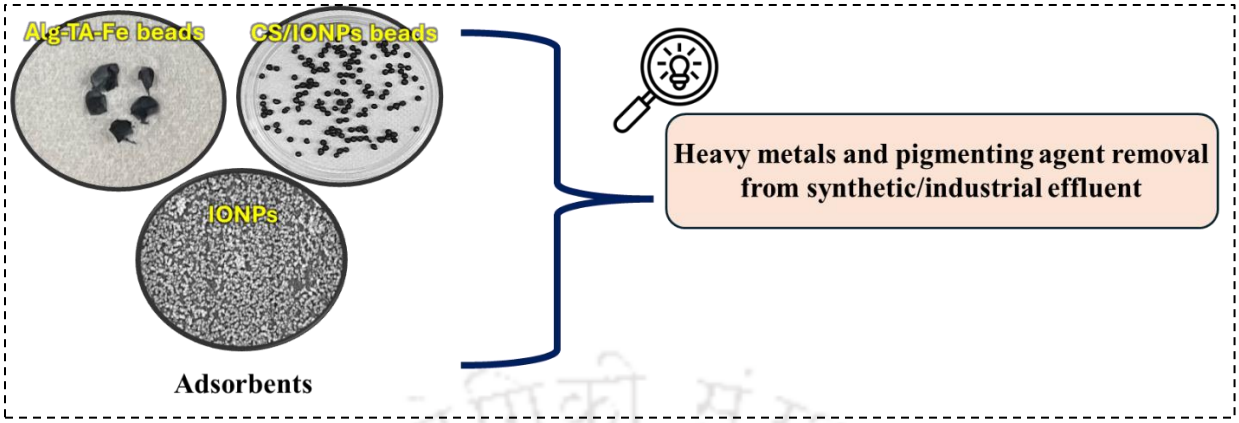

The investigated adsorbents (IONPs, CS/IONPs beads and Alg-TA-Fe beads) offer promising prospects for broader applications in the field of environmental remediation. These materials can be evaluated for their ability to absorb a wide range of heavy metals and dyes, either individually or in combination, from synthetic and industrial effluents. The adsorption study utilizes the explored adsorbents to remove contaminants from synthetic/industrial wastewater under the best possible conditions. Moreover, performing studies with industrial wastewater will provide a good comprehension of practical applications, given the complex mixture of contaminants typically found in industrial effluents. Through a comprehensive investigation of the performance of these adsorbents under different situations, researchers may determine their potential for removing various contaminants, optimizing operational parameters, and designing more efficient and adaptable treatment procedures for environmental remediation.

7.2.3 The efficacy of hexavalent chromium removal can also be checked through various combinations of CS/IONPs and Alg-TA-Fe beads in a continuous operation from synthetic/industrial wastewater

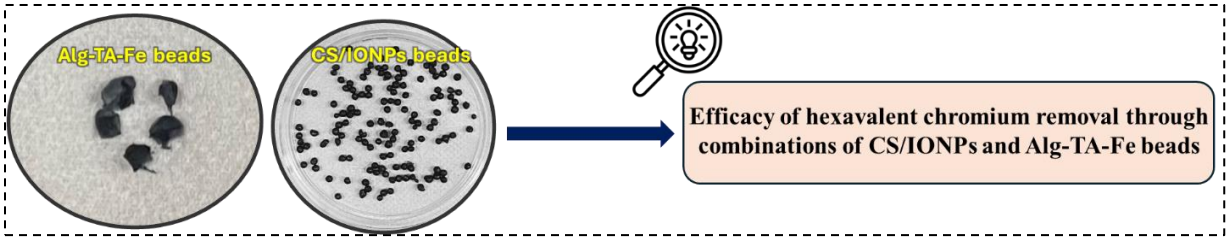

The effectiveness of hexavalent chromium removal can be further tested at lower flow rates (<1 mL/min) and by employing various combinations of CS/IONPs and Alg-TA-Fe beads in continuous operations on synthetic or industrial wastewater. This strategy enables the enhancement of removal efficiency in practical flow circumstances, replicating scenarios of industrial wastewater treatment. The researchers can find combined effects that make hexavalent chromium removal more effective by changing the amounts of CS/IONPs and Alg-TA-Fe beads in varying ratios. This systematic testing is essential to create long-term practical solutions for treating wastewater contaminated with hexavalent chromium, ultimately enhancing environmental management and safeguarding public health.

7.2.4 Exploring the application of the adsorbent (CS/IONPs beads) for hexavalent chromium removal on a larger scale, using a continuous mode operation, as compared to the current bench-top study

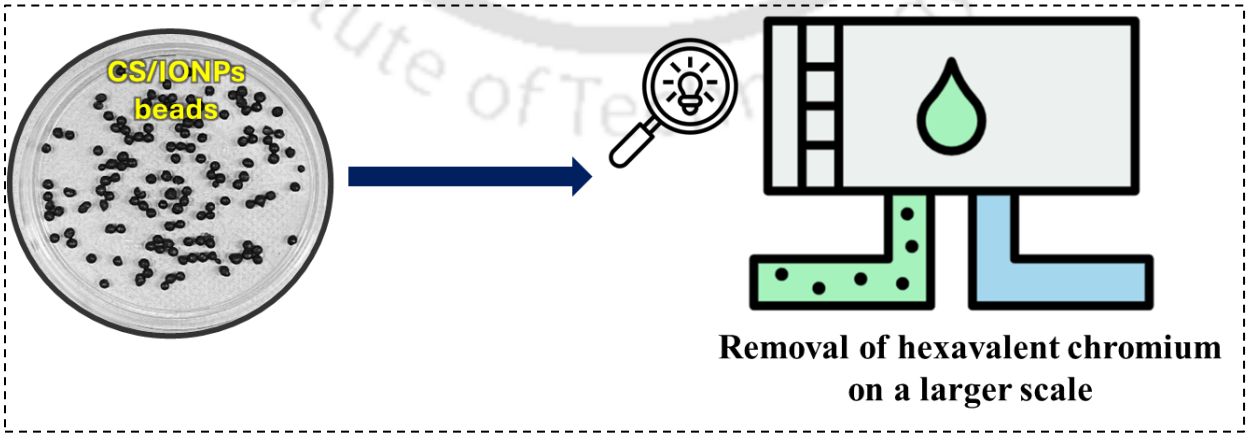

Several obstacles must be overcome to scale up the removal of hexavalent chromium using CS/IONP beads, including maintaining adsorption efficiency over long periods, optimizing flow rates, and ensuring stable bead quality. Continuous mode operation is preferred over batch procedures due to its ability to simulate actual commercial conditions accurately. The expanded utilization of CS/IONPs beads would enable a more comprehensive assessment of their performance, stability, and regenerative capacity in response to varying environmental conditions. Furthermore, it would offer valuable information regarding operating parameters, including contact time and column height, which are crucial for designing complete treatment systems at a larger scale. This continuous mode study could open the path for utilizing CS/IONPs beads in industrial wastewater treatment plants, resulting in more sustainable and efficient hexavalent chromium removal options.

7.2.4 Utilizing various approaches to thoroughly assess the financial aspects of the synthesized adsorbent to achieve cost-effectiveness and improve their sustainability and efficiency

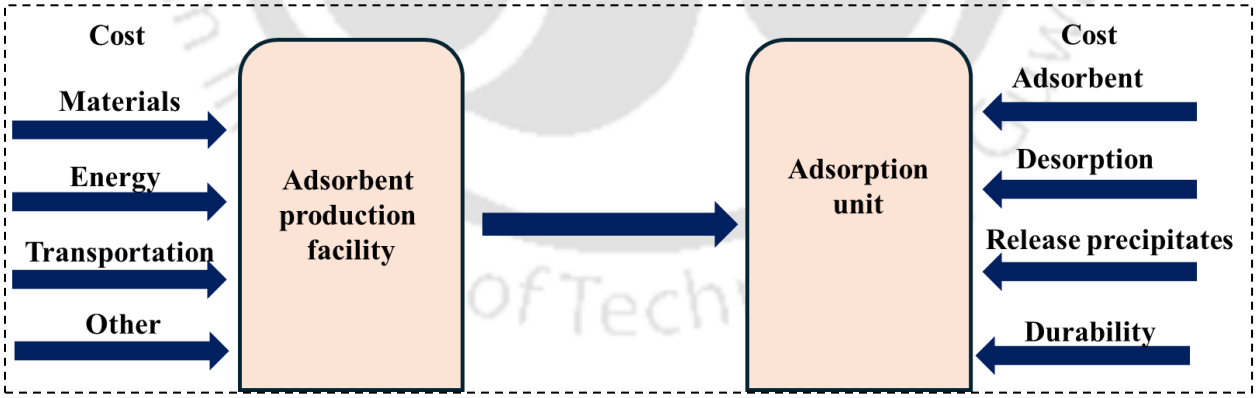

The high treatment cost is the primary obstacle for implementing various approaches to remove hexavalent chromium in the real world. It would be highly beneficial to evaluate the viability of these methodologies in industrial-based field applications by investigating cost analysis using various strategies.

Appendices

Appendix Chapter 3

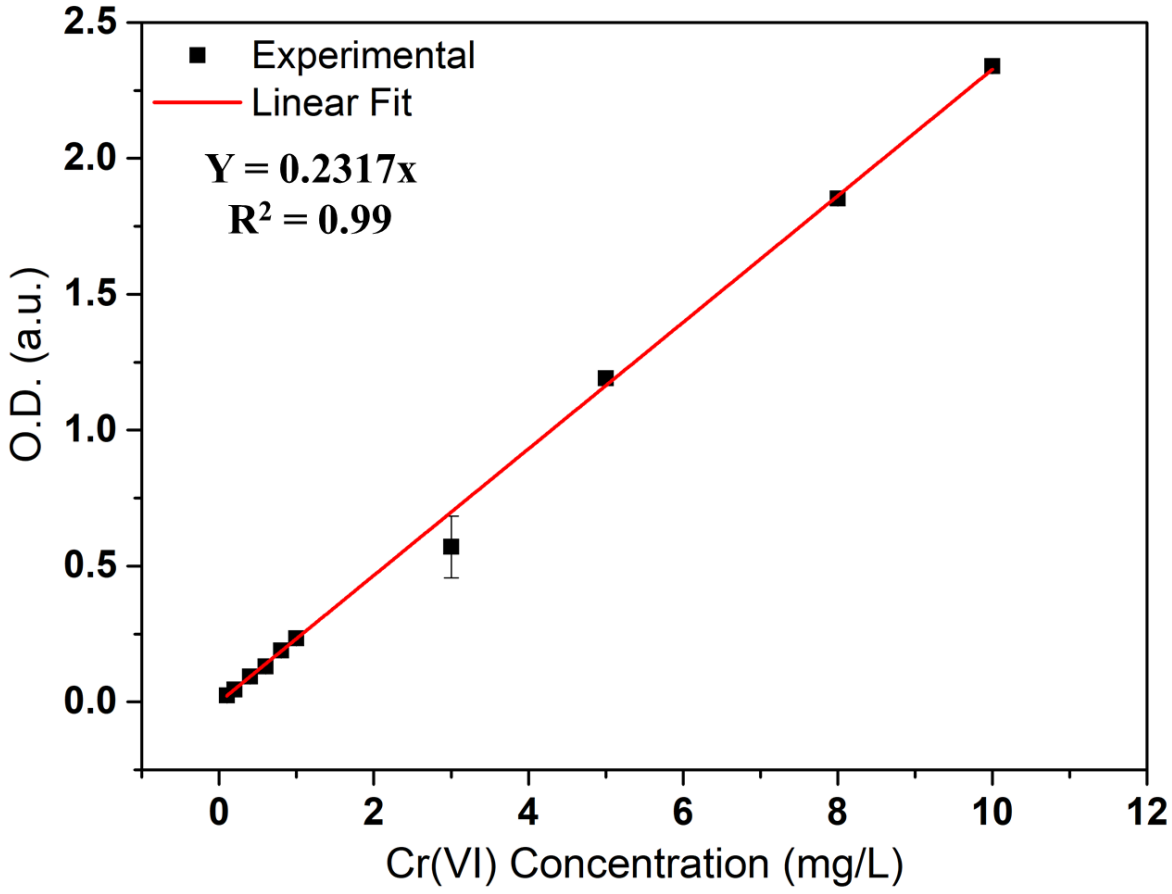

Figure S3 (a): Standard calibration curve of Cr(VI) with DPC reagent.

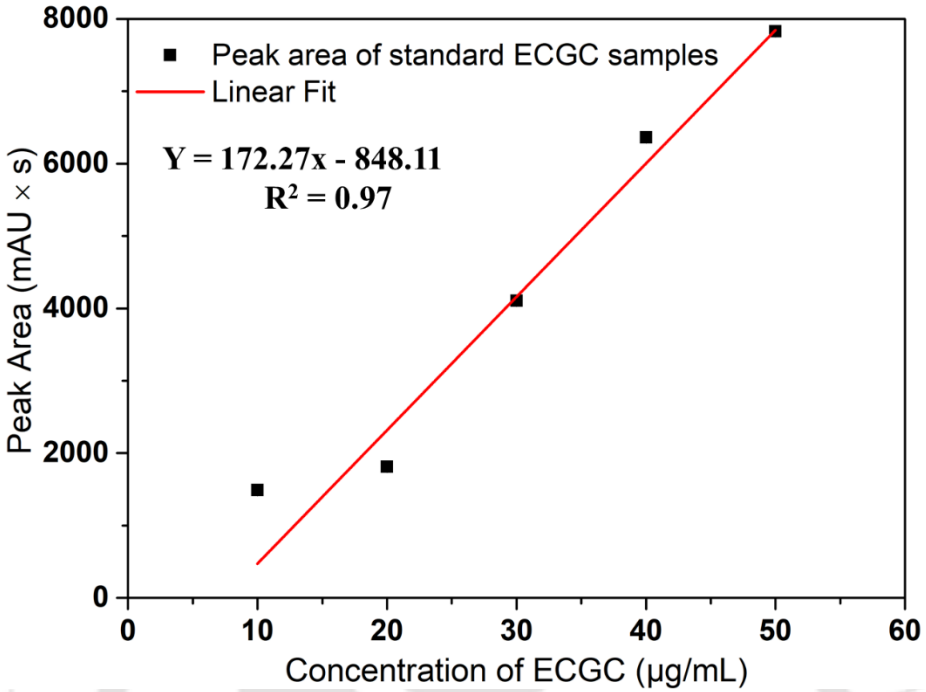

Figure S3 (b): ECGC standard calibration curve.

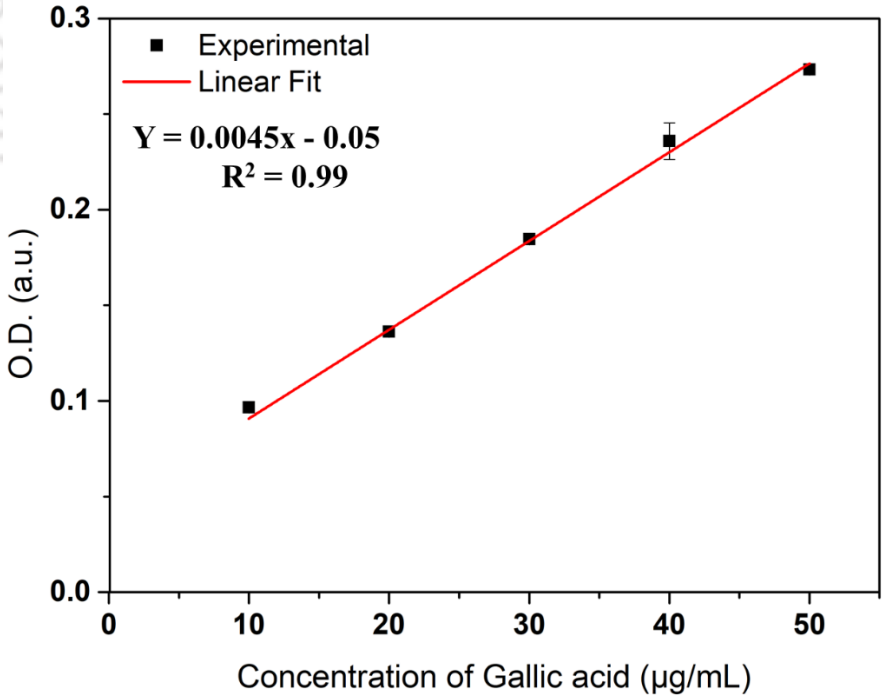

Figure S3 (c): Calibration curve plot of Gallic acid standard at various concentrations in µg/mL versus O.D at 765 nm.

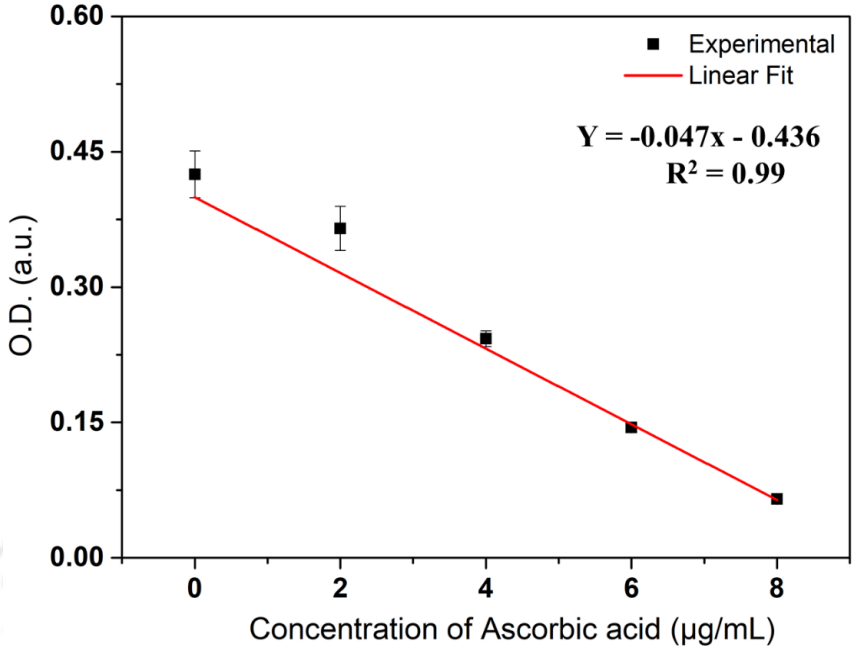

Figure S3 (d): Calibration curve plot of ascorbic acid standard at various concentrations in µg/mL versus O.D at 515 nm.

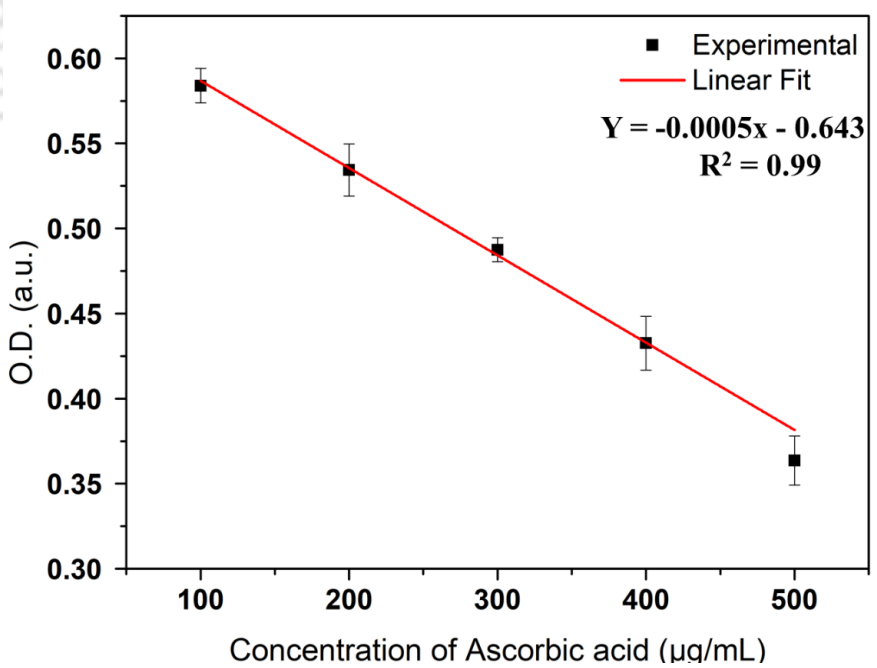

Figure S3 (e): Calibration curve plot of ascorbic acid standard at various concentrations in µg/mL versus O.D at 420 nm.

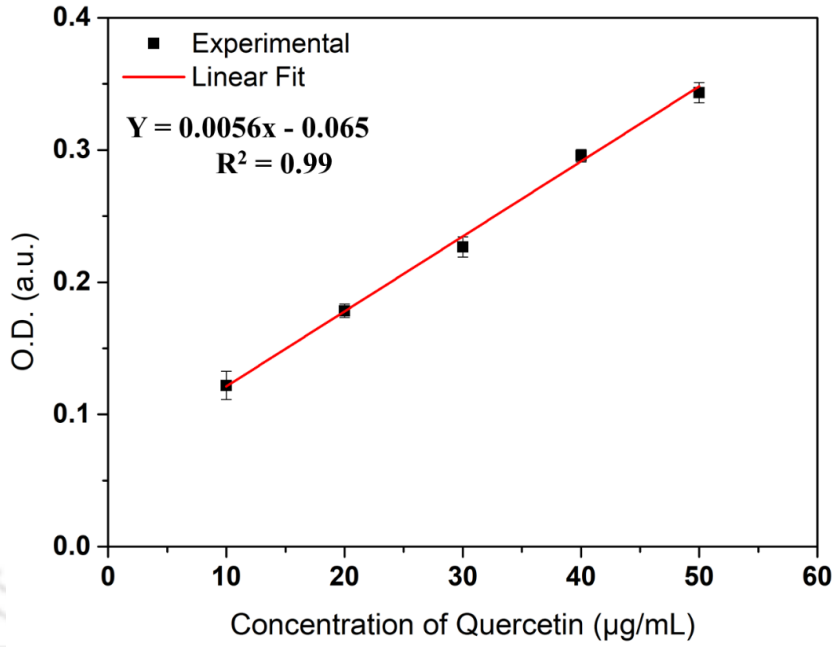

Figure S3 (f): Calibration curve plot of quercetin standard at various concentrations in µg/mL versus O.D at 415 nm.

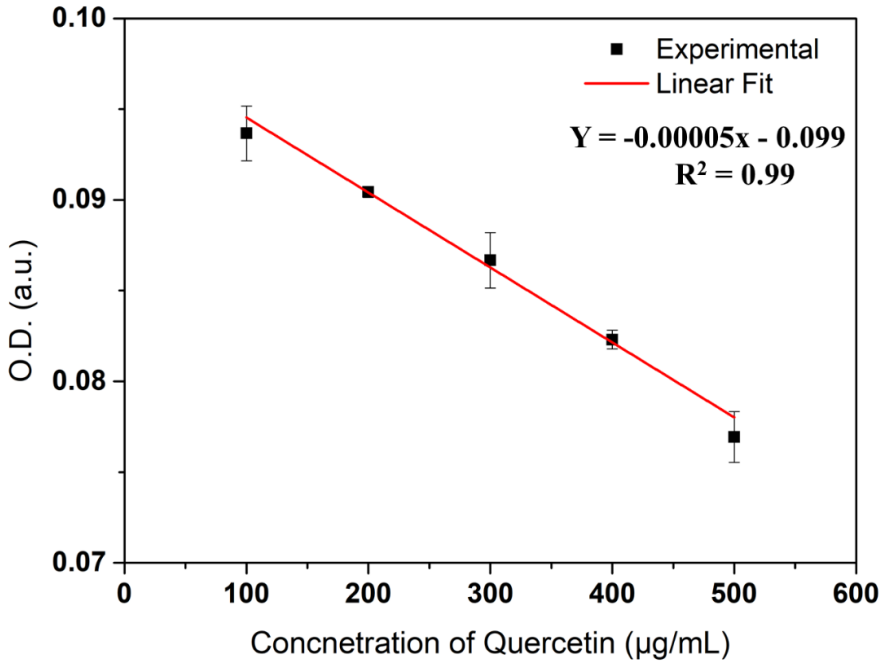

Figure S3 (g): Calibration curve plot of quercetin standard at various concentrations in µg/mL versus O.D at 700 nm.

Appendix Chapter 4

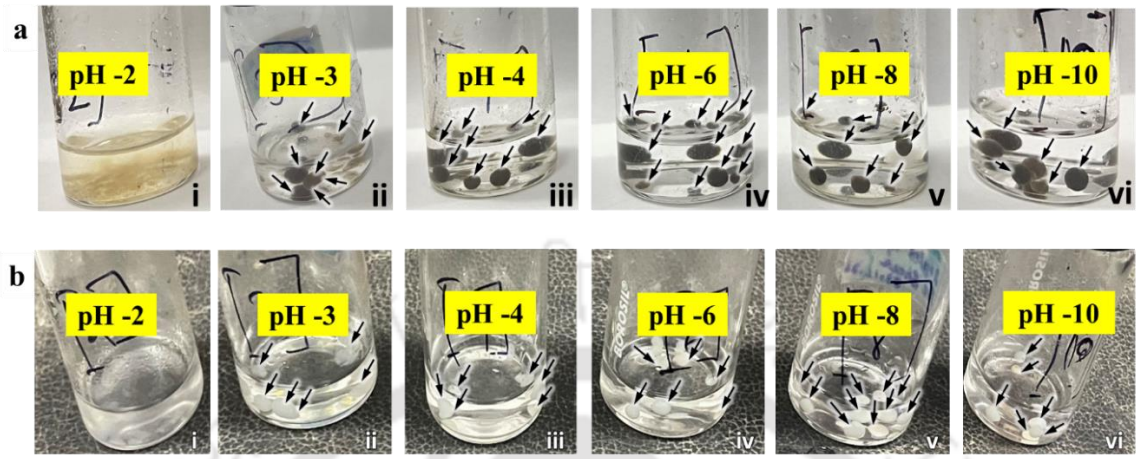

Figure S4: (a) Stability of synthesized (a) CS/IONPs and (b) CS beads at various pH conditions (a (i-vi) and b (i-vi)) of double distilled water, respectively.

Appendix Chapter 5

Table S5 (a): Elemental (O, C, Fe, Ca and Na) compositions in projected particles coverage of Alg-TA55-Fe bead as exposed from SEM-EDS spectrum.

Scan area label	Estimated particle coverage	O %	C %	Fe %	Ca %	Na %
2	42%	47 ± 9%	37 ± 11%	8 ± 3%	8 ± 2%	0%
7	22%	46 ± 10%	35 ± 12%	7 ± 4%	12 ± 3%	0%
3	12%	43 ± 11%	29 ± 16%	14 ± 5%	13 ± 3%	1 ± 1%
5	7%	30 ± 10%	0%	(39 ± 10%)	(25 ± 6%)	6 ± 3%
4	7%	39 ± 11%	30 ± 17%	12 ± 5%	18 ± 5%	0%
1	5%	58 ±2 4%	11 ± 37%	17 ± 9%	15 ± 7%	0%
6	3%	42 ± 8%	36 ± 11%	11 ± 4%	11 ± 2%	0%
Ideal Alg		50%	50%	-	-	-
Ideal TA		38%	62%	-	-	-
Ideal Alg-TA55		43%	57%	-	-	-

Table S5 (b): Enlisted various oxygen species binding energy (eV) and their corresponding areas (eV-cps) as revealed from deconvoluted XPS O1s high resolution spectra's of Alg-Fe and Alg-TA55-Fe beads, respectively.

Peak	Alg/TA	Alg/TA	TA quinone	Alg/TA ester/water	TA hydroquinone	Unassigned species
	O-Fe(x)	O=C-O/Fe-OOH	O=C-Ph	O-C/C-O-C/O-H	O-Ph	-
4pk Alg-Fe	530.4	531.6	0.0	532.3	0.0	534.0
6pk Alg-TA55-Fe	529.7	531.0	531.9	532.8	533.9	534.6

Area	Alg/TA	Alg/TA	TA Quinone	Alg/TA ester/water	TA hydroquinone	Unassigned species
	O-Fe(x)	O=C-O/Fe-OOH	O=C-Ph	O-C/C-O-C/O-H	O-Ph	-
4pk Alg-Fe	740	3130	0	9535	0	2620
6pk Alg-TA55-Fe	10360	22969	20326	36737	20022	0

Table S1 (c): Enlisted various carbon species binding energy (eV) and their corresponding areas (eV-cps) as revealed from deconvoluted XPS C1s high resolution spectra's of Alg-Fe and Alg-TA55-Fe beads, respectively.

Peak	TA aromatic C=C	Adventitious C or TA C-C	Alg	Alg/TA ether/ hydroxyquinone..Fe	TA oxidized	Alg carbonate	Alg acid/TA ester
	C=C	C-C	C-O	O-C-O/C-O..Fe	Ph=O	O-C=O..Ca/Fe	HO-C=O/Ph-O-C=O
Alg-Fe	0.0	284.8	286.0	286.9	0.0	288.0	290.1
6pk Alg-TA55-Fe	284.5	0.0	286.3	286.4	287.5	288.9	290.5
3pk Alg	0.0	284.8	286.0	286.9	0.0	288.0	290.1
4pk Alg-TA55	284.5	284.8	285.9	286.3	287.3	289.0	290.6

Area	TA aromatic C=C	Adventitious C	Alg	Alg/TA ether/ hydroxyquinone..Fe	TA oxidized	Alg carbonate	Alg acid/TA ester
	C=C	C-C	C-O	O-C-O/C-O..Fe	Ph=O	O-C=O..Ca/Fe	HO-C=O/Ph-O-C=O
Alg-Fe	0	110	3206	749	0	457	278
6pk Alg-TA55-Fe	3819	0	6081	1338	5169	3060	1445
3pk Alg	0	1471	13504	3076	0	1731	1948
4pk Alg-TA55	3271	3874	4064	753	1408	1227	153

Table S5 (d): XPS high resolution spectrum's (i) $Fe2p_{3/2}$, (ii) O1s, and (ii) C1s deconvoluted binding energy (eV) peaks

i

Environment	$Fe2p_{3/2}$
Fe metal	706.7 eV
$Fe(C_6H_5OOH)_2$	707.7 eV
FeO	708.2 eV
Fe_2O_3	708.4 eV
FeOOH	709.4 eV

ii

Environment	O1s
Fe_2O_3	529.6 eV
FeO	529.8 eV
FeO*OH	530.1 eV
FeOO*H	531.2 eV
$Fe(OH)_2$	531.3 eV
PhCOONa	531.4 eV
Ph=O benzoquinone	532.2 eV
H_2O	532.8 eV
Ph-OH hydroquinone	533.2 eV

iii

Environment	C1s
C=C	284.5 eV
C-C	284.8 eV
C-O cellulose	286.2 eV
Ph-OH hydroquinone	286.4 eV
O-C-O	~287 eV
Ph=O benzoquinone	287.4 eV
CH_3COONa acetate	288.2 eV
CH_3COOAg acetate	288.3 eV
Ph-COOH	288.9 eV
CH_3COOH acetic acid	289.4 eV
Ph-O-(C=O)-O-Ph aromatic ester	290.7 eV

References

[1] P.B. Tchounwou, C.G. Yedjou, A.K. Patlolla, D.J. Sutton, Heavy metal toxicity and the environment, Molecular, clinical and environmental toxicology: volume 3: Environmental Toxicology (2012) 133-164.

[2] A. Zhitkovich, Chromium in drinking water: sources, metabolism, and cancer risks, Chemical Research in Toxicology 24(10) (2011) 1617-1629.

[3] S.A. Cavaco, S. Fernandes, M.M. Quina, L.M. Ferreira, Removal of chromium from electroplating industry effluents by ion exchange resins, Journal of hazardous materials 144(3) (2007) 634-638.

[4] J. Barnhart, Occurrences, uses, and properties of chromium, Regulatory toxicology and pharmacology 26(1) (1997) S3-S7.

[5] K. Sreeram, T. Ramasami, Sustaining tanning process through conservation, recovery and better utilization of chromium, Resources, conservation and recycling 38(3) (2003) 185-212.

[6] A. Baral, R.D. Engelken, Chromium-based regulations and greening in metal finishing industries in the USA, Environmental Science & Policy 5(2) (2002) 121-133.

[7] T. Sanyal, A. Kaviraj, S. Saha, Deposition of chromium in aquatic ecosystem from effluents of handloom textile industries in Ranaghat–Fulia region of West Bengal, India, Journal of Advanced Research 6(6) (2015) 995-1002.

[8] L. Li, Q. Liao, B. Hou, C. He, J. Liu, B. Li, M. Yu, Y. Liu, B. Lai, B. Yang, Synchronous reduction and removal of hexavalent chromium from wastewater by modified magnetic chitosan beads, Separation and Purification Technology. 304 (2023) 122363.

[9] E. Kaprara, N. Kazakis, K. Simeonidis, S. Coles, A. Zouboulis, P. Samaras, M. Mitrakas, Occurrence of Cr (VI) in drinking water of Greece and relation to the geological background, Journal of Hazardous Materials 281 (2015) 2-11.

[10] S. Mohanty, A. Benya, S. Hota, M.S. Kumar, S. Singh, Eco-toxicity of hexavalent chromium and its adverse impact on environment and human health in Sukinda Valley of India: A review on pollution and prevention strategies, Environmental Chemistry and Ecotoxicology (2023).

[11] K. Rong, J. Wang, Z. Zhang, J. Zhang, Green synthesis of iron nanoparticles using Korla fragrant pear peel extracts for the removal of aqueous Cr (VI), Ecological Engineering 149 (2020) 105793.

[12] R. Hao, D. Li, J. Zhang, Insights into the removal of Cr (VI) from aqueous solution using plant-mediated biosynthesis of iron nanoparticles, Environmental Technology & Innovation 23 (2021) 101566.

[13] A. Truskewycz, R. Shukla, A.S. Ball, Phytofabrication of iron nanoparticles for hexavalent chromium remediation, ACS Omega 3(9) (2018) 10781-10790.

[14] V.E. Pakade, N.T. Tavengwa, L.M. Madikizela, Recent advances in hexavalent chromium removal from aqueous solutions by adsorptive methods, RSC Advances 9(45) (2019) 26142-26164.

[15] S.K. Sharma, B. Petrusevski, G. Amy, Chromium removal from water: a review, Journal of Water Supply: Research and Technology - AQUA 57(8) (2008) 541-553.

[16] M.M. Islam, A.A. Mohana, M.A. Rahman, M. Rahman, R. Naidu, M.M. Rahman, A Comprehensive Review of the Current Progress of Chromium Removal Methods from Aqueous Solution, Toxics 11(3) (2023) 252.

[17] H.N. Alavijeh, M. Sadeghi, M.R.K. Kashani, A. Moheb, Efficient chemical coagulation-electrocoagulation-membrane filtration integrated systems for baker's yeast wastewater treatment: experimental and economic evaluation, Cleaner Chemical Engineering 3 (2022) 100032.

[18] H. Karimi-Maleh, A. Ayati, S. Ghanbari, Y. Orooji, B. Tanhaei, F. Karimi, M. Alizadeh, J. Rouhi, L. Fu, M. Sillanpää, Recent advances in removal techniques of Cr (VI) toxic ion from aqueous solution: A comprehensive review, Journal of Molecular Liquids 329 (2021) 115062.

[19] S. Vijayaram, H. Razafindralambo, Y.-Z. Sun, S. Vasantharaj, H. Ghafarifarsani, S.H. Hoseinifar, M. Raeeszadeh, Applications of Green Synthesized Metal Nanoparticles - A Review, Biological Trace Element Research (2023) 1-27.

[20] S. Pallavi, S.R. Yashas, K.M. Anilkumar, B. Shahmoradi, H.P. Shivaraju, Comprehensive understanding of urban water supply management: towards sustainable water-socio-economic-health-environment nexus, Water Resources Management 35 (2021) 315-336.

[21] N. Khatri, S. Tyagi, Influences of natural and anthropogenic factors on surface and groundwater quality in rural and urban areas, Frontiers in Life Science 8(1) (2015) 23-39.

[22] D. Pradhan, L.B. Sukla, M. Sawyer, P.K. Rahman, Recent bioreduction of hexavalent chromium in wastewater treatment: A review, Journal of Industrial and Engineering Chemistry 55 (2017) 1-20.

[23] V.A. Tzanakakis, N.V. Paranychianakis, A.N. Angelakis, Water Supply and Water Scarcity, MDPI, 2020, p. 2347.

[24] G. Chandnani, P. Gandhi, D. Kanpariya, D. Parikh, M. Shah, A comprehensive analysis of contaminated groundwater: Special emphasis on nature-ecosystem and socio-economic impacts, Groundwater for Sustainable Development (2022) 100813.

[25] A. Boretti, L. Rosa, Reassessing the projections of the world water development report, NPJ Clean Water 2(1) (2019) 15.

[26] O. Al-Hashimi, K. Hashim, E. Loffill, T. Marolt Čebašek, I. Nakouti, A.A. Faisal, N. Al-Ansari, A comprehensive review for groundwater contamination and remediation: occurrence, migration and adsorption modelling, Molecules 26(19) (2021) 5913.

[27] I. Mukherjee, U.K. Singh, R.P. Singh, An overview on heavy metal contamination of water system and sustainable approach for remediation, Water Pollution and Management Practices (2021) 255-277.

[28] M.M. Osiemo, G.M. Ogendi, C. M'Erimba, Microbial quality of drinking water and prevalence of water-related diseases in Marigat Urban Centre, Kenya, Environmental Health Insights 13 (2019) 1178630219836988.

[29] P. Kumar, S. Srivastava, A. Banerjee, S. Banerjee, Prevalence and predictors of water-borne diseases among elderly people in India: evidence from Longitudinal Ageing Study in India, 2017–18, BMC public health 22(1) (2022) 993.

[30] M. Varsha, P.S. Kumar, B.S. Rathi, A review on recent trends in the removal of emerging contaminants from aquatic environment using low-cost adsorbents, Chemosphere 287 (2022) 132270.

[31] M. Holt, Sources of chemical contaminants and routes into the freshwater environment, Food and chemical toxicology 38 (2000) S21-S27.

[32] E. Dinwiddie, X.-M. Liu, Examining the geologic link of arsenic contamination in groundwater in Orange County, North Carolina, Frontiers in Earth Science 6 (2018) 111.

[33] L.E. Lesser, A. Mora, C. Moreau, J. Mahlknecht, A. Hernández-Antonio, A.I. Ramírez, H. Barrios-Piña, Survey of 218 organic contaminants in groundwater derived from the world's largest untreated wastewater irrigation system: Mezquital Valley, Mexico, Chemosphere 198 (2018) 510-521.

[34] S. Sharma, A. Bhattacharya, Drinking water contamination and treatment techniques, Applied Water Science 7(3) (2017) 1043-1067.

[35] P. Li, D. Karunanidhi, T. Subramani, K. Srinivasamoorthy, Sources and consequences of groundwater contamination, Archives of Environmental Contamination and Toxicology 80 (2021) 1-10.

[36] S. Schulze, D. Zahn, R. Montes, R. Rodil, J.B. Quintana, T.P. Knepper, T. Reemtsma, U. Berger, Occurrence of emerging persistent and mobile organic contaminants in European water samples, Water Research 153 (2019) 80-90.

[37] C.A. Damalas, I.G. Eleftherohorinos, Pesticide exposure, safety issues, and risk assessment indicators, International Journal of Environmental Research and Public Health 8(5) (2011) 1402-1419.

[38] I.S. BIS, 10500 Indian Standard Drinking Water–Specification, first revision, Bureau of Indian Standards, New Delhi, India (1991).

[39] M. Irfan, X. Liu, K. Hussain, S. Mushtaq, J. Cabrera, P. Zhang, The global research trend on cadmium in freshwater: a bibliometric review, Environmental Science and Pollution Research (2021) 1-14.

[40] K.D. Bradham, C.M. Nelson, T.D. Sowers, D.A. Lytle, J. Tully, M.R. Schock, K. Li, M.D. Blackmon, K. Kovalcik, D. Cox, A national survey of lead and other metal (loids) in residential drinking water in the United States, Journal of Exposure Science & Environmental Epidemiology 33(2) (2023) 160-167.

[41] H. Hossini, B. Shafie, A.D. Niri, M. Nazari, A.J. Esfahlan, M. Ahmadpour, Z. Nazmara, M. Ahmadimanesh, P. Makhdoumi, N. Mirzaei, A comprehensive review on human health effects of chromium: Insights on induced toxicity, Environmental Science and Pollution Research 29(47) (2022) 70686-70705.

[42] S. Gardham, A.A. Chariton, G.C. Hose, Direct and indirect effects of copper-contaminated sediments on the functions of model freshwater ecosystems, Ecotoxicology 24 (2015) 61-70.

[43] M. David, R. Kartheek, Histopathological alterations in spleen of freshwater fish Cyprinus carpio exposed to sublethal concentration of sodium cyanide, Open Veterinary Journal 5(1) (2015) 1-5.

[44] P. Jankong, C. Chalhoub, N. Kienzl, W. Goessler, K.A. Francesconi, P. Visoottiviseth, Arsenic accumulation and speciation in freshwater fish living in arsenic-contaminated waters, Environmental Chemistry 4(1) (2007) 11-17.

[45] T.M. Missimer, C. Teaf, R.G. Maliva, A. Danley-Thomson, D. Covert, M. Hegy, Natural radiation in the rocks, soils, and groundwater of Southern Florida with a discussion on potential health impacts, International Journal of Environmental Research and Public Health 16(10) (2019) 1793.

[46] U. EPA, National recommended water quality criteria, United States Environmental Protection Agency, Office of Water, Office of Science and Technology (2009).

[47] M. Seidel, L. Jurzik, I. Brettar, M.G. Höfle, C. Griebler, Microbial and viral pathogens in freshwater: current research aspects studied in Germany, Environmental Earth Sciences 75 (2016) 1-20.

[48] J.A. Castro-Hermida, I. García-Presedo, A. Almeida, M. González-Warleta, J.M.C. Da Costa, M. Mezo, Detection of Cryptosporidium spp. and Giardia duodenalis in surface water: a health risk for humans and animals, Water Research 43(17) (2009) 4133-4142.

[49] J.H. Duffus, " Heavy metals" a meaningless term?(IUPAC Technical Report), Pure and Applied Chemistry 74(5) (2002) 793-807.

[50] E. Malkoc, Y. Nuhoglu, M. Dundar, Adsorption of chromium (VI) on pomace—an olive oil industry waste: batch and column studies, Journal of Hazardous Materials 138(1) (2006) 142-151.

[51] M. Lenz, P.N. Lens, The essential toxin: the changing perception of selenium in environmental sciences, Science of the Total Environment 407(12) (2009) 3620-3633.

[52] M.K. Abd Elnabi, N.E. Elkaliny, M.M. Elyazied, S.H. Azab, S.A. Elkhalifa, S. Elmasry, M.S. Mouhamed, E.M. Shalamesh, N.A. Alhorieny, A.E. Abd Elaty, Toxicity of heavy metals and recent advances in their removal: A review, Toxics 11(7) (2023) 580.

[53] H.A. Maitlo, K.-H. Kim, V. Kumar, S. Kim, J.-W. Park, Nanomaterials-based treatment options for chromium in aqueous environments, Environment International 130 (2019) 104748.

[54] S.A. Katz, H. Salem, The biological and environmental chemistry of chromium, VCH Publishers1994.

[55] U.S. Geological Survey (2022) Chromium, minerals yearbook. https://www.usgs.gov/centers/national-minerals-information-center/chromium-statistics-and-information.

[56] T. ATSDR, ATSDR (Agency for toxic substances and disease registry), Prepared by clement international corp., under contract 205 (2000) 88-0608.

[57] D.E. Kimbrough, Y. Cohen, A.M. Winer, L. Creelman, C. Mabuni, A critical assessment of chromium in the environment, Critical Reviews in Environmental Science and Technology 29(1) (1999) 1-46.

[58] R. Shrivastava, R. Upreti, P. Seth, U. Chaturvedi, Effects of chromium on the immune system, FEMS Immunology & Medical Microbiology 34(1) (2002) 1-7.

[59] E.W. Huffman Jr, W.H. Allaway, Chromium in plants. Distribution in tissues, organelles, and extracts and availability of bean leaf chromium to animals, Journal of Agricultural and Food Chemistry 21(6) (1973) 982-986.

[60] D. Rai, L. Eary, J.M. Zachara, Environmental chemistry of chromium, Science of the Total Environment 86(1-2) (1989) 15-23.

[61] S.E. Fendorf, Surface reactions of chromium in soils and waters, Geoderma 67(1-2) (1995) 55-71.

[62] S. De Flora, M. Bagnasco, D. Serra, P. Zanacchi, Genotoxicity of chromium compounds. A review, Mutation Research/Reviews in Genetic Toxicology 238(2) (1990) 99-172.

[63] A. Hartwig, Carcinogenicity of metal compounds: possible role of DNA repair inhibition, Toxicology Letters 102 (1998) 235-239.

[64] A. Zhitkovich, Importance of chromium− DNA adducts in mutagenicity and toxicity of chromium (VI), Chemical Research in Toxicology 18(1) (2005) 3-11.

[65] K. Mandiwana, N. Panichev, M. Kataeva, S. Siebert, The solubility of Cr (III) and Cr (VI) compounds in soil and their availability to plants, Journal of Hazardous Materials 147(1-2) (2007) 540-545.

[66] C. Cervantes, J. Campos-García, S. Devars, F. Gutiérrez-Corona, H. Loza-Tavera, J.C. Torres-Guzmán, R. Moreno-Sánchez, Interactions of chromium with microorganisms and plants, FEMS Microbiology Reviews 25(3) (2001) 335-347.

[67] H.P. Singh, P. Mahajan, S. Kaur, D.R. Batish, R.K. Kohli, Chromium toxicity and tolerance in plants, Environmental Chemistry Letters 11(3) (2013) 229-254.

[68] T.K. Tokunaga, J. Wan, T.C. Hazen, E. Schwartz, M.K. Firestone, S.R. Sutton, M. Newville, K.R. Olson, A. Lanzirotti, W. Rao, Distribution of chromium contamination and microbial activity in soil aggregates, Journal of Environmental Quality 32(2) (2003) 541-549.

[69] F. Edition, Guidelines for drinking-water quality, WHO chronicle 38(4) (2011) 104-8.

[70] C.o.E. Union, European Commission Council Directive 98/83/EC of 3 November 1998 on the quality of water intended for human consumption, Official J Eur Communities L 330 (1998) 32-54.

[71] CPCB, The Environment (protection) Rules, 1986, Schedule VI (Amended 1993), Central Pollution Control Board New Delhi, 1986.

[72] R. Saha, R. Nandi, B. Saha, Sources and toxicity of hexavalent chromium, Journal of Coordination Chemistry 64(10) (2011) 1782-1806.

[73] A. Banchhor, M. Pandey, P.K. Pandey, A review of hexavalent chromium contamination in India, Research Journal of Chemical Sciences 7 (2017) 39-44.

[74] M.G. Dalcin, M.M. Pirete, D.A. Lemos, E.J. Ribeiro, V.L. Cardoso, M.M. de Resende, Evaluation of hexavalent chromium removal in a continuous biological filter with the use of central composite design (CCD), Journal of Environmental Management 92(4) (2011) 1165-1173.

[75] S. Jain, L. Kamimoto, A.M. Bramley, A.M. Schmitz, S.R. Benoit, J. Louie, D.E. Sugerman, J.K. Druckenmiller, K.A. Ritger, R. Chugh, Hospitalized patients with 2009 H1N1 influenza in the United States, April–June 2009, New England Journal of Medicine 361(20) (2009) 1935-1944.

[76] D.S. Thambavani, V. Prathipa, Physico-chemical characteristics of leather tannery effluent-current scenario in Dindigul town (Tamil Nadu), India, Asian Journal of Environmental Science 6(2) (2011) 119-124.

[77] V. Singh, C. Ram, A. Kumar, Physico-chemical characterization of electroplating industrial effluents of Chandigarh and Haryana Region, Journal of Civil and Environmental Engineering 6(237) (2016) 2.

[78] G. Sathiyaraj, K.C. Ravindran, Z.H. Malik, Physico-chemical characteristics of textile effluent collected from Erode, Pallipalayam and Bhavani polluted regions, Tamilnadu, India, Journal of Ecobiotechnology 9 (2017).

[79] R. Hao, D. Li, J. Zhang, T. Jiao, Green synthesis of iron nanoparticles using green tea and its removal of hexavalent chromium, Nanomaterials 11(3) (2021) 650.

[80] U. EPA, Health effects test guidelines: OPPTS 870.3465 90-day inhalation toxicity, EPA 712-C-98-204 (1998).

[81] IARC, IARC Monographs on the Evaluation of Risk to Humans, 2019. https://monographs.iarc.who.int/list-of-classifications.

[82] J. Zhang, X. Li, Chromium pollution of soil and water in Jinzhou, Chinese Journal of Preventive Medicine 21(5) (1987) 262-264.

[83] A. Linos, A. Petralias, C.A. Christophi, E. Christoforidou, P. Kouroutou, M. Stoltidis, A. Veloudaki, E. Tzala, K.C. Makris, M.R. Karagas, Oral ingestion of hexavalent chromium through drinking water and cancer mortality in an industrial area of Greece-an ecological study, Environmental Health 10 (2011) 1-8.

[84] P. Sharma, V. Bihari, S.K. Agarwal, V. Verma, C.N. Kesavachandran, B.S. Pangtey, N. Mathur, K.P. Singh, M. Srivastava, S.K. Goel, Groundwater contaminated with hexavalent chromium [Cr (VI)]: a health survey and clinical examination of community inhabitants (Kanpur, India), PLoS One 7(10) (2012) e47877.

[85] N.A. Qasem, R.H. Mohammed, D.U. Lawal, Removal of heavy metal ions from wastewater: A comprehensive and critical review, Npj Clean Water 4(1) (2021) 36.

[86] Y. Xu, J. Chen, R. Chen, P. Yu, S. Guo, X. Wang, Adsorption and reduction of chromium (VI) from aqueous solution using polypyrrole/calcium rectorite composite adsorbent, Water Research 160 (2019) 148-157.

[87] Y.A. Shaban, Effective photocatalytic reduction of Cr (VI) by carbon modified (CM)-n-TiO2 nanoparticles under solar irradiation, World Journal of Nano Science and Engineering (2013).

[88] L. Pikna, M. Hezelova, A. Morillon, D. Algermissen, O. Milkovic, R. Findorak, M. Cesnek, J. Briancin, Recovery of chromium from slags leachates by electrocoagulation and solid product characterization, Metals 10(12) (2020) 1593.

[89] Y. Liu, H. Wang, Y. Cui, N. Chen, Removal of Copper Ions from Wastewater: A Review, International Journal of Environmental Research and Public Health 20(5) (2023) 3885.

[90] T.Z. Sadyrbaeva, Removal of chromium (VI) from aqueous solutions using a novel hybrid liquid membrane—electrodialysis process, Chemical Engineering and Processing: Process Intensification 99 (2016) 183-191.

[91] C.S. Turchi, D.F. Ollis, Photocatalytic degradation of organic water contaminants: mechanisms involving hydroxyl radical attack, Journal of Catalysis 122(1) (1990) 178-192.

[92] A. Jawed, P. Kar, R. Verma, K. Shukla, P. Hemanth, V.K. Thakur, L.M. Pandey, R.K. Gupta, Integration of biological control with engineered heterojunction nano-photocatalysts for sustainable and effective management of water hyacinth weed, Journal of Environmental Chemical Engineering 10(1) (2022) 106976.

[93] W.S. Koe, J.W. Lee, W.C. Chong, Y.L. Pang, L.C. Sim, An overview of photocatalytic degradation: photocatalysts, mechanisms, and development of photocatalytic membrane, Environmental Science and Pollution Research 27 (2020) 2522-2565.

[94] C. Modrogan, D.G. Apostol, O.D. Butucea, A.R. Miron, C. Costache, R. Kouachi, Kinetic study of hexavalent chromium removal from wastewaters by ion exchange, Environmental Engineering & Management Journal (EEMJ) 12(5) (2013).

[95] F. Gode, E. Pehlivan, Removal of Cr (VI) from aqueous solution by two Lewatit-anion exchange resins, Journal of Hazardous Materials 119(1-3) (2005) 175-182.

[96] A.S. Dharnaik, P.K. Ghosh, Hexavalent chromium [Cr (VI)] removal by the electrochemical ion-exchange process, Environmental technology 35(18) (2014) 2272-2279.

[97] X.-Z. Wei, Z.-Q. Gan, Y.-J. Shen, Z.-L. Qiu, L.-F. Fang, B.-K. Zhu, Negatively-charged nanofiltration membrane and its hexavalent chromium removal performance, Journal of Colloid and Interface Science (2019).

[98] F. Fu, Q. Wang, Removal of heavy metal ions from wastewaters: a review, Journal of Environmental Management 92(3) (2011) 407-418.

[99] M. Baig, M. Mir, S. Murtaza, Z.I. Bhatti, Laboratory scale studies on removal of chromium from industrial wastes, Journal of Environmental Sciences 15(3) (2003) 417-422.

[100] C. Ramakrishnaiah, B. Prathima, Hexavalent chromium removal from industrial wastewater by chemical precipitation method, International Journal of Applied Engineering Research 2(2) (2012) 599-603.

[101] S. Haydar, J.A. Aziz, Coagulation–flocculation studies of tannery wastewater using combination of alum with cationic and anionic polymers, Journal of Hazardous Materials 168(2-3) (2009) 1035-1040.

[102] A. Demirbas, Heavy metal adsorption onto agro-based waste materials: a review, Journal of Hazardous Materials 157(2-3) (2008) 220-229.

[103] M.E. El-Sayed, Nanoadsorbents for water and wastewater remediation, Science of the Total Environment 739 (2020) 139903.

[104] F.C. C, T. Kamalesh, P.S. Kumar, G. Rangasamy, A Critical Review on the Sustainable Approaches for the Removal of Toxic Heavy Metals from Water Systems, Industrial & Engineering Chemistry Research 62(22) (2023) 8575-8601.

[105] A. Bernardes, M.A.S. Rodrigues, J.Z. Ferreira, Electrodialysis and water reuse, Springer 2016.

[106] J.R. Rao, B. Prasad, V. Narasimhan, T. Ramasami, P. Shah, A. Khan, Electrodialysis in the recovery and reuse of chromium from industrial effluents, Journal of Membrane Science 46(2-3) (1989) 215-224.

[107] A. Deghles, U. Kurt, Treatment of tannery wastewater by a hybrid electrocoagulation/electrodialysis process, Chemical Engineering and Processing: Process Intensification 104 (2016) 43-50.

[108] S. Rengaraj, K.-H. Yeon, S.-H. Moon, Removal of chromium from water and wastewater by ion exchange resins, Journal of Hazardous Materials 87(1-3) (2001) 273-287.

[109] M.M. Uddin, M.J. Hasan, M.D. Islam, A. Rahaman, S.M. Shamsuddin, Removal of chromium (III) and other physical parameters from chrome tan wastewater and recovery of chromium from the precipitating sludge, Textile & Leather Review 3(2) (2020) 64-77.

[110] M. Kostrzewa, K. Staszak, D. Ginter-Kramarczyk, I. Kruszelnicka, W. Góra, M. Baraniak, G. Lota, M. Regel-Rosocka, Chromium (III) Removal from Nickel (II)-Containing Waste Solutions as a Pretreatment Step in a Hydrometallurgical Process, Materials 15(18) (2022) 6217.

[111] O. Amuda, I. Amoo, K. Ipinmoroti, O. Ajayi, Coagulation/flocculation process in the removal of trace metals present in industrial wastewater, Journal of Applied Sciences and Environmental Management 10(3) (2006) 159-162.

[112] Z. Song, C. Williams, R. Edyvean, Treatment of tannery wastewater by chemical coagulation, Desalination 164(3) (2004) 249-259.

[113] K. Mohammed, O. Sahu, Recovery of chromium from tannery industry waste water by membrane separation technology: Health and engineering aspects, Scientific African 4 (2019) e00096.

[114] A. Tripathi, A. Dwivedi, Studies on recovery of chromium from tannery wastewater by reverse osmosis, Journal of Industrial Pollution Control 28 (2012) 29-34.

[115] L. Fan, S. Zhang, X. Zhang, H. Zhou, Z. Lu, S. Wang, Removal of arsenic from simulation wastewater using nano-iron/oyster shell composites, Journal of Environmental Management 156 (2015) 109-114.

[116] H. Hao, G. Liu, Y. Wang, B. Shi, K. Han, Y. Zhuang, Y. Kong, Simultaneous cationic Cu (II)–anionic Sb (III) removal by NH_2-Fe_3O_4-NTA core-shell magnetic nanoparticle sorbents synthesized via a facile one-pot approach, Journal of Hazardous Materials 362 (2019) 246-257.

[117] A. Jawed, L.M. Pandey, Application of bimetallic Al-doped ZnO nano-assembly for heavy metal removal and decontamination of wastewater, Water Science and Technology 80(11) (2019) 2067-2078.

[118] A. Jawed, V. Saxena, L.M. Pandey, Engineered nanomaterials and their surface functionalization for the removal of heavy metals: A review, Journal of Water Process Engineering 33 (2020) 101009.

[119] J. Hu, C. Chen, X. Zhu, X. Wang, Removal of chromium from aqueous solution by using oxidized multiwalled carbon nanotubes, Journal of Hazardous Materials 162(2-3) (2009) 1542-1550.

[120] M. Bhattu, J. Singh, Recent advances in nanomaterials based sustainable approaches for mitigation of emerging organic pollutants, Chemosphere (2023) 138072.

[121] N. Mubarak, J. Sahu, E. Abdullah, N. Jayakumar, P. Ganesan, Single stage production of carbon nanotubes using microwave technology, Diamond and Related Materials 48 (2014) 52-59.

[122] M. Yap, N. Mubarak, J. Sahu, E. Abdullah, Microwave induced synthesis of magnetic biochar from agricultural biomass for removal of lead and cadmium from wastewater, Journal of Industrial and Engineering Chemistry 45 (2017) 287-295.

[123] N.M. Mubarak, R.K. Thines, N.R. Sajuni, E.C. Abdullah, J.N. Sahu, P. Ganesan, N.S. Jayakumar, Adsorption of chromium (VI) on functionalized and non-functionalized carbon nanotubes, Korean Journal of Chemical Engineering 31(9) (2014) 1582-1591.

[124] S.S. Sambaza, M.L. Masheane, S.P. Malinga, E.N. Nxumalo, S.D. Mhlanga, Polyethyleneimine-carbon nanotube polymeric nanocomposite adsorbents for the removal of Cr6+ from water, Physics and Chemistry of the Earth, Parts A/B/C 100 (2017) 236-246.

[125] J.Y. Lim, N. Mubarak, E. Abdullah, S. Nizamuddin, M. Khalid, Recent trends in the synthesis of graphene and graphene oxide based nanomaterials for removal of heavy metals - A review, Journal of Industrial and Engineering Chemistry 66 (2018) 29-44.

[126] W. Gao, M. Majumder, L.B. Alemany, T.N. Narayanan, M.A. Ibarra, B.K. Pradhan, P.M. Ajayan, Engineered graphite oxide materials for application in water purification, ACS Applied Materials & interfaces 3(6) (2011) 1821-1826.

[127] N. Li, Q. Yue, B. Gao, X. Xu, Y. Kan, P. Zhao, Magnetic graphene oxide functionalized by poly dimethyl diallyl ammonium chloride for efficient removal of Cr (VI), Journal of the Taiwan Institute of Chemical Engineers 91 (2018) 499-506.

[128] L.P. Lingamdinne, J.R. Koduru, Y.-L. Choi, Y.-Y. Chang, J.-K. Yang, Studies on removal of Pb (II) and Cr (III) using graphene oxide based inverse spinel nickel ferrite nano-composite as sorbent, Hydrometallurgy 165 (2016) 64-72.

[129] X. Guo, W. Wang, Y. Yang, Q. Tian, Y. Xiang, Y. Sun, Z. Bai, Magnetic nano capture agent with enhanced anion internal layer diffusion performance for removal of arsenic from human blood, Applied Surface Science 470 (2019) 296-305.

[130] B. Mukherjee, P.K. Maiti, C. Dasgupta, A. Sood, Single-file diffusion of water inside narrow carbon nanorings, ACS Nano 4 (2010) 985-991.

[131] C.-J. Jia, L.-D. Sun, F. Luo, X.-D. Han, L.J. Heyderman, Z.-G. Yan, C.-H. Yan, K. Zheng, Z. Zhang, M. Takano, Large-scale synthesis of single-crystalline iron oxide magnetic nanorings, Journal of the American Chemical Society 130 (2008) 16968-16977.

[132] X. Wen, S. Wang, Y. Ding, Z.L. Wang, S. Yang, Controlled growth of large-area, uniform, vertically aligned arrays of α-Fe2O3 nanobelts and nanowires, The Journal of Physical Chemistry B 109 (2005) 215-220.

[133] J. Liu, Y. Li, H. Fan, Z. Zhu, J. Jiang, R. Ding, Y. Hu, X. Huang, Iron oxide-based nanotube arrays derived from sacrificial template-accelerated hydrolysis: large-area design and reversible lithium storage, Chemistry of Materials 22 (2009) 212-217.

[134] M. Palimi, M. Rostami, M. Mahdavian, B. Ramezanzadeh, Surface modification of Fe2O3 nanoparticles with 3-aminopropyltrimethoxysilane (APTMS): An attempt to investigate surface treatment on surface chemistry and mechanical properties of polyurethane/Fe2O3 nanocomposites, Applied Surface Science 320 (2014) 60-72.

[135] O. Lemine, K. Omri, B. Zhang, L. El Mir, M. Sajieddine, A. Alyamani, M. Bououdina, Sol–gel synthesis of 8 nm magnetite (Fe_3O_4) nanoparticles and their magnetic properties, Superlattices and Microstructures 52(4) (2012) 793-799.

[136] A.M. Awwad, N.M. Salem, A green and facile approach for synthesis of magnetite nanoparticles, Nanoscience and Nanotechnology 2(6) (2012) 208-213.

[137] P. Yuan, D. Liu, M. Fan, D. Yang, R. Zhu, F. Ge, J. Zhu, H. He, Removal of hexavalent chromium [Cr (VI)] from aqueous solutions by the diatomite-supported/unsupported magnetite nanoparticles, Journal of Hazardous Materials 173(1-3) (2010) 614-621.

[138] S. Rajput, C.U. Pittman Jr, D. Mohan, Magnetic magnetite (Fe3O4) nanoparticle synthesis and applications for lead (Pb2+) and chromium (Cr6+) removal from water, Journal of Colloid and Interface Science 468 (2016) 334-346.

[139] K. Zhu, Y. Duan, F. Wang, P. Gao, H. Jia, C. Ma, C. Wang, Silane-modified halloysite/Fe3O4 nanocomposites: Simultaneous removal of Cr (VI) and Sb (V) and positive effects of Cr (VI) on Sb (V) adsorption, Chemical Engineering Journal 311 (2017) 236-246.

[140] A. Hasan, L. Pandey, Self-assembled monolayers in biomaterials, Nanobiomaterials, Elsevier, pp. 137-178.

[141] L.M. Pandey, S.K. Pattanayek, Properties of competitively adsorbed BSA and fibrinogen from their mixture on mixed and hybrid surfaces, Applied Surface Science 264 (2013) 832-837.

[142] L.M. Pandey, S. Le Denmat, D. Delabouglise, F. Bruckert, S.K. Pattanayek, M. Weidenhaupt, Surface chemistry at the nanometer scale influences insulin aggregation, Colloids and Surfaces B: Biointerfaces 100 (2012) 69-76.

[143] L.M. Pandey, S.K. Pattanayek, D. Delabouglise, Properties of adsorbed bovine serum albumin and fibrinogen on self-assembled monolayers, The Journal of Physical Chemistry C 117 (2013) 6151-6160.

[144] P.S. De Velasco-Maldonado, V. Hernández-Montoya, M.A. Montes-Morán, N.A.-R. Vázquez, M.A. Pérez-Cruz, Surface modification of a natural zeolite by treatment with cold oxygen plasma: Characterization and application in water treatment, Applied Surface Science 434 (2018) 1193-1199.

[145] A.N. Baghani, A.H. Mahvi, M. Gholami, N. Rastkari, M. Delikhoon, One-Pot synthesis, characterization and adsorption studies of amine-functionalized magnetite nanoparticles for removal of Cr (VI) and Ni (II) ions from aqueous solution: Kinetic, isotherm and thermodynamic studies, Journal of Environmental Health Science & Engineering 14 (2016) 11.

[146] S.-H. Huang, D.-H. Chen, Rapid removal of heavy metal cations and anions from aqueous solutions by an amino-functionalized magnetic nano-adsorbent, Journal of Hazardous Materials 163(1) (2009) 174-179.

[147] S. Koushkbaghi, A. Zakialamdari, M. Pishnamazi, H.F. Ramandi, M. Aliabadi, M. Irani, Aminated-Fe3O4 nanoparticles filled chitosan/PVA/PES dual layers nanofibrous membrane for the removal of Cr (VI) and Pb (II) ions from aqueous solutions in adsorption and membrane processes, Chemical Engineering Journal 337 (2018) 169-182.

[148] S.A. Elfeky, S.E. Mahmoud, A.F. Youssef, Applications of CTAB modified magnetic nanoparticles for removal of chromium (VI) from contaminated water, Journal of Advanced Research 8(4) (2017) 435-443.

[149] J.-C. Wang, J. Ren, H.-C. Yao, L. Zhang, J.-S. Wang, S.-Q. Zang, L.-F. Han, Z.-J. Li, Synergistic photocatalysis of Cr (VI) reduction and 4-Chlorophenol degradation over hydroxylated α-Fe2O3 under visible light irradiation, Journal of Hazardous Materials 311 (2016) 11-19.

[150] L. Wei, G. Yang, R. Wang, W. Ma, Selective adsorption and separation of chromium (VI) on the magnetic iron–nickel oxide from waste nickel liquid, Journal of Hazardous Materials 164(2-3) (2009) 1159-1163.

[151] J. Hu, I.M. Lo, G. Chen, Performance and mechanism of chromate (VI) adsorption by δ-FeOOH-coated maghemite (γ-Fe_2O_3) nanoparticles, Separation and Purification Technology 58(1) (2007) 76-82.

[152] Y. Jiang, W. Cai, W. Tu, M. Zhu, Facile Cross-Link Method To Synthesize Magnetic Fe3O4@ SiO2–Chitosan with High Adsorption Capacity toward Hexavalent Chromium, Journal of Chemical & Engineering Data 64(1) (2018) 226-233.

[153] M. Bhaumik, A. Maity, V. Srinivasu, M.S. Onyango, Enhanced removal of Cr (VI) from aqueous solution using polypyrrole/Fe_3O_4 magnetic nanocomposite, Journal of Hazardous Materials 190(1-3) (2011) 381-390.

[154] Y. Lei, F. Chen, Y. Luo, L. Zhang, Three-dimensional magnetic graphene oxide foam/Fe_3O_4 nanocomposite as an efficient absorbent for Cr (VI) removal, Journal of Materials Science 49(12) (2014) 4236-4245.

[155] T. Wang, L. Zhang, C. Li, W. Yang, T. Song, C. Tang, Y. Meng, S. Dai, H. Wang, L. Chai, Synthesis of core–shell magnetic Fe_3O_4@poly(m-phenylenediamine) particles for chromium reduction and adsorption, Environmental Science & Technology 49(9) (2015) 5654-5662.

[156] G. Huang, H. Zhang, J.X. Shi, T.A. Langrish, Adsorption of chromium (VI) from aqueous solutions using cross-linked magnetic chitosan beads, Industrial & Engineering Chemistry Research 48(5) (2009) 2646-2651.

[157] H. Zhang, F. Huang, D.-L. Liu, P. Shi, Highly efficient removal of Cr (VI) from wastewater via adsorption with novel magnetic Fe_3O_4@C@MgAl-layered double-hydroxide, Chinese Chemical Letters 26(9) (2015) 1137-1143.

[158] W. Jiang, Q. Cai, W. Xu, M. Yang, Y. Cai, D.D. Dionysiou, K.E. O'Shea, Cr (VI) adsorption and reduction by humic acid coated on magnetite, Environmental Science & Technology 48(14) (2014) 8078-8085.

[159] P. Li, T. Fu, X. Gao, W. Zhu, C. Han, N. Liu, S. He, Y. Luo, W. Ma, Adsorption and Reduction Transformation Behaviors of Cr (VI) on Mesoporous Polydopamine/Titanium Dioxide Composite Nanospheres, Journal of Chemical & Engineering Data (2019).

[160] S.S. Liu, Y.Z. Chen, L. De Zhang, G.M. Hua, W. Xu, N. Li, Y. Zhang, Enhanced removal of trace Cr (VI) ions from aqueous solution by titanium oxide–Ag composite adsorbents, Journal of Hazardous Materials 190(1-3) (2011) 723-728.

[161] Y.-J. Lin, J.-J. Chen, W.-Z. Cao, K.M. Persson, T. Ouyang, L. Zhang, X. Xie, F. Liu, J. Li, C.-T. Chang, Novel materials for Cr (VI) adsorption by magnetic titanium nanotubes coated phosphorene, Journal of Molecular Liquids 287 (2019) 110826.

[162] K. Zhang, H. Li, X. Xu, H. Yu, Synthesis of reduced graphene oxide/NiO nanocomposites for the removal of Cr (VI) from aqueous water by adsorption, Microporous and Mesoporous Materials 255 (2018) 7-14.

[163] I. Ghiloufi, J. El Ghoul, A. Modwi, L. El Mir, Ga-doped ZnO for adsorption of heavy metals from aqueous solution, Materials Science in Semiconductor Processing 42 (2016) 102-106.

[164] J. Guo, X. Cai, Y. Li, R. Zhai, S. Zhou, P. Na, The preparation and characterization of a three-dimensional titanium dioxide nanostructure with high surface hydroxyl group density and high performance in water treatment, Chemical Engineering Journal 221 (2013) 342-352.

[165] P. Yuan, M. Fan, D. Yang, H. He, D. Liu, A. Yuan, J. Zhu, T. Chen, Montmorillonite-supported magnetite nanoparticles for the removal of hexavalent chromium [Cr (VI)] from aqueous solutions, Journal of Hazardous Materials 166(2-3) (2009) 821-829.

[166] J. Hu, I. Lo, G. Chen, Removal of Cr (VI) by magnetite, Water Science and Technology 50(12) (2004) 139-146.

[167] J. Arenas-Alatorre, O. Lukas, A. Rodríguez-Gómez, R.H. Reyes, C. Tapia-del León, Synthesis and characterization of iron oxide nanoparticles grown via a non-conventional chemical method using an external magnetic field, Materials Letters 242 (2019) 13-16.

[168] M. Curcio, J. Rau, A. Santagata, R. Teghil, S. Laureti, A. De Bonis, Laser synthesis of iron nanoparticle for Fe doped hydroxyapatite coatings, Materials Chemistry and Physics 225 (2019) 365-370.

[169] T. Indira, P. Lakshmi, Magnetic nanoparticles–a review, International Journal of Pharmaceutical Sciences and Nanotechnology 3(3) (2010) 1035-1042.

[170] W. Wu, Q. He, C. Jiang, Magnetic iron oxide nanoparticles: synthesis and surface functionalization strategies, Nanoscale Research Letters 3(11) (2008) 397.

[171] Y.S. Kang, S. Risbud, J.F. Rabolt, P. Stroeve, Synthesis and characterization of nanometer-size Fe3O4 and γ-Fe2O3 particles, Chemistry of Materials 8(9) (1996) 2209-2211.

[172] Z. Davoudi, A. Akbarzadeh, M. Rahmatiyamchi, A.A. Movassaghpour, M. Alipour, K. Nejati-Koshki, Z. Sadeghi, H. Dariushnejad, N. Zarghami, Molecular target therapy of AKT and NF-kB signaling pathways and multidrug resistance by specific cell penetrating inhibitor peptides in HL-60 cells, Asian Pacific Journal of Cancer Prevention 15(10) (2014) 4353-4358.

[173] J.-P. Jolivet, M. Henry, J. Livage, Metal oxide chemistry and synthesis: from solution to solid state, Wiley-Blackwell 2000.

[174] P. Tartaj, T. Gonzalez-Carreno, O. Bomati-Miguel, C. Serna, P. Bonville, Magnetic behavior of superparamagnetic Fe nanocrystals confined inside submicron-sized spherical silica particles, Physical Review B 69(9) (2004) 094401.

[175] M. Faraji, Y. Yamini, M. Rezaee, Magnetic nanoparticles: synthesis, stabilization, functionalization, characterization, and applications, Journal of the Iranian Chemical Society 7(1) (2010) 1-37.

[176] R.F. Ziolo, E.P. Giannelis, B.A. Weinstein, M.P. O'Horo, B.N. Ganguly, V. Mehrotra, M.W. Russell, D.R. Huffman, Matrix-mediated synthesis of nanocrystalline γ-Fe2O3: a new optically transparent magnetic material, Science 257(5067) (1992) 219-223.

[177] A.K. Gupta, S. Wells, Surface-modified superparamagnetic nanoparticles for drug delivery: preparation, characterization, and cytotoxicity studies, IEEE transactions on nanobioscience 3(1) (2004) 66-73.

[178] S. Laurent, D. Forge, M. Port, A. Roch, C. Robic, L. Vander Elst, R.N. Muller, Magnetic iron oxide nanoparticles: synthesis, stabilization, vectorization, physicochemical characterizations, and biological applications, Chemical Reviews 108(6) (2008) 2064-2110.

[179] I. Šafařík, K. Horská, M. Šafaříková, Magnetic nanoparticles for biomedicine, Intracellular Delivery, Springer 2011, pp. 363-372.

[180] G. Scherrer, C. Brinker, Sol-gel Science: the Physics and Chemistry of Sol-gel, Boston (MA): Academic Press, 1990.

[181] M. Willard, L. Kurihara, E. Carpenter, S. Calvin, V. Harris, Chemically prepared magnetic nanoparticles, International Materials Reviews 49(3-4) (2004) 125-170.

[182] Z.I. Takai, M.K. Mustafa, S. Asman, K.A. Sekak, Preparation and characterization of magnetite (Fe3O4) nanoparticles by sol-gel method, International Journal of Nanoelectronics and Materials 12 (2019) 37-46.

[183] L. Gao, Y. Tang, C. Wang, L. Yao, J. Zhang, R. Gao, X. Tang, T. Chong, H. Zhang, Highly-efficient amphiphilic magnetic nanocomposites based on a simple sol-gel modification for adsorption of phthalate esters, Journal of Colloid and Interface Science 552 (2019) 142-152.

[184] H. Zhang, G. Zhu, One-step hydrothermal synthesis of magnetic Fe3O4 nanoparticles immobilized on polyamide fabric, Applied Surface Science 258(11) (2012) 4952-4959.

[185] S. Ni, X. Wang, G. Zhou, F. Yang, J. Wang, Q. Wang, D. He, Hydrothermal synthesis of Fe3O4 nanoparticles and its application in lithium ion battery, Materials Letters 63(30) (2009) 2701-2703.

[186] L. Wang, J. Li, Q. Jiang, L. Zhao, Water-soluble Fe_3O_4 nanoparticles with high solubility for removal of heavy-metal ions from waste water, Dalton Transactions 41(15) (2012) 4544-4551.

[187] J. Rockenberger, E.C. Scher, A.P. Alivisatos, A new nonhydrolytic single-precursor approach to surfactant-capped nanocrystals of transition metal oxides, Journal of the American Chemical Society 121(49) (1999) 11595-11596.

[188] P. Tartaj, T. Gonzalez-Carreno, C.J. Serna, Single-step nanoengineering of silica coated maghemite hollow spheres with tunable magnetic properties, Advanced Materials 13(21) (2001) 1620-1624.

[189] J.H. Bang, K.S. Suslick, Sonochemical synthesis of nanosized hollow hematite, Journal of the American Chemical Society 129(8) (2007) 2242-2243.

[190] R. Vijayakumar, Y. Koltypin, I. Felner, A. Gedanken, Sonochemical synthesis and characterization of pure nanometer-sized Fe_3O_4 particles, Materials Science and Engineering: A 286(1) (2000) 101-105.

[191] E.H. Kim, H.S. Lee, B.K. Kwak, B.-K. Kim, Synthesis of ferrofluid with magnetic nanoparticles by sonochemical method for MRI contrast agent, Journal of Magnetism and Magnetic Materials 289 (2005) 328-330.

[192] V. Saxena, P. Chandra, L.M. Pandey, Design and characterization of novel Al-doped ZnO nanoassembly as an effective nanoantibiotic, Applied Nanoscience 8(8) (2018) 1925-1941.

[193] V. Saxena, S. Sharma, L.M. Pandey, Fe (III) doped ZnO nano-assembly as a potential heterogeneous nano-catalyst for the production of biodiesel, Materials Letters 237 (2019) 232-235.

[194] A. Jawed, R. Verma, V. Saxena, L.M. Pandey, Photocatalytic metal nanoparticles: a green approach for degradation of dyes, Photocatalytic Degradation of Dyes, Elsevier 2021, pp. 251-275.

[195] S. Tiwari, A. Hasan, L.M. Pandey, A novel bio-sorbent comprising encapsulated Agrobacterium fabrum (SLAJ731) and iron oxide nanoparticles for removal of crude oil co-contaminant, lead Pb (II), Journal of Environmental Chemical Engineering 5(1) (2017) 442-452.

[196] S. Sharma, A. Hasan, N. Kumar, L.M. Pandey, Removal of methylene blue dye from aqueous solution using immobilized Agrobacterium fabrum biomass along with iron oxide nanoparticles as biosorbent, Environmental Science and Pollution Research 25(22) (2018) 21605-21615.

[197] M. Rai, A. Yadav, A. Gade, CRC 675—current trends in phytosynthesis of metal nanoparticles, Critical reviews in biotechnology 28(4) (2008) 277-284.

[198] M. Latif, S. Abbas, F. Kormin, M. Mustafa, Green synthesis of plant-mediated metal nanoparticles: the role of polyphenols, Asian Journal of Pharmaceutical and Clinical Research 12(7) (2019) 75-84.

[199] R. Revathy, T. Sajini, C. Augustine, N. Joseph, Iron-based magnetic nanomaterials: Sustainable approaches of synthesis and applications, Results in Engineering (2023) 101114.

[200] O.V. Kharissova, H.R. Dias, B.I. Kharisov, B.O. Pérez, V.M.J. Pérez, The greener synthesis of nanoparticles, Trends in biotechnology 31(4) (2013) 240-248.

[201] H. Mukhtar, N. Ahmad, Tea polyphenols: prevention of cancer and optimizing health, The American Journal of Clinical Nutrition 71(6) (2000) 1698S-1702S.

[202] M. Pelillo, M. Bonoli, B. Biguzzi, A. Bendini, T.G. Toschi, G. Lercker, An investigation in the use of HPLC with UV and MS-electrospray detection for the quantification of tea catechins, Food Chemistry 87(3) (2004) 465-470.

[203] T. Wang, J. Lin, Z. Chen, M. Megharaj, R. Naidu, Green synthesized iron nanoparticles by green tea and eucalyptus leaves extracts used for removal of nitrate in aqueous solution, Journal of Cleaner Production 83 (2014) 413-419.

[204] C.A. De León-Condés, G. Roa-Morales, G. Martínez-Barrera, P. Balderas-Hernández, C. Menchaca-Campos, F. Ureña-Núñez, A novel sulfonated waste polystyrene/iron oxide

nanoparticles composite: Green synthesis, characterization and applications, Journal of Environmental Chemical Engineering 7(1) (2019) 102841.

[205] S.S. Carvalho, N.M. Carvalho, Dye degradation by green heterogeneous Fenton catalysts prepared in presence of Camellia sinensis, Journal of Environmental Management 187 (2017) 82-88.

[206] M. Chrysochoou, J. Oakes, M. Dyar, Investigation of iron reduction by green tea polyphenols, Applied Geochemistry 97 (2018) 263-269.

[207] J. Lin, X. Weng, R. Dharmarajan, Z. Chen, Characterization and reactivity of iron based nanoparticles synthesized by tea extracts under various atmospheres, Chemosphere 169 (2017) 413-417.

[208] V.V. Makarov, S.S. Makarova, A.J. Love, O.V. Sinitsyna, A.O. Dudnik, I.V. Yaminsky, M.E. Taliansky, N.O. Kalinina, Biosynthesis of stable iron oxide nanoparticles in aqueous extracts of Hordeum vulgare and Rumex acetosa plants, Langmuir 30(20) (2014) 5982-5988.

[209] G.E. Hoag, J.B. Collins, J.L. Holcomb, J.R. Hoag, M.N. Nadagouda, R.S. Varma, Degradation of bromothymol blue by 'greener'nano-scale zero-valent iron synthesized using tea polyphenols, Journal of Materials Chemistry 19(45) (2009) 8671-8677.

[210] S. Machado, S.L. Pinto, J.P. Grosso, H.P.A. Nouws, J.T. Albergaria, C. Delerue-Matos, Green production of zero-valent iron nanoparticles using tree leaf extracts, Science of The Total Environment 445-446 (2013) 1-8.

[211] Z. Markova, P. Novak, J. Kaslik, P. Plachtova, M. Brazdova, D. Jancula, K.M. Siskova, L. Machala, B. Marsalek, R. Zboril, R. Varma, Iron(II,III)–Polyphenol Complex Nanoparticles Derived from Green Tea with Remarkable Ecotoxicological Impact, ACS Sustainable Chemistry & Engineering 2(7) (2014) 1674-1680.

[212] M. Khatami, H.Q. Alijani, B. Fakheri, M.M. Mobasseri, M. Heydarpour, Z.K. Farahani, A.U. Khan, Super-paramagnetic iron oxide nanoparticles (SPIONs): Greener synthesis using Stevia plant and evaluation of its antioxidant properties, Journal of Cleaner Production 208 (2019) 1171-1177.

[213] Y. Cai, Y. Shen, A. Xie, S. Li, X. Wang, Green synthesis of soya bean sprouts-mediated superparamagnetic Fe3O4 nanoparticles, Journal of Magnetism and Magnetic Materials 322(19) (2010) 2938-2943.

[214] T. Shahwan, S. Abu Sirriah, M. Nairat, E. Boyacı, A.E. Eroğlu, T.B. Scott, K.R. Hallam, Green synthesis of iron nanoparticles and their application as a Fenton-like catalyst for the degradation of aqueous cationic and anionic dyes, Chemical Engineering Journal 172(1) (2011) 258-266.

[215] K. Basavaiah, M.H. Kahsay, D. RamaDevi, Green synthesis of magnetite nanoparticles using aqueous pod extract of Dolichos lablab L for an efficient adsorption of crystal violet, Emergent Materials 1(3-4) (2018) 121-132.

[216] Y.P. Yew, K. Shameli, M. Miyake, N. Kuwano, N.B.B.A. Khairudin, S.E.B. Mohamad, K.X. Lee, Green synthesis of magnetite (Fe 3 O 4) nanoparticles using seaweed (Kappaphycus alvarezii) extract, Nanoscale research letters 11(1) (2016) 276.

[217] H.Y. El-Kassas, M.A. Aly-Eldeen, S.M. Gharib, Green synthesis of iron oxide (Fe 3 O 4) nanoparticles using two selected brown seaweeds: characterization and application for lead bioremediation, Acta Oceanologica Sinica 35(8) (2016) 89-98.

[218] Z. Wang, Iron complex nanoparticles synthesized by eucalyptus leaves, ACS Sustainable Chemistry & Engineering 1(12) (2013) 1551-1554.

[219] S. Eslami, M.A. Ebrahimzadeh, P. Biparva, Green synthesis of safe zero valent iron nanoparticles by Myrtus communis leaf extract as an effective agent for reducing excessive iron in iron-overloaded mice, a thalassemia model, RSC advances 8(46) (2018) 26144-26155.

[220] X. Li, H. Xu, Z.-S. Chen, G. Chen, Biosynthesis of nanoparticles by microorganisms and their applications, Journal of nanomaterials 2011 (2011) 1-16.

[221] A. Padmakumar, C. Pavani, K. Eswar, L. Kong, W. Yang, S. Gopalakrishnan, D.M. Cahill, A.K. Rengan, Bacteria-Premised Nanobiopesticides for the Management of Phytopathogens and Pests, ACS Agricultural Science & Technology (2023).

[222] D. Gupta, A. Thakur, T.K. Gupta, Green and sustainable synthesis of nanomaterials: Recent advancements and limitations, Environmental Research (2023) 116316.

[223] K.A. Crespo, J.L. Baronetti, M.A. Quinteros, P.L. Páez, M.G. Paraje, Intra-and extracellular biosynthesis and characterization of iron nanoparticles from prokaryotic microorganisms with anticoagulant activity, Pharmaceutical research 34 (2017) 591-598.

[224] M.P. Desai, K.D. Pawar, Immobilization of cellulase on iron tolerant Pseudomonas stutzeri biosynthesized photocatalytically active magnetic nanoparticles for increased thermal stability, Materials Science and Engineering: C 106 (2020) 110169.

[225] M. Daneshvar, M.R. Hosseini, From the iron boring scraps to superparamagnetic nanoparticles through an aerobic biological route, Journal of Hazardous Materials 357 (2018) 393-400.

[226] S. Hajiali, S. Daneshjou, S. Daneshjoo, Biomimetic synthesis of iron oxide nanoparticles from Bacillus megaterium to be used in hyperthermia therapy, AMB Express 12(1) (2022) 145.

[227] G.M. de França Bettencourt, J. Degenhardt, L.A.Z. Torres, V.O. de Andrade Tanobe, C.R. Soccol, Green biosynthesis of single and bimetallic nanoparticles of iron and manganese using bacterial auxin complex to act as plant bio-fertilizer, Biocatalysis and Agricultural Biotechnology 30 (2020) 101822.

[228] N.F. Khan, U. Zehra, Z.A. Reshi, M.A. Shah, T.R. Baba, Seasonal Dynamics of Bacterial and Fungal Lineages in Extreme Environments, Climate Change and Microbial Diversity, Apple Academic Press 2023, pp. 63-107.

[229] F. Namvar, M. Moniri, M. Tahir, S. Azizi, R. Mohamad, Nanoparticles Biosynthesized by Fungi and Yeast: A Review of Their Preparation, Properties, and Medical Applications, Molecules (Basel, Switzerland) 20(9) (2015) 16540-16565.

[230] G. De Angelis, G. Simonetti, L. Chronopoulou, A. Orekhova, C. Badiali, V. Petruccelli, F. Portoghesi, S. D'Angeli, E. Brasili, G. Pasqua, A novel approach to control Botrytis cinerea fungal infections: uptake and biological activity of antifungals encapsulated in nanoparticle based vectors, Scientific Reports UK 12(1) (2022) 7989.

[231] S. Chatterjee, S. Mahanty, P. Das, P. Chaudhuri, S. Das, Biofabrication of iron oxide nanoparticles using manglicolous fungus Aspergillus niger BSC-1 and removal of Cr (VI) from aqueous solution, Chemical Engineering Journal 385 (2020) 123790.

[232] S. Mahanty, M. Bakshi, S. Ghosh, S. Chatterjee, S. Bhattacharyya, P. Das, S. Das, P. Chaudhuri, Green synthesis of iron oxide nanoparticles mediated by filamentous fungi isolated from Sundarban mangrove ecosystem, India, BioNanoScience 9 (2019) 637-651.

[233] D.G. Alamilla-Martínez, N.G. Rojas-Avelizapa, I. Domínguez-López, H. Pool, M. Gómez-Ramírez, A. de Querétaro, Biosynthesis of iron nanoparticles (FeNPs) by Alternaria alternata MVSS-AH-5, Mexican Journal of Biotechnology 4 (2019) 1-14.

[234] Y.M. Mohamed, A.M. Azzam, B.H. Amin, N.A. Safwat, Mycosynthesis of iron nanoparticles by Alternaria alternata and its antibacterial activity, African Journal of Biotechnology 14(14) (2015) 1234-1241.

[235] A. Eldeghidy, G.M. Abdel-Fattah, H. Aldesuquy, A. Elsayed, green synthesis and characterization of nano-iron particles by Fusaium oxysporum Running title: Nanparticles from fungi.

[236] S. Bhukal, A. Sharma, Rishi, Divya, S. Kumar, B. Deepak, K. Pal, S. Mona, Spirulina based iron oxide nanoparticles for adsorptive removal of crystal violet dye, Topics in Catalysis 65(19-20) (2022) 1675-1685.

[237] H.Y. El-Kassas, M.A. Aly-Eldeen, S.M. Gharib, Green synthesis of iron oxide (Fe 3 O 4) nanoparticles using two selected brown seaweeds: Characterization and application for lead bioremediation, Acta Oceanologica Sinica 35 (2016) 89-98.

[238] A.D.V. Bensy, G.J. Christobel, K. Muthusamy, A. Alfarhan, P. Anantharaman, Green synthesis of iron nanoparticles from Ulva lactuca and bactericidal activity against enteropathogens, Journal of King Saud University-Science 34(3) (2022) 101888.

[239] S. Mashjoor, M. Yousefzadi, H. Zolgharnain, E. Kamrani, M. Alishahi, Organic and inorganic nano-Fe3O4: Alga Ulva flexuosa-based synthesis, antimicrobial effects and acute toxicity to briny water rotifer Brachionus rotundiformis, Environmental Pollution 237 (2018) 50-64.

[240] F.E. García, A.M. Senn, J.M. Meichtry, T.B. Scott, H. Pullin, A.G. Leyva, E.B. Halac, C.P. Ramos, J. Sacanell, M. Mizrahi, Iron-based nanoparticles prepared from yerba mate extract. Synthesis, characterization and use on chromium removal, Journal of Environmental Management 235 (2019) 1-8.

[241] F. Zhu, S. Ma, T. Liu, X. Deng, Green synthesis of nano zero-valent iron/Cu by green tea to remove hexavalent chromium from groundwater, Journal of Cleaner Production 174 (2018) 184-190.

[242] Y. Liu, X. Jin, Z. Chen, The formation of iron nanoparticles by Eucalyptus leaf extract and used to remove Cr (VI), Science of The Total Environment 627 (2018) 470-479.

[243] X. Jin, Y. Liu, J. Tan, G. Owens, Z. Chen, Removal of Cr (VI) from aqueous solutions via reduction and absorption by green synthesized iron nanoparticles, Journal of Cleaner Production 176 (2018) 929-936.

[244] L.P. Lingamdinne, Y.-Y. Chang, J.-K. Yang, J. Singh, E.-H. Choi, M. Shiratani, J.R. Koduru, P. Attri, Biogenic reductive preparation of magnetic inverse spinel iron oxide nanoparticles for the adsorption removal of heavy metals, Chemical Engineering Journal 307 (2017) 74-84.

[245] R. Sharma, R. Garg, M. Bali, N.O. Eddy, Biogenic synthesis of iron oxide nanoparticles using leaf extract of Spilanthes acmella: antioxidation potential and adsorptive removal of heavy metal ions, Environmental Monitoring and Assessment 195(11) (2023) 1345.

[246] S.A. Idris, H.I. Olabisi, I.H. Yahaya, Green Synthesis of Magnetite Iron Oxide Nanoparticles Using Stem Bark Extract of Prosopisafricana: Application for the Removal of Heavy Metals from Tannery Effluent, International Journal of Advances in Engineering and Management 5(1729) (2023) 10.35629.

[247] Z. Xiao, M. Yuan, B. Yang, Z. Liu, J. Huang, D. Sun, Plant-mediated synthesis of highly active iron nanoparticles for Cr (VI) removal: Investigation of the leading biomolecules, Chemosphere 150 (2016) 357-364.

[248] A. Rao, A. Bankar, A.R. Kumar, S. Gosavi, S. Zinjarde, Removal of hexavalent chromium ions by Yarrowia lipolytica cells modified with phyto-inspired Fe0/Fe3O4 nanoparticles, Journal of Contaminant Hydrology 146 (2013) 63-73.

[249] X. Weng, X. Jin, J. Lin, R. Naidu, Z. Chen, Removal of mixed contaminants Cr (VI) and Cu (II) by green synthesized iron based nanoparticles, Ecological Engineering 97 (2016) 32-39.

[250] Z. Pan, Y. Lin, B. Sarkar, G. Owens, Z. Chen, Green synthesis of iron nanoparticles using red peanut skin extract: Synthesis mechanism, characterization and effect of conditions on chromium removal, Journal of Colloid and Interface Science 558 (2020) 106-114.

[251] Y. Yi, G. Tu, P.E. Tsang, S. Xiao, Z. Fang, Green synthesis of iron-based nanoparticles from extracts of Nephrolepis auriculata and applications for Cr (VI) removal, Materials Letters 234 (2019) 388-391.

[252] A. Soliemanzadeh, M. Fekri, The application of green tea extract to prepare bentonite-supported nanoscale zero-valent iron and its performance on removal of Cr(VI): Effect of relative parameters and soil experiments, Microporous and Mesoporous Materials 239 (2017) 60-69.

[253] M. Saleh, Z. Isik, Y. Aktas, H. Arslan, M. Yalvac, N. Dizge, Green synthesis of zero valent iron nanoparticles using Verbascum thapsus and its Cr (VI) reduction activity, Bioresource Technology Reports 13 (2021) 100637.

[254] V. Madhavi, T.N.V.K.V. Prasad, A.V.B. Reddy, B. Ravindra Reddy, G. Madhavi, Application of phytogenic zerovalent iron nanoparticles in the adsorption of hexavalent chromium, Spectrochimica Acta Part A: Molecular and Biomolecular Spectroscopy 116 (2013) 17-25.

[255] Z. Samadi, K. Yaghmaeian, S. Mortazavi-Derazkola, R. Khosravi, R. Nabizadeh, M. Alimohammadi, Facile green synthesis of zero-valent iron nanoparticles using barberry leaf extract (GnZVI@ BLE) for photocatalytic reduction of hexavalent chromium, Bioorganic Chemistry 114 (2021) 105051.

[256] K. Andrade-Zavaleta, Y. Chacon-Laiza, D. Asmat-Campos, N. Raquel-Checca, Green synthesis of superparamagnetic iron oxide nanoparticles with eucalyptus globulus extract and their application in the removal of heavy metals from agricultural soil, Molecules 27(4) (2022) 1367.

[257] M. Baalousha, Aggregation and disaggregation of iron oxide nanoparticles: Influence of particle concentration, pH and natural organic matter, Science of the Total Environment 407(6) (2009) 2093-2101.

[258] A.W.M. Carvalho Costa, F. Guerhardt, S.E.R. Ribeiro Júnior, G. Cânovas, R.M. Vanale, D. de Freitas Coelho, D.D. Ehrhardt, J.M. Rosa, E. BasileTambourgi, J.C. Curvelo Santana, Biosorption of Cr (VI) using coconut fibers from agro-industrial waste magnetized using magnetite nanoparticles, Environmental technology 42(23) (2021) 3595-3606.

[259] Y. Xu, C. Wang, J. Hou, P. Wang, G. You, L. Miao, B. Lv, Y. Yang, F. Zhang, Application of zero valent iron coupling with biological process for wastewater treatment: a review, Reviews in Environmental Science and Bio/Technology 16(4) (2017) 667-693.

[260] A. Hasan, L. Pandey, Self-assembled monolayers in biomaterials, Nanobiomaterials, Elsevier2018, pp. 137-178.

[261] L.M. Pandey, S.K. Pattanayek, Properties of competitively adsorbed BSA and fibrinogen from their mixture on mixed and hybrid surfaces, Applied Surface Science 264 (2013) 832-837.

[262] L.M. Pandey, S. Le Denmat, D. Delabouglise, F. Bruckert, S.K. Pattanayek, M. Weidenhaupt, Surface chemistry at the nanometer scale influences insulin aggregation, Colloids and Surfaces B: Biointerfaces 100 (2012) 69-76.

[263] L.M. Pandey, S.K. Pattanayek, D. Delabouglise, Properties of adsorbed bovine serum albumin and fibrinogen on self-assembled monolayers, The Journal of Physical Chemistry C 117(12) (2013) 6151-6160.

[264] E.d.S. Reis, F.D. Gorza, G.d.C. Pedro, B.G. Maciel, R.J. da Silva, G.P. Ratkovski, C.P. de Melo, (Maghemite/Chitosan/Polypyrrole) nanocomposites for the efficient removal of Cr (VI) from aqueous media, Journal of Environmental Chemical Engineering 9(1) (2021) 104893.

[265] N.A. Azeez, S.S. Dash, S.N. Gummadi, V.S. Deepa, Nano-remediation of toxic heavy metal contamination: Hexavalent chromium [Cr (VI)], Chemosphere 266 (2021) 129204.

[266] J. Wang, C. Chen, Chitosan-based biosorbents: modification and application for biosorption of heavy metals and radionuclides, Bioresource technology 160 (2014) 129-141.

[267] Y. Sağ, Y. Aktay, Kinetic studies on sorption of Cr (VI) and Cu (II) ions by chitin, chitosan and Rhizopus arrhizus, Biochemical Engineering Journal 12(2) (2002) 143-153.

[268] S. Çınar, Ü.H. Kaynar, T. Aydemir, S.C. Kaynar, M. Ayvacıklı, An efficient removal of RB5 from aqueous solution by adsorption onto nano-ZnO/Chitosan composite beads, International Journal of Biological Macromolecules 96 (2017) 459-465.

[269] A.C. Zimmermann, A. Mecabô, T. Fagundes, C.A. Rodrigues, Adsorption of Cr (VI) using Fe-crosslinked chitosan complex (Ch-Fe), Journal of Hazardous Materials 179(1-3) (2010) 192-196.

[270] J.d.O.M. Neto, C.R. Bellato, D. de Castro Silva, Iron oxide/carbon nanotubes/chitosan magnetic composite film for chromium species removal, Chemosphere 218 (2019) 391-401.

[271] M. Lasheen, I.Y. El-Sherif, M.E. Tawfik, S. El-Wakeel, M. El-Shahat, Preparation and adsorption properties of nano magnetite chitosan films for heavy metal ions from aqueous solution, Materials Research Bulletin 80 (2016) 344-350.

[272] T. Ravi, S. Anuradha Jabasingh, Preparation and characterization of higher degree-deacetylated chitosan-coated magnetic adsorbent for the removal of chromium (VI) from its aqueous mixture, Journal of Applied Polymer Science 135(9) (2018) 45878.

[273] M.F. Horst, M. Alvarez, V.L. Lassalle, Removal of heavy metals from wastewater using magnetic nanocomposites: Analysis of the experimental conditions, Separation Science and Technology 51(3) (2016) 550-563.

[274] T.I. Shalaby, N. Fikrt, M. Mohamed, M. El Kady, Preparation and characterization of iron oxide nanoparticles coated with chitosan for removal of Cd (II) and Cr (VI) from aqueous solution, Water Science and Technology 70(6) (2014) 1004-1010.

[275] R. Bhagat, R.D. Baruah, S. Safique, Climate and tea [Camellia sinensis (L.) O. Kuntze] production with special reference to north eastern India: a review, Journal of Environmental Research and Development 4(4) (2010) 1017-1028.

[276] ASSAM, G.O. and I. COMMERCE. Tea Directory. https://industries.assam.gov.in/portlet-innerpage/about-tea-industries.

[277] C. Xiao, H. Li, Y. Zhao, X. Zhang, X. Wang, Green synthesis of iron nanoparticle by tea extract (polyphenols) and its selective removal of cationic dyes, Journal of Environmental Management 275 (2020) 111262.

[278] M. Ahmad, M. Yousaf, W. Cai, Z.-P. Zhao, Formulation of heterometallic ZIF-8@ Cu/Ni/ZnO@ CNTs heterostructure photocatalyst for Ultra-Deep desulphurization of coal and fuels, Chemical Engineering Journal 453 (2023) 139846.

[279] P. Prema, V.-H. Nguyen, K. Venkatachalam, J. Murugan, H.M. Ali, M.Z. Salem, B. Ravindran, P. Balaji, Hexavalent chromium removal from aqueous solutions using biogenic iron nanoparticles: Kinetics and equilibrium study, Environmental Research 205 (2022) 112477.

[280] V. Madhavi, T. Prasad, A.V.B. Reddy, B.R. Reddy, G. Madhavi, Application of phytogenic zerovalent iron nanoparticles in the adsorption of hexavalent chromium, Spectrochimica Acta Part A: Molecular and Biomolecular Spectroscopy 116 (2013) 17-25.

[281] A. Kaur, H. Singh, T.S. Kang, S. Singh, Sustainable preparation of Fe (OH) 3 and α-Fe2O3 nanoparticles employing Acacia catechu extract for efficient removal of chromium (VI) from aqueous solution, Environmental Nanotechnology, Monitoring & Management 16 (2021) 100593.

[282] U. Dalal, S.N. Reddy, A novel nano zero-valent iron biomaterial for chromium (Cr6+ to Cr3+) reduction, Environmental Science and Pollution Research 26(11) (2019) 10631-10640.

[283] B. Guo, M. Li, S. Li, The comparative study of a homogeneous and a heterogeneous system with green synthesized iron nanoparticles for removal of Cr (VI), Scientific reports 10(1) (2020) 1-11.

[284] P.R. Das, J.-B. Eun, A comparative study of ultra-sonication and agitation extraction techniques on bioactive metabolites of green tea extract, Food Chemistry 253 (2018) 22-29.

[285] H. Wang, K. Helliwell, X. You, Isocratic elution system for the determination of catechins, caffeine and gallic acid in green tea using HPLC, Food Chemistry 68(1) (2000) 115-121.

[286] S.A. Baba, S.A. Malik, Determination of total phenolic and flavonoid content, antimicrobial and antioxidant activity of a root extract of Arisaema jacquemontii Blume, Journal of Taibah University for Science 9(4) (2015) 449-454.

[287] E.J. Garcia, T.L.C. Oldoni, S.M.d. Alencar, A. Reis, A.D. Loguercio, R.H.M. Grande, Antioxidant activity by DPPH assay of potential solutions to be applied on bleached teeth, Brazilian Dental Journal 23 (2012) 22-27.

[288] C.P. Liang, C.H. Chang, C.C. Liang, K.Y. Hung, C.W. Hsieh, In vitro antioxidant activities, free radical scavenging capacity, and tyrosinase inhibitory of flavonoid compounds and ferulic acid from Spiranthes sinensis (Pers.) Ames, Molecules 19(4) (2014) 4681-4694.

[289] A. Dehimat, I. Azizi, V. Barragan-Montero, B. Khettal, Cytotoxicity and antioxidant activities of leaf extracts of Varthemia sericea (Batt. et Trab.) Diels, European Journal of Integrative Medicine 44 (2021) 101338.

[290] A. Lace, D. Ryan, M. Bowkett, J. Cleary, Chromium monitoring in water by colorimetry using optimised 1, 5-diphenylcarbazide method, International Journal of Environmental Research and Public Health 16(10) (2019) 1803.

[291] L.K. Leung, Y. Su, R. Chen, Z. Zhang, Y. Huang, Z.-Y. Chen, Theaflavins in black tea and catechins in green tea are equally effective antioxidants, The Journal of nutrition 131(9) (2001) 2248-2251.

[292] Q. Luo, J.-R. Zhang, H.-B. Li, D.-T. Wu, F. Geng, H. Corke, X.-L. Wei, R.-Y. Gan, Green extraction of antioxidant polyphenols from green tea (Camellia sinensis), Antioxidants 9(9) (2020) 785.

[293] J.S. Santos, C.T.P. Deolindo, L.A. Esmerino, M.I. Genovese, A. Fujita, M.B. Marques, N.D. Rosso, H. Daguer, A.C. Valese, D. Granato, Effects of time and extraction temperature on phenolic composition and functional properties of red rooibos (Aspalathus linearis), Food Research International 89 (2016) 476-487.

[294] L. Armstrong, M.A.V. do Carmo, Y. Wu, L.A. Esmerino, L. Azevedo, L. Zhang, D. Granato, Optimizing the extraction of bioactive compounds from pu-erh tea (Camellia sinensis var. assamica) and evaluation of antioxidant, cytotoxic, antimicrobial, antihemolytic, and inhibition of α-amylase and α-glucosidase activities, Food Research International 137 (2020) 109430.

[295] S. Ahmad, U. Riaz, A. Kaushik, J. Alam, Soft template synthesis of super paramagnetic Fe 3 O 4 nanoparticles a novel technique, Journal of Inorganic and Organometallic Polymers and Materials 19(3) (2009) 355-360.

[296] X. Weng, L. Huang, Z. Chen, M. Megharaj, R. Naidu, Synthesis of iron-based nanoparticles by green tea extract and their degradation of malachite, Industrial Crops and Products 51 (2013) 342-347.

[297] S. Groiss, R. Selvaraj, T. Varadavenkatesan, R. Vinayagam, Structural characterization, antibacterial and catalytic effect of iron oxide nanoparticles synthesised using the leaf extract of Cynometra ramiflora, Journal of Molecular Structure 1128 (2017) 572-578.

[298] A. Hamdan, F. Haider, Study on tea leaves extract as green corrosion inhibitor of mild steel in hydrochloric acid solution, IOP Conference Series: Materials Science and Engineering 290(1) (2018) 012086.

[299] A. Firdous, E. Ringø, P. Elumalai, Effects of green tea-and amla extracts on quality and melanosis of Indian white prawn (Fenneropenaeus indicus, Milne Edwards, 1837) during chilled storage, Aquaculture and Fisheries 6(6) (2021) 617-627.

[300] D.M. Kasote, J.H. Lee, G. Jayaprakasha, B.S. Patil, Seed priming with iron oxide nanoparticles modulate antioxidant potential and defense-linked hormones in watermelon seedlings, ACS Sustainable Chemistry & Engineering 7(5) (2019) 5142-5151.

[301] S. Lakshminarayanan, M.F. Shereen, K. Niraimathi, P. Brindha, A. Arumugam, One-pot green synthesis of iron oxide nanoparticles from Bauhinia tomentosa: Characterization and application towards synthesis of 1, 3 diolein, Scientific Reports 11(1) (2021) 1-13.

[302] N. Ballav, H. Choi, S. Mishra, A. Maity, Synthesis, characterization of Fe3O4@ glycine doped polypyrrole magnetic nanocomposites and their potential performance to remove toxic Cr (VI), Journal of Industrial and Engineering Chemistry 20(6) (2014) 4085-4093.

[303] Z. Wang, Y. Wang, S. Cao, S. Liu, Z. Chen, J. Chen, Y. Chen, J. Fu, Fabrication of core@ shell structural Fe-Fe_2O_3@PHCP nanochains with high saturation magnetization and abundant amino groups for hexavalent chromium adsorption and reduction, Journal of hazardous materials 384 (2020) 121483.

[304] M. Fazlzadeh, K. Rahmani, A. Zarei, H. Abdoallahzadeh, F. Nasiri, R. Khosravi, A novel green synthesis of zero valent iron nanoparticles (NZVI) using three plant extracts and their efficient application for removal of Cr (VI) from aqueous solutions, Advanced Powder Technology 28(1) (2017) 122-130.

[305] S. Sharma, A. Hasan, N. Kumar, L.M. Pandey, Removal of methylene blue dye from aqueous solution using immobilized Agrobacterium fabrum biomass along with iron oxide nanoparticles as biosorbent, Environmental Science and Pollution Research 25 (2018) 21605-21615.

[306] B. Zhang, R. Hu, D. Sun, T. Wu, Y. Li, Fabrication of chitosan/magnetite-graphene oxide composites as a novel bioadsorbent for adsorption and detoxification of Cr (VI) from aqueous solution, Scientific reports 8(1) (2018) 1-12.

[307] Y. Zhang, F. Yu, W. Cheng, J. Wang, J. Ma, Adsorption equilibrium and kinetics of the removal of ammoniacal nitrogen by zeolite X/activated carbon composite synthesized from elutrilithe, Journal of Chemistry 2017 (2017) 1-9.

[308] L.M. Pandey, Enhanced adsorption capacity of designed bentonite and alginate beads for the effective removal of methylene blue, Applied Clay Science 169 (2019) 102-111.

[309] R. Verma, L.M. Kundu, L.M. Pandey, Enhanced melanoidin removal by amine-modified Phyllanthus emblica leaf powder, Bioresource Technology 339 (2021) 125572.

[310] H. Tian, C. Huang, P. Wang, J. Wei, X. Li, R. Zhang, D. Ling, C. Feng, H. Liu, M. Wang, Enhanced elimination of Cr (VI) from aqueous media by polyethyleneimine modified corn straw biochar supported sulfide nanoscale zero valent iron: Performance and mechanism, Bioresource Technology 369 (2023) 128452.

[311] I.Y. Tóth, E. Illés, M. Szekeres, I. Zupkó, R. Turcu, E. Tombácz, Chondroitin-Sulfate-A-Coated Magnetite Nanoparticles: Synthesis, Characterization and Testing to Predict Their Colloidal Behavior in Biological Milieu, International Journal of Molecular Sciences 20(17) (2019) 4096.

[312] Z.-F. Yang, L.-Y. Li, C.-T. Hsieh, R.-S. Juang, Co-precipitation of magnetic Fe3O4 nanoparticles onto carbon nanotubes for removal of copper ions from aqueous solution, Journal of the Taiwan Institute of Chemical Engineers 82 (2018) 56-63.

[313] T. Yamashita, P. Hayes, Analysis of XPS spectra of Fe2+ and Fe3+ ions in oxide materials, Applied Surface Science 254(8) (2008) 2441-2449.

[314] C. Cui, Y.-D. Xie, J.-J. Niu, H.-L. Hu, S. Lin, Poly (amidoamine) dendrimer modified superparamagnetic nanoparticles as an efficient adsorbent for Cr (VI) removal: Effect of high-generation dendrimer on adsorption performance, Journal of Inorganic and Organometallic Polymers and Materials 32(3) (2022) 840-853.

[315] Y. Wei, Z. Fang, L. Zheng, E.P. Tsang, Biosynthesized iron nanoparticles in aqueous extracts of Eichhornia crassipes and its mechanism in the hexavalent chromium removal, Applied Surface Science 399 (2017) 322-329.

[316] J.B. Lu, B.X. Li, W.L. Li, X.T. Zhang, W. Zhang, P. Zhang, R.X. Su, D.F. Liu, Nano iron oxides impregnated chitosan beads towards aqueous Cr(VI) elimination: Components optimization and

performance evaluation, Colloids and Surfaces A: Physicochemical and Engineering Aspect 625 (2021) 126902.

[317] I. Maamoun, O. Falyouna, R. Eljamal, M.F. Idham, K. Tanaka, O. Eljamal, Bench-scale injection of magnesium hydroxide encapsulated iron nanoparticles (nFe0@ Mg (OH) 2) into porous media for Cr (VI) removal from groundwater, Chemical Engineering Journal 451 (2023) 138718.

[318] Y.A. Aydın, N.D. Aksoy, Adsorption of chromium on chitosan: Optimization, kinetics and thermodynamics, Chemical Engineering Journal 151(1-3) (2009) 188-194.

[319] T. Liu, Z.-L. Wang, L. Zhao, X. Yang, Enhanced chitosan/Fe0-nanoparticles beads for hexavalent chromium removal from wastewater, Chemical Engineering Journal189 (2012) 196-202.

[320] Y. Liu, H. Shan, Y. Pang, H. Zhan, C. Zeng, Iron modified chitosan/coconut shell activated carbon composite beads for Cr (VI) removal from aqueous solution, International Journal of Biological Macromolecules 224 (2023) 156-169.

[321] J. Lu, K. Xu, J. Yang, Y. Hao, F. Cheng, Nano iron oxide impregnated in chitosan bead as a highly efficient sorbent for Cr (VI) removal from water, Carbohydrate Polymer 173 (2017) 28-36.

[322] T. Liu, L. Zhao, D. Sun, X. Tan, Entrapment of nanoscale zero-valent iron in chitosan beads for hexavalent chromium removal from wastewater, Journal of Hazardous Materials 184(1-3) (2010) 724-730.

[323] T. Kekes, G. Kolliopoulos, C. Tzia, Hexavalent chromium adsorption onto crosslinked chitosan and chitosan/β-cyclodextrin beads: Novel materials for water decontamination, Journal of Environmental Chemical Engineering 9(4) (2021) 105581.

[324] T. Kekes, C. Tzia, Adsorption of indigo carmine on functional chitosan and β-cyclodextrin/chitosan beads: Equilibrium, kinetics and mechanism studies, Journal of Environmental Management 262 (2020) 110372.

[325] M. Vakili, S. Deng, T. Li, W. Wang, W. Wang, G. Yu, Novel crosslinked chitosan for enhanced adsorption of hexavalent chromium in acidic solution, Chemical Engineering Journal 347 (2018) 782-790.

[326] S.C. Dey, M. Al-Amin, T.U. Rashid, M.Z. Sultan, M. Ashaduzzaman, M. Sarker, S.M. Shamsuddin, Preparation, characterization and performance evaluation of chitosan as an adsorbent for remazol red, International Research Journal of Engineering and Technology 2(2) (2016) 52-62.

[327] J. Kurczewska, Chitosan-montmorillonite hydrogel beads for effective dye adsorption, Journal of Water Process Engineering 48 (2022) 102928.

[328] Z. Anfar, H. Ait Ahsaine, M. Zbair, A. Amedlous, A. Ait El Fakir, A. Jada, N. El Alem, Recent trends on numerical investigations of response surface methodology for pollutants adsorption onto activated carbon materials: A review, Critical Reviews in Environmental Science and Technology 50(10) (2020) 1043-1084.

[329] Y. He, J. Chen, J. Lv, Y. Huang, S. Zhou, W. Li, Y. Li, F. Chang, H. Zhang, T. Wågberg, Separable amino-functionalized biochar/alginate beads for efficient removal of Cr (VI) from original electroplating wastewater at room temperature, Journal of Cleaner Production 373 (2022) 133790.

[330] M. Hassan, Y. Liu, R. Naidu, J. Du, F. Qi, S.W. Donne, M.M. Islam, Mesoporous biopolymer architecture enhanced the adsorption and selectivity of aqueous heavy-metal ions, ACS Omega 6(23) (2021) 15316-15331.

[331] S. Chatterjee, M.W. Lee, S.H. Woo, Enhanced mechanical strength of chitosan hydrogel beads by impregnation with carbon nanotubes, Carbon 47(12) (2009) 2933-2936.

[332] S.-F. Wang, L. Shen, W.-D. Zhang, Y.-J. Tong, Preparation and mechanical properties of chitosan/carbon nanotubes composites, Biomacromolecules 6(6) (2005) 3067-3072.

[333] M.M.A. Aslam, W. Den, H.-W. Kuo, Encapsulated chitosan-modified magnetic carbon nanotubes for aqueous-phase CrVI uptake, Journal of Water Process Engineering 40 (2021) 101793.

[334] Z. Wang, Y. Wang, S. Cao, S. Liu, Z. Chen, J. Chen, Y. Chen, J. Fu, Fabrication of core@ shell structural Fe-Fe_2O_3@PHCP nanochains with high saturation magnetization and abundant amino groups for hexavalent chromium adsorption and reduction, Journal of Hazardous Materials 384 (2020) 121483.

[335] S. Wang, Y. Liu, Y. Hu, W. Shen, A magnetic MIL-125-NH2@chitosan composite as a separable adsorbent for the removal of Cr (VI) from wastewater, International Journal of Biological Macromolecule 226 (2023) 1054-1065.

[336] S. Chatterjee, S. Mahanty, P. Das, P. Chaudhuri, S. Das, Biofabrication of iron oxide nanoparticles using manglicolous fungus Aspergillus niger BSC-1 and removal of Cr (VI) from aqueous solution, Chemical Engineering Journal 385 (2020) 123790.

[337] A. Mishra, P. Tiwari, L.M. Pandey, Surface, interfacial and thermodynamic aspects of the Rhamnolipid-salt systems, Journal of Molecular Liquids (2023) 122245.

[338] R. Verma, L.M. Kundu, L.M. Pandey, Enhanced melanoidin removal by amine-modified Phyllanthus emblica leaf powder, Bioresource Technology 339 (2021) 125572.

[339] E.C. Lima, A. Hosseini-Bandegharaei, J.C. Moreno-Piraján, I. Anastopoulos, A critical review of the estimation of the thermodynamic parameters on adsorption equilibria. Wrong use of equilibrium constant in the Van't Hoof equation for calculation of thermodynamic parameters of adsorption, Journal of Molecular Liquids 273 (2019) 425-434.

[340] H.N. Tran, E.C. Lima, R.-S. Juang, J.-C. Bollinger, H.-P. Chao, Thermodynamic parameters of liquid–phase adsorption process calculated from different equilibrium constants related to adsorption isotherms: A comparison study, Journal of Environmental Chemical Engineering 9(6) (2021) 106674.

[341] S. Koushkbaghi, A. Zakialamdari, M. Pishnamazi, H.F. Ramandi, M. Aliabadi, M. Irani, Aminated-Fe_3O_4 nanoparticles filled chitosan/PVA/PES dual layers nanofibrous membrane for the removal of Cr (VI) and Pb (II) ions from aqueous solutions in adsorption and membrane processes, Chem. Eng. J. 337 (2018) 169-182.

[342] H. Shan, C. Zeng, C. Zhao, H. Zhan, Iron oxides decorated graphene oxide/chitosan composite beads for enhanced Cr (VI) removal from aqueous solution, International Journal of Biological Macromolecules 172 (2021) 197-209.

[343] I. Herath, P. Kumarathilaka, M.I. Al-Wabel, A. Abduljabbar, M. Ahmad, A.R. Usman, M. Vithanage, Mechanistic modeling of glyphosate interaction with rice husk derived engineered biochar, Microporous and Mesoporous Materials 225 (2016) 280-288.

[344] F. Zhao, E. Repo, D. Yin, L. Chen, S. Kalliola, J. Tang, E. Iakovleva, K.C. Tam, M. Sillanpää, One-pot synthesis of trifunctional chitosan-EDTA-β-cyclodextrin polymer for simultaneous removal of metals and organic micropollutants, Scientific Reports 7(1) (2017) 15811.

[345] J. Wang, X. Guo, Adsorption isotherm models: Classification, physical meaning, application and solving method, Chemosphere 258 (2020) 127279.

[346] T.L. Nguyen, A. Ayub, A. Anam, A.M. Aljuwayid, S.W. Alwash, R. Abbass, A.A.K. Ruhaima, E. Potrich, M. Sillanpaa, S. Gul, Fabrication of ZnO decorated porous chitosan beads for the sustainable bioremediation of Cr (VI) contaminated water, Journal of Environmental Chemical Engineering (2023) 110445.

[347] L. Li, Q. Liao, B. Hou, C. He, J. Liu, B. Li, M. Yu, Y. Liu, B. Lai, B. Yang, Synchronous reduction and removal of hexavalent chromium from wastewater by modified magnetic chitosan beads, Separation and Purification Technology 304 (2023) 122363.

[348] X. Liu, Y. Zhang, Y. Liu, T.a. Zhang, Magnetic red mud/chitosan based bionanocomposites for adsorption of Cr (VI) from aqueous solutions: synthesis, characterization and adsorption kinetics, Polymer Bulletin 80(2) (2023) 2099-2118.

[349] C. Jung, J. Heo, J. Han, N. Her, S.-J. Lee, J. Oh, J. Ryu, Y. Yoon, Hexavalent chromium removal by various adsorbents: powdered activated carbon, chitosan, and single/multi-walled carbon nanotubes, Separation and Purification Technology 106 (2013) 63-71.

[350] Ş. Parlayıcı, E. Pehlivan, Removal of chromium (VI) from aqueous solution using chitosan doped with carbon nanotubes, Materials Today: Proceedings 18 (2019) 1978-1985.

[351] P.B. Vilela, A. Dalalibera, E.C. Duminelli, V.A. Becegato, A.T. Paulino, Adsorption and removal of chromium (VI) contained in aqueous solutions using a chitosan-based hydrogel, Environmental Science and Pollution Research 26 (2019) 28481-28489.

[352] J. Mei, H. Zhang, Z. Li, H. Ou, A novel tetraethylenepentamine crosslinked chitosan oligosaccharide hydrogel for total adsorption of Cr (VI), Carbohydrate Polymers 224 (2019) 115154.

[353] T. Huang, Y.-w. Shao, Q. Zhang, Y.-f. Deng, Z.-x. Liang, F.-z. Guo, P.-c. Li, Y. Wang, Chitosan-cross-linked graphene oxide/carboxymethyl cellulose aerogel globules with high structure stability in liquid and extremely high adsorption ability, ACS Sustainable Chemistry & Engineering 7(9) (2019) 8775-8788.

[354] H. Zhang, R. Xiao, R. Li, A. Ali, A. Chen, Z. Zhang, Enhanced aqueous Cr (VI) removal using chitosan-modified magnetic biochars derived from bamboo residues, Chemosphere 261 (2020) 127694.

[355] Y. Yang, Y. Zhang, G. Wang, Z. Yang, J. Xian, Y. Yang, T. Li, Y. Pu, Y. Jia, Y. Li, Adsorption and reduction of Cr (VI) by a novel nanoscale FeS/chitosan/biochar composite from aqueous solution, Journal of Environmental Chemical Engineering 9(4) (2021) 105407.

[356] S. Singh, E. Arputharaj, H.-U. Dahms, A.K. Patel, Y.-L. Huang, Chitosan-based nanocomposites for removal of Cr (VI) and synthetic food colorants from wastewater, Bioresoureorce Technology 351 (2022) 127018.

[357] A. Vasilev, M. Efimov, G. Bondarenko, V. Kozlov, E. Dzidziguri, G. Karpacheva, Thermal behavior of chitosan as a carbon material precursor under IR radiation, IOP Conference Series: Materials Science and Engineering, IOP Publishing, 2019, p. 012002.

[358] K. Wang, Q. Liu, Adsorption of phosphorylated chitosan on mineral surfaces, Colloids and Surfaces A: Physicochemical and Engineering Aspects 436 (2013) 656-663.

[359] A. Grosvenor, B. Kobe, M.C. Biesinger, N. McIntyre, Investigation of multiplet splitting of Fe 2p XPS spectra and bonding in iron compounds, Surface and Interface Analysis 36(12) (2004) 1564-1574.

[360] K. Djebaili, Z. Mekhalif, A. Boumaza, A. Djelloul, XPS, FTIR, EDX, and XRD analysis of Al 2 O 3 scales grown on PM2000 alloy, Journal of Spectroscopy 2015 (2015).

[361] Y. Chen, D. An, S. Sun, J. Gao, L. Qian, Reduction and removal of chromium VI in water by powdered activated carbon, Materials 11(2) (2018) 269.

[362] R. Heacock, L. Marion, The infrared spectra of secondary amines and their salts, Canadian Journal of Chemistry 34(12) (1956) 1782-1795.

[363] M. Boulet-Audet, F. Vollrath, C. Holland, Identification and classification of silks using infrared spectroscopy, Journal of Experimental Biology 218(19) (2015) 3138-3149.

[364] E.M. Dahmane, M. Taourirte, N. Eladlani, M. Rhazi, Extraction and characterization of chitin and chitosan from Parapenaeus longirostris from Moroccan local sources, International Journal of Polymer Analysis and Characterization 19(4) (2014) 342-351.

[365] V. Vats, G. Melton, M. Islam, V.V. Krishnan, FTIR spectroscopy as a convenient tool for detection and identification of airborne Cr (VI) compounds arising from arc welding fumes, Journal of Hazardous Materials 448 (2023) 130862.

[366] C. Shen, H. Li, Y. Wen, F. Zhao, Y. Zhang, D. Wu, Y. Liu, F. Li, Spherical Cu2O-Fe3O4@ chitosan bifunctional catalyst for coupled Cr-organic complex oxidation and Cr (VI) capture-reduction, Chemical Engineering Journal 383 (2020) 123105.

[367] B. Wang, Y. Wan, Y. Zheng, X. Lee, T. Liu, Z. Yu, J. Huang, Y.S. Ok, J. Chen, B. Gao, Alginate-based composites for environmental applications: a critical review, Critical reviews in Environmental Science and Technology 49(4) (2019) 318-356.

[368] K. Varaprasad, D. Nùñez, W. Ide, T. Jayaramudu, E.R. Sadiku, Development of high alginate comprised hydrogels for removal of Pb (II) ions, Journal of Molecular Liquids 298 (2020) 112087.

[369] P. Qu, Y. Li, H. Huang, J. Chen, Z. Yu, J. Huang, H. Wang, B. Gao, Urea formaldehyde modified alginate beads with improved stability and enhanced removal of Pb^{2+}, Cd^{2+}, and Cu^{2+}, Journal of Hazardous Materials 396 (2020) 122664.

[370] S.C. Motshekga, S.S. Ray, A. Maity, Synthesis and characterization of alginate beads encapsulated zinc oxide nanoparticles for bacteria disinfection in water, Journal of Colloid and Interface Science 512 (2018) 686-692.

[371] Y.-N. Chen, L. Peng, T. Liu, Y. Wang, S. Shi, H. Wang, Poly (vinyl alcohol)–tannic acid hydrogels with excellent mechanical properties and shape memory behaviors, ACS Applied Materials & Interfaces 8(40) (2016) 27199-27206.

[372] R. Liao, Z. Tang, Y. Lei, B. Guo, Polyphenol-reduced graphene oxide: mechanism and derivatization, The Journal of Physical Chemistry C 115(42) (2011) 20740-20746.

[373] M. Mohseni, S. Akbari, E. Pajootan, F. Mazaheri, Amine-terminated dendritic polymers as a multifunctional chelating agent for heavy metal ion removals, Environmental Science and Pollution Research 26(13) (2019) 12689-12697.

[374] N.P. Wickramaratne, V.S. Perera, J.M. Ralph, S.D. Huang, M. Jaroniec, Cysteine-assisted tailoring of adsorption properties and particle size of polymer and carbon spheres, Langmuir 29(12) (2013) 4032-4038.

[375] X. Jiang, W. Long, L. Peng, T. Xu, F. He, Y. Tang, W. Zhang, Reductive immobilization of Cr (VI) in contaminated water by tannic acid, Chemosphere 297 (2022) 134081.

[376] A. Üçer, A. Uyanik, Ş. Aygün, Adsorption of Cu (II), Cd (II), Zn (II), Mn (II) and Fe (III) ions by tannic acid immobilised activated carbon, Separation and Purification Technology 47(3) (2006) 113-118.

[377] L. Zou, P. Shao, K. Zhang, L. Yang, D. You, H. Shi, S.G. Pavlostathis, W. Lai, D. Liang, X. Luo, Tannic acid-based adsorbent with superior selectivity for lead (II) capture: Adsorption site and selective mechanism, Chemical Engineering Journal 364 (2019) 160-166.

[378] M. Zhang, S. Zhang, X. Liu, H. Chen, Y. Ming, Q. Xu, Z. Wang, One-pot synthesis of multi-functional and environmental friendly tannic acid polymer with Fe3+ and formaldehyde as double crosslinking agents for selective removal of cation pollutants, Environmental Science and Pollution Research 26(31) (2019) 31834-31845.

[379] C. Cheng, M. Jia, L. Cui, Y. Li, L. Xu, X. Jin, Adsorption of Cr (VI) ion on tannic acid/graphene oxide composite aerogel: kinetics, equilibrium, and thermodynamics studies, Biomass Conversion and Biorefinery (2020) 1-11.

[380] H. Ejima, J.J. Richardson, K. Liang, J.P. Best, M.P. van Koeverden, G.K. Such, J. Cui, F. Caruso, One-step assembly of coordination complexes for versatile film and particle engineering, Science 341(6142) (2013) 154-157.

[381] L. Yang, H. Sun, W. Jiang, T. Xu, B. Song, R. Peng, L. Han, L. Jia, A chemical method for specific capture of circulating tumor cells using label-free polyphenol-functionalized films, Chemistry of Materials 30(13) (2018) 4372-4382.

[382] H. Zhang, C. Lin, X. Hu, B. Zhu, D. Yu, Effective Dual Polysulfide Rejection by a Tannic Acid/FeIII Complex-Coated Separator in Lithium–Sulfur Batteries, ACS applied materials & Interfaces 10(15) (2018) 12708-12715.

[383] T. Hu, Q. Liu, T. Gao, K. Dong, G. Wei, J. Yao, Facile preparation of tannic acid–poly (vinyl alcohol)/sodium alginate hydrogel beads for methylene blue removal from simulated solution, ACS omega 3(7) (2018) 7523-7531.

[384] H. Zhang, Y. Cheng, X. Hou, B. Yang, F. Guo, Ionic effects on the mechanical and swelling properties of a poly (acrylic acid/acrylamide) double crosslinking hydrogel, New Journal of Chemistry 42(11) (2018) 9151-9158.

[385] C.D. Bucak, Porous alginate hydrogel beads cross-linked with citric acid containing tannic acid: structural analysis, antimicrobial properties and release behavior, Cellulose 30(2) (2023) 1117-1132.

[386] E. Haslam, Plant polyphenols (syn. vegetable tannins) and chemical defense—a reappraisal, Journal of Chemical Ecology 14 (1988) 1789-1805.

[387] A.M. Sousa, T.-D. Li, S. Varghese, P.J. Halling, K.H. Aaron Lau, Highly active protein surfaces enabled by plant-based polyphenol coatings, ACS Applied Materials & Interfaces 10(45) (2018) 39353-39362.

[388] J. Briffa, E. Sinagra, R. Blundell, Heavy metal pollution in the environment and their toxicological effects on humans, Heliyon 6(9) (2020).

[389] C. Bertagnolli, A. Grishin, T. Vincent, E. Guibal, Synthesis and application of a novel sorbent (tannic acid-grafted-polyethyleneimine encapsulated in alginate beads) for heavy metal removal, Separation Science and Technology 50(18) (2015) 2897-2906.

[390] J. Kong, Q. Yue, S. Sun, B. Gao, Y. Kan, Q. Li, Y. Wang, Adsorption of Pb (II) from aqueous solution using keratin waste–hide waste: equilibrium, kinetic and thermodynamic modeling studies, Chemical Engineering Journal 241 (2014) 393-400.

[391] WHO, Guidelines for drinking water. Quality, 4th Edition, World Health Organization, (2022).

[392] I. 10500, Indian Standard Drinking Water–Specification, Bureau of Indian Standards, New Delhi, India. , (2012).

[393] C.P.C.B. Delhi, The Environment (protection) Rules, 1986, Schedule VI (Amended 1993). , (1986).

[394] E.O. Eteshola, D.A. Haupt, S.I. Koos, L.A. Siemer, D.L. Morris Jr, The role of metal ion binding in the antioxidant mechanisms of reduced and oxidized glutathione in metal-mediated oxidative DNA damage, Metallomics 12(1) (2020) 79-91.

[395] S. Quideau, D. Deffieux, C. Douat-Casassus, L. Pouységu, Plant polyphenols: chemical properties, biological activities, and synthesis, Angewandte Chemie International Edition 50(3) (2011) 586-621.

[396] S.J. Flora, Structural, chemical and biological aspects of antioxidants for strategies against metal and metalloid exposure, Oxidative Medicine and Cellular Longevity 2 (2009) 191-206.

[397] D.G. Barrett, D.E. Fullenkamp, L. He, N. Holten-Andersen, K.Y.C. Lee, P.B. Messersmith, pH-based regulation of hydrogel mechanical properties through mussel-inspired chemistry and processing, Advanced Functional Materials 23(9) (2013) 1111-1119.

[398] S. Cakar, M. Özacar, The pH dependent tannic acid and Fe-tannic acid complex dye for dye sensitized solar cell applications, Journal of Photochemistry and Photobiology A: Chemistry 371 (2019) 282-291.

[399] A. Haug, Dissociation of alginic acid, Acta Chem. Scand 15(4) (1961) 950-952.

[400] G. Ghigo, S. Berto, M. Minella, D. Vione, E. Alladio, V. Nurchi, J. Lachowicz, P. Daniele, New insights into the protogenic and spectroscopic properties of commercial tannic acid: the role of gallic acid impurities, New Journal of Chemistry 42(10) (2018) 7703-7712.

[401] F.J. Millero, Solubility of Fe (III) in seawater, Earth and Planetary Science Letters 154(1-4) (1998) 323-329.

[402] A. Jawed, L.M. Pandey, Application of bimetallic Al-doped ZnO nano-assembly for heavy metal removal and decontamination of wastewater, Water Science and Technology 80(11) (2019) 2067-2078.

[403] Y. Zhang, Y. Li, L.-q. Yang, X.-j. Ma, L.-y. Wang, Z.-F. Ye, Characterization and adsorption mechanism of Zn^{2+} removal by PVA/EDTA resin in polluted water, Journal of Hazardous Materials 178(1-3) (2010) 1046-1054.

[404] A.C.V. dos Santos, J.C. Masini, Evaluating the removal of Cd (II), Pb (II) and Cu (II) from a wastewater sample of a coating industry by adsorption onto vermiculite, Applied Clay Science 37(1-2) (2007) 167-174.

[405] T.S. Sileika, D.G. Barrett, R. Zhang, K.H.A. Lau, P.B. Messersmith, Colorless multifunctional coatings inspired by polyphenols found in tea, chocolate, and wine, Angewandte Chemie 125(41) (2013) 10966-10970.

[406] H. Guo, L.E. Peng, Z. Yao, Z. Yang, X. Ma, C.Y. Tang, Non-polyamide based nanofiltration membranes using green metal–organic coordination complexes: implications for the removal of trace organic contaminants, Environmental Science & Technology 53(5) (2019) 2688-2694.

[407] Y. Zhang, Y. Su, X. Zhou, C. Dai, A.A. Keller, A new insight on the core–shell structure of zerovalent iron nanoparticles and its application for Pb (II) sequestration, Journal of Hazardous Materials 263 (2013) 685-693.

[408] H.-C. Flemming, Biofouling in water systems–cases, causes and countermeasures, Applied Microbiology and Biotechnology 59 (2002) 629-640.

[409] T. Nguyen, F.A. Roddick, L. Fan, Biofouling of water treatment membranes: a review of the underlying causes, monitoring techniques and control measures, Membranes 2(4) (2012) 804-840.

[410] H.-C. Kim, B.A. Dempsey, Membrane fouling due to alginate, SMP, EfOM, humic acid, and NOM, Journal of Membrane Science 428 (2013) 190-197.

[411] Y. Bashan, J.-P. Hernandez, L.A. Leyva, M. Bacilio, Alginate microbeads as inoculant carriers for plant growth-promoting bacteria, Biology and Fertility of Soils 35 (2002) 359-368.

[412] B. Kaczmarek, Tannic acid with antiviral and antibacterial activity as a promising component of biomaterial - A minireview, Materials 13(14) (2020) 3224.

[413] R. Irshad, K. Tahir, B. Li, A. Ahmad, A.R. Siddiqui, S. Nazir, Antibacterial activity of biochemically capped iron oxide nanoparticles: A view towards green chemistry, Journal of Photochemistry and Photobiology B: Biology 170 (2017) 241-246.

[414] S. Faisal, S. Sadiq, M. Mustafa, M.H. Khan, M. Sadiq, Z. Iqbal, M. Khan, Tailoring the antibacterial and antioxidant activities of iron nanoparticles with amino benzoic acid, RSC Sustainability 1(1) (2023) 139-146.

[415] L. Kosaristanova, M. Rihacek, F. Sucha, V. Milosavljevic, P. Svec, J. Dorazilova, L. Vojtova, P. Antal, P. Kopel, Z. Patocka, Synergistic antibacterial action of the iron complex and ampicillin against *Staphylococcus aureus*, BMC Microbiology 288 (2023).

[416] S.A. Katz, H. Salem, The toxicology of chromium with respect to its chemical speciation: a review, Journal of Applied Toxicology 13(3) (1993) 217-224.

[417] K.Z. Setshedi, M. Bhaumik, M.S. Onyango, A. Maity, High-performance towards Cr (VI) removal using multi-active sites of polypyrrole–graphene oxide nanocomposites: Batch and column studies, Chemical Engineering Journal 262 (2015) 921-931.

[418] R.M. Sedman, J. Beaumont, T.A. McDonald, S. Reynolds, G. Krowech, R. Howd, Review of the evidence regarding the carcinogenicity of hexavalent chromium in drinking water, Journal of Environmental Science and Health Part C 24(1) (2006) 155-182.

[419] M. Costa, Potential hazards of hexavalent chromate in our drinking water, Toxicology and Applied Pharmacology 188(1) (2003) 1-5.

[420] G.H. Chala, T.D. Zeleke, Green synthesis of magnetite nanoparticles using Catha edulis plant leaf extract for removal of hexavalent Chromium from aqueous solution, International Journal of Nano Dimension 14(1) (2023) 73-90.

[421] H. Li, Z.-t. Han, Q. Deng, C.-x. Ma, X.-k. Kong, Assessing the effectiveness of nanoscale zero-valent iron particles produced by green tea for Cr (VI)-contaminated groundwater remediation, Journal of Groundwater Science and Engineering 11(1) (2023) 55-67.

[422] M. López-García, M. Martínez-Cabanas, T. Vilariño, P. Lodeiro, P. Rodríguez-Barro, R. Herrero, J.L. Barriada, New polymeric/inorganic hybrid sorbents based on red mud and nanosized magnetite for large scale applications in As (V) removal, Chemical Engineering Journal 311 (2017) 117-125.

[423] R. Singh, B. Sengupta, R. Bali, B. Shukla, V. Gurunadharao, R. Srivatstava, Identification and mapping of chromium (VI) plume in groundwater for remediation: A case study at Kanpur, Uttar Pradesh, Journal of the Geological Society of India 74 (2009) 49-57.

[424] G.R. Bhagure, S. Mirgane, Heavy metal concentrations in groundwaters and soils of Thane Region of Maharashtra, India, Environmental Monitoring and Assessment 173 (2011) 643-652.

[425] A. Banchhor, M. Pandey, P.K. Pandey, Hexavalent chromium contamination of groundwater in Bhilai City: Potential public health crisis in Central-East India, Ecology, Environment and Conservation Journal 26 (2020) S86-S95.

[426] S.M. Tripathi, S. Chaurasia, Detection of Chromium in surface and groundwater and its bio-absorption using bio-wastes and vermiculite, Engineering Science and Technology, 23(5) (2020) 1153-1161.

[427] R. Li, Q.-D. An, Z.-Y. Xiao, B. Zhai, S.-R. Zhai, Z. Shi, Preparation of PEI/CS aerogel beads with a high density of reactive sites for efficient Cr (VI) sorption: batch and column studies, RSC Advances 7(64) (2017) 40227-40236.

[428] V. Vinodhini, N. Das, Packed bed column studies on Cr (VI) removal from tannery wastewater by neem sawdust, Desalination 264(1-2) (2010) 9-14.

[429] P.K. Gautam, R.K. Gautam, S. Banerjee, M. Chattopadhyaya, J. Pandey, Heavy metals in the environment: fate, transport, toxicity and remediation technologies, Nova Science Publishers 60 (2016) 101-130.

[430] P.R. Rout, P. Bhunia, R.R. Dash, Evaluation of kinetic and statistical models for predicting breakthrough curves of phosphate removal using dolochar-packed columns, Journal of Water Process Engineering 17 (2017) 168-180.

[431] S.K. Mani, R. Bhandari, Efficient Fluoride Removal by a Fixed-Bed Column of Self-Assembled Zr (IV)-, Fe (III)-, Cu (II)-Complexed Polyvinyl Alcohol Hydrogel Beads, ACS omega 7(17) (2022) 15048-15063.

[432] Y. Yan, Q. An, Z. Xiao, W. Zheng, S. Zhai, Flexible core-shell/bead-like alginate@ PEI with exceptional adsorption capacity, recycling performance toward batch and column sorption of Cr (VI), Chemical Engineering Journal 313 (2017) 475-486.

[433] I. Kavianinia, P.G. Plieger, N.G. Kandile, D.R. Harding, Fixed-bed column studies on a modified chitosan hydrogel for detoxification of aqueous solutions from copper (II), Carbohydrate Polymers 90(2) (2012) 875-886.

[434] A. Ahmad, B. Hameed, Fixed-bed adsorption of reactive azo dye onto granular activated carbon prepared from waste, Journal of Hazardous Materials 175(1-3) (2010) 298-303.

[435] H. Patel, Fixed-bed column adsorption study: a comprehensive review, Applied Water Science 9(3) (2019) 45.

[436] G. Bohart, E. Adams, Behavior of charcoal towards chlorine, Journal of the Chemical Society 42(7) (1920) 523-529.

[437] M. Bhaumik, A. Maity, V. Srinivasu, M.S. Onyango, Removal of hexavalent chromium from aqueous solution using polypyrrole-polyaniline nanofibers, Chemical Engineering Journal 181 (2012) 323-333.

[438] M. Banerjee, N. Bar, R.K. Basu, S.K. Das, Comparative study of adsorptive removal of Cr (VI) ion from aqueous solution in fixed bed column by peanut shell and almond shell using empirical models and ANN, Environmental Science and Pollution Research 24 (2017) 10604-10620.

[439] W.W. Ngah, L. Teong, R. Toh, M. Hanafiah, Utilization of chitosan–zeolite composite in the removal of Cu (II) from aqueous solution: adsorption, desorption and fixed bed column studies, Chemical Engineering Journal 209 (2012) 46-53.

[440] W. Zou, L. Zhao, L. Zhu, Adsorption of uranium (VI) by grapefruit peel in a fixed-bed column: experiments and prediction of breakthrough curves, Journal of Radioanalytical and Nuclear Chemistry 295 (2013) 717-727.

[441] A.D. Dorado, X. Gamisans, C. Valderrama, M. Solé, C. Lao, Cr (III) removal from aqueous solutions: a straightforward model approaching of the adsorption in a fixed-bed column, Journal of Environmental Science and Health, Part A 49(2) (2014) 179-186.

[442] B.S. Chittoo, C. Sutherland, Column breakthrough studies for the removal and recovery of phosphate by lime-iron sludge: Modeling and optimization using artificial neural network and adaptive neuro-fuzzy inference system, Chinese Journal of Chemical Engineering 28(7) (2020) 1847-1859.

[443] S. Chen, Q. Yue, B. Gao, Q. Li, X. Xu, K. Fu, Adsorption of hexavalent chromium from aqueous solution by modified corn stalk: a fixed-bed column study, Bioresource Technology 113 (2012) 114-120.

[444] P. Suksabye, P. Thiravetyan, W. Nakbanpote, Column study of chromium (VI) adsorption from electroplating industry by coconut coir pith, Journal of Hazardous Materials 160(1) (2008) 56-62.

[445] D. Chauhan, N. Sankararamakrishnan, Modeling and evaluation on removal of hexavalent chromium from aqueous systems using fixed bed column, Journal of Hazardous Materials 185(1) (2011) 55-62.

[446] L. Tielong, G. Bing, Z. Na, J. Zhaohui, Q. Xinhua, Hexavalent chromium removal from water using chitosan-Fe^0 nanoparticles, Journal of Physics: Conference Series, IOP Publishing, 2009, p. 012057.

[447] M.M.A. Aslam, W. Den, H.-W. Kuo, Removal of hexavalent chromium by encapsulated chitosan-modified magnetic carbon nanotubes: fixed-bed column study and modelling, Journal of Water Process Engineering 42 (2021) 102143.

[448] A. Shokati Poursani, A. Nilchi, A. Hassani, S. Tabibian, L. Asad Amraji, Synthesis of nano-γ-Al_2O_3/chitosan beads (AlCBs) and continuous heavy metals removal from liquid solution, International Journal of Environmental Science and Technology 14 (2017) 1459-1468.

[449] K. Ravikumar, D. Kumar, G. Kumar, P. Mrudula, C. Natarajan, A. Mukherjee, Enhanced Cr (VI) removal by nanozerovalent iron-immobilized alginate beads in the presence of a biofilm in a continuous-flow reactor, Industrial & Engineering Chemistry Research 55(20) (2016) 5973-5982.

[450] S. Liang, W. Cai, C. Dang, X. Peng, Z. Luo, X. Wei, Synthesis of sodium alginate/phosphorus tetramethylmethyl sulfate biocomposite beads with exceptional adsorption rate for Cr (VI) removal, Journal of Environmental Chemical Engineering 11(2) (2023) 109317.

[451] D.-M. Guo, Q.-D. An, Z.-Y. Xiao, S.-R. Zhai, Z. Shi, Polyethylenimine-functionalized cellulose aerogel beads for efficient dynamic removal of chromium (VI) from aqueous solution, RSC Advances 7(85) (2017) 54039-54052.

[452] S. Debnath, K. Biswas, U.C. Ghosh, Removal of Ni (II) and Cr (VI) with Titanium (IV) oxide nanoparticle agglomerates in fixed-bed columns, Industrial & Engineering Chemistry Research 49(5) (2010) 2031-2039.

[453] H.-J. Park, L.L. Tavlarides, Adsorption of chromium (VI) from aqueous solutions using an imidazole functionalized adsorbent, Industrial & Engineering Chemistry Research 47(10) (2008) 3401-3409.

Research output

Award

1. **Commonwealth Split-site Fellowship-2020** for one year (January 2020 to January 2021) to work at Dr. Lau's lab, Dept. of Pure and Applied Chemistry at University of Strathclyde, Glasgow, UK.

Journal Publications (incorporated in the thesis)

1. **Aquib Jawed**, Animes K. Golder, and Lalit M. Pandey (2023), *"Synthesis of iron oxide nanoparticles mediated by Camellia sinensis var. Assamica for Cr (VI) adsorption and detoxification".* **Bioresource Technology, 376, 128816**. **doi: 10.1016/j.biortech.2023.128816.**
2. **Aquib Jawed**, Animes K. Golder, and Lalit M. Pandey (2024), "*Bio-based Iron Oxide Nanoparticles Forming Bi-functional Chitosan Composite Adsorbent for Cr(VI) Decontamination".* **Chemical Engineering Journal, 481, 148411. doi: 10.1016/j.cej.2023.148411.**
3. **Aquib Jawed**, Swati Sharma, Animes K. Golder, and Lalit M. Pandey (2021), "*Plant-polyphenol-mediated synthesis of iron oxide nanomaterials for heavy metal removal: A review".* **New Trends in Removal of Heavy Metals from Industrial Wastewater**, **Elsevier**, **p. 115-129. doi: 10.1016/B978-0-12-822965-1.00006-4.**
4. **Aquib Jawed,** Aiman Rizvi, Michelle Maclean, Christine Davidson, Animes K. Golder, Lalit M. Pandey, and King Hang Aaron Lau, "*Tannic Acid and Fe Enhanced Alginate Hydrogels for Sustainable Water Remediation"* **(Communicated)**
5. **Aquib Jawed**, Animes K. Golder, and Lalit M. Pandey, "*Chromium(VI) Removal in a Fixed-Bed Column using Green Synthesized Iron Oxide Nanoparticles Impregnated in Chitosan and Sodium Alginate Matrix"* **(Communicated)**

Conferences and Workshops

1. **Aquib Jawed**, Animes K. Golder, King Hang Aaron Lau, and Lalit M Pandey, Synthesis of Polyphenols coated Biosorbent beads for Environmental Remediation purposes. One-day workshop on Recent Advances in Water Contaminants Evaluation and Remediation, University of Strathclyde, Glasgow, United Kingdom, Feb 4, 2020.
2. **Aquib Jawed,** Animes K. Golder, King Hang Aaron Lau and Lalit M. Pandey, Preparation of Tannic Acid coated biosorbent beads for environmental remediation purposes. 12th Scottish Symposium on Environmental Analytical Chemistry University of Glasgow Sponsored by Royal Society of Chemistry, Analytical Division, Scottish Region, Dec 7, 2020.
3. **Aquib Jawed,** Animes K. Golder, and Lalit M. Pandey, Green synthesized Iron oxide nanoparticles using leaf extract of *Camellia sinensi* for the removal of hexavalent chromium. International Conference on Biotechnology for Resource Efficiency, Energy, Environment, Chemicals and Health, December 1 - 4, 2021, CSIR Indian Institute of Petroleum, Dehradun, India.
4. **Aquib Jawed,** Animes K. Golder, and Lalit M. Pandey, Green synthesized Iron oxide nanoparticles using leaf extract of *Camellia sinensis var. assamica* for the reduction of hexavalent chromium. North-East Research Conclave, Assam Biotech Conclave 2022 Indian Institute of Technology Guwahati, India, May 20 - 22, 2022.
5. **Aquib Jawed,** Animes K. Golder, and Lalit M. Pandey, Green synthesized Iron oxide nanoparticles using leaf extract of *Camellia sinensis var. assamica* for the removal of hexavalent chromium. International Conference on Biotechnology, Sustainable Bioresources and Bioeconomy (BSBB-2022) Indian Institute of Technology, Guwahati, India December 7-11, 2022.
6. **Aquib Jawed,** Animes K. Golder, King Hang Aaron Lau, and Lalit M. Pandey, International conference on Bioinspired Nanomaterials: From Biomolecular Structure and Soft Matter to Biomimetic Materials and Applications, Technology and Innovation Centre, University of Strathclyde, Glasgow, March 18-19, 2019.
7. **Aquib Jawed,** Animes K. Golder, and Lalit M. Pandey, One-day Workshop on Recent Advances on Bio-inspired Nanomaterials for Environmental Applications, Centre for the Environment, IIT Guwahati, December 18, 2018.

Other Publications

1. **Aquib Jawed,** Varun Saxena, and Lalit M. Pandey (2020), "*Engineered nanomaterials and their surface functionalization for the removal of heavy metals: A review".* **Journal of Water Process Engineering, 33, 101009. doi: 10.1016/j.jwpe.2019.101009.**
2. **Aquib Jawed** and Lalit M. Pandey (2019), "*Application of bimetallic Al-doped ZnO nano-assembly for heavy metal removal and decontamination of wastewater"*. **Water Science and Technology, 80.11, 2067-2078. doi: 10.2166/wst.2019.393.**
3. **Aquib Jawed**, Rahul Verma, Varun Saxena, Lalit M. Pandey (2021), "*Photocatalytic Metal Nanoparticles: A Green approach for Degradation of Dyes".* **Photocatalytic Degradation of Dyes, Elsevier, p. 251-275. doi: 10.1016/B978-0-12-823876-9.00003-2.**
4. **Aquib Jawed**, Prasenjit Kar, Rahul Verma, Komal Shukla, Hemanth, Vijay Kumar Thakur, Lalit M. Pandey, and Raju Kumar Gupta (2022), "*Integration of biological control with engineered heterojunction nano-photocatalysts for sustainable and effective management of water hyacinth weed".* **Journal of Environmental Chemical Engineering, 10, 106976. doi: 10.1016/j.jece.2021.106976.**
5. Hamish Swanson, Marwa El yaagoubi, **Aquib Jawed**, Varun Saxena, Tell Tuttle, Ian W. Hamley, and King Hang Aaron Lau (2023), "*Peptoid Self-Assembly. from Minimal Sequences to Lipidation and Antimicrobial Applications".* **Advanced Design of Self-Assembled Functional Materials, Wiley, 3, p. 969-999. doi: 10.1002/9783527834044.ch36.**
6. Rushikesh Fopase, **Aquib Jawed**, and Lalit M. Pandey (2023), "*Biointerface Phenomenon in Biological Science and Bioengineering: Improtance of Engineering Courses".* **Engineering Pedagogy: A Collection of Articles in Honor of Prof. Amitabha Ghosh. Singapore: Springer Nature, p. 185-204. doi: 10.1007/978-981-19-8016-9_14.**
7. **Aquib Jawed,** Apoorva Sharad, Ayush Chutani, Mehak, and Lalit M. Pandey. "*Amine functionalized Fe(III)-doped-ZnO nanoparticles based alginate beads for the removal of Cu(II) from aqueous solution"* **Nano-Structures & Nano-Objects, 38, 101199. doi: https://doi.org/10.1016/j.nanoso.2024.101199.**
8. **Aquib Jawed,** Anurag Mishra, and Lalit M. Pandey. "*PleInsight on mechanism of green synthesis of iron oxides nanomaterials: Investigation on role of various parameters"* **(Under Review).**